

A systematic study of intermolecular interactions
in non-covalently bound complexes
by using and expanding
advanced broadband rotational spectroscopy.

KUMULATIVE DISSERTATION

zur Erlangung des Doktorgrades
an der Fakultät für Mathematik, Informatik und Naturwissenschaften
Fachbereich Chemie
der Universität Hamburg

Angefertigt am Max-Planck-Institut für
Struktur und Dynamik der Materie
und
am Deutschen Elektronen-Synchrotron,
Ein Forschungszentrum der Helmholtz-Gemeinschaft

Mariyam Fatima
aus Neu-Delhi, Indien

Hamburg
2020

Gutachter der Dissertation:

Prof. Dr. Melanie Schnell

Prof. Dr. Holger Lange

Gutachter der Disputation:

Prof. Dr. Henning Tidow

Prof. Dr. Melanie Schnell

Vorsitzender des Prüfungsausschusses:

Prof. Dr. Horst Weller

Datum der Disputation:

03.06.2020

Druckfreigabe:

14.09.2020

List of Publications

1. D. Bernhard, F. Dietrich, M. Fatima, C. Pérez, A. Poblitzki, G. Jansen, M. A. Suhm, M. Schnell, M. Gerhards *Multi-spectroscopic and theoretical analyses on the diphenyl ether-tert-butyl alcohol complex in the electronic ground and electronically excited state*, Phys. Chem. Chem. Phys. **19**, 18076-18088 (2017). [Impact factor- 3.6]
2. F. Dietrich, D. Bernhard, M. Fatima, C. Pérez, M. Schnell, M. Gerhards *The Effect of Dispersion on the Structure of Diphenyl Ether Aggregates*, Angew. Chem. Int. Ed. **57**, 9534 (2018). [Impact factor- 12.2]
3. D. Bernhard, F. Dietrich, M. Fatima, C. Pérez, H.C. Gottschalk, A. Wuttke, R. A. Mata, M.A. Suhm, M. Schnell, M. Gerhards *The phenyl vinyl ether-methanol complex: a model system for quantum chemistry benchmarking*, Beilstein J. Org. Chem. **14**, 1642–1654 (2018). [Impact factor- 2.6]
4. M. Fatima, A. L. Steber, A. Poblitzki, C. Pérez, S. Zinn, M. Schnell *Rotational Signatures of Dispersive Stacking in the Formation of Aromatic Dimers*, Angew. Chem. Int. Ed. **58**, 3108 (2019). [Impact factor- 12.2]
5. D. Bernhard, M. Fatima, A. Poblitzki, A. L. Steber, C. Pérez, M. A. Suhm, M. Schnell and M. Gerhards *Dispersion-controlled docking preference: multi-spectroscopic study on complexes of dibenzofuran with alcohols and water*, Phys. Chem. Chem. Phys. **21**, 16032-16046 (2019). [Impact factor- 3.6]
6. H. C. Gottschalk, A. Poblitzki, M. Fatima, D. A. Obenchain, C. Pérez, J. Antony, A. A. Auer, L. Baptista, D. M. Benoit, G. Bistoni, F. Bohle, R. Dahmani, D. Firaha, S. Grimme, A. Hansen, M. E. Harding, M. Hochlaf, C. Holzer, G. Jansen, W. Klopper, W. A. Kopp, M. Krasowska, L. C. Kröger, K. Leonhard, M. M. Al-Mogren, H. Mouhib, F. Neese, M. N. Pereira, M. Prakash, I. S. Ulusoy, R. A. Mata, M. A. Suhm, and M. Schnell *The first microsolvation step for furans: New experiments and benchmarking strategies*, J. Chem. Phys. **152**, 164303 (2020). [Impact factor- 2.9]

7. M. Fatima, C. Pérez, B. E. Arenas, M. Schnell, and A. L. Steber, *Benchmarking a new segmented K-band chirped-pulse microwave spectrometer and its application to the conformationally rich amino alcohol isoleucinol*, Phys. Chem. Chem. Phys. (2020). [Impact factor- 3.6]
8. B. E. Arenas, M. Fatima, C. Pérez, S. Fischer, A. L. Steber and M. Schnell, *Facilitating interstellar searches for simple amino alcohols with accurate rest frequencies into the millimeter-wave regime: Alaninol, valinol, and leucinol*, The Astrophysical Journal, 2020, Submitted.
9. M. Fatima, D. Maué, C. Perez, D. Tikhonov, D. Bernhard, A. Stamm, C. Medcraft, M. Gerhards, M. Schnell, *The structures and internal dynamics of diphenylether and its aggregates with water*, Phys. Chem. Chem. Phys. 2020, Submitted.

Abstract

The interplay between intra- and intermolecular forces, with hydrogen bonding and London dispersion interactions being among the most important ones, drives biomolecular aggregation and recognition processes. Although London dispersion interactions were described in 1930 by Fritz London, the importance of their contribution to intra- and intermolecular interactions is still not well understood at the quantitative level. With geometrically well-defined molecular model systems, where the interplay between dispersion and hydrogen bonding is particularly interesting, it is possible to systematically examine and quantify the London dispersion contribution to intermolecular interaction energies.

The spectroscopy of the model systems in a cold environment can give spectroscopic data of these systems at low temperatures and isolated conditions, and this data can be directly compared with the results from various theoretical methods. Further, the experimental information can be taken to benchmark quantum-chemical methods and can be utilized in the development and the testing of newer theoretical methods. Rotational spectroscopy, as employed in this work, is a high resolution and highly sensitive technique, which provides accurate structural information on the different binding sites in the model systems and about the intra- and intermolecular interactions within these complexes.

Within the framework of this thesis, three kinds of complexes were studied in a systematic approach, which can serve as suitable challenging systems for the theoretical description and characterization of dispersion interactions. The first explores the effect of dispersion interactions when complexes are dominated by a strong classical OH–O hydrogen bond, as studied in camphor complexes with methanol and ethanol, respectively. In the second category, the effect of dispersion interaction is explored when complexes can form either via strong, classical OH–O hydrogen bonds and weaker OH– π bonds in the same molecule, as studied in the complexes of phenyl vinyl ether with methanol, diphenyl ether with water, *tert*-butyl alcohol and adamantanol, and dibenzofuran with water, methanol, and *tert*-butyl alcohol. In the third category, the effect of dispersion interaction on molecular aggregation

is investigated via complexes formed only by weak OH- π and/or CH-O hydrogen bonds as well as π - π dispersion interactions, as in the study of homodimers of three similar molecules, diphenyl ether, dibenzofuran, and fluorene, which have different structural flexibility. Through these different model systems, we aim to investigate how a preferred complex structure changes either by introducing small changes in the main molecule or the binding partner or on aggregation.

The development of chirped-pulse Fourier transform microwave spectroscopy has enabled the recording of wide portions of a rotational spectrum in a time-efficient way. With the advancement in electronics, it is now possible to build microwave spectrometers in a cost-effective way. Herein, a new design of a cost-effective 18-26 GHz microwave spectrometer, based on a segmented chirped-pulse approach, is built and evaluated. This new design will help to make the powerful technique of rotational spectroscopy more widespread.

Zusammenfassung

Das Zusammenspiel zwischen intra- und intermolekularen Kräften, von denen die Wasserstoffbrückenbindungen und die London-Kräfte die wichtigsten darstellen, steuert die Aggregation und Erkennungsprozesse von Biomolekülen. Obwohl die London-Kräfte bereits 1930 von Fritz London beschrieben wurden, sind ihre quantitativen Beiträge zu intra- und intermolekularen Wechselwirkungen noch nicht vollständig verstanden. Das Zusammenwirken der London-Dispersionskräfte und Wasserstoffbrückenbindungen ist von besonderem Interesse. Mit strukturell gut definierten, molekularen Modellsystemen ist es möglich, diese systematisch und quantitativ in Hinblick auf intermolekulare Wechselwirkungsenergien zu untersuchen.

Spektroskopische Ergebnisse solcher Modellsysteme bei niedrigen Temperaturen unter isolierten Bedingungen können direkt mit den Ergebnissen verschiedener theoretischer Methoden verglichen werden. Weiterhin können die experimentellen Ergebnisse für die Weiterentwicklung und zum Testen neuer quantenchemischer Methoden verwendet werden. Die in dieser Arbeit beschriebene Rotationsspektroskopie ist eine hochauflösende und empfindliche Methode, mit der man genaue Strukturen und damit auch Informationen über die intra- und intermolekularen Wechselwirkungen in diesen Komplexen gewinnen und Aussagen über die jeweiligen Bindungsstellen treffen kann.

Im Rahmen dieser Arbeit wurden in einem systematischen Ansatz drei unterschiedliche Arten von Molekülkomplexen untersucht, die Herausforderungen an die theoretische Beschreibung und Charakterisierung der Dispersionwechselwirkungen stellen. Zum Ersten wurden Komplexe untersucht, bei welchen klassische OH-O Wasserstoffbrückenbindungen dominieren. Als Modellsysteme dienten Komplexe aus Kampfermolekülen und Methanol oder Ethanol. In einer zweiten Kategorie sind Komplexe mit Molekülen, die sowohl starke klassische Wasserstoffbrückenbindungen als auch schwache OH- π -Bindungen bilden können. Hierzu wurden Komplexe aus Phenyl-Vinyl-Ether mit Methanol, Diphenylether mit Wasser, tert-Butylalkohol und Adamantanol sowie Dibenzofuran mit Wasser, Methanol und tert-Butylalkohol

untersucht. Schließlich wurde in einer dritten Gruppe der Effekt der Dispersionwechselwirkungen auf die Aggregation von Molekülen studiert, welche ausschließlich durch schwache OH- π und/oder CH-O Wasserstoffbindungen sowie π - π Dispersionwechselwirkungen gebildet werden. Untersucht wurden dabei Homodimere aus den drei Molekülen Diphenylether, Dibenzofuran und Fluoren, welche interessante strukturelle Ähnlichkeiten bei unterschiedlicher struktureller Flexibilität aufweisen. Mit diesen verschiedenen Modellsystemen soll aufgedeckt werden, wie sich eine bevorzugte Komplexstruktur durch das Einbringen kleiner Änderungen im Hauptmolekül, der Bindungspartner oder bei der Aggregation ändert.

Die Entwicklung der *Chirped-pulse Fourier-Transform* Mikrowellenspektroskopie ermöglichte es, weite Bereiche eines Rotationsspektrums in kurzer Zeit aufzunehmen. Bedingt durch die rasante Entwicklung im Bereich der Elektronik ist es heute möglich, Mikrowellenspektrometer kostengünstig zu bauen. In dieser Arbeit wurde ein neues, auf dem Prinzip segmentierter, gechirpter Pulse beruhendes Design für ein Spektrometer im Bereich zwischen 18 und 26 GHz aufgebaut und charakterisiert. Dieses neue Design kann dazu beitragen, der Rotationsspektroskopie eine weitere Verbreitung zu sichern.

Contents

Abstract	vi
Zusammenfassung	viii
1 Introduction	1
2 Theoretical background	11
2.1 Rotational Hamiltonian	12
2.2 Internal rotation	18
2.3 Spectral analysis	21
2.4 Structure determination	21
2.5 Quantum chemical calculations	24
3 Experimental details and instrumentation	27
3.1 Supersonic expansion	27
3.2 Chirped-pulse Fourier transform microwave spectroscopy	32
3.3 The Hamburg COMPACT (2-8 GHz) spectrometer	33
3.4 The extended COMPACT (8-18 GHz) spectrometer	37
3.5 A lower-cost newly-designed segmented 18-26 GHz chirped-pulse Fourier transform microwave spectrometer	39
3.5.1 Experimental details	41
3.5.2 Performance	50
4 Cumulative part	63
4.1 Weakly bound complexes of ethers and benzofuran with alcohols . . .	64
4.1.1 The phenyl vinyl ether-methanol complex	67
4.1.2 Structures of diphenyl ether aggregates with water and alcohols	83
4.1.3 Complexes of dibenzofuran with water and alcohols	90
4.2 Dispersive stacking in the aggregates of diphenyl ether, dibenzofuran and fluorene dimers	108

5	Monographic part	119
5.1	Side-chain length influencing dispersion interaction in camphor-alcohol complexes	119
5.1.1	Experimental details	120
5.1.2	Results and discussion	121
5.1.3	SAPT calculations	133
5.1.4	Summary and conclusions	134
6	Summary and outlook	137
	Bibliography	147

Chapter 1

Introduction

How do proteins fold? How are geckos and arthropods able to walk along walls and ceilings? Why are branched alkanes more stable than linear alkanes? What are the forces behind stabilizing graphene stacked sheet structure?

These important questions, based on every-day life observations, have been rationally explained by the interplay of van der Waals interaction [1–4]. One of the weakest intra- and intermolecular interactions, the van der Waals interaction, is omnipresent in all areas of science [5–8]. Intra- and intermolecular interactions comprises of hydrogen bond, induction, and London dispersion interactions [9]. The subtle interplay between these different forces, along with repulsion, determines a full understanding of the structure, stability, and reactivity of a chemical system.

It has been 100 years since hydrogen bonding was first described in 1920 by Latimer and Rodebush [10, 11]. The classical electrostatic donor-acceptor (OH-O) interaction description of hydrogen bonding is the same as defined a century ago. From then onwards, it has been considerably expanded by the International Union of Pure and Applied Sciences (IUPAC) to include different classes of donor-acceptor interactions to accommodate the appearance of new experimental and computational results [12]. Because of hydrogen bonding, the structure, function, and dynamics of a vast number of chemical systems, ranging from inorganic to biological molecules, are being understood. Its strength lies between 0.25 - 40 kcal mol⁻¹ (1 - 167 kJ mol⁻¹, 87 - 14000 cm⁻¹) [13], but this major contribution does not completely cover the attractive part of the intermolecular interactions. There are effects from dispersion interaction, which have shown to play an important role in the formation and stability of a structure [6, 14]. For example, by including dispersion interaction one can fully understand the greater stability of branched over linear alkanes or the $\pi - \pi$ attractive structures of graphene.

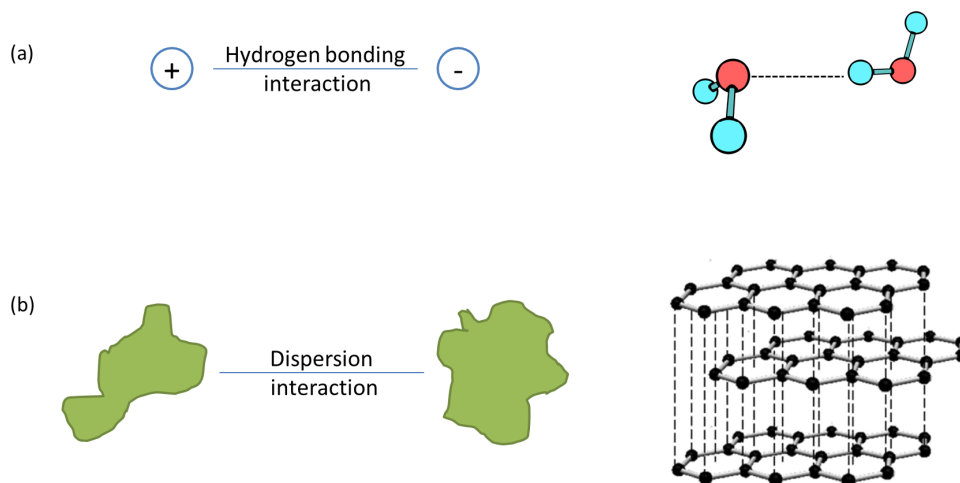


Figure 1.1: a) *Hydrogen bonding interaction, as in the water dimer (adapted from [19]), is represented as an electrostatic interaction between two point charges, b) the interaction between two moieties is governed by dispersion interaction, as in the π -stacked structure of graphene (adapted from [20]). The idea for the figure is adapted from Reference [6].*

The concept of London dispersion interaction was described in 1930 by Fritz London [15]. It is a purely quantum mechanical effect and arises from attractions between instantaneously induced dipole moments on neighboring atoms [9, 16]. It is the force that holds together noble gas clusters, e.g., Ar-Ar [17], and many noble gas/neutral molecule clusters like benzene-Kr and benzene-Xe complexes [18]. The contribution from London dispersion interaction has been underestimated for a long time. Recently, with increasing molecular size, it has been noted that this contribution grows rapidly and can amount to tens of kcal mol⁻¹. It scales with the number of pairwise interactions between atoms and molecules and can thus be added up [6]. But the force between two molecules is influenced by other surrounding molecules so that one cannot simply add all pairwise interactions to determine the total interaction energy of one molecule with the others. Figure 1.1 shows a comparison between hydrogen bonding, as in the water dimer, and dispersion interaction, represented by π -stacked structure of graphene, where the strength of hydrogen bonding is defined by the electrostatic interaction between two point charges, whereas dispersion interaction is present between two interacting moieties.

With the advancement in experimental and theoretical methods/techniques, it has been realized that dispersion interactions, along with hydrogen bonding and induction, are an important element to determine the structure, stability, and reactivity

of a chemical system [6, 16]. They play a role across many areas of science, including molecular physics, surface physics, colloid science, biology, and astrophysics. From protein folding to supramolecular synthesis, the contributions from these weak dispersion interactions are significant. It has potential in nanotechnology applications, to stabilize unusual molecular fragments and also to construct new materials [8].

For a better understanding of dispersion interactions at the molecular level and to use them to benchmark quantum-chemical methods, a priority program on ‘Control of London Dispersion Interactions in Molecular Chemistry’ is being funded by the Deutsche Forschungsgemeinschaft (SPP1807) since 2015 [21]. The research presented in this thesis is embedded in the program. The interplay between hydrogen bonding and dispersion interaction will help in understanding and describing biological phenomena, as well as in designing and developing new materials. Though known for decades, the determination of the strength of dispersive interactions between certain groups is a challenging task [6]. With geometrically well-defined molecular model systems, which are particularly interesting for the interplay between dispersion and hydrogen bonding, it is possible to systematically examine and quantify the London dispersion contribution to interaction energies [16].

Dispersion interaction has shown its importance at both theoretical and experimental levels. In a recent study, on the conformations of allyl isocyanate ($\text{CH}_2=\text{CHC}-\text{H}_2\text{N}=\text{C}=\text{O}$) [22], quantum chemical methods that include dispersion, such as Møller-Plesset second-order perturbation theory (MP2) [23], and dispersion corrected terms D3(BJ) [24, 25] added to density functional theory employing the Becke, three parameter, Lee-Yang-Parr (B3LYP) [26, 27], predicted three different conformers. These conformers were also observed experimentally with microwave spectroscopy. Interestingly, computational methods without dispersion corrections are not able to capture the global minimum conformation. With dispersion interaction already becoming important at the conformational level, this indicates that with increasing molecular complexity and complex formation, a better understanding of dispersion is needed at the theoretical level. In another study on 12-crown-4 ether interacting with water clusters [28], the structures observed using broadband rotational spectroscopy are stabilized by OH-O and CH-O hydrogen bonds along with dispersion interactions. 12-crown-4 ether is a flexible molecule, where the observed conformation of the molecule remarkably changes when interacting with water compared to its bare structure to maximize the interaction. This phenomenon cannot only be explained by hydrogen bonding, making dispersion interaction an important factor in providing extra stability to the changed conformation in cluster formation. In yet another study, the observance of the shortest intermolecular CH-HC distance of 1.566(5) Å to date [29], solely results from London dispersion interaction. This

distance is even shorter than the prototypical classical OH-O hydrogen bond system of water dimer (in water dimer O-O distance is 2.952 Å [19], for OH bond length of 0.96 Å, the OH-O hydrogen bond distance becomes 1.99 Å).

Examples where the interplay of hydrogen bonding and dispersion have been investigated in a systematic approach are presented. Clusters of anisole and its derivatives with methanol have been investigated by Fourier transform infrared (FTIR) spectroscopy. Anisole offers a hydrogen bonding site with the ether oxygen and a π system with the phenyl ring for dispersion interaction. Its interaction with methanol has shown a preference towards the oxygen bound complex [30]. On methylation of anisole, the preferred interaction tips towards a dispersive π bound complex [31]. This observation is explained by the +I (inductive) effect of the methyl and the +M (mesomeric) effect of the methoxy group that is known to interact differently in *ortho/para* and *meta* position of anisole. In another example dimer formation was studied systematically, as in clusters of benzyl alcohol, cyclohexyl methanol and 2-methyl-1-propanol [32]. From the conformational flexibility of these molecules, the dispersion interactions are sometimes adding up and sometimes competing with the OH-O hydrogen bonds. Other examples are the homodimers of anisole [33], phenol [34], and 1-naphthol [35], where the classical OH-O hydrogen bond is taken over by π - π stacking due to increased π system.

With increasing the size of the interaction partner for similar molecules, the intermolecular interaction energy difference between hydrogen-bonded and van der Waals clusters decreases. The synergistic contributions from weak hydrogen bonds like CH-O or OH- π and/or π - π dispersion interactions to intermolecular interaction energy in van der Waals clusters, can result in becoming equal to or take over the OH-O hydrogen-bonded complex. In this thesis, in a systematic approach, three kinds of complexes are studied. These complexes can be used to serve as a challenging benchmarking system for the theoretical representation and analysis of dispersion interactions if their energy differences are small. One kind of complexes explores the effect of dispersion interaction when complexes are dominated by strong classical OH-O hydrogen bond. The second set of complexes are comparing strong, classical OH-O hydrogen bonds and weak OH- π hydrogen bonds, while the third of complexes are formed only by weak OH- π and/or CH-O hydrogen bonds as well as π - π dispersion interaction.

In order to investigate these different kinds of complexes, rotational spectroscopy has been employed. Rotational spectroscopy is a high resolution and highly sensitive technique, which provides accurate structural information on the different docking sites in these clusters. The structure of a complex can be determined by the effects of

the molecular vibrations, centrifugal forces, and internal rotation on the rotational Hamiltonian, and by dipole moments and quadrupole coupling [22, 36–38]. The structural knowledge also provides information about the intra- and intermolecular interactions within these complexes. However, rotational spectroscopy is limited to gas phase molecules which have a non-zero dipole moment. The gas phase condition is advantageous as the complex formation can be probed in a controlled and isolated manner. Further, lowering the temperature of the molecules in the gas phase can give rise to simple and intense spectra of only low-lying energy levels. The rotational spectroscopic parameters obtained from these conditions can have a good agreement with the theory and can further be used to benchmark quantum-chemical methods. The maximum size of the system could be restricted because of the gas-phase requirements. However, this could be (partially) solved by methods such as laser ablation [39]. There are various examples where rotational spectroscopy has been employed for structural determination of molecules or weakly bound complexes and to determine intra- and intermolecular dynamics in these molecules or complexes [34, 35, 40–45].

Microwave spectroscopy is also applicable in the fields of chirality and astrochemistry. It can differentiate between enantiomers of chiral molecules and can determine the excess of one enantiomer over the other by extending the technique from its normal design [46–48]. In the field of astrochemistry, the detection of molecules in the data collected by radio observatories e.g. Atacama Large Millimeter/submillimeter Array (ALMA) [49] and the Herschel space telescope [50], relies on laboratory data, in particular analyzed rotational spectra [51, 52]. The data collected by these observatories provide the molecular signals from dense molecular clouds, which gives information on the chemical inventory of the interstellar medium on the information on how molecules are formed in space.

Other than rotational spectroscopy, complex formation can also be investigated by other spectroscopic techniques, such as Fourier transform infrared (FTIR) spectroscopy [53, 54] and infrared/ultraviolet (IR/UV) double resonance spectroscopy [55, 56]. Both of these techniques can observe complex formation in the gas phase. The FTIR technique gives information on the cluster formation, but due to its resolution, it can often not differentiate small changes in complex structure. Another requirement of this technique is the vibrational stretching mode of the molecule should be IR active. The IR/UV double resonance technique can often differentiate between different complexes, but it requires a UV chromophore.

Spectroscopic techniques, which are not limited by the size of the molecules or can study solution or solid-phase samples, are nuclear magnetic resonance (NMR) spectroscopy, X-ray diffraction, and electron diffraction. NMR spectroscopy, performed

in the solution phase, provides excellent structures of molecules or complexes and can even be applied to investigate the structure of larger (bio) molecules like protein [57–60]. Another method for structure determination is X-ray diffraction [61, 62]. In this technique, the molecules usually exist in the form of molecular crystals, or isolated molecules/particles. They are placed in ultrahigh vacuum conditions, and the structure is determined by X-ray diffraction pattern produced from the electron clouds of the molecules. In electron diffraction, instead of creating a diffraction pattern as in X-ray, electrons interact with the electron cloud of the molecule [63–66]. The samples for electron diffraction should be very thin (typically less than 100 nm) and therefore, its preparation is time-consuming.

Rotational spectroscopy

The field of rotational spectroscopy gained momentum after World War II. From then onwards, there have been many modifications in the field, leading to the present spectrometer designs. During the war, with the advancement in radar technology, instruments like Stark-modulator [67] and Zeeman-modulator [68] were developed. These instruments were based on broadcasting a continuous wave of microwave radiation through a gas cell and monitoring the reduction of the wave amplitude. These instruments were based on the absorption signal, which is typically less sensitive, leading to the investigation of emission signals [69]. A drawback of both the instruments was that they were operated at room temperature [70, 71]. This resulted in the molecular population being distributed over many rotational and vibrational states, which further results in less intense and more complex spectra. This limitation was overcome with the combination of the supersonic jet technique with microwave spectroscopy [72–74].

The next large advance for microwave spectroscopy came with the development of Fourier transform microwave (FTMW) spectroscopy, leading to the Balle-Flygare design of the Fabry-Perot cavity FTMW spectrometer, which was used together with the supersonic jet [75–78]. In this setup, much like the FT-NMR technique [79], a pulse of radiation was used to excite the molecular transition, and the molecular emission was collected in the form of its free induction decay (FID). The time-domain FID signal was Fourier transformed to yield the frequency spectrum. The ability to take the Fourier transform of the time domain yields high-frequency resolution, and because it is a background-free technique, the instrument enjoys high sensitivity. The resolution of this instrument was further improved by Grabow et.al. [80], where they modified the design of the FTMW spectrometer by arranging the molecular beam and the microwave field coaxially and perpendicularly. These features enhanced the use of FTMW technique.

But even with the success of this instrument, there was a major constraint. The Balle-Flygare FTMW instrument can only operate over small bandwidths per acquisition (1 MHz). Therefore, to acquire a spectrum over several GHz can be very time-consuming and heavily relied on the predicted rotational constants. For a molecular complex that has never been studied before, depending on the level of theory used, the calculated transition frequencies are not accurate, making the spectrum analysis tedious.

With the advancement in technology, a significant breakthrough in terms of bandwidth per acquisition led to the development of chirped-pulsed Fourier transform microwave (CP-FTMW) spectroscopy [83]. The digital synthesis of a chirped pulse spanning several GHz became available. This allowed the collection of a broad spectrum at once and in a very short time, for example, 6 GHz bandwidth (between 2-8 GHz) can be spanned in 4 μ s. With the observation of the rotational spec-

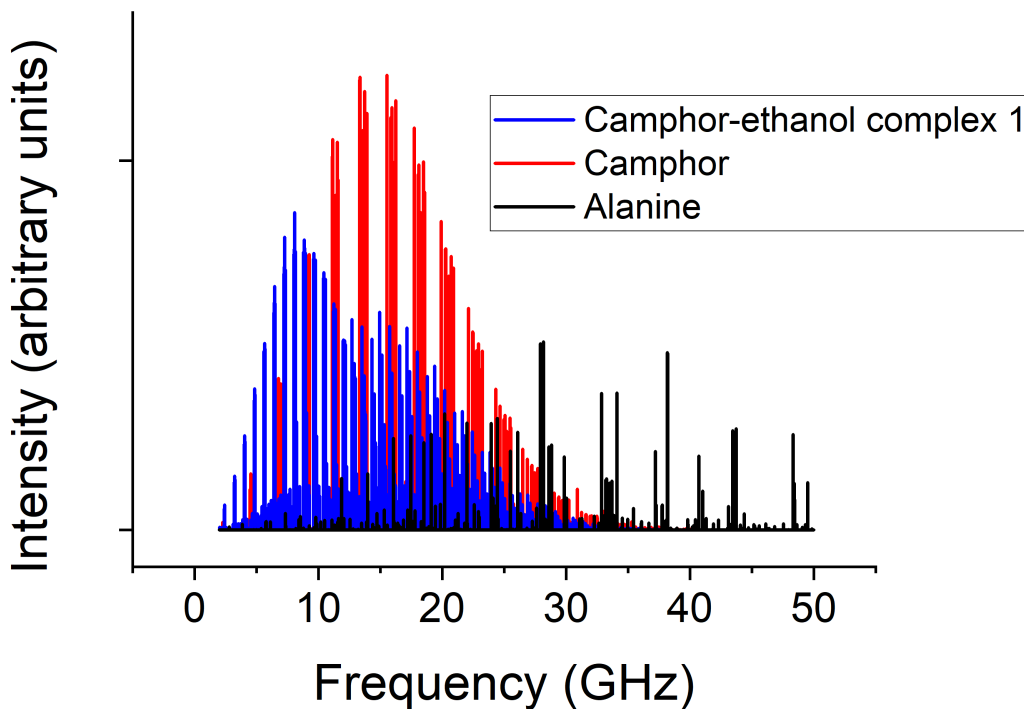


Figure 1.2: *Simulation of camphor-ethanol complex 1 (presented in Chapter 5), camphor [81], and alanine [82] at 1.5 K, highlighting their spectral patterns in a broad frequency range. The intensity of a studied system in a frequency range varies with the size of the system.*

trum in a broad frequency range, the identification of spectral patterns belonging to different species enhanced the spectrum analysis process. Figure 1.2 shows the simulation of camphor-ethanol complex 1 ($C_{12}H_{22}O_2$, presented in Chapter 5), camphor ($C_{10}H_{16}O$) [81] and alanine ($C_3H_7NO_2$) [82] at 1.5 K, highlighting their spectral pattern in a broad frequency range. This figure also illustrates the influence of the size of a molecule on the density and intensity of the rotational transitions in a frequency range. The CP-FTMW spectroscopy facilitated the structure determination of increasingly large and complex systems [37] and the generation of molecules and complexes through chemistry occurring within transient plasma [84].

Outline of the thesis

The work presented in this thesis have two main objective. The first is oriented towards understanding the interplay between hydrogen bonding and dispersion interactions in weakly bound complexes in a systematic approach, by using a home-built 2-8 GHz microwave spectrometer. The second objective is the construction and evaluation of a newly-designed segmented 18-26 GHz chirped-pulse spectrometer. The theoretical background for the work described in this thesis is presented in Chapter 2. The Hamburg COMPACT 2-8 GHz broadband CP-FTMW spectrometer used for studying the weakly bounded molecular clusters is described in Chapter 3, where the low-frequency range is chosen as it is suitable for the analysis of relatively large molecular clusters presented here. During this thesis, the COMPACT spectrometer has been extended to cover 8-18 GHz. The setup of the instrumentation is also described in Chapter 3.

One focus of this thesis is the development of a lower-cost instrument in the microwave regime (18-26 GHz) both for analytical uses as well as for astrochemistry. This instrument design is based on a segmented chirped-pulse approach. The segmented chirped-pulse method has been applied to built spectrometers in the millimeter and sub-millimeter range [85]. With the advancement in technology, it is now possible to design and decrease the cost of microwave spectrometers while still maintaining the characteristics of the instrument. The design, construction and evaluation of this spectrometer is presented in Chapter 3, Section 3.5 (*A lower-cost newly-designed segmented chirped-pulse 18-26 GHz Fourier transform microwave spectrometer*).

The influence of dispersion interactions on strong classical (OH-O) hydrogen bond is presented through complexes of a ketone (camphor) and two alcohols (methanol and ethanol) and is combined with the already-studied camphor-water complexes [86]. This study is presented in Chapter 5 - Monographic Part, Section 5.1 - *Side-*

chain length influencing dispersion interaction in camphor-alcohol complexes. For comparing strong, classical OH-O hydrogen bonds and weak OH- π hydrogen bonds, complexes between an ether/furan and an alcohol have been systematically studied to understand the role of dispersion interactions (Chapter 4, section 4.1). The cumulative part of this thesis presents the study of phenyl vinyl ether with methanol in Section 4.1.1 (*The phenyl vinyl ether-methanol complex*). Section 4.1.2 (*Structures of diphenyl ether aggregates with water and alcohols*) comprises of complexes of DPE with water, *tert-butyl* alcohol, adamantanol, and combines it with the already studied diphenyl ether-methanol study [87]. With a small structural change from diphenyl ether to dibenzofuran, the molecular complexes of dibenzofuran with water, methanol, and *tert-butyl* alcohol are investigated in Section 4.1.3 (*Complexes of dibenzofuran with water and alcohols*). The non-covalently bonded molecular complexes of an ether/furan and an alcohol have been investigated by broadband rotational spectroscopy, complemented by Fourier transform infrared (FTIR) and infrared/ultraviolet (IR/UV) double resonance spectroscopy. The homodimer clusters diphenyl ether, dibenzofuran, and fluorene are studied to investigate how molecules start to aggregate in the absence of classical OH-O hydrogen bond formation: two different arrangements are possible (π stacking and hydrogen bonded T-shaped structures). This study is presented in Chapter 4 - Section 4.2 (*Dispersive stacking in the aggregates of diphenyl ether, dibenzofuran and fluorene dimers*).

In the microwave spectra of the above complexes, features like internal motion of water and methyl internal rotation are observed. The barrier to methyl internal rotation is calculated for all the methanol containing complexes. For where the signal-to-noise ratio of the complex is sufficient, the experimental structure of those complexes are presented. Through these fourteen different systems, we aim to investigate how a preferred complex structure changes by introducing small changes in either the main molecule or the binding partner or on aggregation.

Chapter 2

Theoretical background

Spectroscopy is defined as the analysis of the interaction between a physical system (atoms and molecules) with any portion of the electromagnetic radiation. The absorption or emission of photons from different energy levels of a system gives rise to transitions in a spectrum. Molecular spectra can be complex, as they reflect changes in the electronic, vibrational or rotational motions of a system. Quantum mechanics are employed to understand the spectrum obtained from different spectroscopic techniques. The theoretical background allows us to determine different aspects of a molecule like structure, bond strengths, and electric dipole and nuclear electric quadrupole moments.

For a molecule, the quantized energy of its states can be calculated with the time independent Schrödinger equation,

$$\hat{H}\psi = E\psi, \tag{2.1}$$

where ψ is the eigenfunction of the Hamiltonian operator \hat{H} and E is its corresponding eigenvalue.

Within the Born-Oppenheimer approximation, the electronic and nuclear motion can be separated as they occur at different timescales [88]. The total eigenfunction ψ_{tot} of a molecule can be written as the product of vibrational ψ_{vib} , rotational ψ_{rot} , translational ψ_{trans} and electronic ψ_{elec} eigenfunctions:

$$\psi_{tot} = \psi_{vib}\psi_{rot}\psi_{trans}\psi_{elec}. \tag{2.2}$$

Its corresponding total Hamiltonian operator and the total energy of a molecule can be presented as the sum of electronic, vibrational, rotational and translational parts [89]:

$$\hat{H}_{tot} = \hat{H}_{vib} + \hat{H}_{rot} + \hat{H}_{trans} + \hat{H}_{elec} \quad (2.3)$$

$$E = E_{vib} + E_{rot} + E_{trans} + E_{elec} \quad (2.4)$$

In this work only the rotational energy of a system in their electronic and vibrational ground states is evaluated via microwave spectroscopy, and its corresponding time-independent Schrödinger equation

$$\hat{H}_{rot}\psi_{rot} = E_{rot}\psi_{rot} \quad (2.5)$$

are discussed in the following section.

2.1 Rotational Hamiltonian

Rigid rotor Hamiltonian

To calculate the E_{rot} in quantum mechanics, an analogy with the rigid rotor model from classical mechanics is made, where the rotational energy of a rigid body is given as:

$$E_{rot} = \frac{1}{2}\omega^\dagger I \omega \quad (2.6)$$

with the inertia tensor I , and the angular velocity ω .

For a rotating system formed by N atoms, each one with mass m_i and spatial coordinates x_i, y_i, z_i in a Cartesian axis system, the inertia tensor can be written as:

$$I = \sum_{n=0}^N m_i \begin{pmatrix} y_i^2 + z_i^2 & -x_i y_i & -x_i z_i \\ -y_i x_i & x_i^2 + z_i^2 & -y_i z_i \\ -z_i x_i & -z_i y_i & x_i^2 + y_i^2 \end{pmatrix} = \begin{pmatrix} I_{xx} & I_{xy} & I_{xz} \\ I_{yx} & I_{yy} & I_{yz} \\ I_{zx} & I_{zy} & I_{zz} \end{pmatrix} \quad (2.7)$$

The inertia tensor I can be simplified by placing the origin of the axis system at the center of mass of the rotating body in such a way that the tensor becomes diagonal. This molecular axis system is called the principal axis system, where the axes are denoted as a, b, c , and it is unique for each rotating system. There are six ways to correlate the Cartesian axis system to the principal axis system, as summarized in Table 2.1. Other than the center of mass condition, the axis system is chosen such that the diagonal elements of I , called the principal moments of inertia, are defined with increasing size $I_a \leq I_b \leq I_c$.

Table 2.1: Possible identification of the principal axis system axes a , b , c with the reference axes x , y , z leading to six different representations.

	I^r	I^l	II^r	II^l	III^r	III^l
x	b	c	c	a	a	b
y	c	b	a	c	b	a
z	a	a	b	b	c	c

Based on symmetry, molecules are classified into four different categories:

1. **Linear top molecules** ($I_a = 0$ and $I_b = I_c$) have a zero moment of inertia about one of their molecular axes, and the other two principal moments of inertia are equal in value, e.g., carbon dioxide (CO_2), carbonyl sulfide (OCS).
2. **Spherical top molecules** ($I_a = I_b = I_c$) have all three principal moments of inertia equal to each other, e.g. methane (CH_4), carbon tetrachloride (CCl_4).
3. **Symmetric top molecules** have one unique and two equal moments of inertia. They are characterized by a threefold or higher symmetry axis and can be divided into two cases:
 - **Prolate tops** ($I_a < I_b = I_c$) have the unique moment of inertia smaller than the other two. These molecules have a cigar shape, as the symmetry axis lies on the a axis, e.g. propyne ($\text{CH}_3\text{C}\equiv\text{CH}$), chloroform (CH_3Cl).
 - **Oblate tops** ($I_a = I_b < I_c$) have a disc shape, with the unique moment of inertia being greater than the other two. For these molecules, the symmetry axis lies on the c axis, e.g. ammonia (NH_3), benzene (C_6H_6).
4. **Asymmetric top molecules** ($I_a < I_b < I_c$) are rotors where all the three principal moments of inertia are different, e.g. water (H_2O), phenol ($\text{C}_6\text{H}_5\text{OH}$).

In the principal axis system, the rotational energy takes the form:

$$E_{rot} = \frac{1}{2} (I_a \omega_a^2 + I_b \omega_b^2 + I_c \omega_c^2) = \frac{1}{2} \left(\frac{J_a^2}{I_a} + \frac{J_b^2}{I_b} + \frac{J_c^2}{I_c} \right) \quad (2.8)$$

where J is the angular momentum. In quantum mechanics, the equivalent of J is the angular momentum operator $\hat{\mathbf{J}}$. The relation between $\hat{\mathbf{J}}$ and the components of angular moment in an axis system is given as $\hat{\mathbf{J}}^2 = \hat{J}_x^2 + \hat{J}_y^2 + \hat{J}_z^2$. Therefore, the

rotational Hamiltonian for a molecule in the principal axis system describing the rigid rotor system becomes:

$$\hat{H}_{rig} = \frac{\hbar^2 \hat{J}_a^2}{2I_a} + \frac{\hbar^2 \hat{J}_b^2}{2I_b} + \frac{\hbar^2 \hat{J}_c^2}{2I_c} \quad (2.9)$$

The rotational constants \mathbf{A} , \mathbf{B} , \mathbf{C} for a molecule are inversely proportional to the moments of inertia about the three principal axes, a , b , and c , as follows:

$$\mathbf{A} = \frac{\hbar^2}{2I_a}; \mathbf{B} = \frac{\hbar^2}{2I_b}; \mathbf{C} = \frac{\hbar^2}{2I_c} \quad (2.10)$$

From this inverse relation it follows that $\mathbf{A} \geq \mathbf{B} \geq \mathbf{C}$. For cases when the moments of inertia are equal, I_b is used as a conventional notation.

From equation (2.10), (2.9) becomes:

$$\hat{H}_{rig} = A\hat{J}_a^2 + B\hat{J}_b^2 + C\hat{J}_c^2 \quad (2.11)$$

The solution for the energy levels in a quantum mechanical system is obtained from the Schrödinger equation of the rigid rotor as given in equation (2.5). The components of the angular momentum operators are defined in the molecular axis system (x, y, z) as \hat{J}_g where $g = x, y, z$. \hat{J}_g operators do not commute with each other, but only one component of \hat{J}_g commutes with the $\hat{\mathbf{J}}^2$ operator. Similarly, the components of the angular momentum operator in the laboratory axis (X, Y, Z) system do not commute with each other and only one component commutes with the $\hat{\mathbf{J}}^2$ operator. For both the axes systems, z and Z axes are conventionally chosen to commute with the $\hat{\mathbf{J}}^2$ operator.

From quantum mechanics, the operators that commute have a common set of eigenfunctions. For the $\hat{\mathbf{J}}^2$, \hat{J}_z and \hat{J}_Z operators a complete set of eigenfunctions ψ_{JKM} can be calculated. The derivation of wave functions ψ_{JKM} is long, but they can be written in a closed form as given in equation 11.15, page 241 of Reference [90].

The eigenvalues of $\hat{\mathbf{J}}^2$, \hat{J}_z and \hat{J}_Z operators are:

$$\hat{\mathbf{J}}^2 \psi_{JKM} = \hbar^2 J(J+1) \psi_{JKM} \quad (2.12)$$

$$\hat{J}_z \psi_{JKM} = K \hbar \psi_{JKM} \quad (2.13)$$

$$\hat{J}_Z \psi_{JKM} = M \hbar \psi_{JKM} \quad (2.14)$$

The quantized eigenvalues are the quantum numbers J , K , and M . The quantum number J is a measure of the total angular momentum, and the K and M quantum numbers describe the projections of the total angular momentum onto the z -axis and Z -axis, respectively. J can take any positive integer value starting from 0, and both K and M can take any integer value ranging from $-J$ to $+J$, and are thus $2J+1$ degenerate.

Using the properties of the angular momentum operator and its corresponding eigenvalues, it is possible to calculate the rotational transitions of linear and symmetric top molecules.

For a linear and symmetric top, the selection rules are:

$$\Delta J = \pm 1; \Delta K = 0, \Delta M = 0, \pm 1$$

where the K quantum number for a symmetric top molecule becomes doubly degenerate.

The rotational transitions for both cases are given as:

$$\nu = 2B(J + 1).$$

Spherical top cannot be studied by microwave spectroscopy as they do not have a permanent dipole moment resulting from a high degree of symmetry.

With three unique moments of inertia, the method for energy level determination of an asymmetric top molecule is more complicated. The Hamiltonian for an asymmetric top can no longer be only related to $\hat{\mathbf{J}}^2$ and \hat{J}_z operators, as in linear and symmetric top cases. There are contributions from \hat{J}_x and \hat{J}_y operators and \hat{H}_{rig} is no longer diagonal, making it impossible to analyse analytically, but can be solved numerically. Most polyatomic molecules belong to this category, and the large molecular clusters investigated in this work belong to this class.

The Hamiltonian of an asymmetric-top molecule is set considering the asymmetry of the molecule, which is described in terms of Ray's asymmetry parameter κ , as below,

$$\kappa = \frac{2B - A - C}{A - C} \quad (2.15)$$

where κ can vary between the limiting cases of the prolate symmetric top ($B = C$) with $\kappa = -1$ and the oblate symmetric top ($A = B$) with $\kappa = +1$. The highest

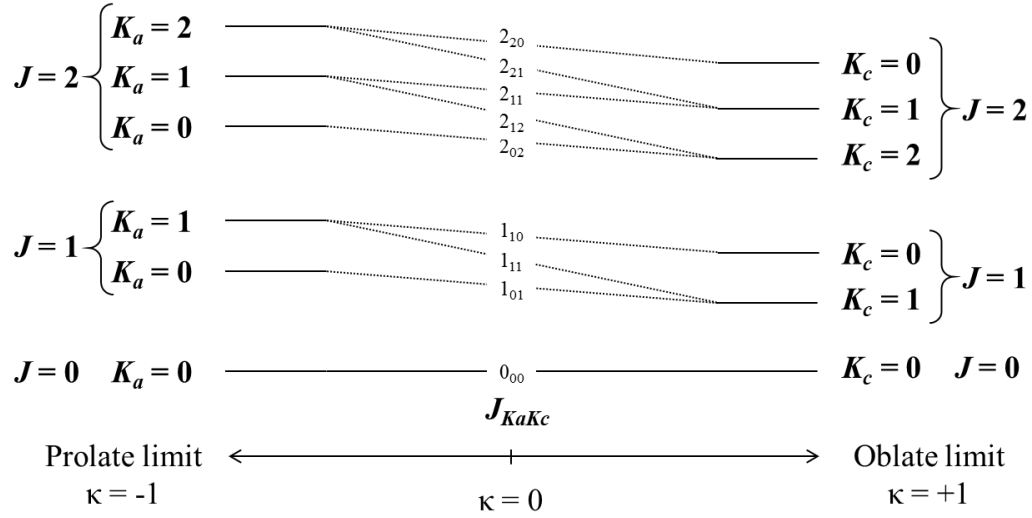


Figure 2.1: Correlation diagram for the energy levels of prolate and oblate limiting cases for an asymmetric top. Only the three lowest J levels are depicted.

degree of asymmetry is reached when $\kappa = 0$. To set the asymmetric Hamiltonian and thus calculate the energy of the molecule, within the prolate limiting case, I^r representation and for an oblate limiting case, III^r , are commonly used .

The asymmetric Hamiltonian employing the I^r ($A \gg B > C$) representation gives the following non-vanishing terms of the energy matrix:

$$E_{J,K} = \frac{1}{2}(B + C)J(J + 1) + \left[A - \frac{1}{2}(B + C) \right] K^2 \quad (2.16)$$

$$E_{J,K\pm 2} = \frac{1}{4}(B - C)[(J(J + 1) - K(K \pm 1))(J(J + 1) - (K \pm 1)(K \pm 2))]^{\frac{1}{2}} \quad (2.17)$$

For an asymmetric top, a given rotational level is no longer labelled only by the J and K quantum numbers as in symmetric tops. In comparison to the symmetric top, the two fold degeneracy in K is lifted. The rotational energy levels are labeled using the King-Hainer-Cross notation $J_{K_a K_c}$, where K_a and K_c are the pseudo quantum numbers. They represents the K -values for the limiting cases of a prolate and oblate symmetric-top molecule, respectively [91]. The energy level scheme of an asymmetric-top molecule related with the two limiting cases of κ is illustrated in Figure 2.1.

The selection rules for rotational transitions in asymmetric-top molecules with re-

Table 2.2: Selection rules for an asymmetric-top molecule with respect to changes in K_a and K_c .

dipole	transition type	ΔK_a	ΔK_c
μ_a	a -type	$0, \pm 2, \dots$	$\pm 1, \pm 3, \dots$
μ_b	b -type	$\pm 1, \pm 3, \dots$	$\pm 1, \pm 3, \dots$
μ_c	c -type	$\pm 1, \pm 3, \dots$	$0, \pm 2, \dots$

spect to J and M are:

$$\Delta J = 0, \pm 1; \Delta M = 0 \quad (2.18)$$

where the condition $\Delta J = 0$ gives rise to Q-branch, $\Delta J = -1$ to P-branch and $\Delta J = +1$ to R-branch transitions. In addition, these molecules can have three nonzero components of the dipole moment (μ_a , μ_b and μ_c), giving rise to three types of selection rules based on the change in K_a and K_c , as summarized in Table 2.2.

Non-rigid rotor Hamiltonian

The rigid rotor model is an approximation to calculate the energy levels of a molecule. However, real molecules are not rigid and undergo distortions in their average nuclear positions as rotation occurs. These contributions, referred to as centrifugal distortions, are more enormous for an asymmetric rotor than for symmetric molecules. Fortunately, the energy due to centrifugal distortion accounts for only a small part of the total rotational energy, and therefore can be treated with sufficient accuracy by adding various correction terms from perturbation theory to the rigid rotor Hamiltonian [92].

For an asymmetric molecule, the rotational Hamiltonian, \hat{H}_{rot} becomes:

$$\hat{H}_{rot} = \hat{H}_{rig} + \frac{\hbar^4}{4} \sum_{\alpha\beta\gamma\delta} \tau_{\alpha\beta\gamma\delta} \hat{J}_\alpha \hat{J}_\beta \hat{J}_\gamma \hat{J}_\delta \quad (2.19)$$

where α , β , γ and δ can take any value of x , y or z in the molecule fixed axis system. Watson demonstrated that due to commutation relations and symmetry properties, the number of components in the correction term can be reduced to five determinable linear combinations of the fourth-order [91, 93, 94]. To analyse the

centrifugal distortion, he proposed two possible combinations of the terms giving rise to A (asymmetric) and S (symmetric) reduced Hamiltonians. The A reduced Hamiltonian is best suited for most asymmetric top molecules, and the S reduced Hamiltonian for symmetric and slightly asymmetric top molecules.

Watson's A reduction Hamiltonian in the I^r representation including the five quartic centrifugal distortion constants Δ_J , Δ_{JK} , Δ_K , δ_J and δ_K gives the following energy matrix elements:

$$E_{J,K} = A^{(A)}K^2 + \frac{1}{2}(B^{(A)} + C^{(A)})[J(J+1) - K^2] - \Delta_J J^2(J+1)^2 - \Delta_{JK}J(J+1)K^2 - \Delta_K K^4 \quad (2.20)$$

$$E_{J,K\pm 2} = \left\{ \frac{1}{4}(B^{(A)} - C^{(A)}) + \delta_J J(J+1) + \frac{1}{2}\delta_K [K^2 + (K \pm 2)^2] \right\} \times [(J(J+1) - K(K \pm 1))(J(J+1) - (K \pm 1)(K \pm 2))]^{\frac{1}{2}} \quad (2.21)$$

The complete S-reduced Hamiltonian with the corresponding matrix elements can be found in Reference [91]. The effect of centrifugal distortion on the observed spectra is to shift the transitions to lower frequency from the value predicted for a rigid rotor. Therefore, Δ_J must always be positive since it already has a negative sign (equation (2.20)). These effects are generally within a few kHz for small $J \leq 10$, but can become significant, that is on the order of several MHz and more, for high J transitions [95].

2.2 Internal rotation

Some flexible molecules show additional features in a rotational spectrum as a result of large amplitude motions such as internal rotation, ring puckering, inversion or proton tunneling. From quantum mechanics, these motions are a result of coupling between conventionally well-isolated vibration and rotation degrees of freedom in molecules, which have a shallow double or even multi-well potentials. In particular internal rotation of the methyl (CH_3) group for asymmetric tops has been explored extensively during this work.

In the case of CH_3 internal rotation, the rotation of the methyl top in a molecule or a molecular cluster leads to three equivalent minima in the potential energy surface along the rotation coordinate of the methyl top (as shown in Figure 2.2). To calculate the effect of internal motion on the molecule, the rotational Hamiltonian is extended:

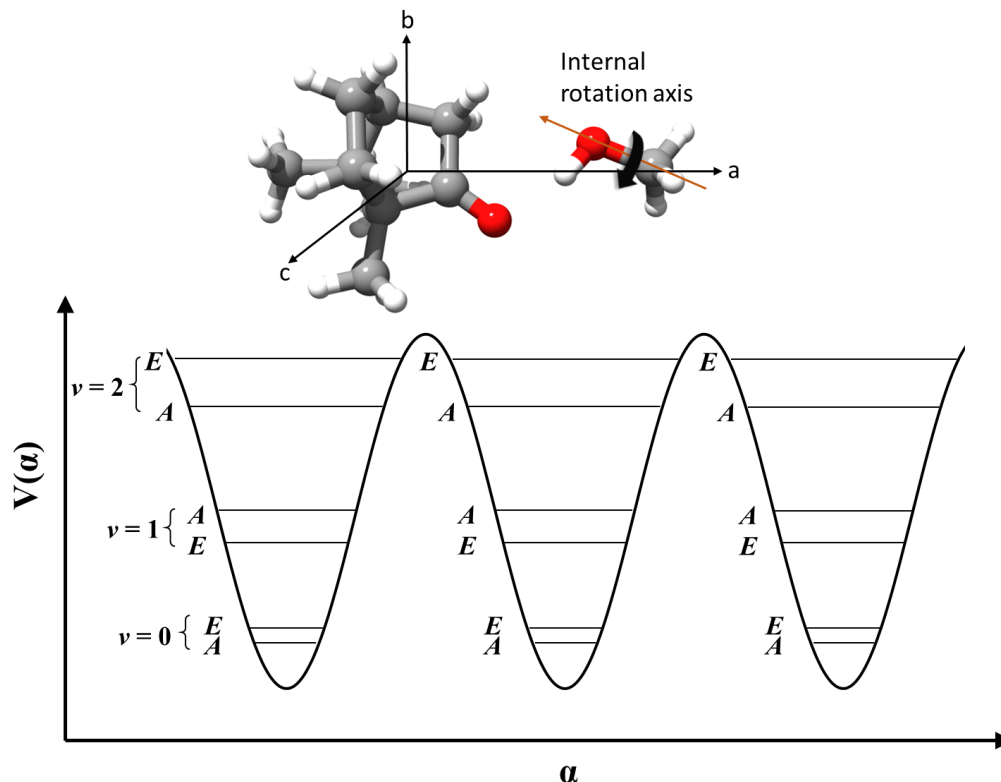


Figure 2.2: *Schematic potential energy for the internal rotation of the methyl group of methanol by an angle α around the internal axis (orange) for the camphor-methanol complex (see Chapter 5, section 5.1). The potential function is depicted showing the corresponding minima and maxima and the A-E splitting of each torsional state.*

$$\hat{H} = \hat{H}_{rot} + \hat{H}_I \quad (2.22)$$

where \hat{H}_{rot} is the rotational Hamiltonian as given in equation (2.19), and \hat{H}_I is the internal rotation Hamiltonian for a methyl group, which is defined as:

$$\hat{H}_I = F(\hat{j}_\alpha + \hat{J})^2 + V(\alpha) \quad (2.23)$$

where F is the rotational constant for the internal rotor, \hat{j}_α is the angular momentum operator of the internal rotation, \hat{J} is the total angular momentum operator and $V(\alpha)$ is the potential barrier with the internal rotation angle α . The rotation of the methyl group is $2\pi/3$ periodic based on the C_3 symmetry axis of the methyl top.

The height of $V(\alpha)$ is given by:

$$V(\alpha) = \frac{1}{2}V_3(1 - \cos 3\alpha) + \frac{1}{2}V_6(1 - \cos 6\alpha) + \dots \quad (2.24)$$

where V_3 and V_6 are the three-fold and six-fold barriers. Usually in a first approximation to solve the problem, it is considered that $V_3 \gg V_6$, and therefore the other terms in the series are neglected.

F can be calculated from the moment of inertia of the internal top (I_α). The direction cosines, λ_x ($x = a, b, c$), give the orientation of the internal rotation axes with respect to the principal axis system:

$$F = \frac{\hbar^2}{2rI_\alpha}, \quad \text{where} \quad r = 1 - \sum_x \frac{\lambda_x^2 I_\alpha}{I_x} \quad (2.25)$$

In the case of very high V_3 barrier ($> 11\text{-}12 \text{ kJ mol}^{-1}$, 1000 cm^{-1}), the internal motion due to the CH_3 group is quenched, and the molecule corresponds to the non-rigid Hamiltonian solution as given in equation (2.19). For a low barrier, the internal top would essentially be free to rotate across the equivalent minima in the potential energy surface via tunneling. In the case of an intermediate barrier, it is possible to obtain the height of the internal rotation barrier V_3 and the orientation of the methyl group with respect to the principal axes in the molecule with accuracy. In this way, the V_3 barrier height can also be helpful to analyze the chemical environment around the methyl top.

The energy levels split into a non-degenerated A component and a doubly-degenerated E component. As a result, each transition appears to split into two components in the spectrum. The spacing between the A and E components in the spectrum depends on the V_3 barrier height. For the methyl group internal rotation, an additional selection rule arises, where transitions are only allowed between states of the same symmetry, $A \leftarrow A$ or $E \leftarrow E$.

This work also included the analysis of an almost-free internal rotation of a water molecule hydrogen-bonded to diphenylether and dibenzofuran, respectively. The rotation of the water molecule is π periodic based on the C_{2v} symmetry group. In this case, the observed doublets are labeled as 0^+ and 0^- , and the allowed transitions for this situation are $0^+ \leftarrow 0^+$ or $0^- \leftarrow 0^-$ [96].

2.3 Spectral analysis

There are a number of fitting programs available to assist the assignment of complicated rotational spectra, e.g. JB95 [97], PGOPHER [98], AABS program suite [99, 100] and XIAM [101]. The latter two programs can be found on the PROSPE homepage [102]. All of the programs are developed to fit the rigid rotor and non-rigid rotor Hamiltonian for the assigned transitions to calculate the experimental rotational constants. In the work presented in this thesis, the spectra were first fit using the JB95 program or PGOPHER program, and then further refined using Pickett's SPFIT/SPCAT programs as implemented in the AABS program suite. The analysis of the observed tunneling splitting arising from methyl group internal rotation in complexes with methanol was performed using the XIAM program. A detailed description of the properties of the programs can be found in the corresponding literature. Other than these, additional programs are available on the PROSPE homepage for analyzing rotational spectra.

2.4 Structure determination

The knowledge of the experimental rotational constants of a molecule gives information about its structure, as the rotational constants are related to the moments of inertia. For an asymmetric molecule composed of N atoms, the molecular structure is determined from its $3N-6$ independent internal parameters, containing $N-1$ bond lengths, $N-2$ bond angles, and $N-3$ dihedral angles. The determination of molecular structures (with high accuracy) using only the rotational constants from the main isotopologue is not possible, and more information is required from rare stable isotopes. Microwave spectroscopy is known for its high sensitivity, allowing us to often observe rare isotopologues in natural abundance, such as those containing ^{13}C (1.1%), ^{34}S (4.22%), ^{15}N (0.368%), and ^{18}O (0.204%). In some cases, where the signal-to-noise ratio (SNR) is not sufficient, isotopically enriched samples can also be used. The rare stable isotopes generate new sets of rotational constants for all the singly substituted atoms in the molecule. From this information, there are different ways to construct the experimental structure of a molecule, as discussed below [103, 104].

Equilibrium structure (r_e)

The equilibrium structure corresponds to a minimum in the potential energy surface as shown in Figure 2.3. This structure represents the distances between nuclei in a hypothetical vibrationless configuration. The relation between the equilibrium rotational constant and the rotational constants of different vibrational states is

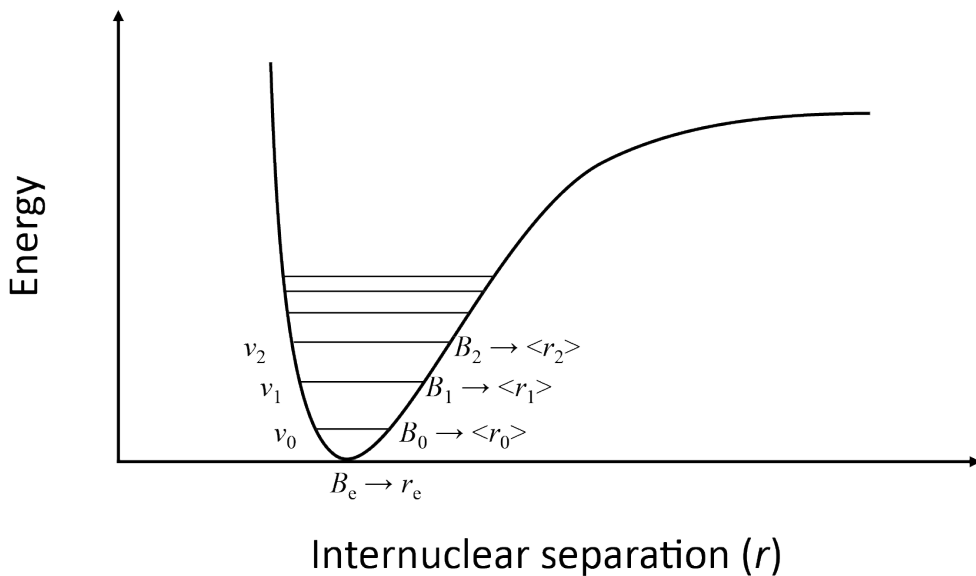


Figure 2.3: *Potential energy function with vibrational states, rotational constants and the structures derived from them.*

given by:

$$B_e = B_v + \sum_I^{3N-6} \alpha_i \left(\nu_i + \frac{d_i}{2} \right) \quad (2.26)$$

where α_i is the rotation-vibration interaction constant and d_i is the vibrational degeneracy. Equation (2.26) is applicable to all the three rotational constants in an asymmetric-top molecule. The (r_e) structure cannot be directly determined from the experiment, but the value of α_i can be typically taken from calculations.

Effective structure (r_0)

The effective structure represents the experimental structure in a certain vibrational state [105]. Usually, the structure at the ground vibrational state, $v = 0$, is determined, and is known as the r_0 structure. In this method, the structural parameters are fit in a least squares manner to get a good agreement with the experimentally obtained rotational constants of the parent and all the available isotopologue species. This method may not be reliable in cases where the molecule contains large amplitude motions or out-of-plane bending.

Substitution structure (r_s)

The Kraitchman's equations method or the r_s method determines the magnitude of the coordinates of each atom from the information of the isotopologue rotational constants [106]. This method uses the ground state moments of inertia I_x ($x = a, b, c$) of the parent and of the substituted species and relates them to the planar moments of inertia P_x as given below:

$$P_a = \frac{1}{2}(I_b + I_c - I_a), \quad P_b = \frac{1}{2}(I_c + I_a - I_b), \quad P_c = \frac{1}{2}(I_a + I_b - I_c) \quad (2.27)$$

For an asymmetric top, the coordinates can be calculated by the expressions:

$$|a| = \left[\frac{\Delta P_a}{\mu} \left(1 + \frac{\Delta P_b}{I_a - I_b} \right) \left(1 + \frac{\Delta P_c}{I_a - I_c} \right) \right]^{1/2} \quad (2.28)$$

$$|b| = \left[\frac{\Delta P_b}{\mu} \left(1 + \frac{\Delta P_c}{I_b - I_c} \right) \left(1 + \frac{\Delta P_a}{I_b - I_a} \right) \right]^{1/2} \quad (2.29)$$

$$|c| = \left[\frac{\Delta P_c}{\mu} \left(1 + \frac{\Delta P_a}{I_c - I_a} \right) \left(1 + \frac{\Delta P_b}{I_c - I_b} \right) \right]^{1/2} \quad (2.30)$$

where μ is the reduced mass for the isotopic substitution and is given by:

$$\mu = \frac{M\Delta m}{M + \Delta m} \quad (2.31)$$

where M is the total mass of the molecule and Δm is the change in mass on isotopic substitution.

The change of the moment of inertia upon isotopic substitution leads to a partial cancellation of the ro-vibrational contribution. This partial cancellation reveals a structure which is closer to the equilibrium structure r_e than the effective r_0 structure. The r_s method does not consider any structural changes due to isotopic substitution. This method gives absolute values for the coordinates of each atom so further information is required to set the proper signs. In cases where the coordinate values are too small, the Kraitchman method yields imaginary values i.e., when the substituted atom is close to an inertia axis. In the case of large amplitude motions (LAM), isotopic substitution breaks the symmetry and the LAM are quenched, and so an average structure can be obtained.

2.5 Quantum chemical calculations

In general, the analysis of a rotational spectrum is assisted by the spectroscopic parameters obtained from quantum chemical calculations. The following section briefly describes the quantum chemical methods used to optimize structures and to obtain their energy and rotational parameters, in this work. All the calculations were performed with the GAUSSIAN 09 program suite [107] or ORCA 4.1 program suite [108].

In this work, weakly bound molecular clusters were investigated. In a first step, an initial search was conducted to find the minimum energy structures of the complexes by either structures designed from chemical intuition or by using the Artificial Bee Colony (ABCcluster) method [109]. The ABCcluster program calculates local minimum structures using force field parameters of the molecules.

To optimize the obtained structures, the density functional theory (DFT) method at B3LYP and ab-initio second order Møller-Plesset perturbation theory (MP2) method, are mainly used in this work. The B3LYP method is composed of a number of terms: B3LYP (Becke, three parameter, Lee-Yang-Parr) is a hybrid functional which uses a linear combination of the exact Hartree-Fock functional with the electron-electron and exchange-correlation to describe the system [26, 27]. A further empirical correction was made for dispersion correction (D3) including Becke-Johnson damping (BJ), which is especially important for weakly bound complexes [24, 25]. The MP2 [23] is based on the Hartree-Fock (HF) method [110] and also includes electronic correlation, thus this method includes dispersion. The DFT level of theory requires shorter computational time compared to the ab-initio method for structural optimization.

Three kinds of basis sets, def2-TZVP, 6-311++G(d, p) and aug-cc-pVTZ, were chosen to model the orbitals of the molecule. They were based on the computational time, data storage, and their performance from the previous studies related to the molecular systems presented in this work [86, 87]. The def2-TZVP basis set represents the polarized triple zeta basis set, where def stands for default in Turbomole [111]. The 6-311++G(d,p) are a member of the Pople basis sets, where 6-311G is a split-valence triple-zeta basis, and can be adjusted for the use of diffuse functions (++) or polarization functions (d,p) [112, 113]. The aug-cc-pVTZ basis sets represents the Dunning-type basis sets (cc-pVnZ) basis sets including correlation correction and can be augmented (aug) by adding diffuse functions [114].

Additionally, for a quantitative analysis of the inter-molecular interactions present

in large clusters, symmetry adapted perturbation theory (SAPT) calculations were performed [115, 116]. This method calculates the total interaction energy in a cluster without computing the total energy of the monomers or dimer. The interaction energy is further used to determine the contribution of electrostatic, induction, exchange, and dispersion energy, in a perturbative approach. The first-order expansion to the interaction energy gives the electrostatic and exchange terms, and the second-order gives the dispersion and induction terms. These calculations were performed using the Psi4 electronic structure package [117]. The simplest SAPT calculations only include the first and second order expansion of the interaction energy, as is denoted as SAPT0. Higher order terms can also be included, which can add higher accuracy to the obtained results, but this requires relative more computational time. For adequate values of the different contributions to the inter-molecular interactions, SAPT0 calculations are optimal.

Chapter 3

Experimental details and instrumentation

The following chapter summarizes the setup and operation principle of a chirped-pulse microwave spectrometer, the Hamburg "COMPACT" spectrometer, which operates between 2-8 GHz and which was employed for the study of intermolecular interactions in large complexes in this thesis. The home-built COMPACT spectrometer was extended to work up to 18 GHz, and the setup of this extension is also described. In the second part of this work, a newly-designed segmented chirped-pulse spectrometer within the 18-26 GHz range has been built-up. All the instruments described here use a supersonic expansion, which provide a cold environment for molecules to be cooled into their vibronic ground state and only low-lying rotational energy levels are populated. This allows for an intense spectra with only rotational levels being observed in the spectra. Furthermore, the configurations of flexible molecules can be frozen, which allows the study of low energy conformers. In the case of complex formation in the first stages of supersonic expansion, where there is high molecular density, the cold environment preserves the weakly bound cluster [118].

3.1 Supersonic expansion

A supersonic jet is created by expanding a gas mixture from a region of high pressure to a region of low pressure through a small orifice. The gas mixture is usually composed of a few percentages of the sample molecules under analysis diluted with a carrier gas (He, Ne, Ar, or mixtures of them). In the supersonic expansion, the opening of the orifice is larger than the mean free path lengths of the atom. Therefore, multiple collisions of the molecules with the carrier gas atoms can occur during the expansion, resulting in exchange of kinetic energy (KE) among them. The ex-

change of KE narrows down the velocity distribution of the molecules and carrier gas atoms than that of before expansion. This narrow velocity distribution causes decrease in translational temperature of the molecules, leading to efficient cooling of their internal and external degrees of freedom. This brings down all the excited state population of the molecule to their vibronic ground states, which leads to an increase of the intensity of the populated energy levels. A typical temperature of the supersonic jet after expansion, along the translational, rotational, and vibrational degrees of freedom, is of the order of the 1 K, 10 K, and 50 K, respectively. The narrow velocity distribution further leads to narrow line shapes, and since the molecules are diluted, there is no collisional broadening.

In our experimental setups, the high-pressure area (reservoir) and the low-pressure area (the vacuum chamber) are separated by a pulsed nozzle. By controlling the opening time of the nozzle, defined molecular packets are allowed to expand into the chamber. If the sample of interest is a liquid or a solid, it can be heated in the reservoir and mix with the carrier gas before expansion.

The velocity distribution of the molecules can be calculated according to the

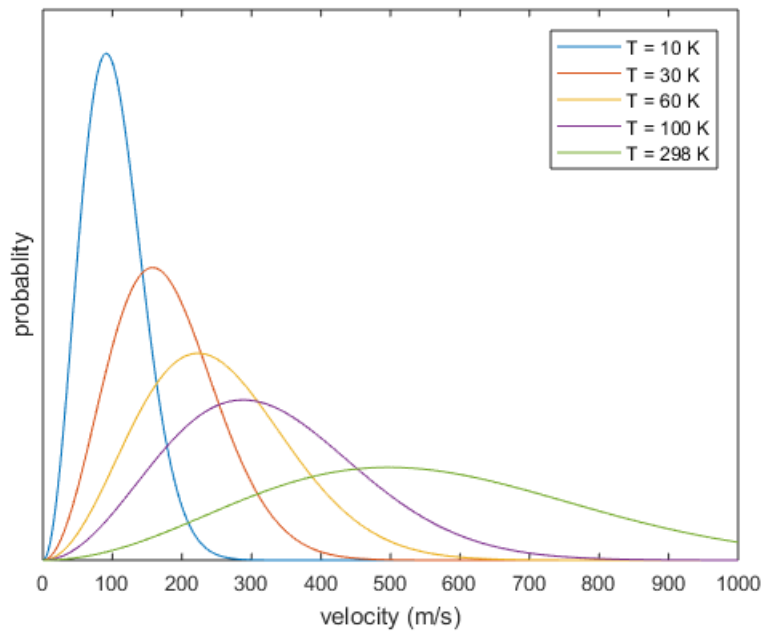


Figure 3.1: *The Maxwell-Boltzmann velocity distribution of neon calculated at different temperatures.*

Maxwell-Boltzmann distribution:

$$P(\nu) = 4\pi \left(\frac{m}{2\pi k_B T} \right)^{\frac{3}{2}} \nu^2 e^{-\frac{m\nu^2}{2k_B T}} \quad (3.1)$$

where k_B is the Boltzmann constant. Figure 3.1 shows the velocity distribution of neon at different temperatures using equation 3.1.

For an monoatomic ideal gas undergoing supersonic jet expansion, an adiabatic and isentropic behavior is considered, and the maximum velocity of the molecules can be calculated using:

$$\nu_{max} = \sqrt{\frac{5k_B T}{m}} \quad (3.2)$$

where T is the temperature of the reservoir, and m is the mass of the atoms and molecules in the supersonic expansion. Equation 3.2 is only valid for ideal gases, and for a real system an approximation can be made. As the gas mixture in the supersonic expansion contains only a few percentage of the molecule, the carrier gas can be used to calculate the terminal velocity of the gas mixture in the expansion. For helium, neon, and argon a terminal velocities of 1760, 790, and 560 m s⁻¹, respectively, are achieved during the expansion, for $T = 300$ K.

The most common way to describe the different areas of the supersonic expansion process is by using the Mach number, M ,

$$M = \frac{v}{c} \quad (3.3)$$

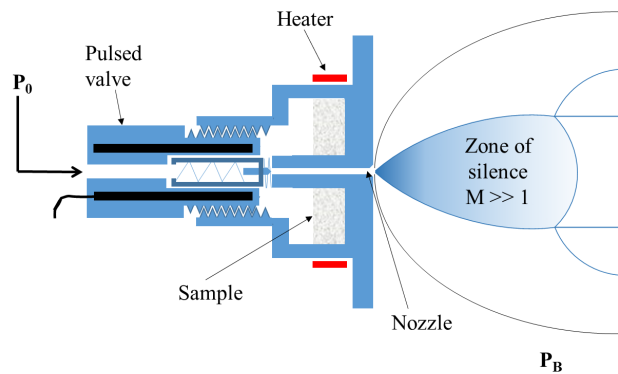


Figure 3.2: Schematic drawing of the valve with the supersonic jet structure. The valve and the supersonic jet are not drawn to the same scale.

where v is the velocity of the atomic jet at a specific position, and c is the local speed of sound. The supersonic expansion can be described in terms of the speed of sound because the propagation of sound in a gas can also be treated as an adiabatic and nearly isentropic process.

As shown in Figure 3.2, the gas is in a "stagnation state" in the reservoir defined by the temperature T_0 and the pressure P_0 . The Mach number in the reservoir is smaller than one ($M < 1$) because the atoms frequently collide, which gives a much slower velocity than the sound velocity. The pressure difference ($P_0 - P_B$) between the two areas, inside the reservoir and the vacuum chamber, accelerates the gas at the throat of the orifice exit, as the volume of the reservoir decreases, reaching a Mach number equal to 1 at the reservoir exit. The greater the difference in pressure between the two areas, the greater the gas acceleration. During the expansion, the density of the atoms as well as the number of collisions decreases, and the mean velocity increases. At this point of the expansion, the Mach number is greater than one ($M \gg 1$), and the jet can be treated as a supersonic jet. This area is also called the zone of silence since the molecules in this area are so dilute that no collisions take place any more.

The length x of the "zone of silence" depends on the diameter (D) of the orifice and on the difference in pressure between the two areas, inside the reservoir and the vacuum chamber, and is given by:

$$x = 0.67D\sqrt{\frac{P_0}{P_B}} \quad (3.4)$$

The experimental performance will be influenced by the pumping speed, which defines the ultimate pressure, P_B , in the vacuum chamber. In our experimental setup, low rotational temperatures leads to only low energy rotational states being populated and therefore, to more intense and simple spectra. Additionally, different carrier gases show different cooling behaviors. As the result of the exchange of energy of the molecules with heavier carrier gas atoms is efficient, argon would be a good choice for reaching low temperatures in the molecular jet. However, argon has a tendency to form weakly bound complexes with the molecules of interest and thus can affect the monomer intensity and compete with the other molecules in case of complex formation. Therefore, the choice of the best carrier gas is, therefore, a compromise between optimal cooling and the tendency to form complexes. For our experiments, the supersonic expansion is created by using neon as a carrier gas, which results in achieving rotational temperatures of 1-3 Kelvin, and does not show tendency to form complexes with the molecules.

The main goal in this work was to study weakly bound complexes of the molecules

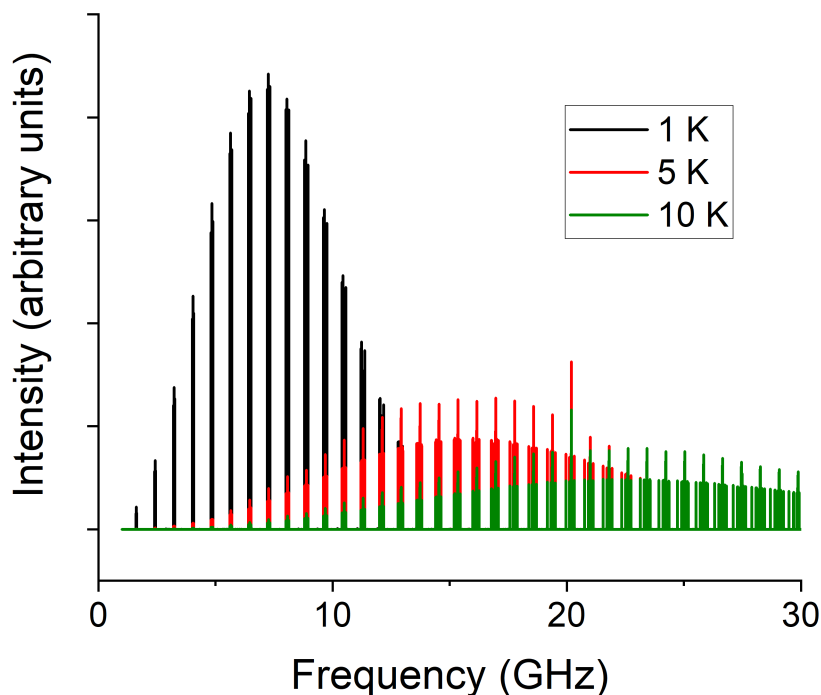


Figure 3.3: *The simulated spectra of camphor-ethanol complex 1 (Chapter 5) at different temperatures. Only the a-type transitions are shown for simplicity. At higher temperatures more energy levels are populated, which leads to a decrease of the intensities in the spectrum.*

of interest. At the translational temperatures available in the supersonic jet, the binding energy produced by the weakly bound complexes are larger than the translational kinetic energy of the atoms and molecules in the jet and therefore, the complexes formed during the expansion do not dissociate during collisions and are stable [118]. However, the formation of complexes requires at least three-body collisions, while the cooling of the molecules in the supersonic jet requires only two-body collisions. The ratio of three-body collisions to two-body collisions is proportional to the number density of atoms, n_0 , and the mass throughput through the nozzle is proportional to $n_0 D^2$. Therefore, for a constant D , increasing n_0 , can increase complex formation [118]. Figure 3.3 shows the simulated spectra of camphor-ethanol complex 1 (Chapter 5) at different temperatures. Only the a-type transitions are shown for simplicity. At higher temperatures more energy levels are populated, which leads to a decrease of the intensities in the spectrum.

Nevertheless, the optimal parameters for the expansion for each experiment have to be adjusted to obtain a better signal level of the complexes in the spectra. This was

performed by varying the opening time of the nozzle, or the pressure or the choice of the carrier gas or by adjusting the temperature of the molecules in the reservoir.

3.2 Chirped-pulse Fourier transform microwave spectroscopy

In 2006, chirped-pulse Fourier transform microwave spectroscopy (CP-FTMW) spectroscopy was developed by the research group of Brooks Pate (at the University of Virginia, USA), which added a new dimension to the field of rotational spectroscopy [83], compared to a high-quality Fabry-Perot cavity FTMW spectrometer. In the CP-FTMW technique, a short chirped pulse covering a broad spectral range of several gigahertz (GHz) is broadcast to simultaneously excite molecular transitions which are resonant with a frequency in the chirp. The resulting molecular emission is collected in the form of its free induction decay (FID) and averaged in the time domain on a fast broadband oscilloscope. The averaged FID is Fourier transformed to convert the data in-to the frequency domain. Using CP-FTMW spectroscopy, it is possible to record rotational spectra of complex, flexible molecules spanning several GHz bandwidth within a few microseconds. With this method, the data acquisition time and sample consumption are decreased by a factor of 100[83] and 30[83], respectively, compared to a cavity based spectrometer.

CP-FTMW spectroscopy is based on a fast passage excitation of a linear microwave chirp [83, 119]. The excitation pulse needs to be faster than the relaxation time of the excited states and is typically 1-4 μs long. With advancement in technology, the digital synthesis of a chirp became achievable and was first applied by Brown et al. [83] to build the CP-FTMW spectrometer. According to Reference [83], the electric field waveform of a linear chirp is given by:

$$\mathcal{E}(t) = \mathcal{E}_0 e^{i(\omega_s t + \frac{\alpha t^2}{2})} \quad (3.5)$$

where \mathcal{E}_0 is the amplitude of the electric field and is kept constant, α is the chirp rate, and is defined as:

$$\alpha = \frac{\omega_e - \omega_s}{\tau_{pul}} \quad (3.6)$$

where ω_s and ω_e are the start and end frequency of the chirp, respectively, and τ_{pul} is the pulse duration.

In a chirped-pulse based microwave spectrometer, the intensity of emitted molecular

signal (S) is proportional to the transition frequency ω , the square of the transition dipole moment μ^2 , the amplitude of the excitation electric field \mathcal{E}_0 , the population difference of the two states involved in the transition ΔN_0 , and the inverse square root of the chirp rate α [83]:

$$S \propto \omega \cdot \mu^2 \cdot \mathcal{E}_0 \cdot \Delta N_0 \cdot \sqrt{\frac{\pi}{\alpha}} \quad (3.7)$$

All these factors are needed to be considered for designing, building, and operating a CP-FTMW instrument.

The instrument described below cover together the 2-26 GHz range and is based on the linear sweep chirps as described in equation (3.5). The 2-8 GHz Hamburg **compact-passage acquired coherence technique** (COMPACT) spectrometer is home-built [36], with constant developments to improve the performance [86]. The design of the spectrometer follows the CP-FTMW approach introduced by Brown et al. [83] and is based on a design proposed by Grabow [120]. An extension to increase the frequency range of the COMPACT to 18 GHz is implemented. The 18-26 GHz spectrometer is based on the segmented chirped-pulse approach as discussed in Section 3.5.

The 2-18 GHz frequency range is optimal for the investigation of large and complex molecules with substantial moments of inertia and thus small rotational constants, leading to transitions with low frequencies. The 18-26 GHz range is chosen for medium sized molecules. This frequency range is optimal for astrochemically relevant molecules, as medium sized molecules have their peak intensities in this region at the cold conditions of the interstellar medium.

3.3 The Hamburg COMPACT (2-8 GHz) spectrometer

A schematic of the 2-8 GHz spectrometer design is given in Figure 3.3. A 24 GS/s arbitrary waveform generator (AWG, Tektronix 7122A) is used to create a 4 μ s chirped excitation pulse from 2-8 GHz. The excitation chirp is amplified by an adjustable traveling wave tube amplifier (Amplifier Research 300T2G8) with more than 300 W output power, which has a frequency bandwidth of 6 GHz (2-8 GHz).

After amplification, the excitation chirp is transmitted into a vacuum chamber (operating pressure 10^{-5} mbar), using a high gain microwave horn antenna (Q-par Angus WBH 2-18-NHG), operating between 2-18 GHz. As shown in Figure 3.3, another

receiver horn antenna is placed approximately 20 cm away from the emitting antenna. The molecules, along with an inert carrier gas, are supersonically expanded into the vacuum chamber using a pulsed nozzle (Parker General Valve, Series 9). The valve is mounted on the top of the vacuum chamber and perpendicular to the microwave propagation. Usually, neon is used as a backing gas at stagnation pressures of 2-5 bar, but helium and argon can also be used for this purpose. Depending on the molecule being studied, a gas mixture can be prepared (typically 0.1-0.5% of molecules in an inert gas). For solid or liquids, the sample can be heated if needed in order to bring enough molecules into the gas phase. For this, the sample is placed in a modified pulsed nozzle which is equipped with a heatable reservoir close to the orifice. In the present setup, the sample can be heated to a maximum temperature of approximately 200 °C, due to the operating specification of the pulse valve.

The high power excitation pulses during molecular excitation are blocked by a high-power diode limiter (Aeroflex ACLM-4535) and a solid-state, single-pole single-throw switch (SPST, Advanced Technical Materials S1517D) to protect the sensitive receiver electronics. After excitation, the FID of the polarized ensemble of molecules is received by the second horn antenna. The FID is then amplified with a low-noise amplifier (LNA, AMF-7D-01001800-22-10P) and digitized on a 100 GS/s oscilloscope (Tektronix DPO 72004C). The oscilloscope has an adjustable digitization rate and is set to 25 GS/s for the 2-8 GHz experiment. The FID is collected for 40 μ s and Fourier transformed using a Kaiser Bessel windowing function for baseline improvement, giving a resolution of \sim 25 kHz and frequency accuracy of 10 kHz. Other time-domain filters such as Hamming and Gaussian are also available to improve the baseline resolution of the spectrum.

The sensitivity of the spectrometer depends on the ability to average coherent FID signals in the time domain over many acquisitions. For this, phase reproducibility is mandatory. To ensure phase stability, the AWG, the TWT amplifier, the oscilloscope and a delay generator (Stanford Research Systems DG645) are phase-locked to a 10 MHz Rb oscillator (Stanford Research FS 725). As shown in Figure 3.3, the pulse generator triggers the AWG and the valve. One channel of the AWG triggers the delay generator, which then triggers the TWT amplifier and the SPST (protection) switch. Another channel triggers the oscilloscope to start collecting the FID after the excitation pulse.

The abundance of weakly bound complexes relative to their parent species is often low. Therefore, to observe these weakly bound complexes, several million averages of the FID are necessary to obtain a good signal-to-noise ratio (SNR), depending on the molecular density and the strength of the dipole moment. With the advance-

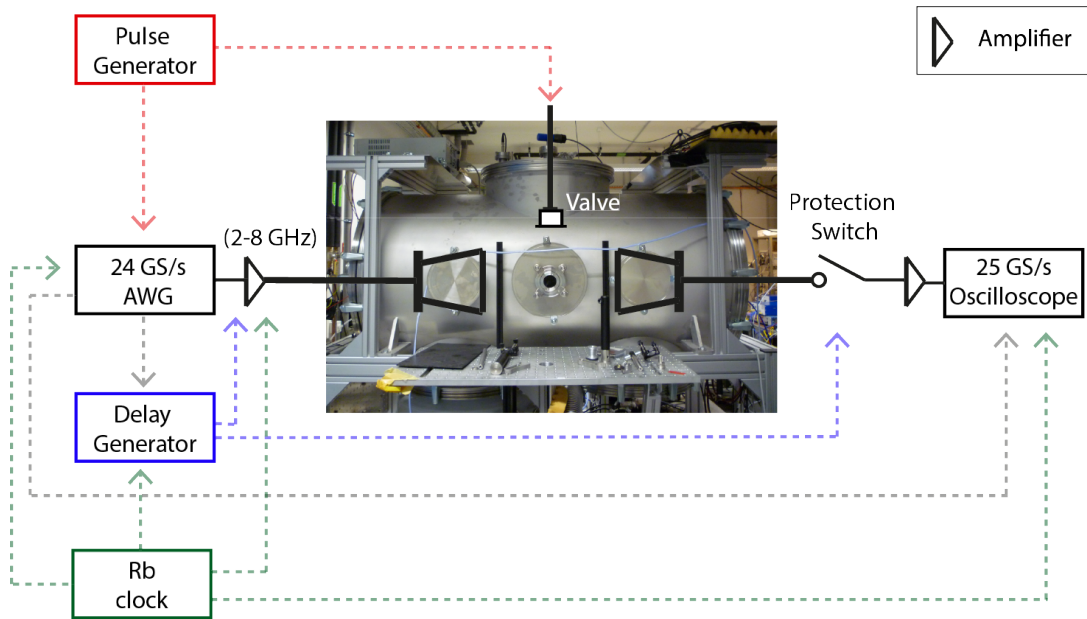


Figure 3.4: *Experimental setup of the Hamburg COMPACT (2-8 GHz) microwave spectrometer. The colored dotted lines are used to indicate triggers. The valve and the AWG are triggered by the pulse generator (red dashed lines). The chirp is generated by the AWG, amplified by the TWT amplifier, and transmitted into the vacuum chamber via a horn antenna. The FID is received with another horn antenna, amplified with a low-noise amplifier, and recorded on an oscilloscope. The delay generator, the oscilloscope, the TWT amplifier and the AWG are phase-locked to a Rb-frequency standard (green dashed lines). To ensure phase stability, the AWG triggers the delay generator and the oscilloscope by its two marker channels (grey dashed lines). The delay generator then triggers the TWT amplifier and the protection switch (purple dashed lines).*

ment in digital electronics, especially for the digital oscilloscope used in this setup, it is possible to implement a fast-frame approach. In this method, for one gas pulse of about $600 \mu\text{s}$, eight microwave chirps of $4 \mu\text{s}$ are used for excitation in a series, with a $45 \mu\text{s}$ distance between two consecutive chirps for $40 \mu\text{s}$ FID collection and $1 \mu\text{s}$ buffer time for the electronics. The resulting FIDs are then summed up. With the Hamburg COMPACT spectrometer, the fast-frame setup can be performed together with a gas pulse repetition rate of 9 Hz, giving an effective repetition rate of 72 Hz. The main limitation to further increase this rate is the pumping speed of the roughing pump. The spectrometer is currently equipped with an oil diffusion pump (Leybold DIP 12000, pump speed 12 000 l/s) backed by a mechanical pump (Leybold D40B Trivac Vacuum pump) and a booster pump (Leybold WAU251 RUVAC pump). With this setup, it is possible to record 6.2 million averages in approximately 24 hours.

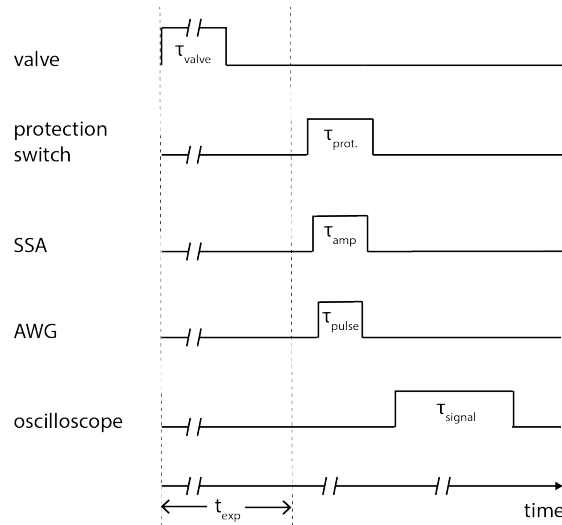


Figure 3.5: *Trigger scheme of the experiment carried out on the Hamburg COMPACT spectrometer. An experimental sequence starts with a gas pulse. The valve is opened for a time τ_{valve} . After a time t_{exp} , the expansion reaches the interaction region, and the chirped-pulse excitation sequence starts with opening the protection switch for a time $\tau_{prot.}$ After a short delay, the TWTA is turned on, followed by the emission of the excitation pulse. The FID recording is set such that the excitation pulse does not interfere with the recorded signal.*

3.4 The extended COMPACT (8-18 GHz) spectrometer

The schematic for the extension of the COMPACT spectrometer to the 8-18 GHz frequency range is shown in Figure 3.4. The Nyquist frequency range of the AWG is up to 12 GHz. Therefore, $2 \mu\text{s}$ duration chirps between 4-9 GHz are generated with the AWG, amplified (Minicircuits, ZX60-123LN-S+) and doubled to 8-18 GHz (ECLIPSE MICROWAVE, Model D2010LZ1), where the doubler only multiplies the bandwidth of the chirp by two without changing the pulse duration. The intermediate amplification step is necessary to ensure adequate power requirement for the doubler. The chirped pulses are then amplified with a 50 W solid state amplifier (SSA, Mercury Systems, L0618-46-T680) and broadcasted into the vacuum chamber with the horn antenna. The SSA operates between 6-18 GHz. Following each excitation, the electronics for collecting and digitizing the FID are the same as the 2-8 GHz setup. The FID is recorded on the 100 GS/s oscilloscope, with the digitization

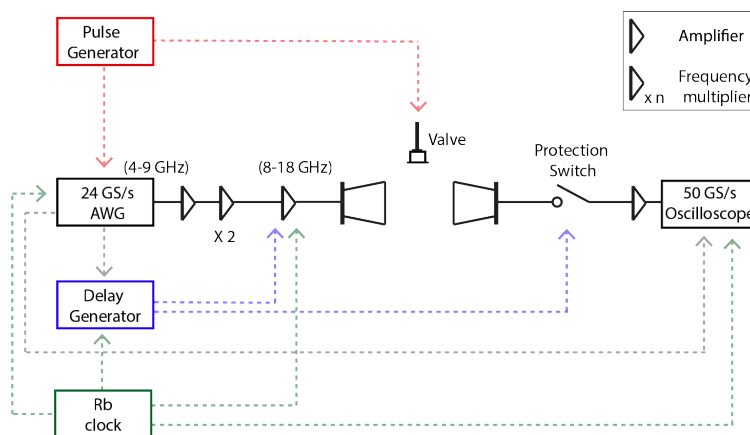


Figure 3.6: *Experimental setup of the extended COMPACT (8-18 GHz) microwave spectrometer. The colored dotted lines are used to indicate triggers. The valve and the AWG are triggered by the pulse generator (red dashed lines). The chirp is generated by the AWG, amplified and doubled to 8-18 GHz, amplified by the SSA, and transmitted into the vacuum chamber via a microwave horn antenna. The FID is received with another microwave horn antenna, amplified with a low-noise amplifier, and recorded on an oscilloscope. The delay generator, the oscilloscope, the SSA and the AWG are phase locked to a Rb-frequency standard (green dashed lines). To ensure phase stability, the AWG triggers the delay generator and the oscilloscope by its two marker channels (grey dashed lines). The delay generator then triggers the SSA and the protection switch (purple dashed lines).*

rate set to 50 GS/s and collected for 20 μ s yielding a frequency resolution of \sim 50 kHz, but maintaining the frequency accuracy of the measurement.

Due to the limitations on the memory of the oscilloscope at high digitization rate, it is not possible to run the experiments at 72 Hz effective repetition rate. With eight frames, the maximum repetition rate of the gas pulse is set to 4 Hz, and an effective repetition rate of 32 Hz is achieved.

To better match the power per GHz distribution of the 8-18 GHz range compared to a previously known 8-18 GHz spectrometer [83, 84] for which a 300 W power amplifier is available, the 8-18 GHz chirps are synthesized in smaller bandwidths and amplified with the 50 W SSA. The 10 GHz bandwidth is divided into 3 segments of 5 GHz, 2.5 GHz and 2.5 GHz each (8-13 GHz, 13-15.5 GHz and 15.5-18 GHz). But, all microwave components (cables, connections, microwave horn antennas, switches etc.) operating up to 18 GHz do not have a flat performance across the whole band and show larger power losses at higher frequencies compared to low frequencies. This results in a lower intensity of molecular transitions in the spectrum at higher frequencies.

3.5 A lower-cost newly-designed segmented 18-26 GHz chirped-pulse Fourier transform microwave spectrometer

The 18-26 GHz frequency range of the spectrometer presented in this work, also known as the K-band region, is well suited for the study of medium-sized molecules and for studying astrochemically relevant molecules. This frequency range overlaps with some modern radio observatories around the world, for example, the Jansky Very Large Array (JVLA) in Mexico, the Radio Telescope Effelsberg in Germany, the Australian Square Kilometer Array Pathfinder (ASKAP) in Australia, among others where small to medium sized astrochemically relevant molecules are observed. The detection of molecules in datasets from facilities such as these observatories relies on high-level laboratory data, in particular analyzed rotational spectra. The broadband CP-FTMW design to build rotational spectrometers is best suited for collecting rotational spectra of unknown molecules.

However, the application of CP-FTMW spectroscopy is limited to still a few research groups, and one of the factors governing this is the high cost involved in building microwave spectrometers. In a CP-FTMW spectrometer, the most expensive electronics are arbitrary waveform generators (AWG) that synthesize a chirped pulse, travelling wave tube amplifiers (TWTAs) that amplify a broad spectral range to high output powers, and fast broadband oscilloscopes to average and digitize the free induction decay (FID) in real time. This limitation is further enhanced in the millimeter wave (MMW) and submillimeter range, where the availability of electronics is rare and therefore the cost of the instrument can be higher than in the microwave range.

A cost reduction method has been applied before to design MMW and submillimeter instruments [85, 121]. These spectrometers have been based on the segmented chirped-pulse approach. As the name suggest, in this method the entire bandwidth of the spectrometer is divided into small chirped-pulse segments called a pulse train. A general scheme of the principle difference between a broadband chirped-pulse and segmented chirped-pulses is show in Figure 3.7. Usually, an AWG creates a low frequency excitation pulse train, which is frequency up-converted by an active multiplier chain to give a chirped-pulse segment which lie within the spectrometer's bandwidth. The AWG is needed to achieve the sweep rates required for chirp generation, which are not attainable with conventional microwave sources. The FID from each segment is then frequency down-converted and digitized on a narrow band digitizer card, replacing the cost of broadband oscilloscopes. Finally, the en-

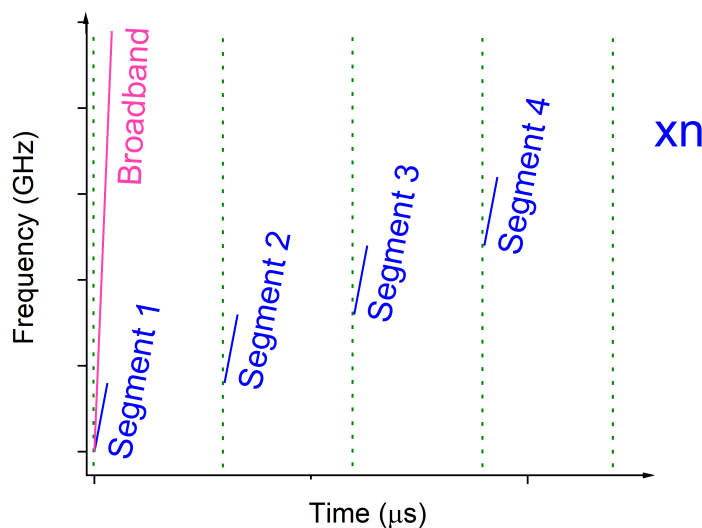


Figure 3.7: A general scheme showing the principle difference between a broadband chirped-pulse and segmented chirped-pulses. A broadband chirp spans the entire bandwidth of a spectrometer at a time. In segmented chirps, the broadband chirp is divided into several small segments, and one segmented-chirp spans one region of the spectrometers bandwidth at a time. In this way, a number of segmented-chirps cover the entire bandwidth of the spectrometer.

tire bandwidth is frequency corrected and constructed by adding together smaller segments of the rotational spectrum.

With the advancement in technology it is now possible to decrease the cost of chirped-pulse instruments in the microwave region. Using the segmented approach we present a new design for the 18-26 GHz spectrometer. This new design has the capability to decrease the total cost of expensive broadband microwave instruments by at least two-third, compared to the previously reported broadband CP-FTMW instruments, without compromising the quality of the data [122]. Similar to the fast frame method, in this spectrometer each molecular pulse is scanned by three pulse trains (multi-train). The instrument's performance is characterized using molecular signals of carbonyl sulphide and hexanal. A detailed analysis of the phase stability, frequency accuracy, resolution and dynamic range of the spectrometer, including a comparison with the first 18-26.5 GHz CP-FTMW spectrometer [123], is presented.

3.5.1 Experimental details

A schematic of the newly designed segmented CP-FTMW spectrometer operating between 18-26 GHz is shown in Figure 3.8. The design of the excitation pulse generation, free induction decay (FID) collection, optimization process, timing scheme, sample chamber, and automation are described below.

Excitation pulse

This section describes the creation of the excitation pulse. In contrast to the COMPACT spectrometer (Section 3.3), the entire bandwidth from 18-26 GHz is covered in a few steps.

The chirped excitation pulses are created via channel 1 (CH1) of a 25 GS/s dual-channel arbitrary waveform generator (AWG, Tektronix AWG70000A series). As

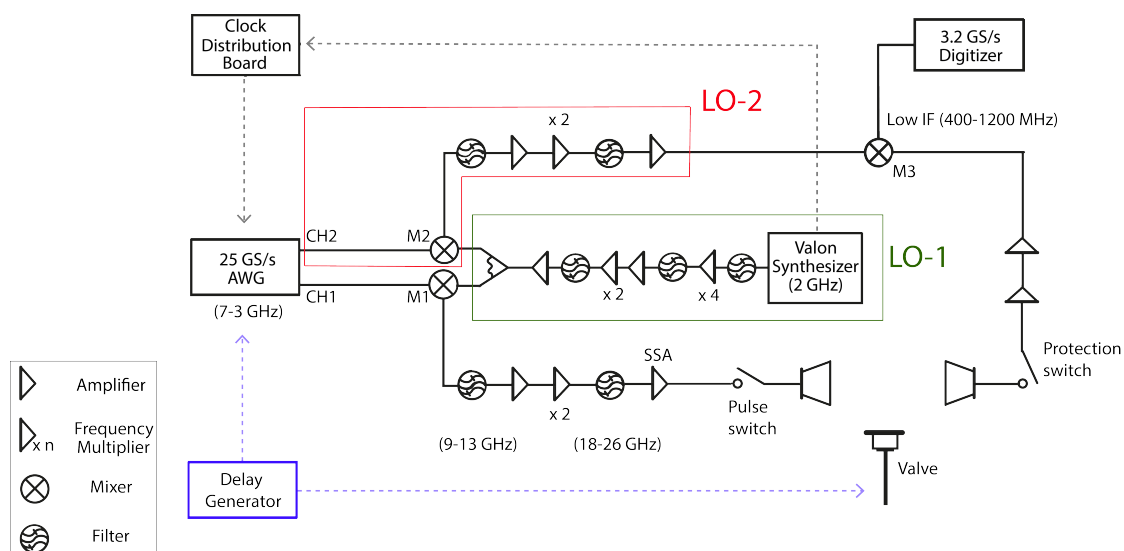


Figure 3.8: *Experimental setup of the segmented 18-26 GHz chirped-pulse microwave spectrometer. The colored dotted lines are used to indicate triggers. The valve and the AWG are triggered by the delay generator (purple dashed lines). The pulse train is generated by the AWG, up-converted by LO-1 pulse (see text), doubled, amplified by the SSA, and transmitted into the vacuum chamber via a microwave horn antenna. The FID is received by another microwave horn antenna, amplified with two low-noise amplifiers, and down-converted by LO-2 pulses (see text) to be digitized on the digitizer. The AWG is phase locked to a TCXO oscillator of the Valon synthesizer via a clock distribution board (grey dashed lines). To ensure phase stability, the AWG triggers the SSA, the pulse switch, the protection switch, and the digitizer.*

given in Section 3.2, the waveform of the linear chirp and chirp rate are defined by equations (3.5) and (3.6), respectively. These chirps cover the frequency range from 7 - 3 GHz in 10 segments (known as the pulse train). Each segment is of 15 μs duration and has a 1.5 μs chirp covering 400 MHz bandwidth. This pulse train is up-converted by mixing (M1, Marki T320LS-1521) it with a 16 GHz single frequency local oscillator (LO-1, green box, Figure 3.8) pulse. The generation of LO-1 is described later in this section. The mixer M1 combines the two input frequencies and results in both sum and difference frequencies, which in this case is 9-13 GHz and 23-19 GHz. Only the lower side-bands of this mixing stage are selected by a bandpass filter (Lorch 9IZ7-11000/4000S) to obtain segmented chirps in the 9-13 GHz range. After the mixing stage, the chirped pulses are then amplified (Marki A-0126EZP5-1523) and doubled (Marki MLD0632LS-1452), where the doubler only doubles the frequency range without changing the pulse duration. The amplification step before the doubler is required to meet the power requirement for the doubler. A bandpass filter (Reactel 9CX11-22G-X8G S11) is used to only allow frequencies between 18-26 GHz to pass through, and then each segmented chirp of 800 MHz bandwidth is amplified using a solid state amplifier (SSA) from Quinstar (QPP-18273840MPI) resulting in an output power of around 38 dBm (6 W). The internal switch of the SSA does not allow a pulse duration of less than 2 μs ; therefore an SPST switch (Kratos Microwave Electronics Division F9012) is used to allow a high

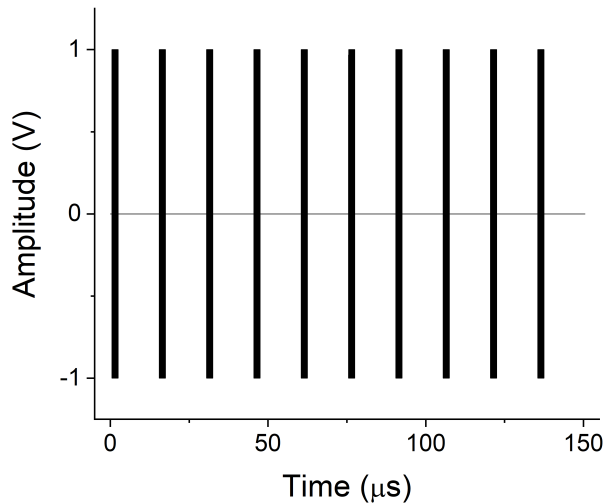


Figure 3.9: *The 18-26 GHz range of the instrument is divided into 10 segments, called a pulse train. Each segment of 15 μs duration has a 1.5 μs chirp of 800 MHz bandwidth.*

power chirp of 1.5 μ s duration. The microwave pulse train (as shown in Figure 3.9) is then broadcast across the vacuum chamber using a microwave 20 dBm gain horn antenna (ATM, Model number 42-442-6) which is separated by 20 cm from the same model FID receiver antenna.

The single frequency 16 GHz LO-1 pulse (green box in Figure 3.8) is created by quadrupling (Quadrupler - Marki AQA-1933), amplifying (Minicircuits, ZRON-8G+) and doubling (Doubler - Eclipse D2010LZ1) a transform limited 2 GHz pulse generated by a Valon synthesizer (Valon Technology 5008 Dual Frequency Synthesizer). Cavity filters are used at each stage to remove any sideband signals from the LO-1 pulse (2 GHz - DBWAVE DBBF0402000200A, 8 GHz - DBWAVE DBBF0408000800B, 16 GHz - Lorch 2CF7-16000/80-S). The 16 GHz LO-1 pulse is then amplified (Minicircuits, ZVA-183+) and passed through a power divider (Minicircuits ZX10-2-183-S+) to have the same LO-1 pulse for the excitation and the free induction decay (FID) collection stages. This is further discussed in the next section.

FID collection

In summary, the free induction decays (FIDs) collected after the excitation of the molecular ensemble are down-converted by mixing (M3, Marki M20240LP) with a

Table 3.1: The final up-converted chirped-pulse frequencies from CH1 of the AWG for each segment, and their corresponding up-converted local oscillator (LO-2) frequencies from CH2 of the AWG.

Segment	Excitation chirped-pulse (MHz)	LO-2 pulse (MHz)
1	18000-18800	19200
2	18800-19600	18400
3	19600-20400	20800
4	20400-21200	20000
5	21200-22000	20800
6	22000-22800	23200
7	22800-23600	24000
8	23600-24400	23200
9	24400-25200	24000
10	25200-26000	24800

local oscillator pulse (LO-2) to result in frequencies between 400-1200 MHz and digitized on a 3.2 GS/s digitizer card (Keysight U5303A). The details of the process follow.

Upon FID collection via the second horn antenna, the high-power SSA pulses are blocked by an SPST switch (American Microwave Corporation SWCH1K-Dc40-SK), which has a typical isolation of 65 dB. Only the FIDs of the molecular ensemble are allowed to pass through, and they are amplified by two low noise amplifiers (LNA) operating from 14-27 GHz (Hittite HMC504LC4B) and 17-27 GHz (Hittite HMC751LC4). The amplified FIDs are then down-converted by mixing (M3, Marki M20240LP) with a local oscillator pulse (LO-2), where the generation of LO-2 is explained below. The intermediate frequency (IF) output of M3 is made to span 400-1200 MHz for each segment, and it is then digitized on a 3.2 GS/s digitizer card (Keysight U5303A). This digitizer card is a 12-bit PCIe signal acquisition card with

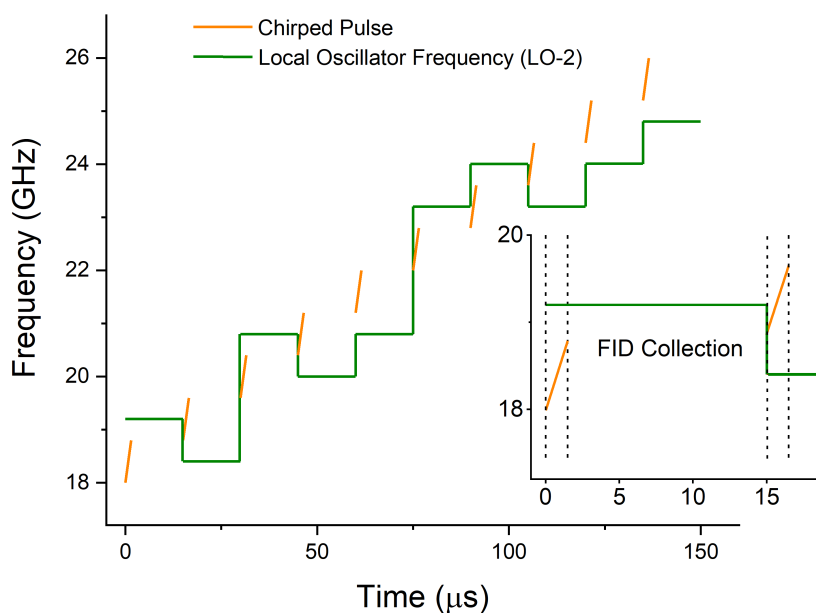


Figure 3.10: *Conceptual segmented 18-26 GHz CP-FTMW spectrogram of the chirp pulses and LO-2 frequencies. The orange trace is the sequence of 800 MHz bandwidth chirped pulses, 1.5 μ s in duration, which are used to excite the molecular ensemble. Simultaneously, the LO-2 frequencies (green trace) down-converted the FID signals before being digitized on a 3.2 GS/s digitizer card.*

on-board data processing unit and can perform real time averaging.

The second channel (CH2) of the AWG is used to create a train of single-frequency waves (subset LO-2, Figure 3.8), simultaneously to CH1, between 7-3 GHz. The output of CH2 is then up-converted by mixing (M2, same as M1) with the second divided output of the 16 GHz LO-1. In a similar way as the excitation pulse creation, the lower side-bands of this mixing stage are selected, amplified, doubled, and again filtered to only allow frequencies between 18-26 GHz to pass through. The final single frequencies are then amplified (Marki A-0126EZP5-1534) and passed through the triple balanced mixer (M3) to down-convert the FID signals. The resulting LO-2 pulse is a train of 10 different single-frequency sine waves, synchronized in time to each segment in CH1 and with an offset of 400 MHz above the end (for segments 1, 3, 6 and 7) or below the start (for segments 2, 4, 5, 8, 9 and 10) of the corresponding chirp. The mixing from above or below was chosen to decrease spurious signals generated by electronics for each segment. The output of the two up-converted AWG waveforms is given in Table 3.1 and a conceptual spectrogram is presented in Figure 3.10.

Timing scheme

The AWG is phase-locked by using the internal 10 MHz temperature compensated crystal oscillator (TCXO) of the Valon. A clock distribution board (Digikey AD9513/PCBZ-ND) takes the TCXO clock reference as input, and it is used to phase lock the AWG. The SSA, digitizer card, and SPST switches are then triggered with the marker channels of the AWG. A delay generator is employed for generating the triggered pulses, where it triggers the valve driver and the AWG.

The experiment sequence is depicted in Figure 3.11. At first, the valve is triggered at time zero, and the valve driver holds it open for a time τ_{valve} . The valve opening time is usually set to $> 450 \mu s$ to account for the three pulse trains. Then the AWG is triggered after a time (t_{exp}) when the expansion reaches the interaction region. The AWG triggers the protection switch, which protects the sensitive detection electronics from the strong excitation pulse. The protection switch stays open for the time ($\tau_{prot.}$) the SSA is on, and the microwave chirps are emitted. The protection switch and the SSA starts 200 ns before the excitation pulse is emitted, to account for the response time of the amplifier. Finally, the AWG emits the microwave pulses and triggers the digitizer card to record the entire time domain for $\tau_{signal} = 150.5 \mu s$. The total time of the experiment is $150 \mu s$, and the extra time of $0.5 \mu s$ accounts for the rearm time of the digitizer card. After each pulse train, the digitizer card requires 500 ns to transfer the data to the computer before it starts collecting the next pulse train.

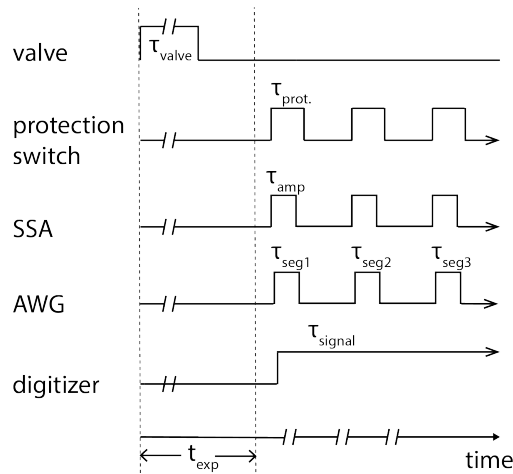


Figure 3.11: *Trigger scheme of the experiment carried out on the segmented 18-26 GHz chirped-pulse spectrometer. An experimental sequence starts with a gas pulse. The valve is opened for a time τ_{valve} . After a time t_{exp} , the expansion reaches the interaction region, and the excitation sequence starts with opening the protection switch for a time τ_{prot} . After a short delay, the SSA is turned on for time τ_{amp} , followed by the emission of a segment of the excitation pulse for time τ_{seg_n} . The digitizer card collects the entire time domain for τ_{signal} , and the FID signal is processed from it.*

The signal is then processed by extracting $10 \mu\text{s}$ of the FID from each segment, beginning 200 ns after the end of the excitation pulse, applying a Kaiser-Bessel window function for side-lobe suppression and FFTing the result. The LO-2 frequency is then added or subtracted from each segment to reconstruct the molecular frequency axis, and the segments are concatenated. After applying background subtraction, a final spectrum is generated.

Sample chamber

The sample chamber, as shown in Figure 3.12 is a CF300 6-way cross chamber, with ISO-KF250 extensions to account for the lengths of the horn antennae. It achieves vacuum through HiPace 2300U and 1200 Pfeiffer turbomolecular pumps, backed by a Leybold booster pump and an ACP 40 mechanical pump. Typical pressures inside the chamber during the experiment are approximately 10^{-5} mbar . The pulsed nozzle is operated at 10 Hz with an opening time $> 450 \mu\text{s}$. The long opening time allows for the incorporation of three pulse trains for each molecular pulse, thereby making the effective repetition rate 30 Hz . The experimental repetition rate is ultimately limited by the pumping speed of the vacuum system. The sample is introduced

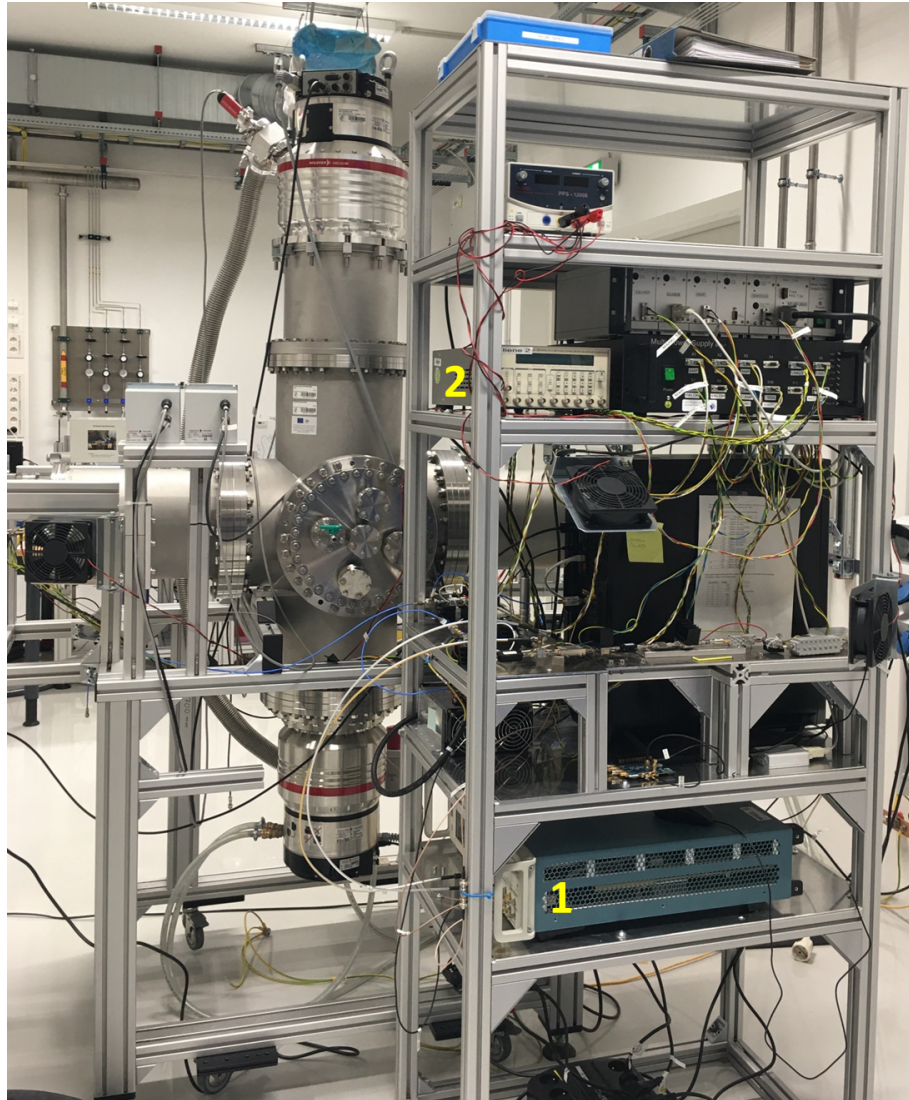


Figure 3.12: *The segmented 18-26 GHz chirped-pulse spectrometer at DESY. The sample chamber is a CF300 6-way cross chamber, with ISO-KF250 extensions to account for the lengths of the horn antennae. The electronics of the spectrometer are placed on the rack next to the sample chamber, where the highlighted components are 1) the AWG, which is used to create the excitation segmented chirps, and 2) the delay generator, used to control the delay between the gas pulse and the AWG.*

into the chamber by using a pulsed valve (Parker General Valve, Series 9), which is positioned perpendicular to the axis of microwave propagation and is equipped with a heatable reservoir for liquid and solid samples.

Optimization process

This section presents the multiple train (multi-train) method employed to collect FIDs in a fast approach, and a background subtraction method to remove electronic spurious responses from the final molecular spectrum.

a. Multi-train method

The fast frame option of the Hamburg COMPACT spectrometer allows for fast data acquisition in a short interval of time. In the Hamburg COMPACT spectrometer operating between 2-8 GHz, each experiment cycle (frame) is 45 μ s long. The experiment is optimised in such a way, that the maximum number of frames can be overlapped in space and time with one gas pulse. Presently, the Hamburg COMPACT spectrometer can include eight frames in one gas pulse. In a similar approach to the fast frame option of the Hamburg COMPACT spectrometer, we included the multi-frame option on the segmented 18-26 GHz CP-FTMW spectrometer. In this spectrometer, each pulse train is 150.5 μ s. Compared to the Hamburg COMPACT spectrometer, in this spectrometer, each pulse train is approximately three times longer, therefore, the number of pulse train per gas pulse is decreased by three. This leads to a possibility to incorporate two to three pulse trains into each gas pulse.

In the present design of the 18-26 GHz spectrometer, three pulse trains have been incorporated in one gas pulse. The multi-train method is demonstrated using a molecular signal of a 0.2% mixture of carbonyl sulphide (OCS) in neon at 3 bar backing pressure, as it has a well characterized rotational spectrum and numerous rare isotopologues, which can be used to characterize and compare the sensitivity of the setup. Figure 3.13 shows a comparison of one average and ten averages, which was collected using the multi-train method, for a molecular signal of the $J=2\leftarrow 1$ rotational transition (at 24325.9453 MHz) of OCS. It can be seen that the decrease in the signal level from one to ten averages is around 10%. This decrease can be attributed to the inhomogeneity of the gas pulse in each shot, and therefore a slight decrease in the signal level on averaging can be expected. With the multi-train method, the FID collection time is increased by a factor of three and allows us to record around 2.5 million averages in a day.

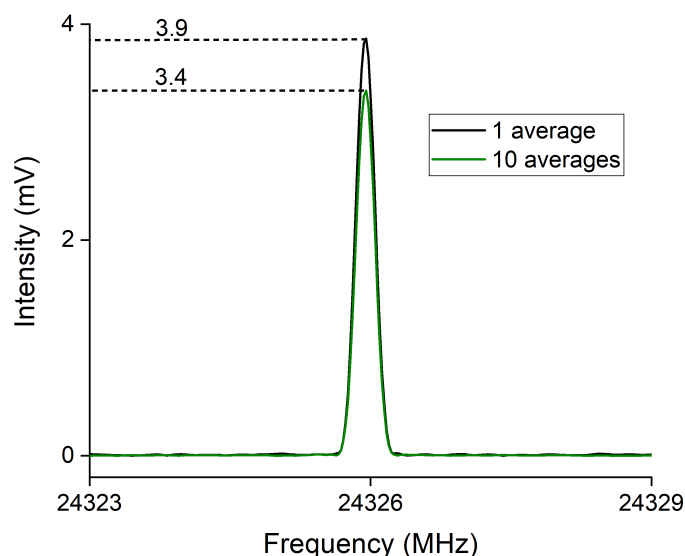


Figure 3.13: A comparison of 1 average and 10 averages (collected using the multi-train method) for a molecular signal of the $J=2\leftarrow 1$ rotational transition (at 24325.9453 MHz) of OCS.

b. Background subtraction

The mixing of electronic signals at multiple stages leads to random and unwanted/spurious signals. The response of the electronic components without the molecular signals can be captured by turning off CH1 of the AWG. This prevents the generation of the pulse train. Without CH1, the mixing of LO-1 and outputs of CH2 of the AWG will give a spectrum representing the response of electronics, as shown in Figure 3.14. In the present design, due to this mixing, there are strong spurious signals (spurs) every 200 MHz and some weak spurs in between, as shown in the zoom-in of Figure 3.14. These unwanted signals can crowd a spectrum with unwanted lines and can also mix with molecular signals leading to false intensity patterns. To remove these spurious signals, the electronics response spectrum of the spectrometer is subtracted from the molecular spectrum, matching the number of acquisitions as in the molecular spectrum. As the intensity fluctuation of the electronics response is random, the subtraction process does not guarantee removal of all the spurs, and it can sometimes result in negative "intensities" in the final spectrum.

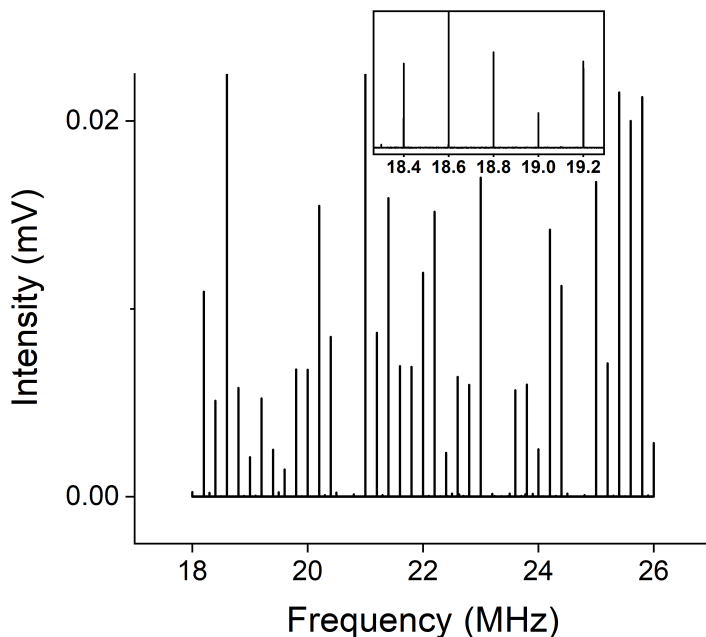


Figure 3.14: *Electronics response spectrum without CH1 of the AWG. In the present design, due to the mixing of electronic signals, there are strong spurious signals every 200 MHz, as shown in the zoom-in. The y scale of the zoom-in is the same as the main spectrum.*

Automation

The instrument is controlled by home-built scripts written in Python 3.5 by Dr. Amanda Steber, and the software packages available for Valon synthesizer and for Keysight digitizer card. The 2 GHz pulse is created by Valon software, and the data acquisition is controlled by Keysight soft front panel. Various steps involving averaging and FFTing the time domain, adding the LO-2 frequencies to each FID segment, stitching the spectrum together, and subtracting the background signal is controlled by a combination of scripts written in Python. After data acquisition, the complete process of obtaining the 18-26 GHz spectrum takes 1 minute.

3.5.2 Performance

As this approach has not been implemented before and the instrument is newly constructed, it is important to benchmark the performance of this spectrometer to the first CP-FTMW instrument constructed in this frequency range from the University of Virginia (UVa), USA, which is presented in Reference [122]. The first subsection shows the phase stability achieved by the TCXO clock of the Valon synthesizer and

compares with the standard rubidium clock using a molecular signal of hexanal. In the next subsection, the frequency accuracy of the instrument is demonstrated using hexanal and OCS. Hexanal has a characteristically dense spectrum, allowing for the identification of multiple conformers within its spectrum as well as isotopologue species, and its study is presented in Reference [122]. OCS is a well characterized molecule, and it exhibits distinct and easily identifiable spectral lines for various isotopologues in natural abundance. The last subsection demonstrates the dynamic range of the spectrometer again using hexanal and OCS.

Phase stability

As mentioned in the Hamburg COMPACT section (3.2), phase stability is a key parameter of a CP-FTMW spectrometer. The sensitivity to observe weak signals and the dynamic range of the spectrometer comes from the ability to average the FID signal in the time domain over many spectrum acquisitions coherently. For this purpose, phase reproducible excitation pulses are required. Generally, this is dictated by a low phase noise, standard 10 MHz rubidium (Rb) oscillator used as a reference, to phase lock microwave instrument [36, 83]. On the COMPACT spectrometer, this cost of the Rb clock is €3000. To remove the cost of the expensive Rb clock and still maintaining phase reproducibility, in the segmented 18-26 GHz CP-FTMW instrument, the phase stability is achieved by using an internal 10 MHz TCXO clock of the Valon synthesizer.

The phase stability of the instrument has been evaluated using both clocks as references and the signal level of a transition of conformer 1 of hexanal. The phase noise offered by the Rb clock is < -120 dBc/Hz and by the TCXO clock < -90 dBc/Hz at 10 MHz. To change the reference of the instrument from the TCXO clock to the 10 MHz Rb oscillator, the input for the clock distribution board was attached to one output of the Rb clock and one output of the clock distribution board was sent to the Valon synthesizer (which can also be set to accept an External reference), and another one to the AWG. Figure 3.15 shows a comparison of the signal level of a transition of conformer 1 of hexanal taken with one average and 1 million averages, using a standard Rb clock or a TCXO clock offered by Valon as references. It can be seen that in both the cases, the decrease in the signal on long averaging is approximately 10%, and the signal levels are comparable. This shows that the TXCO clock is offering the same phase stability as the Rb clock on long averaging.

Frequency accuracy and resolution

The frequency accuracy of the instrument is benchmarked by comparing the center frequencies determined for all of the measured rotational transitions of conformer 1

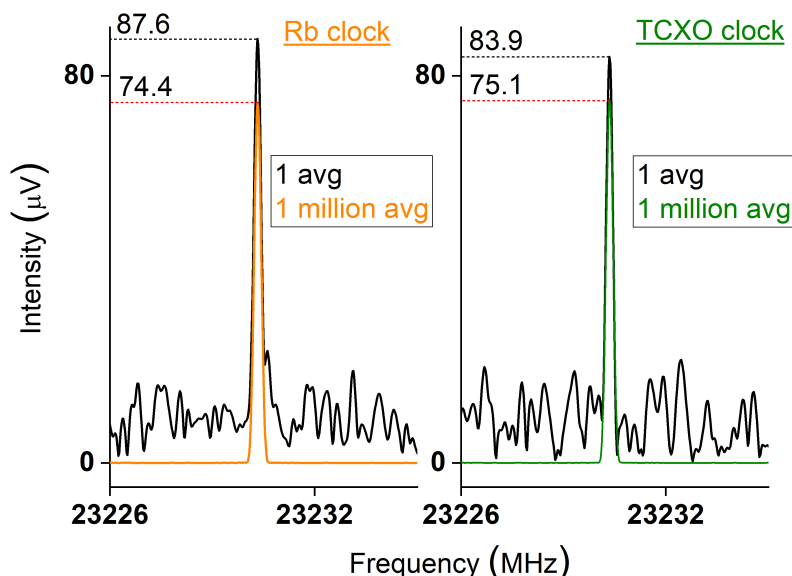


Figure 3.15: A comparison between a standard rubidium (*Rb*) clock and the TCXO clock offered by the Valon synthesizer used as references for the segmented 18-26 GHz CP-FTMW instrument. Both spectra compare the signal level for one versus one million averages for a rotational transition of conformer 1 of hexanal.

of hexanal and its ^{18}O isotopologue, obtained from the UVa 18-26 GHz CP-FTMW spectrometer [122], to those obtained from the segmented 18-26 GHz CP-FTMW spectrometer. For simplicity in the following discussion, the UVa 18-26 GHz CP-FTMW spectrometer is referred as ‘UVa’, and the segmented 18-26 GHz CP-FTMW spectrometer as ‘Hamburg’. The measured transitions obtained from UVa were fit to an asymmetric rotational Hamiltonian to generate a set of rotational constants and calculated frequency values corresponding to conformer 1 of hexanal and its ^{18}O isotopologue. These calculated frequency values of UVa were then compared with the measured transitions obtained from Hamburg, and the difference between the two values is observed to be less than 20 kHz, except for one discrepancy. In the case that the measured transitions obtained from Hamburg were fit to an asymmetric rotational Hamiltonian, the difference between the measured and calculated frequency values is below 10 kHz, for both conformer 1 and its ^{18}O isotopologue. The two comparisons of the calculated frequencies with the observed transitions obtained from Hamburg for conformer 1 of hexanal and its ^{18}O isotopologue are given in Appendix 1. A summary of the fitted rotational constants and distortion constants for conformer 1 of hexanal and its ^{18}O isotopologue obtained from UVa and Hamburg is given in Table 3.2. In microwave spectroscopy, a microwave root mean square

(RMS) values of the measured transitions with the calculated frequencies is used to determine the accuracy of the experimentally obtained rotational parameters, which is used to calculate the structural parameters of a molecule. From the assigned rotational transitions of hexanal with UVa, an RMS value of ~ 4 kHz and ~ 7 kHz is obtained for conformer 1 of hexanal and its ^{18}O isotopologue, respectively. With Hamburg, RMS values of ~ 12.7 kHz for conformer 1 and ~ 17 kHz for the ^{18}O isotopologue are obtained when the rotational and distortion constants are fixed to the values obtained from UVa. RMS values of ~ 6 kHz for conformer 1 and ~ 9 kHz for the ^{18}O isotopologue are obtained when the rotational and distortion constants are allowed to be fit to the transitions obtained from Hamburg. The obtained rotational parameters from Hamburg, when the fit is allowed to be float, is comparable to the obtained rotational parameters from UVa, for both conformer 1 of hexanal and its ^{18}O isotopologue. Therefore, it can be concluded that the performance of Hamburg with respect to frequency accuracy is similar to UVa.

Table 3.2: A comparison of the rotational constants (A, B, C) and distortion constants (Δ_J , Δ_{JK} , Δ_K , δ_J) for conformer 1 of hexanal and its ^{18}O isotopologue, obtained from the UVa CP-FTMW spectrometer, as presented in Reference [122], and the Hamburg segmented CP-FTMW spectrometer, as presented in this work.

	Conformer 1			^{18}O Conformer 1		
	UVa [122]	Hamburg		UVa [122]	Hamburg	
		Fixed	Float		Fixed	Float
A (MHz)	9769.6385(41)	<i>a</i>	9769.6429(61)	9511.5910(64)	<i>b</i>	9511.6030(87)
B (MHz)	868.84583(21)	<i>a</i>	868.84861(32)	843.5515(31)	<i>b</i>	843.5600(42)
C (MHz)	818.51887(19)	<i>a</i>	818.52102(28)	794.2703(11)	<i>b</i>	794.2745(15)
Δ_J (kHz)	0.04597(48)	<i>a</i>	0.05281(72)	<i>a</i>	<i>b</i>	<i>c</i>
Δ_{JK} (kHz)	-0.8782(47)	<i>a</i>	-0.8497(70)	<i>a</i>	<i>b</i>	<i>c</i>
Δ_K (kHz)	25.70(79)	<i>a</i>	24.5(11)	<i>a</i>	<i>b</i>	<i>c</i>
δ_J (kHz)	0.00514(18)	<i>a</i>	0.00530(27)	<i>a</i>	<i>b</i>	<i>c</i>
N_{lines}	46	46	46	6	6	6
σ (kHz) ^a	4.1	12.7	6.0	6.7	17.0	9.0

a: fixed to the assignments from the UVa CP-FTMW spectrometer for conformer 1.

b: fixed to the assignments from the UVa CP-FTMW spectrometer for ^{18}O conformer 1.

c: fixed to the assignments from the segmented CP-FTMW spectrometer for the fitted value of the parent isotopologue of conformer 1.

Another example to show the frequency accuracy of the instrument is performed by comparing the experimental frequency values for some of the isotopologues of OCS from literature with the frequencies obtained with the segmented CP-FTMW spectrometer, as presented in Table 3.3. The agreement between the segmented CP-FTMW frequencies and the literature frequencies are of the order of 20 kHz.

With the hexanal and OCS examples it can be concluded that the frequency accuracy of the segmented 18-26 CP-FTMW spectrometer is around 20 kHz. The resolution of the spectrometer based on the digitization rate of the Keysight digitizer card is 100 kHz. After applying the Kaiser Bessel window function, in practice a linewidth of 240 kHz is achieved.

Dynamic range

To compare the dynamic range, hexanal was measured under similar experimental conditions as were employed in Reference [122]. In that study, a mixture of 0.2% hexanal in neon was supersonically expanded into the vacuum chamber with 1 bar backing pressure using three nozzles, and a total of 1.9 million averages were collected. They observed 12 conformers of hexanal, and they provided an experimental relative energy ordering, with conformer 1 being the global minimum. For conformers 1-4, all ^{13}C isotopologues were assigned, with ^{18}O isotopologues being assigned for conformers 1 and 2 in natural abundance. With the segmented 18-26 GHz CP-FTMW spectrometer, 1.9 million averages of hexanal were collected using one nozzle. All 12 of the conformers of hexanal were identified, as shown in Figure 3.16, and the same isotopologues were also observed in natural abundance.

The signal-to-noise ratio (SNR) of each conformer in both spectra can be compared to benchmark the dynamic range of our instrument. Seifert et al. [122] obtained an SNR of ca. 5000:1 for conformers 1 and 2, and ca. 300:1 for conformers 3 and 4. With our instrument, for conformer 1 and 2, the SNR was found to be approximately 2400:1 and 3200:1, respectively. For conformers 3 and 4, the SNR was greater than 300:1. In order to directly compare our SNR to theirs, a linear scaling was used to account for the fact that Seifert et al. [122] used three nozzles, while only one was employed in our setup. This reduces their effective SNR per nozzle to ca. 1666:1 for conformers 1 and 2, and ca. 100:1 for conformer 3 and 4. With the segmented 18-26 GHz CP-FTMW spectrometer, we were able to achieve the expected SNR for conformers 1-4, compared to the UVa CP-FTMW spectrometer. Therefore, it can be safely concluded that the SNR ratio observed with the segmented 18-26 GHz CP-FTMW spectrometer is comparable with the CP-FTMW 18-26 GHz instrument, establishing that the dynamic range of the spectrometer is comparable with the broadband instrument.

Table 3.3: Comparison of the $J=2\leftarrow 1$ rotational transition of OCS obtained with the segmented CP-FTMW spectrometer with reported values in the literature.

Isotopologue	F' \leftarrow F''	Segmented CP-FTMW freq. (MHz)	Lit. freq. (MHz)	Difference (kHz)
OCS		24325.9453	24325.930(10) ^a	15.3
OC ³⁴ S		23731.3112	23731.302(10) ^a	9.2
O ¹³ CS		24247.6799	24247.668(10) ^a	11.9
OC ³³ S				
	3/2-1/2	24012.3693	24012.345(5) ^b	24.3
	5/2-5/2	24012.9908	24012.964(5) ^b	26.8
	5/2-3/2		24020.249(5) ^{b,+}	
	7/2-5/2	24020.2733	24020.249(5) ^{b,+}	24.3
	3/2-3/2	24025.4709	24025.488(5) ^b	22.9
¹⁸ OCS		22819.4130	22819.3930(10) ^c	20.0
O ¹³ C ³⁴ S		23646.9155	23646.8935(10) ^c	22.0
¹⁷ OCS	9/2-7/2	23534.6933	23534.6780(5) ^b	15.3
OC ³⁶ S		23198.7541	23198.7344(10) ^c	19.7
¹⁸ OC ³⁴ S		22239.8590	22239.8438(10) ^c	15.2
O ¹³ C ³³ S		23938.8379	23938.8340(21) ^d	3.9
¹⁸ O ¹³ CS		22764.2483	22764.240(20) ^e	8.3

^a Bomsdorf, H., Dreizler, H. & Mäder, H. (1980). *Zeitschrift für Naturforschung A*, 35(7), pp. 723-730.

^b Merke, I. & Dreizler, H. (1987). *Zeitschrift für Naturforschung A*, 42(9), pp. 1043-1044.

^c R. D. Suenram, private communications (1998).

^d F. J. Lovas, *J. Phys. Chem.*, 7, (1978), 1445-1750.

^e H. S. P. Müller, F. Schlöder, J. Stutzki, and G. Winnewisser, *J. Mol. Struct.* 742, (2005), 215-227.

+ For OC³³S, the F=5/2-3/2 and the 7/2-5/2 transitions are blended at the experiment resolution.

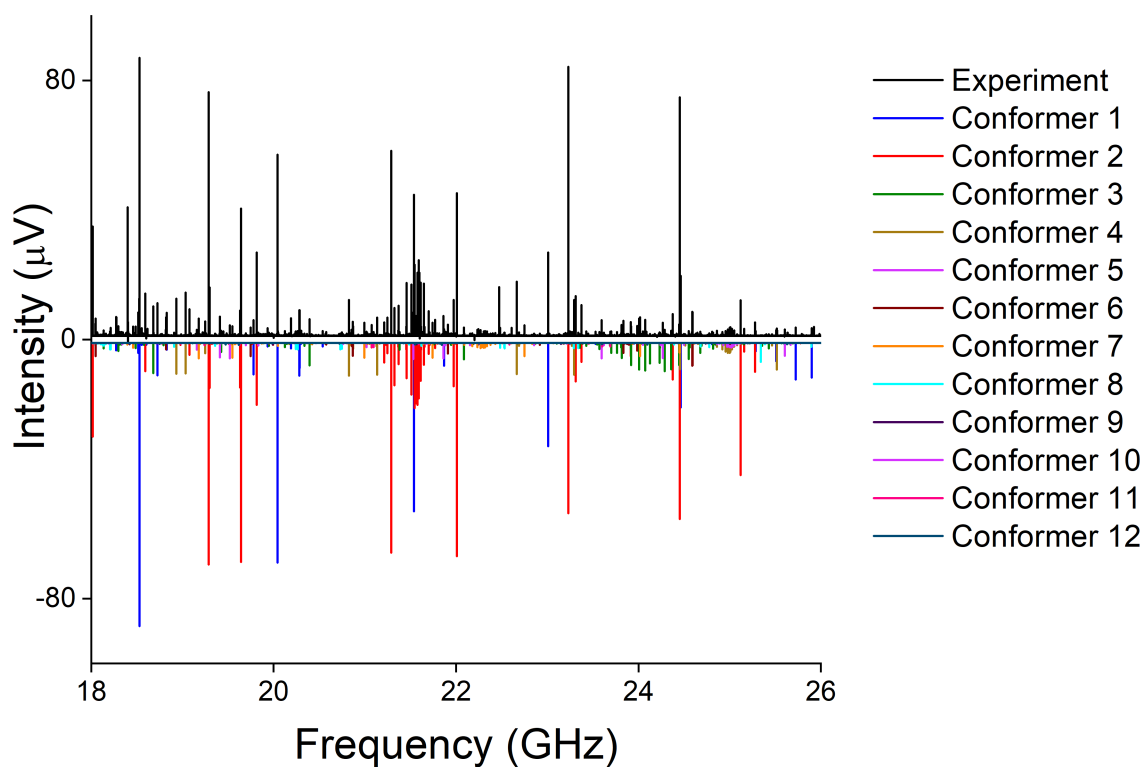


Figure 3.16: *The rotational spectrum of 1-hexanal measured with the segmented 18-26 GHz CP-FTMW spectrometer. The black trace shows the experimental spectrum, and the simulations of all the 12 assigned conformers are shown in color.*

Figure 3.17 shows a comparison of the hexanal spectrum recorded in Hamburg (black

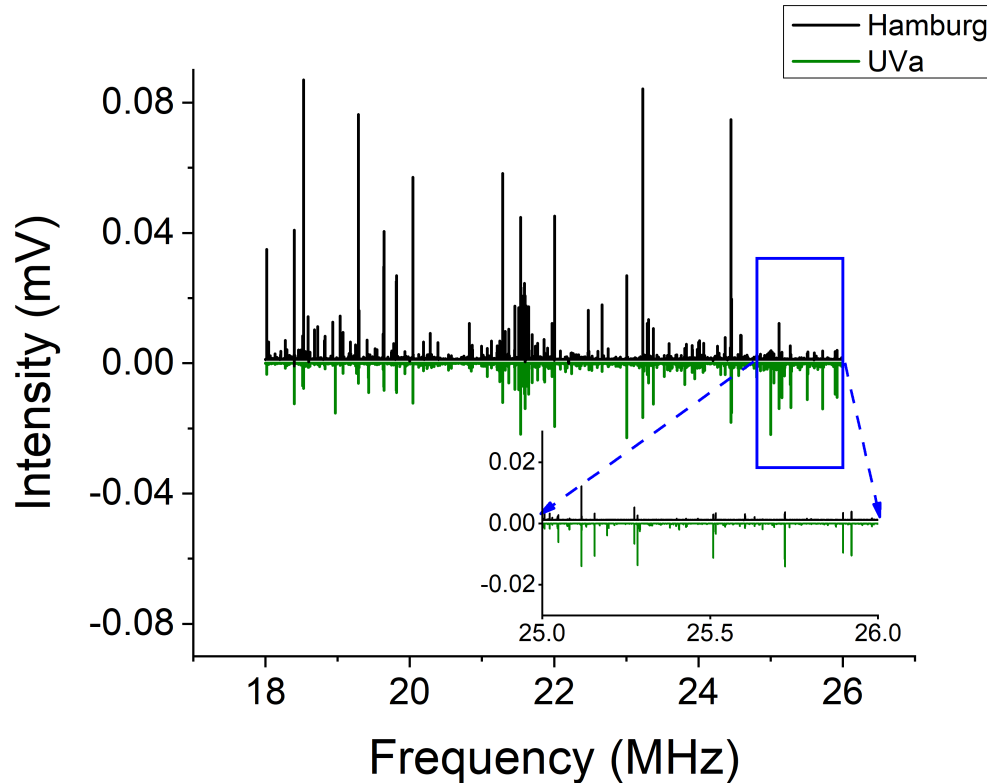


Figure 3.17: Comparison of the 1-hexanal spectrum recorded in Hamburg (black trace) with the UVa spectrum previously reported (green trace). The blue box highlights the sharp cutoff in the intensity > 25 GHz. The x and the y scale of the zoom-in are the same as the main spectrum.

trace showing 1.9 million averages) with the UVa spectrum previously reported (green trace) [122]. The strongest line from the UVa spectrum has been scaled to be compared with the Hamburg spectrum. The intensity profile of the Hamburg spectrum is comparable to the UVa spectrum, but there is a sharp intensity cut-off around 25 GHz. An important factor affecting the intensity distribution across the whole range is the excitation pulse power in each segment. It can be seen that the excitation pulse power between 25-26 GHz is weaker compared to the 18-25 GHz range, highlighted with a blue box in Figure 3.17. This will be corrected in the future by performing intensity calibrations for each segment. This would involve measuring the power loss in the excitation pulses across the whole band, and a function, which will be derived from determining this power loss, will be applied to the spectrum to account for intensity variation.

Another example demonstrating the dynamic range of the instrument is presented using the molecular signals of OCS. To measure the weak isotopologues of OCS, the experiment was performed by using a 0.2% gas mixture of OCS in neon. This mixture was supersonically expanded in the vacuum chamber using one nozzle, with 3 bar backing pressure. A total of 200 000 averages were collected and FFTed. Figure 3.18 shows the spectrum of OCS, where the strongest transition belongs to $J = 2 \leftarrow 1$ transition of the parent species, $^{16}\text{O}^{12}\text{C}^{32}\text{S}$, and its $^{18}\text{O}^{13}\text{C}^{32}\text{S}$ isotopologue is shown in the zoom-in. The natural abundance of this isotopologue is 0.00211%. The SNR obtained for the parent species transition is approximately 100 000:1.

The 18-26.5 GHz CP-FTMW spectrometer is also presented in the PhD thesis of Dr.

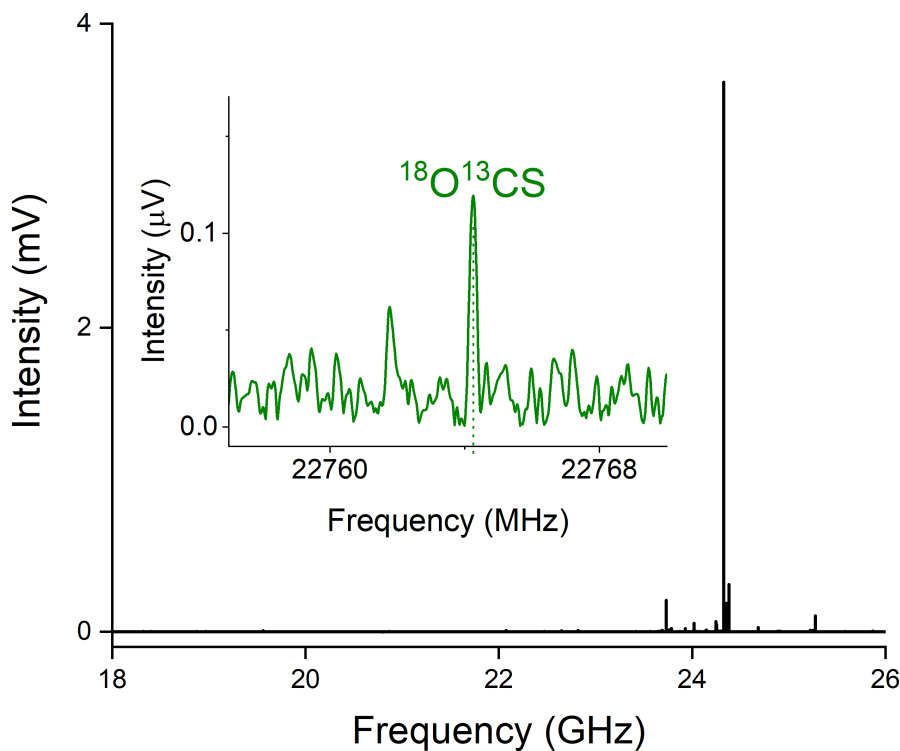


Figure 3.18: *The spectrum for the $J=2 \leftarrow 1$ rotational transition (at 24325.9453 MHz) of OCS (0.2% in neon, 200 000 avgs). The inset shows a zoom-in on the $^{18}\text{O}^{13}\text{C}^{32}\text{S}$ isotopologue which has a natural abundance of 0.00211% (44 000 times less abundant than the normal species).*

Daniel P. Zaleski [124], and displays that with 200 000 averages of OCS, the weakest isotope observed with their instrument was also the $^{18}\text{O}^{13}\text{CS}$ isotopologue. In their experiment, the SNR obtained for the parent species transition is approximately 180 000:1 using three nozzles, which, on scaling for one nozzle, is 90 000. This example also proves that the dynamic range of the segmented 18-26 GHz CP-FTMW instrument is comparable with the broadband instrument.

Cumulative part

Chapter 4

Cumulative part

The interplay of different forces of intermolecular interactions, in particular, hydrogen bonding and dispersion interactions, plays a key role in the formation and stability of chemical and biological systems. These forces can either act in a synergistic way or can compete against each other. This interplay can be observed in molecular aggregation and recognition processes, where some structures are stabilized mainly by hydrogen bonding, and others by dispersion interactions. To date, the mechanism of these forces to stabilize certain structures is not well known, and counter-intuitive results may be found [6]. A better understanding of this interplay of hydrogen bonding and dispersion interactions can be obtained by studying molecular model systems to systematically examine and quantify the London dispersion contribution to interaction energies [16]. For this, three kinds of molecular model systems are presented in this work. The first kind investigates the effect of dispersion interactions on a strong classical hydrogen OH-O bonded complex in a systematic approach. The second kind of complexes are studied to compare strong, classical OH-O hydrogen bonds and weak OH- π hydrogen bonds, where dispersion interactions play an important role in forming the preferred structure. In the third kind, in the absence of a classical OH-O hydrogen bond formation, the effect of dispersion interactions on dimer formation, by weak OH- π and/or CH-O hydrogen bonds as well as π - π interaction, are investigated.

To investigate the first kind of model systems, complexes of camphor with alcohol are studied, where the size of the binding partner is increased from methanol to ethanol, and compared with a previous study on camphor-water [86]. This work is presented in the Monographic part (Chapter 5, Section 5.1), where it is observed that on increasing the side chain length of the alcohol, the contribution from dispersion interaction is increasing. In this chapter, the second and the third kinds of model systems are investigated. For the second kind, complexes of ether/benzofuran with different sizes of alcohols are studied and presented in Section 4.1, where the

complexes of phenyl vinyl ether with methanol is presented in Section 4.1.1. The complexes of diphenyl ether with water, methanol, *tert*-butyl alcohol and adamantanol are presented in Section 4.1.2, and the complexes of dibenzofuran with water, methanol, and *tert*-butyl alcohol are presented in section 4.1.3. Through these different systems investigated in Section 4.1, the outcome of the binding process with partners of different sizes and complexity will allow for a systematic understanding of the recognition process governed by the interplay of the individual forces. To investigate the third kind, homodimers of diphenyl ether, dibenzofuran and fluorene are studied and presented in Section 4.2. The interplay of weak OH- π and/or CH-O hydrogen bonds as well as π - π interactions will give an insight into the stability of the preferred structure of the respective homodimers.

4.1 Weakly bound complexes of ethers and benzofuran with alcohols

The complexes between an ether and an alcohol molecule were studied with three spectroscopic methods, within a priority program on ‘Control of London Dispersion Interactions in Molecular Chemistry’ by the Deutsche Forschungsgemeinschaft (SPP1807). These three techniques are Fourier-transform infrared spectroscopy (FTIR spectroscopy, performed by the group of Prof. Dr. Martin Suhm, Göttingen), infrared/ultraviolet (IR/UV) double resonance spectroscopy (performed by the group of Prof. Dr. Markus Gerhards, Kaiserslautern), and chirped-pulse Fourier transform microwave spectroscopy (CP-FTMW, as part of this work). A short description of the three techniques with respect to the study of weakly bound clusters within the collaboration follows.

FTIR spectroscopy [125] is a sensitive linear spectroscopic technique. As long as the molecules are volatile enough to realize carrier gas mixtures in the 100 ppm range [126] and their vibrational modes are IR active, they can be probed by FTIR technique. This technique can provide an important insight into the intermolecular interactions on cluster formation based on certain band patterns in the spectrum. In an FTIR spectrum, clusters with direct hydrogen bonds to polar atoms tend to show larger downshifts of the hydride (OH) stretching frequency than with the π -systems. Also, cooperative hydrogen bond patterns lead to larger shifts than isolated hydrogen bonds due to their larger bond strengths. Further confirmation is obtained from harmonic quantum-chemical calculations, which predict the frequency shifts of OH fundamental stretching modes with different binding sites and provides a helpful assignment. However, this technique becomes limited when comparing different orientations of the solvent molecule for the same binding site. The spectral resolution

provided by this technique is typically not sufficient to distinguish moments of inertia and thus different structures in a direct way [126].

The IR/UV double resonance [55, 56] is a non-linear spectroscopic technique, which can often differentiate between different clusters. In this technique, the UV laser is parked on an $S_1 \leftarrow S_0$ electronic transition of a complex, and the IR laser is scanned to probe its corresponding vibrational state [127, 128]. Similar to the FTIR spectroscopy, confirmation is obtained from harmonic quantum-chemical calculations for the OH stretching mode. Additionally, theoretical predictions of electronic excitation energy differences between complexes can further support an assignment and differentiate between them.

Microwave spectroscopy, only restricted to polar molecules, is a high-resolution and high-sensitivity technique [28, 38, 83, 86]. It allows one to detect isotopologues of molecules and complexes in natural abundance if the signal-to-noise ratio of a complex transition is sufficient. The structure of a complex can, in principle, be worked out by systematic isotope substitution. However, with increasing system size this can become a limitation. In such cases, it is often sufficient to compare theoretically predicted rotational constants and dipole moment components with experimental

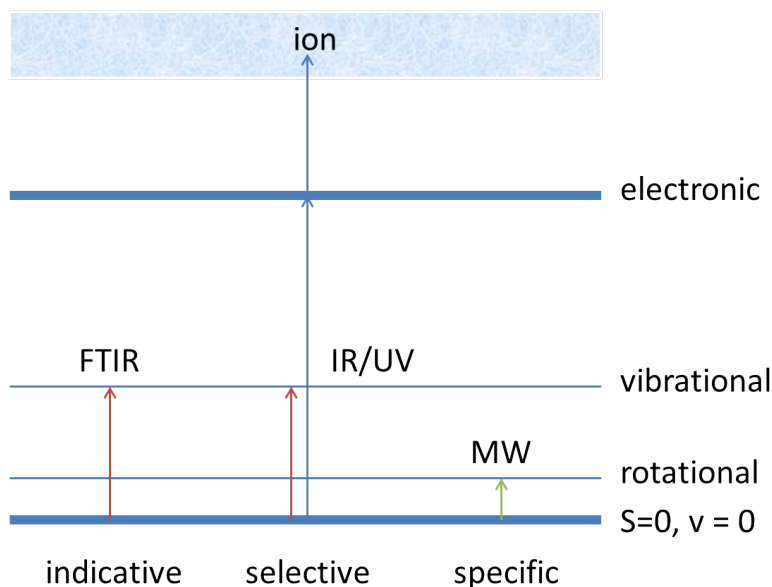


Figure 4.1: *Schematic levels and transitions involved in the multi-spectroscopic method used to identify the complexes between an ether and an alcohol, presented in this thesis. Figure adapted from Reference [126].*

rotational constants and relative intensities of each type of transitions to distinguish isomers and achieve an unambiguous assignment. A schematic diagram, connecting the three techniques in this collaboration, is represented in Figure 4.1.

The three different ether molecules studied in this work are phenyl vinyl ether (PVE), diphenyl ether (DPE), and dibenzofuran (DBF). As shown in Figure 4.2, the three molecules are structurally similar and can be visualized as having a phenoxy group attached to either an ethenyl group for PVE, phenyl group for DPE, or benzyl group for DBF. All ethers offer both a hydrogen bond acceptor site via the ether oxygen as well as good dispersion interactions via the phenyl ring or ethenyl/phenyl/benzyl groups. The binding partner R-OH is selected by increasing the bulkiness of the R group (where R = H for H₂O, CH₃ in methanol, C(CH₃)₃ in *tert-butyl* alcohol, and

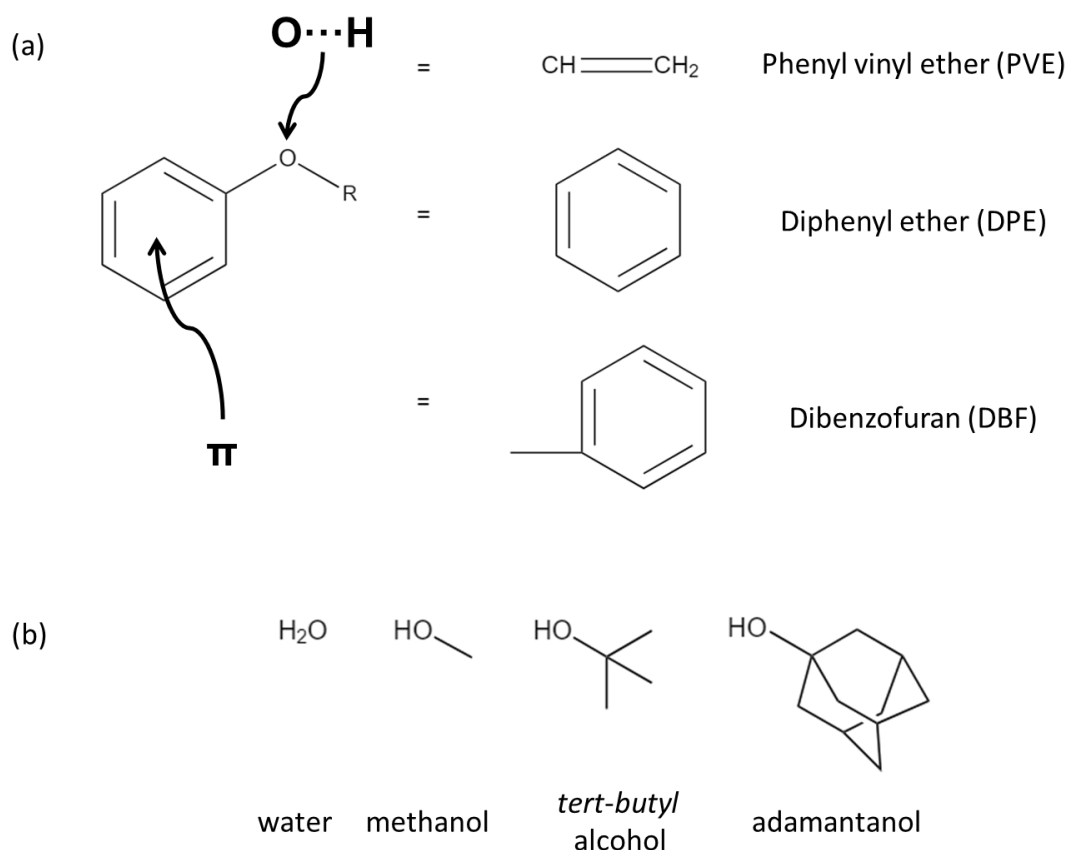


Figure 4.2: a) Structures showing the similarity of the three ether molecules studied in this work. b) Structures of the binding partner R-OH as water, methanol, *tert-butyl* alcohol, and adamantanol.

C₁₀H₁₅ in adamantanol), as shown in Figure 4.2.

An aliphatic alcohol can attach to an ether molecule either to its dispersive binding pocket via OH- π interactions, or to the oxygen lone pairs resulting in a classical OH-O hydrogen bond. Thus, the outcome of the binding process with partners of different sizes and complexity will allow for a systematic understanding of the recognition process governed by the interplay of the individual forces. This will help us in determining the preferred binding positions, interactions, and the associated binding energies. A comparison of the transition intensities recorded for different cluster geometries to theoretical calculations will further give us information about the relative energy ordering of the observed clusters.

4.1.1 The phenyl vinyl ether-methanol complex

The study of phenyl vinyl ether (PVE) with methanol has been performed to understand the role of dispersion interactions on structural preference in the presence of multiple binding sites. In PVE-methanol complexes, a methanol molecule can form a complex with PVE at any of the binding sites (the ether oxygen (O), the phenyl (P) group, or the ethenyl (E) group). Quantum-chemical calculations were performed at different levels in order to investigate the preferences of the different binding sites. Energy orderings of these complexes at the three levels of theory described below are inconsistent. At the B3LYP-D3(BJ)/def2-TZVP level of theory, the OH-E structure is predicted to be the global minimum. According to SCS-CC2/def2-TZVP calculations performed by another group in the collaboration, OH-P is the global minimum. Calculations at a sophisticated local coupled cluster method, the LCCSD(T0)-F12/CBS[T:Q]//B3LYP-D3/def2-TZVP level of theory gives OH-O' as the global minimum when only relative electronic energies are compared, and OH-O as the global minimum when zero-point corrected relative electronic energies are compared. This ambiguity from the calculations makes it an interesting system for the multi-spectroscopic study.

As methanol is a small binding partner, its tendency to form an OH-O complex will be higher than the OH- π . The results of the FTIR and the IR-UV technique reveal the preference of a hydrogen bounded complex of PVE-methanol (OH-O) over the π bound (OH-P or OH-E). This preference is confirmed by microwave spectroscopy, and an additional less populated OH-P isomer is also detected only in the rotational spectrum. In the microwave spectrum, the splitting of transitions due to internal rotation of the methanol methyl group is observed. From this, the V_3 barrier height and the orientation of the methyl group with respect to the principal axis system for the OH-O hydrogen bound complex is determined. The experimentally deter-

mined V_3 value is 261 cm^{-1} (3.1 kJ mol^{-1}) and is less than the calculated value of 341 cm^{-1} (4.1 kJ mol^{-1}) at the SCS-CC2/def2-TZVP level of theory. Further, in the rotational spectrum, all the mono-substituted ^{13}C isotopologues of the OH-O hydrogen bound complex in natural abundance is observed. With this the carbon backbone structure of the OH-O bound complex is determined using the Kraitchman's equations (r_s structure).

On comparing the experimental results with the quantum-chemical calculations for these isomers, it can be seen that the correct energy ordering is only predicted with the sophisticated local coupled cluster method. A further quantification and visualization of dispersion interactions provides insights into the role of the secondary CH- π interactions in deciding the binding preference. This study was published in the Thematic Series "Dispersion interactions" in the Beilstein Journal of Organic Chemistry in 2018, and is given below.

Title	The phenyl vinyl ether–methanol complex: a model system for quantum chemistry benchmarking
Authors	Dominic Bernhard, Fabian Dietrich, Mariyam Fatima, Cristóbal Pérez, Hannes C. Gottschalk, Axel Wuttke, Ricardo A. Mata, Martin A. Suhm, Melanie Schnell and Markus Gerhards
Journal	Beilstein Journal of Organic Chemistry
Volume	14
Year	2018
Pages	1642–1654
DOI	10.3762/bjoc.14.140
Pages	14 pages of main article and 30 pages of supplementary material

Proportion of authors for the microwave part

Experiment	Mariyam Fatima and Dominic Bernhard
Analysis	Mariyam Fatima and Cristóbal Pérez
Manuscript Preparation	Mariyam Fatima, Cristóbal Pérez, Melanie Schnell



The phenyl vinyl ether–methanol complex: a model system for quantum chemistry benchmarking

Dominic Bernhard¹, Fabian Dietrich¹, Mariyam Fatima^{2,3}, Cristóbal Pérez^{2,3}, Hannes C. Gottschalk⁴, Axel Wuttke⁴, Ricardo A. Mata^{*4}, Martin A. Suhm^{*4}, Melanie Schnell^{*2,3,5} and Markus Gerhards^{*1}

Full Research Paper

[Open Access](#)

Address:

¹Fachbereich Chemie & Research Center Optimas, Technische Universität Kaiserslautern, Erwin-Schrödinger-Str. 52, D-67663 Kaiserslautern, Germany, ²Max Planck Institute for the Structure and Dynamics of Matter, Luruper Chaussee 149, D-22761 Hamburg, Germany, ³Deutsches Elektronen Synchrotron (DESY), Notkestrasse 85, D-22607 Hamburg, Germany, ⁴Institut für Physikalische Chemie, Georg-August-Universität Göttingen, Tammannstrasse 6, D-37077 Göttingen, Germany and ⁵Institute of Physical Chemistry, Christian-Albrechts-Universität zu Kiel, Max-Eyth-Strasse 1, D-24118 Kiel, Germany

Email:

Ricardo A. Mata^{*} - rmata@gwdg.de;
Martin A. Suhm^{*} - msuhm@gwdg.de;
Melanie Schnell^{*} - melanie.schnell@desy.de;
Markus Gerhards^{*} - gerhards@chemie.uni-kl.de

* Corresponding author

Keywords:

dispersion interactions; IR spectroscopy; quantum-chemical calculations; rotational spectroscopy; structure determination; weak hydrogen bonds

Beilstein J. Org. Chem. **2018**, *14*, 1642–1654.

doi:10.3762/bjoc.14.140

Received: 16 March 2018

Accepted: 02 June 2018

Published: 02 July 2018

This article is part of the Thematic Series "Dispersion interactions".

Guest Editor: P. Schreiner

© 2018 Bernhard et al.; licensee Beilstein-Institut.

License and terms: see end of document.

Abstract

The structure of the isolated aggregate of phenyl vinyl ether and methanol is studied by combining a multi-spectroscopic approach and quantum-chemical calculations in order to investigate the delicate interplay of noncovalent interactions. The complementary results of vibrational and rotational spectroscopy applied in molecular beam experiments reveal the preference of a hydrogen bond of the methanol towards the ether oxygen (OH \cdots O) over the π -docking motifs via the phenyl and vinyl moieties, with an additional less populated OH \cdots P(phenyl)-bound isomer detected only by microwave spectroscopy. The correct prediction of the energetic order of the isomers using quantum-chemical calculations turns out to be challenging and succeeds with a sophisticated local coupled cluster method. The latter also yields a quantification as well as a visualization of London dispersion, which prove to be valuable tools for understanding the role of dispersion on the docking preferences. Beyond the structural analysis of the electronic ground state (S_0), the electronically excited (S_1) state is analyzed, in which a destabilization of the OH \cdots O structure compared to the S_0 state is observed experimentally and theoretically.

Introduction

The balance of different noncovalent interactions is crucial for chemical and biochemical processes as it controls molecular recognition and aggregation [1-6]. In order to gain a deeper understanding of these processes, knowledge on exact structural arrangements and the respective role of different intermolecular forces such as electrostatic, dispersion and induction forces is needed. Thus, experimental examination as well as the precise prediction of a preferred molecular docking site for different molecules is of crucial importance. Despite the remarkable progress made in experiments and theory/computational chemistry, there is still a need for improvement and benchmarking [7].

Many aromatic solute–solvent complexes have been studied in the gas phase (cf. [8-10] and references therein). Studied systems involving methanol as attached solvent molecule include the works on benzene–methanol clusters by the Zwier group [11] and on fluorobenzene–methanol clusters by the Brutschy group [12], to mention only two examples. Complexes of aromatic ethers with polar solvent molecules are of special interest due to the presence of different competing hydrogen bond acceptor sites. An extensive study on diphenoxyethane–water clusters was performed by the Zwier group [13-15] including studies in the excited S_1 and S_2 states. Concerning aggregates of aromatic ethers with alcohols, there is a work of Pietraperzia et al. [16] on the anisole–phenol complex in which an $\text{OH}\cdots\text{O}$ structure was identified. In a systematic study by the Suhm group on complexes of anisole derivatives with methanol, a balance between $\text{OH}\cdots\text{O}$ and $\text{OH}\cdots\pi$ structures being very sensitive to the substitution pattern at the anisole moiety was identified [17,18]. In previous multi-spectroscopic studies by the Schnell, Suhm and Gerhards groups on diphenyl ether (DPE)–solvent complexes [19-22], the influence of different attached solvent molecules on the structural preference was compared. It could be shown that the balance between $\text{OH}\cdots\pi$ - and $\text{OH}\cdots\text{O}$ -bound structures is very sensitive to the size of the attached alcohol. Torsional balances in solution have been used to probe aromatic $\text{OH}\cdots\pi$ interactions and to show that these interactions remain important at room temperature [23].

In such aromatic solute–solvent systems, one frequently encounters hydrogen bonds formed towards oxygen or nitrogen lone pairs, or $\text{R}-\text{H}\cdots\pi$ binding motifs ($\text{R} = \text{O}, \text{N}, \text{C}, \text{S}, \dots$) involving aromatic π systems. Less often, $\text{R}-\text{H}\cdots\pi$ bound complexes are found involving nonconjugated, localized $\text{C}=\text{C}$ double bonds. Exceptions include the ethene–methanol complex [24] as well as bulky olefin–*tert*-butyl alcohol complexes [25] investigated by jet FTIR spectroscopy. The observed OH stretching red-shifts compared to the free alcohols are small,

indicating a comparatively weak hydrogen bond, which is also reflected in calculated binding energies [24,25].

With the herein presented work, we now extend our overall multi-spectroscopic study to mixed aromatic olefinic ethers: in the case of phenyl vinyl ether (PVE), there is an ethenyl moiety replacing one of the phenyl rings compared to DPE. This introduces a localized π system along with the delocalized phenyl π system as hydrogen bond acceptor sites. Thereby, the complexity of the system is increased, as now three qualitatively different basic binding motifs have to be regarded instead of only two for DPE. This also provides an enhanced challenge for theory, with no clear preference for one of the motifs to be expected. As shown, e.g., in the case of DPE–*t*-BuOH [20], there is a need for benchmarking systems in order to improve and develop better theoretical approaches especially for non-covalently bound complexes. The study on PVE–MeOH is meant to present a further benchmark system, probably even more challenging than DPE–*t*-BuOH.

For an experimental elucidation of structural arrangements and energetic preferences, investigations on a molecular level are required on isolated molecular aggregates, allowing for an ideal comparison with gas phase calculations. This can be achieved by molecular beam experiments, which can be combined with a variety of spectroscopic techniques. For our multi-spectroscopic studies, we utilize FTIR spectroscopy, mass- and isomer-selective IR/UV techniques (IR/R2PI, for methodical developments, cf., e.g., [8,26-29] and UV/IR/UV spectroscopy, cf., e.g., [30-43]) and chirped-pulse Fourier transform microwave (CP-FTMW) spectroscopy. Comparing spectroscopic results with quantum-chemical calculations is often mandatory for the interpretation of experiments. Furthermore, such comparison enables a critical evaluation of the approximations used, comparing the relative stability of different binding motifs.

In this paper, the first structural investigation on the complex of phenyl vinyl ether with methanol is presented. An established multi-spectroscopic approach [19,20] is used, coupling FTIR, IR/UV and microwave spectroscopy with theoretical treatments including dispersion-corrected density functional theory (DFT-D3) [44,45], spin-component-scaled approximated coupled cluster-singles-doubles (SCS-CC2) [46] as well as explicitly correlated local coupled cluster theory (LCCSD(T0)-F12) [47] calculations, the latter allowing for a quantification and visualization of London dispersion interactions [48]. The aim of the presented study is the unambiguous experimental identification of the preferred binding site of a first methanol solvent molecule to the multivalent hydrogen bond scaffold of phenyl vinyl ether, followed by a classification of theoretical methods in

terms of success or failure to predict this preference. Visualization of possible reasons for the subtle preference is a valuable additional asset.

Experimental Setup

FTIR setup

For the FTIR experiments, the so-called filet-jet setup, as described in detail in [49], was used. In this setup, the scans of a Bruker IFS 66 v/s spectrometer (80 kHz, resolution 2 cm^{-1}) are synchronized to a pulsed supersonic expansion through a $600 \times 0.2\text{ mm}^2$ slit nozzle. Using two separate cooled saturators, low concentrations ($<0.1\%$) of PVE (Sigma-Aldrich, 97%, used as purchased) and methanol (Sigma-Aldrich, $\geq 99.8\%$, used as purchased) were added to the carrier gas helium (Linde, 99.996%) and premixed at a pressure of 0.75 bar in a 67 L reservoir before being expanded through the slit nozzle. The pulsed operation with waiting times of 30–90 s between 150 ms long pulses combined with a buffer volume of 12–23 m^3 and a pumping capacity of 500–2500 m^3/h resulted in background pressures of less than 0.1 mbar before expansions. This facilitated measurements of clusters of methanol and PVE in the zone of silence of the expansion at an average distance of 10 mm to the nozzle. A calcium fluoride beam splitter, lenses and windows were used in combination with a 150 W tungsten filament and an optical filter ($4200\text{--}2450\text{ cm}^{-1}$) to maximize the signal-to-noise ratio in the OH stretching range of the vibrational spectra. For the final spectra, 150 to 775 pulses were co-added to further improve signal-to-noise.

IR/UV setup

The experimental setup for the IR/UV experiments is described in detail elsewhere [29,50], thus only a brief description is given here. All experiments were carried out in a molecular beam apparatus consisting of a differentially pumped linear time-of-flight (TOF) mass spectrometer with a pulsed valve (Series 9 and pulse driver Iota One, General Valve, 500 μm orifice) for skimmed jet expansion. PVE was synthesized according to the procedure reported in [51] (cf. Supporting Information File 1 for details). MeOH (Sigma-Aldrich, $\geq 99.7\%$) and PVE were both supplied via separate cooled reservoirs (approx. $-8\text{ }^\circ\text{C}$ and $-13\text{ }^\circ\text{C}$, respectively) and co-expanded with the carrier gas neon (2.5–3.0 bar).

For the one- and two-color R2PI, the IR/R2PI and the UV/IR/UV experiments up to three tunable nanosecond laser systems were necessary, including two independent UV laser systems and one IR laser system. The UV laser radiation is obtained via second harmonic generation in a BBO crystal using the output of a dye laser (Cobra-Stretch and PrecisionScan, Sirah). They are pumped by the second harmonic (532 nm) of a Nd:YAG laser (SpitLight 600 and SpitLight 1000, Innolas). The IR laser

radiation in the range of $3520\text{--}3750\text{ cm}^{-1}$ is generated by difference frequency mixing (DFM) in a LiNbO_3 crystal using the fundamental (1064 nm) of a seeded Nd:YAG laser (Quanta-Ray Pro-230, Spectra-Physics) and the output of a further dye laser (PrecisionScan, Sirah), which is pumped by the second harmonic (532 nm) of the same Nd:YAG laser. Amplification of the resulting IR radiation is obtained by an optical parametric amplification (OPA) process in a further LiNbO_3 crystal using the output of the DFM process and the fundamental (1064 nm) of the Nd:YAG laser.

For the IR/R2PI spectra, the IR laser was fired 50 ns prior to the UV excitation laser, whereas for the UV/IR/UV spectra the IR laser was fired 2.0–3.0 ns after the UV excitation laser. The time delay between UV excitation and ionizing laser was 4.0–4.5 ns.

CP-FTMW setup

The rotational spectroscopy measurements were performed with the Hamburg chirped-pulse Fourier transform microwave (CP-FTMW) spectrometer COMPACT covering the 2–8 GHz frequency range, which has been described in detail in [52]. The molecules were seeded into a supersonic expansion with neon as the carrier gas by using a pulse nozzle (Parker General Valve, Series 9, 0.9 mm diameter orifice) equipped with a heatable reservoir close to the valve orifice, operating at 8 Hz. PVE was synthesized as described above and used without further purification.

The liquid sample was held in the reservoir at room temperature, which resulted in sufficient vapor pressure (standard boiling point of about $155\text{ }^\circ\text{C}$) for recording the rotational spectrum. MeOH was kept in a separate reservoir. PVE–MeOH clusters were generated by first flowing the carrier gas (neon) through the reservoir containing methanol that was external to the chamber, followed by picking up PVE vapor. After supersonic expansion into vacuum using neon at 3 bar, the molecular jet was polarized with a 4 μs chirp spanning 2–8 GHz. The chirp was generated with an arbitrary waveform generator, amplified to 300 W with a traveling wave tube amplifier, and transmitted into the vacuum chamber via a horn antenna. Following excitation, 40 μs of the free induction decay (FID) of the macroscopic ensemble of polarized molecules was recorded. The fast frame capability [53] of the Tektronix DPO 71254C was used in which eight consecutive excitation chirps, each followed by 40 μs during which the FID could be collected, were recorded and averaged. This resulted in an effective repetition rate of 64 Hz.

For the spectrum of the PVE–MeOH dimer, 3 million FIDs were co-added. A resulting signal-to-noise ratio of about 500:1

to 600:1 for the stronger transitions of the dominant complex allowed us to determine the positions of the carbon atoms with respect to the center of mass of the overall complex (see below) exploiting the presence of ^{13}C isotopologues in natural abundance and using the Kraitchman approach [54]. Fourier transformation of the averaged time domain FID, recorded at point spacings of 10 ps, resulted in a frequency domain rotational spectrum with frequency resolution of 25 kHz.

The assignment was performed with the program JB95 [55], then the fits to an asymmetric-rotor Hamiltonian were performed using SPFIT/SPCAT. The experimental results were complemented by and compared with the results of electronic structure calculations. B3LYP-D3/aug-cc-pVTZ calculations were performed using the Gaussian 09, rev. D.01 program suite [56] to guide the assignment.

Computational Methods

Various input structures for the PVE–MeOH complex were generated by using the MMFF94s force field [57] as implemented in Avogadro [58]. Afterwards, geometry optimizations were performed by applying the Berny optimization algorithm of Gaussian 09 [56] with energies and gradients obtained from Turbomole 7.0 [59]. The DFT functional B3LYP with Grimme's two-body D3 corrections and Becke–Johnson damping [45] was used in combination with the def2-TZVP basis set based on the documented performance of this level of theory for the similar diphenyl ether–methanol system [19]. Furthermore, the obtained structures were re-optimized with the SCS-CC2 method using the def2-TZVP basis set, both in the electronic ground (S_0) and first excited state (S_1). The *ricc2* module in Turbomole 7.0 requires an auxiliary Coulomb fitting basis set (cbas) for the resolution-of-identity approximation (RI) for which def2-TZVP-cbas was chosen [60]. All obtained geometries were confirmed as minima by harmonic frequency calculations.

In order to evaluate the relative stability of the different conformers found on the potential hypersurface, density fitted explicitly correlated local coupled cluster with singles and doubles excitations and perturbative triples (DF-LCCSD(T0)-F12) calculations were carried out [47]. In order to converge the energies relative to the one particle basis, the VTZ-F12 and VQZ-F12 basis sets [61,62] were used together with a Schwenke style basis set extrapolation, as proposed in [63]. The orbitals were Pipek–Mezey [64] localized and orbital domains determined by natural population analysis with a threshold of $\text{TNPA} = 0.03$ [65]. Defaults were used for the pair classification, with all pairs included in the F12 treatment. Furthermore, the intermolecular pairs were classified as strong (meaning that they were treated at the highest level of theory). The latter

method will be denoted as LCCSD(T0)-F12/CBS[T:Q]. In all correlated calculations the 1s electrons were removed from the treatment (frozen-core approximation). Furthermore, we analyzed the relative impact of dispersion interactions in the different complexes through a local orbital analysis of the CCSD (connected) doubles energy terms. The latter discussion is complemented with dispersion interaction density (DID) plots [48]. The coupled cluster calculations were carried out with Molpro 2015.1 [66].

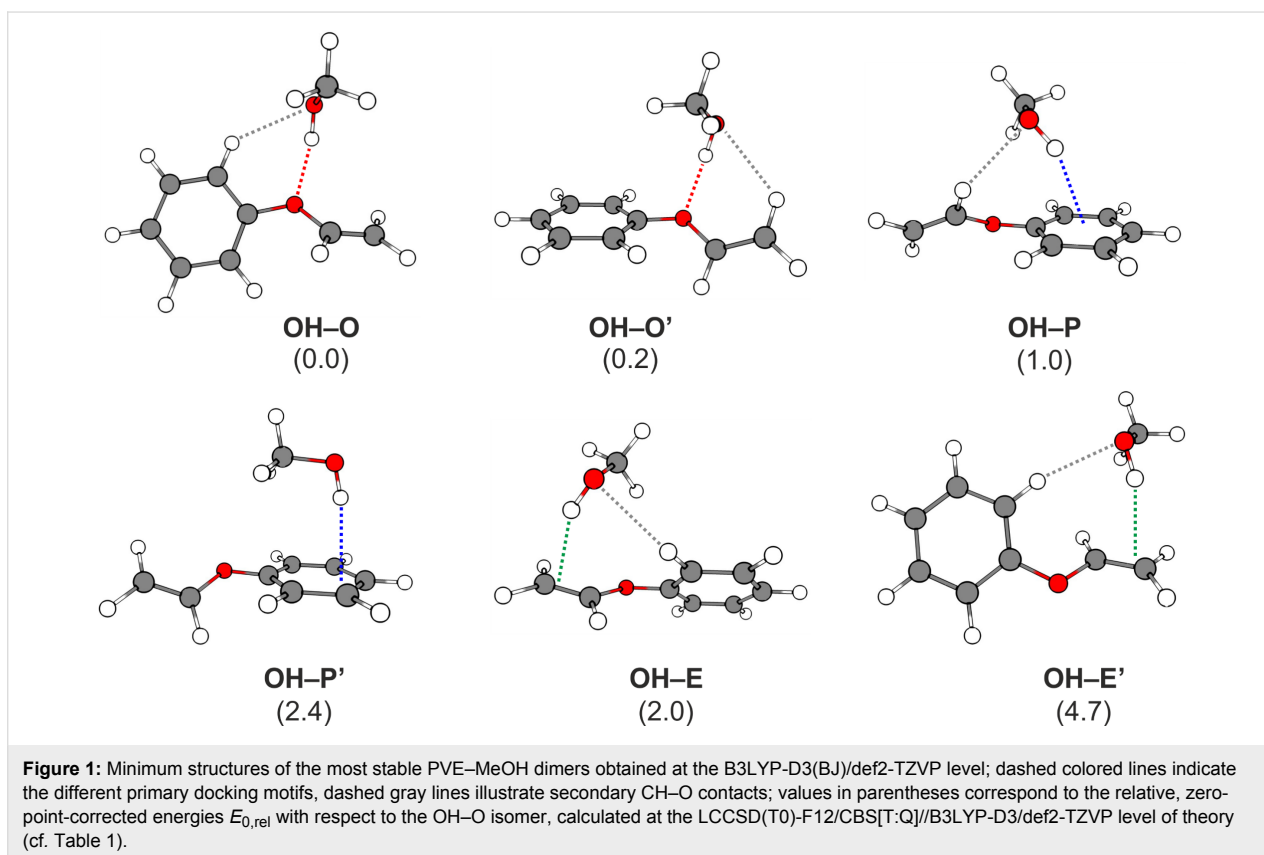
Results and Discussion

Theoretical results

In contrast to the already studied diphenyl ether–alcohol clusters [19,20,22], phenyl vinyl ether offers three different binding sites for possible interactions with small solvent molecules: the ether oxygen, the phenyl ring and the vinyl moiety. Since both the phenyl ring and the vinyl moiety interact with the solvent via a π cloud, preferred binding sites are indicated using the following nomenclature: P (phenyl) and E (ethenyl), respectively. The optimizations using B3LYP-D3(BJ)/def2-TZVP yield six different structures, representing each binding motif with two isomers (cf. Figure 1).

In order to verify the structures of the complexes, a second level of theory was applied, namely SCS-CC2/def2-TZVP. Similar minima were found in the latter calculations, confirming the rich variety of binding motifs. However, distinct differences were found between the two methods: While B3LYP-D3 predicted the OH–E conformer as the most stable complex SCS-CC2 gave OH–P as the lowest minimum (cf. Table S1 in Supporting Information File 1). This is in contrast to our results of diphenyl ether–alcohol clusters [19,20,22], where both computational levels predicted the same energetic order of the isomers. The two structures correspond to quite different docking positions, reflecting well the demanding test this system imposes on quantum chemical methods. Several minima are separated by energy differences of 1 kJ/mol or less. The complete energetic analysis at both levels of theory is presented in Supporting Information File 1 (cf. Tables S1 and S2). The reasons behind the discrepancies are manifold, ranging from the method to the small basis set used. In order to obtain a more reliable theoretical prediction, LCCSD(T0)-F12/CBS[T:Q] calculations were carried out on top of the DFT-optimized geometries. The results are presented in Table 1, with and without zero-point vibrational energy (ZPVE) corrections.

The coupled cluster results show a clear energetic preference for the OH–O and OH–O' isomers. Observing the intermolecular contacts, which may or may not be designated as weak hydrogen bonds but are expected to stabilize the complexes, the main difference between the two structures is a phenyl vs



ethenyl CH to methanol O contact (cf. dashed gray lines in Figure 1). Both are separated by only a few tenths of a kJ/mol, which is within the error of the method used (considering that the coupled cluster expansion is truncated at triples excitations and the neglect of core-valence correlation effects, which should be the largest sources of error along with the harmonic B3LYP ZPVE error). It also confirmed the subtle difference between the six conformers, with an energy span of approximately 4–5 kJ/mol (≈ 1 kcal/mol, the commonly accepted definition of chemical accuracy) among all structures.

Also featured in Table 1 are the computed O–H stretch fundamentals together with the IR intensity at the two different levels of theory used in the optimizations. The frequencies were scaled according to the experimental value of the OH– π isomer of DPE–MeOH [19]. Based on the computational results, the vibrational spectral signals of the OH–O and OH–O' isomers will be extremely hard to distinguish, as they lie less than 3 cm^{-1} apart, with very similar intensities. The same can be asserted for the less stable OH–E and OH–E' structures. This is not surprising, given the similarities of the OH binding pattern for both sets of structures.

Table 1: Comparison of different structures for PVE–MeOH dimers in the S_0 state with LCCSD(T0)-F12/CBS[T:Q]/B3LYP-D3/def2-TZVP electronic energies E_{rel} and B3LYP zero-point corrected energies $E_{0,\text{rel}}$ relative to the minimum OH–O structure. The scaled wavenumbers $\tilde{\nu}$ of the OH-stretching vibration together with the respective IR intensity I are presented for two levels of theory: B3LYP-D3 (scaling factor: 0.9600) and SCS-CC2/def2-TZVP (scaling factor: 0.9635).

	E_{rel} [kJ/mol]	$E_{0,\text{rel}}$ [kJ/mol]	B3LYP-D3		SCS-CC2	
			$\tilde{\nu}$ [cm^{-1}]	I [km/mol]	$\tilde{\nu}$ [cm^{-1}]	I [km/mol]
OH–O	0.0	0.0	3597	219	3619	160
OH–O'	–0.3	0.2	3600	193	3621	144
OH–P	1.4	1.0	3619	112	3631	67
OH–P'	3.9	2.4	3631	127	3636	110
OH–E	1.5	2.0	3567	187	3607	121
OH–E'	4.8	4.7	3567	197	3606	128

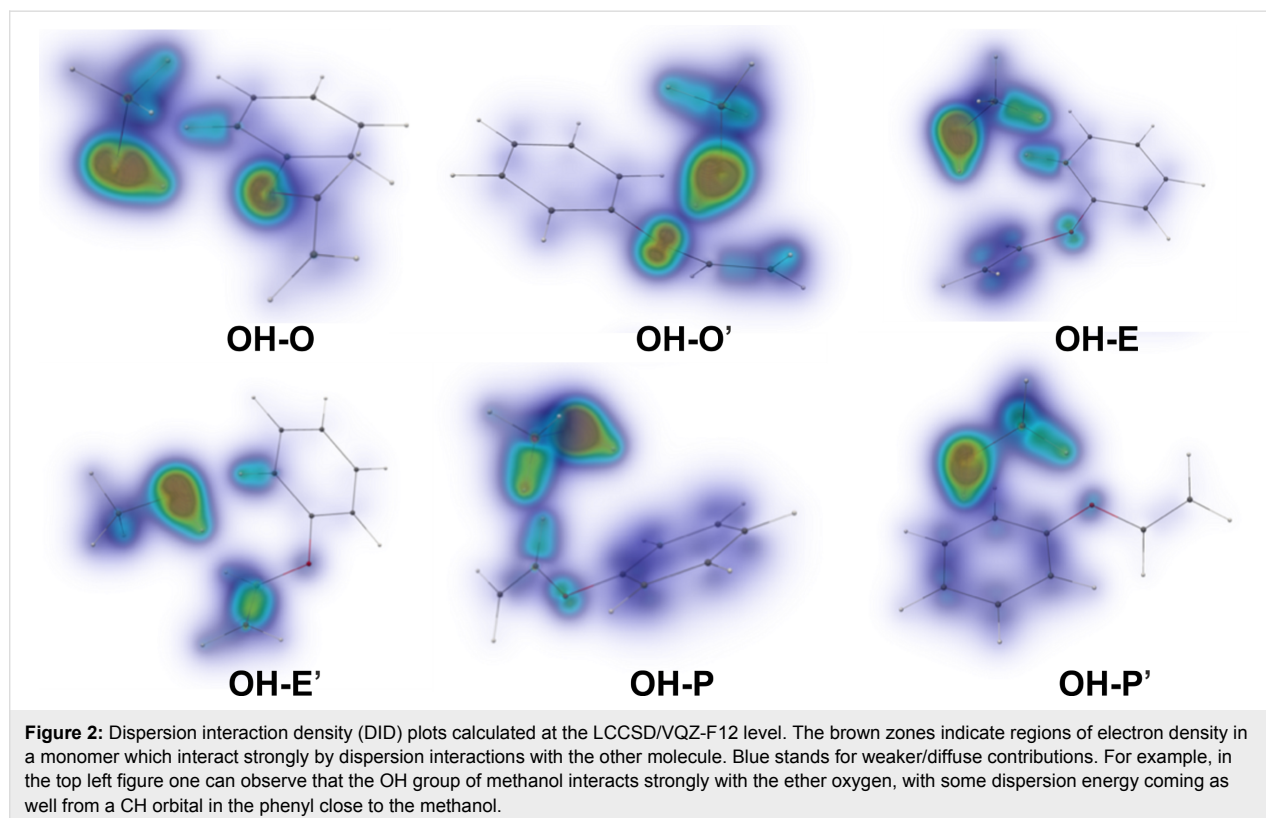
In order to gain further insight into the energetic order of the different isomers, we conducted an analysis of the dispersion interactions present in the system by decomposing the CCSD energy terms obtained with the largest basis set (VQZ-F12). The latter procedure is based on the classification of the intermolecular excitation classes as detailed in [48,67]. The results are shown in Table 2. Beyond the total dispersion contributions, we also made use of the local analysis to separate the contribution of different molecular moieties in the PVE molecule (phenyl, ether oxygen and ethenyl). Shared orbitals are split up according to their NPA (natural population analysis) charges as described in [68].

The dispersion interaction energies show an interesting pattern. Although all structures are significantly stabilized by disper-

sion, with a maximum energy difference of 2.6 kJ/mol when summed all together, the relative weight of the different molecular fragments varies quite significantly. The moiety with the largest potential as dispersion energy donor (DED) is the phenyl ring. This results in the strongest stabilization for the two conformers whereby the methanol is closest to the ring (OH-P and OH-P'). The other conformers have much more spread out contributions. What is surprising is that even for the ethenyl binding complexes the contribution of the phenyl ring is sizeable. Geometrically, this seems unlikely, given that the methanol moiety is not oriented favorably relative to the ring. The effect can, however, be understood by inspecting the respective dispersion interaction densities (DIDs, cf. Figure 2), which allow for an even finer-grained analysis. There, one can observe that the major contributor is not the π -system of the phenyl ring,

Table 2: Comparison of different structures for PVE–MeOH dimers, with dispersion energies calculated at the LCCSD/VQZ-F12 level of theory (the parentheses contain the percentage of the fragment's dispersion relative to the total dispersion energy).

	$\Delta E_{\text{disp}}(\text{total})$ [kJ/mol]	$\Delta E_{\text{disp}}(\text{phenyl})$ [kJ/mol]	$\Delta E_{\text{disp}}(\text{O})$ [kJ/mol]	$\Delta E_{\text{disp}}(\text{ethenyl})$ [kJ/mol]
OH-O	-14.3	-6.2 (43.2)	-5.1 (35.8)	-3.0 (21.1)
OH-O'	-15.7	-6.1 (38.7)	-4.9 (31.5)	-4.7 (29.8)
OH-P	-16.9	-11.9 (70.4)	-1.5 (9.2)	-3.5 (20.5)
OH-P'	-16.0	-14.0 (87.6)	-1.3 (8.0)	-0.7 (4.4)
OH-E	-15.6	-6.9 (44.3)	-2.1 (13.3)	-6.6 (42.4)
OH-E'	-13.1	-4.5 (34.0)	-0.9 (6.7)	-7.8 (59.3)



but a C–H contact to the methanol (a similar effect had already been observed in diphenyl ether–methanol complexes [19]). This contact is reminiscent of stabilization effects observed in coupled diamondoids [69] or supramolecular complexes [70], where such interactions can be found in large numbers.

Electronic ground state spectra

FTIR spectroscopy

The results of an FTIR exploration of the conformational diversity of this system are shown in Figure 3. Besides methanol monomer, methanol dimer and a signal clearly attributed to a larger cluster, only a single, reasonably narrow absorption at 3625 cm^{-1} is observed. It can be attributed to mixed dimers of MeOH with PVE and allows for a single rigorous conclusion, due to the linearity of the technique and the comparable IR absorption cross section of all predicted dimer conformations (cf. Table 1 and Table S1, Supporting Information File 1): the global minimum structure and any other, higher lying isomers which are initially formed and impeded from relaxation to the global minimum due to broad or high interconversion barriers must have their OH stretching fundamental at $3625 \pm 5\text{ cm}^{-1}$ or be significantly less abundant.

If one were to trust the relative harmonic wavenumber predictions from the preceding subsection (cf. Table 1), this would imply a single docking motif, as different docking motifs are predicted to lead to larger spectral separations. However, different extents of anharmonicity do not allow to completely ruling out overlapping docking motifs. Therefore, conformationally selective methods are desirable to investigate this possibility. Finally, the actual docking site has to be identified by structural or electronic excitation spectroscopy.

IR/R2PI spectroscopy

Additional insight can be gained by using the mass- and isomer-selective IR/R2PI technique. This method requires knowledge on electronic excitation energies of the PVE–MeOH complex. For this reason, one-color R2PI spectra were recorded in the range of $36100\text{--}37600\text{ cm}^{-1}$ (cf. Figure S1 in Supporting Information File 1). While the R2PI spectrum of the PVE monomer shows well-resolved vibrational progressions (cf. Figure S1a, Supporting Information File 1), the spectrum of the solvent aggregate is broadened and affected by ionization-induced fragmentation of larger clusters (cf. Figure S1b, Supporting Information File 1). This is also reflected in the recorded IR/R2PI

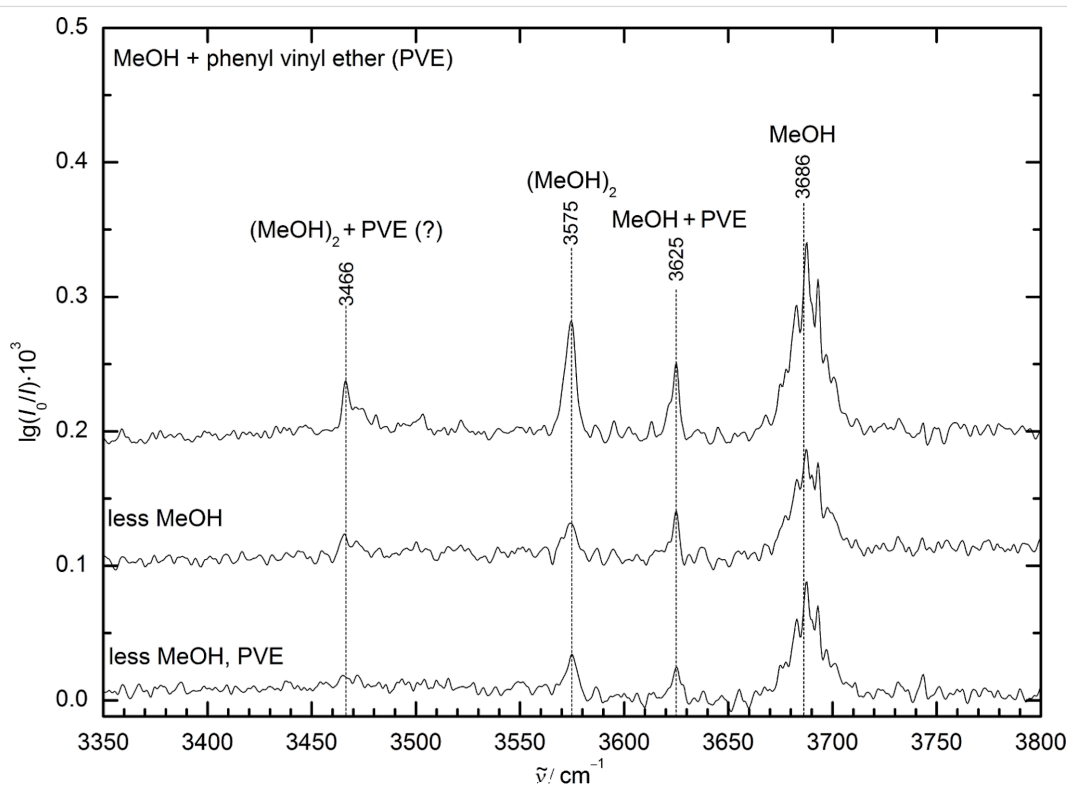


Figure 3: FTIR spectra of the supersonic expansion of methanol (MeOH) and phenyl vinyl ether (PVE) at different concentrations in helium. The spectra are spread out along the ordinate to improve visualization. Only one dominant mixed dimer band is visible in the spectra, lying at 3625 cm^{-1} (marked MeOH + PVE) between the methanol monomer at 3686 cm^{-1} (MeOH) and methanol dimer at 3575 cm^{-1} ((MeOH)₂). By comparing the spectrum at the top with the other two spectra recorded at reduced concentrations of methanol (middle) or methanol and PVE (bottom), the further downshifted band at 3466 cm^{-1} can be attributed to a higher cluster, probably a methanol-rich mixed trimer ((MeOH)₂ + PVE (?)), due to its scaling with the variation of the concentrations.

spectra (cf. Figure S2, Supporting Information File 1), yielding solely the spectrum shown in Figure 4 via the excitation energy of 36885 cm^{-1} containing an OH stretching vibration of a PVE–MeOH dimer.

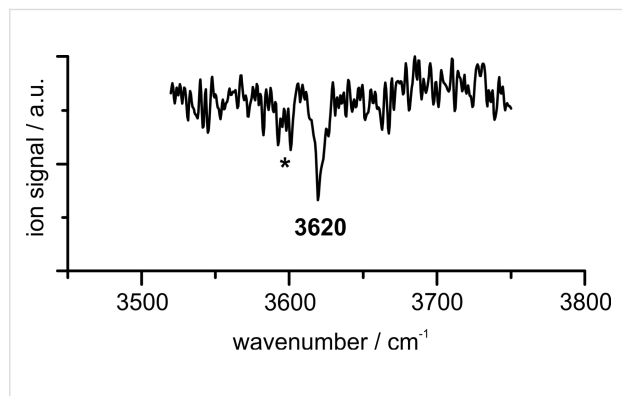


Figure 4: The IR/R2PI spectrum in the range of $3520\text{--}3750\text{ cm}^{-1}$ was obtained via the excitation energy of 36885 cm^{-1} using the carrier gas neon; the asterisk (*) indicates ionization-induced fragmentation from larger clusters (cf. Figure S2 in Supporting Information File 1).

Comparing the calculated OH stretching frequencies for the different isomers obtained at the DFT-D3 and SCS-CC2 levels (cf. Table 1) to the experiment does not allow for a clear structural assignment: the DFT-D3 calculations show the best agreement for the OH–P structure (3619 cm^{-1} , scaling factor 0.9600). Regarding the relative electronic energies, the OH–O structure is somewhat favored, with OH–O' coming as a close second. The latter frequencies are 3597 and 3600 cm^{-1} , respectively, at the same level of theory. On the other hand, the computed SCS-CC2 frequencies would provide a coincident assignment, as both O-docking isomers would have the closest fundamentals compared to the measured frequency (3619 and 3621 cm^{-1}). The assignment, however, would be tentative at best with this information alone. The OH–E isomers on the other hand can be excluded due to their lower OH stretching frequencies as well as the energetic disadvantage at the LCCSD(T0)-F12/CBS[T:Q] level (cf. Table 1).

In order to elucidate this problem, the electronic excitation energies can serve as a further indication for the binding motif, as shown for DPE–alcohol clusters before [20–22]. Comparing the vertical excitation energies for the different isomers with the experimental excitation energy of 36885 cm^{-1} yields the best agreement for the OH–O or OH–O' isomer, which also show a significantly blue-shifted $S_1\leftarrow S_0$ transition compared to the PVE monomer (adiabatic excitation energies of 38291 and 38164 cm^{-1} , respectively, compared to 38034 cm^{-1} for the PVE monomer, cf. Table S2, Supporting Information File 1), as observed experimentally. In contrast to that, a red-shifted $S_1\leftarrow S_0$ transition compared to PVE is predicted for the OH–P isomer

(37907 cm^{-1}), which would coincide with the fragmentation-dominated region of the R2PI spectrum, where, however, only signatures of larger clusters could be identified. These considerations strengthen the arguments for the presence of an OH...O structure laid before, on the basis of the computed coupled cluster energies and the SCS-CC2 fundamental stretch frequencies. Additional experimental insight will be gained from the UV/IR/UV spectrum of the S_1 state as well as the microwave investigations in the following section.

Chirp pulse Fourier transform microwave (CP-FTMW) spectroscopy

From the broadband CP-FTMW spectra obtained with neon as a carrier gas, we assigned two PVE–MeOH complexes with significantly different intensities. Complex 1 is about ten times more intense than complex 2. The experimental rotational constants (Table 3) for the two isomers agree the best with the values calculated for the OH–O' isomer (as also indicated in the FTIR and the IR–UV investigations, which are, however, unable to distinguish OH–O from OH–O') and the OH–P isomer, respectively. The identification of the two complexes to the OH–O' and the OH–P isomers is guided by the absolute and relative values of the B and C rotational constants. Generally, the rotational constants calculated at the SCS-CC2/def2-TZVP level of theory agree somewhat better with the experimental values than the B3LYP-D3(BJ)/def2-TZVP values (note that we compare experimental B_0 rotational constants with theoretical B_e rotational constants here). For the OH–P complex, however, we find that the B3LYP-D3(BJ)/def2-TZVP level of theory provides a better prediction of the magnitudes of the dipole-moment components. Experimentally, we only observe a-type transitions for this complex, which points to rather low values for μ_b and μ_c . SCS-CC2 calculations predict all three dipole-moment components to be of comparable magnitude. At the B3LYP-D3(BJ) level, μ_a is predicted to be significantly stronger than μ_b and μ_c . This change in magnitude for the dipole-moment components for different levels of calculation is more often observed for weakly bound complexes because the exact arrangement of the two monomers with respect to each other can have a major influence on the dipole-moment components. Also note that in none of the spectroscopic experiments, we observe the OH–E isomer that is also predicted to be of relatively low energy (cf. Table 1).

The rotational spectra of the two isomers are qualitatively different. For the OH–O' isomer (complex 1), we observe a characteristic line splitting into so-called A and E components (cf. Figure 5) arising from internal rotation of the methyl group of methanol, similar to the case of the DPE–MeOH complex. For the OH–P isomer (complex 2), no line splitting due to internal rotation was observed. This is consistent with the higher barrier

Table 3: Experimental rotational constants of the two observed complexes, using neon as carrier gas, that are assigned to the OH–O' and the OH–P isomers, respectively. The experimental rotational parameters for the OH–O' isomer (called Exp 1) are the results of a fit to a rigid-rotor asymmetric Hamiltonian including solely the A lines of the internal rotation splitting. Rotational parameters of a global fit (XIAM) including both A and E levels due to internal rotation for the OH–O' isomer are presented in the Table S9 of Supporting Information File 1.

	Complex 1 (OH–O' isomer)		Complex 2 (OH–P isomer)	
	Exp 1	SCS-CC2/def2-TZVP	Exp 1	SCS-CC2/def2-TZVP
A [MHz]	1466.59120(26)	1501.94	1275.7623(49)	1297.89
B [MHz]	697.48965(11)	697.58	818.45271(73)	818.01
C [MHz]	572.109900(95)	589.94	640.2184(11)	646.81
Δ_J [kHz]	0.72697(62)		0.070(14)	
Δ_{JK} [kHz]	–0.6669(26)		2.19(10)	
Δ_K [kHz]	5.6217(62)		–	
δ_J [kHz]	0.15121(11)		–	
δ_K [kHz]	2.5783(29)		–	
A state transition	213 (49/104/60)		20(20/0/0)	
Dipole moment (D) ($\mu_a/\mu_b/\mu_c$)		2.2/1.9/1.2		0.8/0.4/0.8
σ [kHz]	6.7		7.9	

for this motion due to the secondary interactions of the methyl group with PVE (cf. Figure 2).

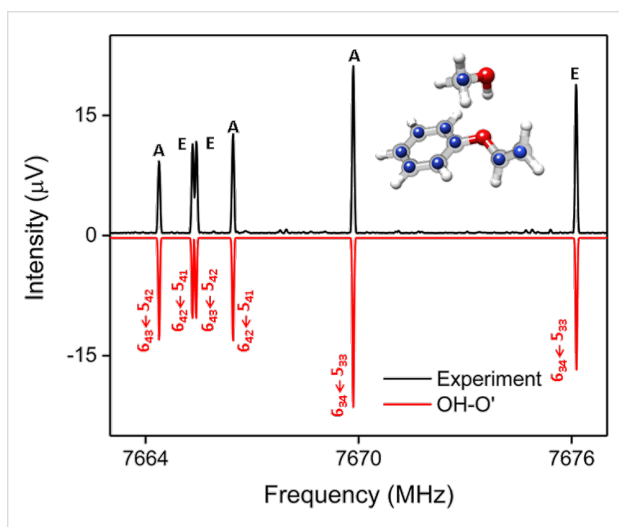


Figure 5: A section of the experimental 2–8 GHz spectrum using a mixture of PVE and MeOH (3 million acquisitions). The upper experimental trace in black is compared with simulations, based on fitted parameters that can be assigned to the OH–O' isomer (complex 1, red) for the PVE–MeOH complex. The observed complex has a clear splitting pattern due to the internal rotation of the methyl group of methanol, labeled with A and E. The experimental ^{13}C positions (blue atoms) (r_s substitution structure) deduced from a Kraitchman analysis are compared to the calculated structure at the SCS-CC2/def2-TZVP level of theory and further confirm the observation of the OH–O' isomer.

Two different ways of analyzing the rotational spectrum of the OH–O' isomer (complex 1) were performed. In Table 3, the results from a fit to an asymmetric-top Hamiltonian of only the A state species of the internal rotation splitting pair, which is

often a good approximation, is summarized (Exp 1). In addition, we used the program XIAM to perform a global fit including both A and E lines. This global fit does not only provide the rotational constants, but also parameters of the internal rotor, in this case the methyl group. This includes the barrier height for internal rotation as well as the geometrical arrangement of the rotor with respect to the overall rotating molecule, as also discussed for the DPE–MeOH complex [19]. For PVE–MeOH, the barrier height was determined to be 261 cm^{-1} , as summarized in Table S9 of Supporting Information File 1. This value is in agreement to barrier heights observed for other complexes with methanol [19]. It is somewhat lower than in the case of free methanol (373 cm^{-1}) and also lower than the calculated barrier height of 341 cm^{-1} (cf. Table S9, Supporting Information File 1). This somewhat lower methyl group internal rotation barrier for the OH–O' isomer could point to a softening of the C–O bond of methanol due to the hydrogen bond. The DID plots in Figure 2 also indicate that the methyl group is basically free from other interactions, so that no additional hindering is expected.

Furthermore, the transition intensities for the OH–O' isomer are strong enough (with a signal-to-noise (SNR) of about 500:1 to 600:1 for the stronger transitions) to assign rotational transitions arising from all nine singly substituted ^{13}C isotopologues in natural abundance (about 1%, cf. Figure S3, Supporting Information File 1). The additional data sets of rotational constants are summarized in Supporting Information File 1 (Table S12) together with line lists of the main isotopologues (Tables S10–S11) and the ^{13}C isotopologues (Tables S13–S21). They allow us, using Kraitchman's equations, to determine the

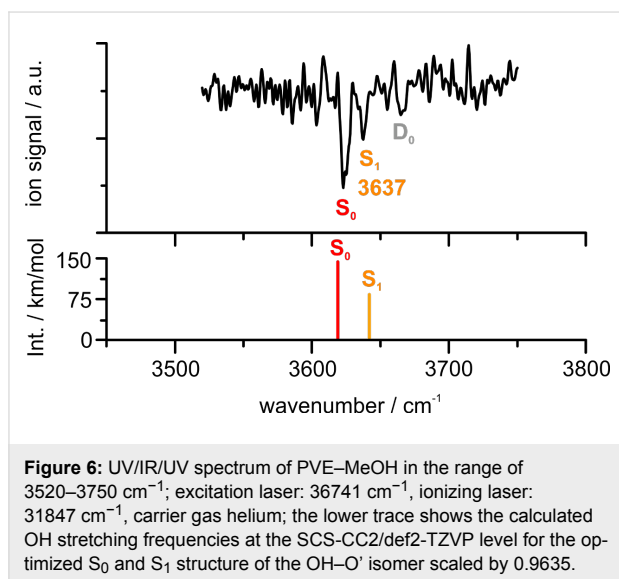
carbon substitution structure, r_s , of the complexes, which are the positions of the respective substituted carbon atoms with respect to the center of mass of the complex and thus the carbon backbone structure. The obtained r_s structure for complex 1 (cf. Figure 5) further confirms the assignment of complex 1 as the OH–O' isomer, where the methyl group of the methanol moiety points towards the phenyl ring.

As mentioned, the OH–O' isomer is about ten times more intense than the OH–P isomer. The intensity observed in CP-FTMW spectroscopy directly depends on the number of molecules, i.e., the population of the respective isomers, as well as the square of the transition dipole moments. Since the μ_a values for the two isomers differ by a factor of two (cf. Table S11 in Supporting Information File 1), the OH–P isomer can be considered to be about 2.5 times less populated than the OH–O' isomer, as an upper estimate. Taking the predicted energy difference of 0.8 kJ/mol for granted, this ratio would correspond to a plausible [18] conformational freezing temperature of 100 K. A three-fold lower or three-fold higher conformational temperature appears unlikely, and thus a tentative experimental energy penalty for OH–P relative to OH–O' ranges from 0.3 to 2 kJ/mol. This contradicts both inexpensive approaches (B3LYP-D3 and SCS-CC2 with def2-TZVP) and suggests that these methods somewhat underestimate the stability of OH \cdots O contacts.

Electronically excited state spectrum

For the investigation of the electronically excited state by using the UV/IR/UV technique, a two-color R2PI signal is required. For this reason, the one-color R2PI signal was suppressed by attenuating the laser power of the excitation laser. On the other hand, higher pulse energies were used for the ionizing laser. The latter was set to 31847 cm^{-1} for the UV/IR/UV experiment in order to yield the best two-color R2PI signal. Figure 6 shows the recorded UV/IR/UV spectrum for the PVE–MeOH mass trace.

Due to temporally overlapping laser pulses, the spectrum contains transitions from the S_0 state, the electronically excited (S_1 , at 3637 cm^{-1}) and also the ionic D_0 state (at 3667 cm^{-1}). This could not be avoided, as the lifetime of the excited state, which is estimated to be in the order of 5–7 ns, is shorter than the laser pulse-widths of 7–10 ns. The OH stretching vibration at 3637 cm^{-1} originating from the electronically excited state of the PVE–MeOH complex is blue-shifted compared to the ground state, which indicates a decrease of the hydrogen bond strength in the S_1 compared to the S_0 state. A comparison with SCS-CC2 calculations shows a good agreement of a blue-shifted OH stretching frequency at 3642 cm^{-1} (cf. Table S2, Supporting Information File 1, scaled by 0.9635) compared to



the ground state at 3619 cm^{-1} (cf. Table 1) for the OH–O' isomer, which is also reflected in an increase of the H \cdots O hydrogen bond distance from 2.068 to 2.168 Å from S_0 to S_1 state geometry. This destabilization of the OH \cdots O hydrogen bond is further reflected in the calculated binding energies of the PVE–MeOH complex obtained at the SCS-CC2/def2-TZVP level, which are reduced by 0.9 kJ/mol regarding D_0 and 1.6 kJ/mol regarding D_e in the S_1 state compared to the S_0 state for OH–O' (cf. Table S3, Supporting Information File 1). The spectral shift can be explained by regarding the HOMO and LUMO orbitals involved in the $S_1 \leftarrow S_0$ transition, which is predicted to be mainly a $\pi \rightarrow \pi^*$ transition with a small charge transfer contribution from the ether oxygen to the phenyl ring. The latter leads to a slightly decreased electron density at the binding site for the methanol molecule and therefore weakens the hydrogen bond. These findings are in line with observations in previous studies on diphenyl ether–alcohol complexes [20,21].

In principle, as the OH–O' isomer has been identified in the S_0 state, the observation of a respective OH \cdots O-bound structure can be expected in the S_1 state as well. However, the OH–P isomers are predicted to be significantly stabilized in the S_1 state (cf. Table S2, Supporting Information File 1). Nevertheless, due to the predicted red-shifts of the OH stretching frequencies of the OH–P isomers (indicating an increased hydrogen bond strength compared to the S_0 state), their presence, i.e., by a rearrangement reaction from the OH–O' isomer, can be excluded. By exciting the electronic origin of the OH–O' isomer the formation of OH–E isomers can also be excluded as their expected excitation energies are higher than the one for OH–O' and in addition they are energetically less stable (cf. Table S2, Supporting Information File 1).

Conclusion

In this paper, the first spectroscopic and theoretical investigation on the isolated phenyl vinyl ether–methanol complex is presented. From the FTIR spectra, the existence of one isomer is concluded, which is confirmed by IR/UV spectroscopy in the electronic ground state (S_0). The combined vibrational and electronic spectroscopic investigations, including a comparison of vibrational frequencies and electronic excitation energies, allow for an assignment of an OH \cdots O-bound structure. Broadband rotational (CP-FTMW) spectroscopy ultimately identifies OH–O' as the observed isomer, ruling out the presence of the nearly isoenergetic OH–O. One explanation for its elusiveness would be a low interconversion barrier. However, rotational spectroscopy further reveals the presence of the OH–P isomer as a second isomer, being less populated, which is not observed with the less sensitive FTIR technique and might be superimposed by fragmentation of larger clusters in the usually more sensitive IR/UV experiments or it is even not populated due to different expansion conditions. No evidence was found for an OH \cdots ethenyl-bound structure, which is in agreement with the more pronounced energetic discrimination of OH–E isomers compared to the other binding motifs predicted at the LCCSD(T0)-F12/CBS[T:Q] level of theory.

In the electronically excited state (S_1), the OH stretching vibration of the attached methanol undergoes a blue-shift compared to the S_0 state. This indicates a weakening of the OH \cdots O bond upon electronic excitation compared to the ground state and is in good agreement with the calculated frequency shift for the S_0 and S_1 state structures obtained at the SCS-CC2/def2-TZVP level and is furthermore in line with findings for similar diphenyl ether–alcohol complexes from previous investigations [20,21].

In summary, we present a multi-spectroscopic analysis on a molecular complex with a very delicate balance between, for the first time, three different binding motifs. This provides an excellent benchmark system for theory, since DFT-D3 as well as SCS-CC2 methods fail in predicting the correct energetic order, whereas LCCSD(T0)-F12 succeeds in the preferred docking motif. These differences are in the range of only 2 kJ/mol, when considering relative electronic energies, but that is already enough to tip the scales in the wrong direction. Comparing VTZ-F12 and VQZ-F12 results, we observe that the electronic energies are well converged for the smaller basis (Table S6, Supporting Information File 1). This would place the main accuracy bottleneck in the electronic structure method (i.e., functional, correlation truncation) chosen.

Finally, regarding the docking preference in comparison to the previously investigated diphenyl ether complex with methanol,

a conclusion might be that methanol needs the interaction with a second phenyl ring in order to prefer the OH \cdots π motif over OH \cdots O, as observed for diphenyl ether. The secondary interaction of methanol with a smaller ethenyl moiety being present in phenyl vinyl ether instead of a phenyl ring seems to be insufficient to favor the phenyl docking site.

Supporting Information

Supporting Information File 1

Additional computational and experimental data.
[<https://www.beilstein-journals.org/bjoc/content/supplementary/1860-5397-14-140-S1.pdf>]

Acknowledgements

The authors thank the Deutsche Forschungsgemeinschaft (DFG, Ge 961/9-1, Schn 1280/4-1, Su 121/5-1, and Ma 5063/3-1) for financial support in context of the priority program SPP 1807 on the Control of London dispersion interactions in molecular chemistry. M.F. acknowledges support from the Hamburg International Max Planck Research School UFAST. This work is part of the Ph.D. theses of D.B., M.F., H.G. and A.W.

ORCID® IDs

Dominic Bernhard - <https://orcid.org/0000-0002-6148-0445>
 Fabian Dietrich - <https://orcid.org/0000-0001-5813-5248>
 Cristóbal Pérez - <https://orcid.org/0000-0001-5248-5212>
 Hannes C. Gottschalk - <https://orcid.org/0000-0003-4343-9542>
 Ricardo A. Mata - <https://orcid.org/0000-0002-2720-3364>
 Martin A. Suhm - <https://orcid.org/0000-0001-8841-7705>
 Melanie Schnell - <https://orcid.org/0000-0001-7801-7134>
 Markus Gerhards - <https://orcid.org/0000-0002-8748-2940>

References

- van der Waals, J. D. Ph.D. Thesis, Leiden, 1873.
- London, F. Z. *Phys.* **1930**, *63*, 245–279. doi:10.1007/BF01421741
- Müller-Dethlefs, K.; Hobza, P. *Chem. Rev.* **2000**, *100*, 143–168. doi:10.1021/cr9900331
- Lehn, J.-M. *Angew. Chem., Int. Ed. Engl.* **1988**, *27*, 89–112. doi:10.1002/anie.198800891
- Černý, J.; Hobza, P. *Phys. Chem. Chem. Phys.* **2007**, *9*, 5291–5303. doi:10.1039/b704781a
- Meyer, E. A.; Castellano, R. K.; Diederich, F. *Angew. Chem., Int. Ed.* **2003**, *42*, 1210–1250. doi:10.1002/anie.200390319
- Mata, R. A.; Suhm, M. A. *Angew. Chem., Int. Ed.* **2017**, *56*, 11011–11018. doi:10.1002/anie.201611308
- Zwier, T. S. *Annu. Rev. Phys. Chem.* **1996**, *47*, 205–241. doi:10.1146/annurev.physchem.47.1.205
- Ebata, T.; Fujii, A.; Mikami, N. *Int. Rev. Phys. Chem.* **1998**, *17*, 331–361. doi:10.1080/014423598230081
- Brutschy, B. *Chem. Rev.* **2000**, *100*, 3891–3920. doi:10.1021/cr990055n
- Pribble, R. N.; Hagemeister, F. C.; Zwier, T. S. *J. Chem. Phys.* **1997**, *106*, 2145. doi:10.1063/1.473784

12. Djafari, S.; Barth, H.-D.; Buchhold, K.; Brutschy, B. *J. Chem. Phys.* **1997**, *107*, 10573–10581. doi:10.1063/1.474221
13. Buchanan, E. G.; Gord, J. R.; Zwier, T. S. *J. Phys. Chem. Lett.* **2013**, *4*, 1644–1648. doi:10.1021/jz400641p
14. Walsh, P. S.; Buchanan, E. G.; Gord, J. R.; Zwier, T. S. *J. Chem. Phys.* **2015**, *142*, 154304. doi:10.1063/1.4917307
15. Walsh, P. S.; Buchanan, E. G.; Gord, J. R.; Zwier, T. S. *J. Chem. Phys.* **2015**, *142*, 154303. doi:10.1063/1.4917305
16. Pietraperzia, G.; Pasquini, M.; Mazzoni, F.; Piani, G.; Becucci, M.; Biczysko, M.; Michalski, D.; Bloino, J.; Barone, V. *J. Phys. Chem. A* **2011**, *115*, 9603–9611. doi:10.1021/jp200444a
17. Gottschalk, H. C.; Altnöder, J.; Heger, M.; Suhm, M. A. *Angew. Chem., Int. Ed.* **2016**, *55*, 1921–1924. doi:10.1002/anie.201508481
18. Poblitzki, A.; Gottschalk, H. C.; Suhm, M. A. *J. Phys. Chem. Lett.* **2017**, *8*, 5656–5665. doi:10.1021/acs.jpcclett.7b02337
19. Medcraft, C.; Zinn, S.; Schnell, M.; Poblitzki, A.; Altnöder, J.; Heger, M.; Suhm, M. A.; Bernhard, D.; Stamm, A.; Dietrich, F.; Gerhards, M. *Phys. Chem. Chem. Phys.* **2016**, *18*, 25975–25983. doi:10.1039/C6CP03557D
20. Bernhard, D.; Dietrich, F.; Fatima, M.; Perez, C.; Poblitzki, A.; Jansen, G.; Suhm, M. A.; Schnell, M.; Gerhards, M. *Phys. Chem. Chem. Phys.* **2017**, *19*, 18076–18088. doi:10.1039/C7CP02967E
21. Bernhard, D.; Holzer, C.; Dietrich, F.; Stamm, A.; Klopfer, W.; Gerhards, M. *ChemPhysChem* **2017**, *18*, 3634–3641. doi:10.1002/cphc.201700722
22. Dietrich, F.; Bernhard, D.; Fatima, M.; Perez, C.; Schnell, M.; Gerhards, M. *Angew. Chem., Int. Ed.* **2018**, in press. doi:10.1002/anie.201801842
23. Maier, J. M.; Li, P.; Vik, E. C.; Yehl, C. J.; Strickland, S. M. S.; Shimizu, K. D. *J. Am. Chem. Soc.* **2017**, *139*, 6550–6553. doi:10.1021/jacs.7b02349
24. Heger, M.; Mata, R. A.; Suhm, M. A. *Chem. Sci.* **2015**, *6*, 3738–3745. doi:10.1039/C5SC01002K
25. Medel, R.; Heger, M.; Suhm, M. A. *J. Phys. Chem. A* **2015**, *119*, 1723–1730. doi:10.1021/jp508424p
26. Mons, M.; Robertson, E. G.; Simons, J. P. *J. Phys. Chem. A* **2000**, *104*, 1430–1437. doi:10.1021/jp993178k
27. Page, R. H.; Shen, Y. R.; Lee, Y. T. *J. Chem. Phys.* **1988**, *88*, 4621. doi:10.1063/1.453775
28. Riehn, C.; Lahmann, C.; Wassermann, B.; Brutschy, B. *Chem. Phys. Lett.* **1992**, *197*, 443–450. doi:10.1016/0009-2614(92)85798-F
29. Gerhards, M.; Unterberg, C. *Phys. Chem. Chem. Phys.* **2002**, *4*, 1760–1765. doi:10.1039/b110029g
30. Loquais, Y.; Gloaguen, E.; Habka, S.; Vaquero-Vara, V.; Brenner, V.; Tardivel, B.; Mons, M. *J. Phys. Chem. A* **2015**, *119*, 5932–5941. doi:10.1021/jp509494c
31. Ebata, T.; Fujii, A.; Mikami, N. *Int. J. Mass Spectrom. Ion Processes* **1996**, *159*, 111–124. doi:10.1016/S0168-1176(96)04445-X
32. Gerhards, M.; Schumm, S.; Unterberg, C.; Kleinermanns, K. *Chem. Phys. Lett.* **1998**, *294*, 65–70. doi:10.1016/S0009-2614(98)00823-9
33. Palmer, P. M.; Chen, Y.; Topp, M. R. *Chem. Phys. Lett.* **2000**, *318*, 440–447. doi:10.1016/S0009-2614(00)00036-1
34. Robertson, E. G. *Chem. Phys. Lett.* **2000**, *325*, 299–307. doi:10.1016/S0009-2614(00)00661-8
35. Chen, Y.; Palmer, P. M.; Topp, M. R. *Int. J. Mass Spectrom.* **2002**, *220*, 231–251. doi:10.1016/S1387-3806(02)00772-8
36. Chen, Y.; Topp, M. R. *Chem. Phys.* **2002**, *283*, 249–268. doi:10.1016/S0301-0104(02)00613-4
37. Ishiuchi, S.-i.; Daigoku, K.; Saeki, M.; Sakai, M.; Hashimoto, K.; Fujii, M. *J. Chem. Phys.* **2002**, *117*, 7077–7082. doi:10.1063/1.1508103
38. Stearns, J. A.; Das, A.; Zwier, T. S. *Phys. Chem. Chem. Phys.* **2004**, *6*, 2605–2610. doi:10.1039/b313831c
39. Fricke, H.; Bartl, K.; Funk, A.; Gerlach, A.; Gerhards, M. *ChemPhysChem* **2008**, *9*, 2592–2600. doi:10.1002/cphc.200800499
40. Bartl, K.; Funk, A.; Gerhards, M. *J. Chem. Phys.* **2008**, *129*, 234306. doi:10.1063/1.3037023
41. Bartl, K.; Funk, A.; Gerhards, M. *ChemPhysChem* **2009**, *10*, 1882–1886. doi:10.1002/cphc.200900097
42. Stamm, A.; Weiler, M.; Brächer, A.; Schwing, K.; Gerhards, M. *Phys. Chem. Chem. Phys.* **2014**, *16*, 21795–21803. doi:10.1039/C4CP02546F
43. Miyazaki, M.; Fujii, M. *Phys. Chem. Chem. Phys.* **2017**, *19*, 22759–22776. doi:10.1039/C7CP03480F
44. Grimme, S. *Wiley Interdiscip. Rev.: Comput. Mol. Sci.* **2011**, *1*, 211–228. doi:10.1002/wcms.30
45. Grimme, S.; Ehrlich, S.; Goerigk, L. *J. Comput. Chem.* **2011**, *32*, 1456–1465. doi:10.1002/jcc.21759
46. Hellweg, A.; Grün, S. A.; Hättig, C. *Phys. Chem. Chem. Phys.* **2008**, *10*, 4119–4127. doi:10.1039/b803727b
47. Adler, T. B.; Werner, H.-J. *J. Chem. Phys.* **2009**, *130*, 241101. doi:10.1063/1.3160675
48. Wuttke, A.; Mata, R. A. *J. Comput. Chem.* **2017**, *38*, 15–23. doi:10.1002/jcc.24508
49. Suhm, M. A.; Kollipost, F. *Phys. Chem. Chem. Phys.* **2013**, *15*, 10702–10721. doi:10.1039/c3cp51515j
50. Unterberg, C.; Jansen, A.; Gerhards, M. *J. Chem. Phys.* **2000**, *113*, 7945. doi:10.1063/1.1315610
51. Iwasaki, T.; Miyata, Y.; Akimoto, R.; Fujii, Y.; Kuniyasu, H.; Kambe, N. *J. Am. Chem. Soc.* **2014**, *136*, 9260–9263. doi:10.1021/ja5043534
52. Schmitz, D.; Alvin Shubert, V.; Betz, T.; Schnell, M. *J. Mol. Spectrosc.* **2012**, *280*, 77–84. doi:10.1016/j.jms.2012.08.001
53. Pérez, C.; Lobsiger, S.; Seifert, N. A.; Zaleski, D. P.; Temelso, B.; Shields, G. C.; Kisiel, Z.; Pate, B. H. *Chem. Phys. Lett.* **2013**, *571*, 1–15. doi:10.1016/j.cplett.2013.04.014
54. Kraitchman, J. *Am. J. Phys.* **1953**, *21*, 17–24. doi:10.1119/1.1933388
55. *JB95 Spectral fitting program*; NIST. Plusquellic, D.
56. *Gaussian 09*, revision D.01; Gaussian, Inc.: Wallingford, CT, USA, 2009.
57. Halgren, T. A. *J. Comput. Chem.* **1996**, *17*, 490–519. doi:10.1002/(SICI)1096-987X(199604)17:5/6<490::AID-JCC1>3.0.CO;2-P
58. Hanwell, M. D.; Curtis, D. E.; Lonie, D. C.; Vandermeersch, T.; Zurek, E.; Hutchison, G. R. *J. Cheminf.* **2012**, *4*, 17. doi:10.1186/1758-2946-4-17
59. Furche, F.; Ahlrichs, R.; Hättig, C.; Klopfer, W.; Sierka, M.; Weigend, F. *Wiley Interdiscip. Rev.: Comput. Mol. Sci.* **2014**, *4*, 91–100. doi:10.1002/wcms.1162
60. Weigend, F.; Köhn, A.; Hättig, C. *J. Chem. Phys.* **2002**, *116*, 3175. doi:10.1063/1.1445115
61. Peterson, K. A.; Adler, T. B.; Werner, H.-J. *J. Chem. Phys.* **2008**, *128*, 84102. doi:10.1063/1.2831537
62. Yousaf, K. E.; Peterson, K. A. *J. Chem. Phys.* **2008**, *129*, 184108. doi:10.1063/1.3009271

63. Hill, J. G.; Peterson, K. A.; Knizia, G.; Werner, H.-J. *J. Chem. Phys.* **2009**, *131*, 194105. doi:10.1063/1.3265857
64. Pipek, J.; Mezey, P. G. *J. Chem. Phys.* **1989**, *90*, 4916–4926. doi:10.1063/1.456588
65. Reed, A. E.; Weinstock, R. B.; Weinhold, F. *J. Chem. Phys.* **1985**, *83*, 735–746. doi:10.1063/1.449486
66. *MOLPRO*, version 2015.1; a package of ab initio programs, <http://www.molpro.net>.
67. Schütz, M.; Rauhut, G.; Werner, H.-J. *J. Phys. Chem. A* **1998**, *102*, 5997–6003. doi:10.1021/jp981168y
68. Andrejić, M.; Mata, R. A. *Phys. Chem. Chem. Phys.* **2013**, *15*, 18115–18122. doi:10.1039/c3cp52931b
69. Schreiner, P. R.; Chernish, L. V.; Gunchenko, P. A.; Tikhonchuk, E. Y.; Hausmann, H.; Serafin, M.; Schlecht, S.; Dahl, J. E. P.; Carlson, R. M. K.; Fokin, A. A. *Nature* **2011**, *477*, 308–311. doi:10.1038/nature10367
70. Löffler, S.; Wuttke, A.; Zhang, B.; Holstein, J. J.; Mata, R. A.; Clever, G. H. *Chem. Commun.* **2017**, *53*, 11933–11936. doi:10.1039/C7CC04855F

License and Terms

This is an Open Access article under the terms of the Creative Commons Attribution License (<http://creativecommons.org/licenses/by/4.0>), which permits unrestricted use, distribution, and reproduction in any medium, provided the original work is properly cited.

The license is subject to the *Beilstein Journal of Organic Chemistry* terms and conditions: (<https://www.beilstein-journals.org/bjoc>)

The definitive version of this article is the electronic one which can be found at:
[doi:10.3762/bjoc.14.140](https://doi.org/10.3762/bjoc.14.140)

4.1.2 Structures of diphenyl ether aggregates with water and alcohols

Diphenyl ether (DPE)-alcohol aggregates are systematically studied to investigate the interplay of different forces of the intermolecular interactions. DPE has two binding sites (the ether oxygen (O), or the phenyl (P) group), compared to three in VPE (Section 4.1.1) for an alcohol. DPE is also a floppy molecule, as the molecule is free to rotate along the two CO bonds, and as a result, the CCOC dihedral angles, which connect its two phenyl rings, can change. The minimum energy form of the molecule is when the two dihedral angles are equal to 37° . The floppiness of DPE further adds the study of structural flexibility of the molecule on complex formation. The complexes of DPE with water, *tert-butyl* alcohol (TBA), and adamantanol have been investigated, and compared with a previous study of DPE with methanol (MeOH), in a multi-spectroscopic approach. Quantum-chemical calculations have been performed at the B3LYP-D3(BJ)/def2-TZVP level of theory and at the SCS-CC2/def2-TZVP level of theory (by another group within the collaboration). Further, quantitative analysis of the intermolecular energy decomposition for these complexes was performed using symmetry adapted perturbation theory (SAPT) at the SAPT0/jun-cc-pvtz level of theory. Additionally, dispersion percentages are obtained from LMP2/aug-cc-pVQZ calculations (by another group within the collaboration).

For complexes of DPE with water, as water is a small binding partner, on a first glimpse the probability of it forming an OH-O oxygen bond complex can be expected, but the calculations predicted OH- π to be the global minimum. In the spectra obtained from the three techniques, the OH- π is observed to be more intense than OH-O, agreeing with the calculations. From the microwave spectra, the experimental structure of the OH- π complex is also determined. Additionally, in this complex, transitions are split into doublets due to the internal motion of the water molecule within the complex. In the OH-O complex, in addition to splitting of transitions into doublets due to the internal motion of the water molecule, splitting of only a-type transitions into four components is observed. This is attributed to a concerted large-amplitude motion of both the water and DPE molecule in the complex and is not discussed further in detail here. Only by fitting the center frequencies from this splitting, the obtained rotational constants confirmed the assignment to the OH-O complex.

In a previous study for DPE-MeOH complexes [87], from the complementary techniques, the FTIR and IR/UV spectroscopy, two complexes as OH-O and OH- π were observed, with OH- π more abundant than OH-O. In the microwave spectrum, only

the OH- π complex was observed. Compared to VPE-methanol complexes (Section 4.1.1), this observation is opposite in the DPE-methanol, as the preferred interaction is changing from OH-O to OH- π .

On increasing the size of the binding partner to TBA, as presented in a separate study for DPE-TBA complexes [129], using the FTIR and IR/UV techniques, two complexes (OH-O and OH- π) were detected. With the chirped-pulse microwave study, using neon as the carrier gas for the supersonic expansion, only the OH-O complex was identified. When helium was used as the carrier gas, both OH-O and OH- π complexes were observed, indicating that the OH-O isomer is more stable than the OH- π isomer. Hence, the preference of complex formation is reversed with TBA, compared to DPE-water and DPE-methanol systems. For complexes of DPE with adamantanol, only the OH-O isomer was observed experimentally using microwave spectroscopy while the second isomer (the OH- π) remained untraceable.

The resulting solvent-size-dependent trend for the structural preference in DPE-alcohol is counter-intuitive. For small binding partners, OH- π structure is more stable and for larger alcohols, which are expected to be stronger dispersion energy donors, the OH-O bound complex is preferred. From a combined intermolecular energy analysis for all the DPE-alcohol complexes, it is observed that the dispersion interaction contribution in the OH- π complex for small binding partner is greater than the OH-O, due to additional CH- π interaction. When the size of the binding partner is increased, the contribution from dispersion interaction is similar or more in the OH-O complex because of increase in the overlapping interaction area, and therefore it is preferred. In these complexes, the DPE molecule is twisting along its dihedral angles to increase the interaction area. The results obtained from this study can help in understand unusual binding behaviors in cluster formation due to contributions from dispersion interactions. This study was published in *Angewandte Chemie* in 2018, and is given below.

Title	The Effect of Dispersion on the Structure of Diphenyl Ether Aggregates
Authors	Fabian Dietrich, Dominic Bernhard, Mariyam Fatima, Cristóbal Pérez, Melanie Schnell, and Markus Gerhards
Journal	Angewandte Chemie
Volume	57
Year	2018
Pages	9534-9537
DOI	International Edition:10.1002/anie.201801842 German Edition:10.1002/ange.201801842
Pages	4 pages of main article and 30 pages of supplementary material
Proportion of authors for the microwave part	
Experiment	Mariyam Fatima and Cristóbal Pérez
Analysis	Mariyam Fatima and Cristóbal Pérez
Manuscript Preparation	Mariyam Fatima, Cristóbal Pérez, Melanie Schnell

The Effect of Dispersion on the Structure of Diphenyl Ether Aggregates

Fabian Dietrich[†], Dominic Bernhard[†], Mariyam Fatima[†], Cristóbal Pérez, Melanie Schnell,^{*} and Markus Gerhards^{*}

Abstract: Dispersion interactions can play an important role in understanding unusual binding behaviors. This is illustrated by a systematic study of the structural preferences of diphenyl ether (DPE)–alcohol aggregates, for which OH...O-bound or OH... π -bound isomers can be formed. The investigation was performed through a multi-spectroscopic approach including IR/UV and microwave methods, combined with a detailed theoretical analysis. The resulting solvent-size-dependent trend for the structural preference turns out to be counter-intuitive: the hydrogen-bonded OH...O structures become more stable for larger alcohols, which are expected to be stronger dispersion energy donors and thus should prefer an OH... π arrangement. Dispersion interactions in combination with the twisting of the ether upon solvent aggregation are key for understanding this preference.

Dispersion interactions play an important role as intra- and intermolecular forces, since they are omnipresent.^[1] As a part of van der Waals interactions, they appear as attractive forces between non-polar molecules or molecular parts. Systematic studies of the influence of molecular interactions on structural preferences are of fundamental interest since they offer valuable insight beyond the stand-alone investigation of single systems. They reveal occasionally surprising systematic trends. These trends can be transferred to predict the structural properties of larger molecular systems, which, due to their size, cannot always be described in detail by the available experimental and theoretical methods. One established approach is to systematically change the size of substituents in a molecular system. An inherent factor accompanying variation in size is a change in dispersion

interactions, which must not be neglected. An example of a systematic analysis is the stability of a molecule depending on the size of the alkyl substituents, which has been studied based on the dimerization behavior of the Gomberg radical, for example.^[2]

Recently, we started a systematic analysis of aggregates of diphenyl ether (DPE) with alcohols to elucidate the preference of the hydrogen-bond acceptor site depending on the alkyl group of the alcohol molecule, which is strongly influenced by the magnitude of dispersion contributions. The experiments were performed under the cold and isolated gas-phase conditions of a molecular jet, so that we were solely probing the respective aggregates, free from solvent effects. The investigations of DPE with methanol (MeOH)^[3] and *tert*-butanol (*t*BuOH)^[4] revealed an unexpected behavior. In both cases, hydrogen bonding (either to the ether oxygen or the phenyl ring) is the primary interaction, with dispersion as a secondary interaction with a major influence on the preferred geometries. Because of the different strength of dispersion interactions of the methyl group with the DPE phenyl ring, the isomer with MeOH binding to the phenyl ring (OH- π) is more stable than the isomer with a hydrogen bond towards the ether oxygen (OH-O). This energetic preference is inverted for *t*BuOH, for which, intuitively, we expected a dominance of dispersion and thus stabilizing the OH- π isomer because of its three methyl groups. Part of the explanation is that *t*BuOH is bulky enough to always allow dispersion interaction with DPE, even in the OH-O isomer, which has the stronger hydrogen bond.

Here, we extend this analysis by studying aggregates of DPE with water and adamantanol (AdOH), which completes both the lighter and heavier end of the series. We used mass- and isomer-selective IR/UV spectroscopy as well as chirped-pulse Fourier transform microwave (CP-FTMW) spectroscopy in a molecular beam. Quantum chemical calculations, as described later, aided in the development of a quantitative understanding of the underlying interactions.

For the DPE–H₂O complexes, IR/R2PI spectra^[5] were recorded at different UV excitation wavenumbers obtained from an R2PI spectrum (see Figure S6 in the Supporting Information). This leads to partly isomer-selective IR spectra as shown in Figure 1. The IR/R2PI spectrum shown in Figure 1a (UV excitation wavenumber of 35 852 cm⁻¹) exhibits vibrational transitions at 3619 and 3723 cm⁻¹, representing the two OH-stretching vibrations of the attached water molecule. The lower trace (Figure 1b, UV excitation wavenumber of 36 250 cm⁻¹) contains four transitions. Two of them are equal to the ones observed in Figure 1a (see the Supporting Information for further explanation), whereas

[*] F. Dietrich,^[†] D. Bernhard,^[†] Prof. Dr. M. Gerhards
Fachbereich Chemie and Research Center Optimas
TU Kaiserslautern
Erwin-Schrödinger-Str. 52, 67663 Kaiserslautern (Germany)
E-mail: gerhards@chemie.uni-kl.de

M. Fatima,^[†] Dr. C. Pérez, Prof. Dr. M. Schnell
Deutsches Elektronen-Synchrotron (DESY)
Max-Planck-Institut für Struktur und Dynamik der Materie
Notkestrasse 85, 22607 Hamburg (Germany)
E-mail: melanie.schnell@desy.de

Prof. Dr. M. Schnell
Christian-Albrechts-Universität zu Kiel
Institut für Physikalische Chemie
Max-Eyth-Strasse 1, 24118 Kiel (Germany)

[†] These authors contributed equally to this work.

Supporting information and the ORCID identification number(s) for the author(s) of this article can be found under:
<https://doi.org/10.1002/anie.201801842>.

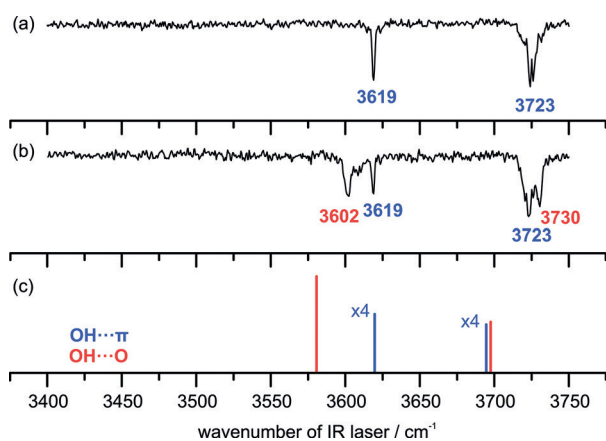


Figure 1. IR/R2PI spectra in the OH stretching region with different UV excitation wavenumbers: 35 852 cm^{-1} (a) and 36 250 cm^{-1} (b) compared to calculated stick spectra at the B3LYP-D3(BJ)/def2-TZVP level (c); scaling factor 0.9600.

two additional transitions at 3602 and 3730 cm^{-1} indicate an additional isomer. The experimentally observed vibrational transitions are compared with results from DFT and SCS-CC2 calculations (compare Figure 1 and Table S1). The transitions at 3619 and 3723 cm^{-1} are assigned to the OH- π structure, whereas the transitions at 3602 and 3730 cm^{-1} belong to the OH-O arrangement.

In particular, the significant red-shift of the vibration at 3602 cm^{-1} compared to the transition at 3619 cm^{-1} strongly indicates the formation of an O-H \cdots O bond. The structural assignment is further confirmed by the predicted UV excitation energies (see Table S2). In accordance with the already investigated DPE-MeOH^[6] and DPE-*t*BuOH^[4] complexes, the OH- π isomer has a lower excitation energy compared to the OH-O arrangement.

In parallel, we performed CP-FTMW spectroscopy^[7] to obtain further spectroscopic proof for the existence of more than one isomer for the DPE-H₂O complex, as well as structural information. A section of the experimental spectrum compared to the simulation based on rotational constants fitted to an asymmetric-rotor Hamiltonian is shown in Figure 2. Rotational signatures corresponding to two 1:1 DPE-H₂O complexes were observed. The stronger of the two spectra can be assigned to the OH- π isomer by comparison with calculated rotational constants (Table S7). The second spectrum, which is weaker by about a factor of two, arises from the OH-O isomer. In CP-FTMW spectroscopy, the transition intensities depend, among other factors, on the square of the dipole-moment components and the number of molecules. Considering that the μ_b dipole-moment component of OH-O is, at 3D, about three times stronger than the strongest dipole-moment component of the OH- π isomer, we can estimate the population of the OH-O isomer for DPE-water to be about 5–6% of that of the OH- π isomer. This is in accordance with the calculated energetic preference of the OH- π isomer over OH-O (Table S1). Details on the experiment, the analysis, and the experimentally determined molecular parameters are given in the Supporting Information. Both complexes show splitting patterns due to tunneling

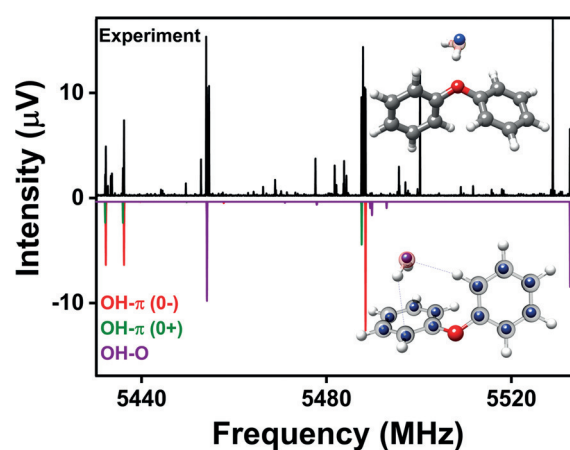


Figure 2. A section of the measured 2–8 GHz spectrum of DPE-H₂O (5 million acquisitions). The upper experimental trace in black is compared with simulations based on fitted parameters for the two isomers of DPE-H₂O. The two tunneling states for the OH- π isomers are indicated with 0- (red) and 0+ (green). The experimentally determined substitution structures based on Kraitchman's equations are also included. The inner spheres represent the experimental atom positions in comparison to B3LYP-D3(BJ)/def2-TZVP calculations. For the OH-O isomer, only the experimental position of the water-oxygen atom was determined.

motion of the water moiety^[8] with respect to DPE. For the OH-O isomer, we observe indications of an additional large-amplitude motion of the two phenyl rings of DPE with respect to each other. A detailed analysis of these splittings for this complex is beyond the scientific scope of this work and will be addressed separately in a compilation with higher-order water clusters.

For the OH- π isomer, the signal-to-noise ratio (SNR) of about 400:1 is fully sufficient to also observe the spectra of all singly substituted ¹³C isotopologues in natural abundance (about 1%). This allows us to determine the carbon backbone substitution (r_s) structure using Kraitchman's equations.^[9]

Furthermore, we performed a second set of experiments using an isotopically enriched sample of water with 50% H₂¹⁸O, which provided us with the positions of the H₂O oxygen atoms for both isomers. The experimental structures are included in Figure 2. A detailed description of the structure determination for the two isomers using the Kraitchman method is given in the Supporting Information.

Another set of experiments using CP-FTMW spectroscopy was performed to investigate the DPE-AdOH cluster. Analysis of the spectrum revealed the presence of the OH-O isomer in the molecular beam. No experimental evidence for the OH- π isomer was observed. The rotational parameters as well as the experimental frequencies can be found in Figure S8 and Tables S12, S32.

With our investigations on DPE-H₂O and DPE-AdOH, we now have a series of aggregates with increasingly large side chains (from H₂O to MeOH, *t*BuOH, and AdOH). The results of the spectroscopic experiments and the quantum chemical calculations (DFT and SCS-CC2) indicate an overall stabilization of the OH-O motif with increasing side-chain size in comparison with the OH- π motif (Table S3). This behavior is counter-intuitive at first sight, since a larger side

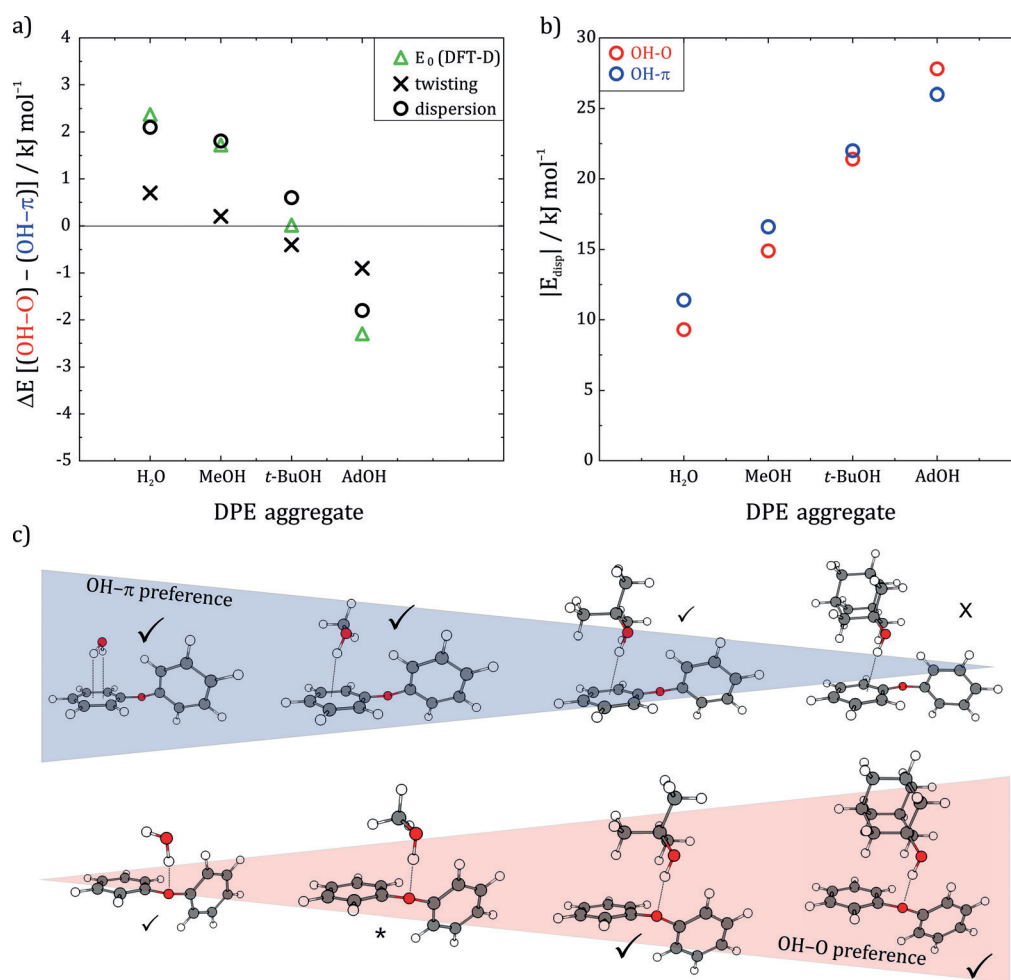


Figure 3. a) Differences ΔE between OH-O and OH- π isomers, regarding contributions of twisting (black crosses) and LMP2 dispersion energies (black circles, see Tables S4 and S5) in comparison with the difference in zero-point and BSSE corrected energies calculated at the B3LYP-D3(BJ)/def2-TZVP level (green triangles). b) Absolute values of the dispersion energy in dependence on the solvent molecule (obtained from LMP2/AVQZ calculations, see Table S4). c) Overview of calculated OH-O and OH- π structures for different DPE-solvent complexes. Ticks indicate experimental evidence for the respective structures, with their size indicating the observed abundance for the microwave experiments (neon expansion). A cross means that no experimental evidence was found. *: Only observed in IR experiments with helium expansion.^[3]

chain represents a better dispersion energy donor and should stabilize the OH- π isomer. In order to explain this unexpected preference, we analyzed two aspects: dispersion and an approximation of the twisting energy of the DPE caused by the aggregation of the solvent molecule. The corresponding change in the dihedral angles on both sides of the ether oxygen can be seen in Figure 3 and Table S4.

The twisting energy of DPE was quantified by removing the solvent molecule from the corresponding aggregate, applying single-point calculations at the B3LYP-D3(BJ)/def2-TZVP level, and comparing them with the energy of the optimized DPE molecule (Table S4). This approach illustrates in a simple picture the impact of the solvent molecule on the DPE backbone, summing up different electronic effects including geometry changes like the elongation of C-H bonds and distortion of the phenyl rings. Concerning the twisting energy, the OH-O structure is less stable than the OH- π isomer for the DPE-H₂O cluster. The difference between the two structural motifs decreases with a larger alkyl chain, resulting in a switch of the preference for

aggregates of *t*BuOH and AdOH. This difference in E_{twist} (Table S4) is shown in Figure 3a as black cross marks.

Besides the twisting energy difference, the dispersion energy plays a crucial role in the isomer preference. A short discussion of the results of SAPT(0) calculations, which describe the trend of dispersion and electrostatic interactions qualitatively (Table S6), is included in the Supporting Information.

In addition, we extracted the percentage of dispersion energy from less expensive localized MP2 calculations as introduced by Wuttke et al.^[10] This approach also provides an illustration of the dispersion forces between two molecules in an aggregate. These dispersion interaction densities for all aggregates and isomers are given in the Supporting Information (Figures S2-S5). The absolute values of the dispersion energies are shown in Table S5 and Figure 3b, the difference between the OH-O and OH- π isomers in Figure 3a as black circles. There is a general increase of the dispersion energies calculated with this method going from the small molecule (water) to the bulky moiety (adamantanol). This is not

surprising since the interaction area also increases with the increasingly large alkyl group. However, the difference between the two isomers changes its sign with increasing size of the alkyl moiety (Figure 3b). While the OH- π isomer contains significantly more dispersion energy for both the water and the methanol cluster, the contribution of dispersion is similar for both structures of the DPE-*t*BuOH aggregate. For the DPE-AdOH clusters, the OH-O structure contains more dispersion energy due to the larger interaction area of the phenyl ring and the adamantyl moiety than in the OH- π isomer. Both the twisting and the dispersion contributions show the same trend, preferring OH-O over OH- π with increasing alkyl-group size. The same trend is observed for the energetic difference between OH-O and OH- π structures calculated at the B3LYP-D3(BJ)/def2-TZVP level considering zero point and BSSE corrections (green triangles in Figure 3a).

In summary, we present experimental evidence and characterization of the OH-O and OH- π isomers of DPE-H₂O, which shows a clear preference for the OH- π isomer, by applying IR/UV and microwave spectroscopy in molecular beam experiments. In the case of DPE-AdOH, the OH-O complex was identified using microwave spectroscopy. We used these experiments together with the results for DPE-MeOH^[3] and DPE-*t*BuOH^[4] complexes in combination with a variety of calculations to describe and explain a counter-intuitive behavior with respect to competing structures in DPE-alcohol clusters with increasing side-chain size. These effects are driven by dispersion energies, which become stronger for larger side chains. Our systematic series points out and quantifies the importance of different competing interaction energies, a phenomenon relevant in almost all areas of chemistry.

Acknowledgements

This work was supported by the Priority Program “Control of London dispersion interactions in molecular chemistry” SPP1807 of the Deutsche Forschungsgemeinschaft (GE 961/9-1 and SCHN 1280/4-1). We thank Axel Wuttke and Ricardo Mata for introduction of the DID plots and supplying the computational resources. The use of the GWDG computer cluster is acknowledged. M.F. acknowledges support from the

Hamburg International Max Planck Research School UFAST. This work is part of the PhD theses of F.D., D.B., and M.F.

Conflict of interest

The authors declare no conflict of interest.

Keywords: dispersion · molecular complexes · non-covalent interactions · rotational spectroscopy · vibrational spectroscopy

How to cite: *Angew. Chem. Int. Ed.* **2018**, *57*, 9534–9537
Angew. Chem. **2018**, *130*, 9678–9682

- [1] J. P. Wagner, P. R. Schreiner, *Angew. Chem. Int. Ed.* **2015**, *54*, 12274; *Angew. Chem.* **2015**, *127*, 12446.
- [2] a) S. Grimme, P. R. Schreiner, *Angew. Chem. Int. Ed.* **2011**, *50*, 12639; *Angew. Chem.* **2011**, *123*, 12849; b) S. Rösel, C. Balestrieri, P. R. Schreiner, *Chem. Sci.* **2017**, *8*, 405.
- [3] C. Medcraft, S. Zinn, M. Schnell, A. Poblitzki, J. Altnöder, M. Heger, M. A. Suhm, D. Bernhard, A. Stamm, F. Dietrich, M. Gerhards, *Phys. Chem. Chem. Phys.* **2016**, *18*, 25975.
- [4] D. Bernhard, F. Dietrich, M. Fatima, C. Perez, A. Poblitzki, G. Jansen, M. A. Suhm, M. Schnell, M. Gerhards, *Phys. Chem. Chem. Phys.* **2017**, *19*, 18076.
- [5] a) A. Stamm, D. Maué, A. Schaly, S. Schlicher, J. Bartl, S. Kubik, M. Gerhards, *Phys. Chem. Chem. Phys.* **2017**, *19*, 10718; b) M. Gerhards, C. Unterberg, *Phys. Chem. Chem. Phys.* **2002**, *4*, 1760; c) C. Unterberg, A. Jansen, M. Gerhards, *J. Chem. Phys.* **2000**, *113*, 7945; d) K. Schwing, C. Reyheller, A. Schaly, S. Kubik, M. Gerhards, *ChemPhysChem* **2011**, *12*, 1981.
- [6] D. Bernhard, C. Holzer, F. Dietrich, A. Stamm, W. Klopper, M. Gerhards, *ChemPhysChem* **2017**, *18*, 3634–3641.
- [7] a) G. G. Brown, B. C. Dian, K. O. Douglass, S. M. Geyer, S. T. Shipman, B. H. Pate, *Rev. Sci. Instrum.* **2008**, *79*, 053103; b) D. Schmitz, V. A. Shubert, T. Betz, M. Schnell, *J. Mol. Spectrosc.* **2012**, *280*, 77.
- [8] C. Calabrese, Q. Gou, A. Maris, W. Caminati, S. Melandri, *J. Phys. Chem. Lett.* **2016**, *7*, 1513.
- [9] J. Kraitchman, *Am. J. Phys.* **1953**, *21*, 17.
- [10] A. Wuttke, R. A. Mata, *J. Comput. Chem.* **2017**, *38*, 15.

Manuscript received: February 10, 2018

Revised manuscript received: March 30, 2018

Accepted manuscript online: April 30, 2018

Version of record online: June 27, 2018

4.1.3 Complexes of dibenzofuran with water and alcohols

In the study of dibenzofuran (DBF)-alcohol aggregates, the structural preference on complex formation is investigated in a systematic approach by introducing structural deformation in diphenyl ether (DPE). DBF also offers two intermolecular interaction sites, one as the (furan) oxygen for hydrogen bonding (OH-O), and another as π cloud of phenyl rings (OH- π). The complexes of DBF with water, methanol (MeOH), and *tert-butyl* alcohol (TBA) have been investigated using the multi-spectroscopic approach.

Quantum-chemical calculations were performed at various levels of theory within the collaboration. For all DBF-alcohol complexes, dispersion energy contribution to the total interaction energy was obtained at the DLPNO-CCSD(T)/cc-pVQZ level via a local decomposition (LED) scheme (performed by other groups within the collaboration). The intermolecular energy decomposition for these complexes was performed using symmetry adapted perturbation theory (SAPT) at SAPT0/jun-cc-pvtz level of theory.

For complexes of DBF with water, the IR/UV technique suggested OH-O bound complex of DBF-water, which was further confirmed with the microwave spectroscopy. In the microwave spectra, as in the DPE-water complexes, the transitions were split into doublet due to the internal motion of the water molecule with respect to the DBF moiety. As the water molecule is also interacting with the CH part of DBF, the observed splitting is not equal to the internal motion of the free water molecule, and therefore the rotational constants for this complex was obtained by fitting the center frequencies of the split transitions. Here the preferred complex is OH-O over OH- π , as expected for small binding partners, but opposite to DPE-water clusters (4.1.1).

In the DBF-MeOH complex, using the multi-spectroscopic approach, the OH-O bound complex is observed to be more abundant than the OH- π bound complex. In the microwave spectrum for the OH- π complex, splitting due to the internal rotation of the methyl group of methanol is observed. The V_3 barrier height and the orientation of the methyl group with respect to the principal axis system is determined. The experimentally determined V_3 value is 338.99 cm^{-1} (4.055 kJ mol^{-1}), and is in decent agreement with the calculated value of 420 cm^{-1} (5 kJ mol^{-1}) at B3LYP-D3(BJ)/def2-TZVP level of theory. For the OH-O complex, the observed splitting patterns of the complex could not be fit to the internal motion of the methyl group of methanol, suggesting towards a second internal motion. This preference of OH-O bound complex is in agreement with the VPE-methanol complexes (Section 4.1.1). However, compared to DPE-methanol complexes (Section 4.1.2), this observation is

opposite. For complexes of DBF with TBA, only the OH- π isomer was observed experimentally using the multi-spectroscopic approach, resulting in a similar observation as DPE-methanol study.

From a combined analysis of the intermolecular interactions for all the DBF-ROH complexes, it is found that the dispersion interaction contribution increases for OH- π complexes with increasing size of the alcohol molecule compared to OH-O. Though this contribution is smaller in the OH- π isomer of DBF-water than DPE-water, therefore, the OH-O isomer remains dominant. Interestingly, even though the structures of DPE and DBF are similar, the observed pattern of the complex formation (OH-O or OH- π) with increasing size of the alcohol molecule is reversed in DBF compared to DPE. The results obtained from this study will help to expand the knowledge about the binding preference in cluster formation and how they are changed from the small difference in the intermolecular forces. This study was published in Physical Chemistry Chemical Physics in 2019, and is given below.

Title Dispersion-controlled docking preference: multi- spectroscopic study on complexes of dibenzofuran with alcohols and water

Authors Fabian Dietrich, Mariyam Fatima, Anja Poblitzki, Amanda Steber, Cristóbal Pérez, Martin Suhm, Melanie Schnell, and Markus Gerhards

Journal Physical Chemistry Chemical Physics

Volume 21

Year 2019

Pages 16032-16046

DOI 10.1039/c9cp02635e

Pages 15 pages of main article and 30 pages of supplementary material

Proportion of authors for the microwave part

Experiment Mariyam Fatima and Anja Poblitzki

Analysis Mariyam Fatima and Cristóbal Pérez

Manuscript Preparation Mariyam Fatima, Cristóbal Pérez, Amanda Steber, and Melanie Schnell



Cite this: *Phys. Chem. Chem. Phys.*,
2019, 21, 16032

Dispersion-controlled docking preference: multi-spectroscopic study on complexes of dibenzofuran with alcohols and water†

D. Bernhard,^a M. Fatima,^b A. Poblitzki,^c A. L. Steber,^b C. Pérez,^b
M. A. Suhm,^{*c} M. Schnell^{*b} and M. Gerhards^{*a}

The structural preferences within a series of dibenzofuran–solvent complexes have been investigated by electronic, vibrational, and rotational spectroscopic methods probing supersonic jet expansions. The experimental study is accompanied by a detailed theoretical analysis including dispersion-corrected density functional theory, symmetry adapted perturbation theory, as well as coupled cluster approaches. The complementary, multi-spectroscopic results reveal a preferred OH...O structure for the smallest complex of dibenzofuran–water, whereas for the methanol complex an OH... π isomer is simultaneously observed. For the largest complex, dibenzofuran–*tert*-butyl alcohol, only a π -bound structure is found. These comprehensive investigations show that a completely inverse trend regarding the docking preference is observed by comparing the present results with the ones for analogous diphenyl ether complexes. This can be rationalized on the basis of the planarity/non-planarity and rigidity/flexibility of the different systems, providing valuable insight into the interplay between different non-covalent interactions. This analysis is a further step towards a quantitative description of very delicate energetic balances with the overall goal of yielding reliable structural predictions for non-covalently bound systems.

Received 9th May 2019,
Accepted 22nd June 2019

DOI: 10.1039/c9cp02635e

rsc.li/pccp

1 Introduction

Non-covalent attraction plays a key role in molecular recognition and aggregation, which can be fundamental for governing (bio)chemical processes.^{1–4} Already small changes within the interplay of intermolecular forces can affect these processes significantly. London dispersion is one of the major attractive contributors, along with ambivalent Keesom and always attractive Debye forces. These forces may compete with or reinforce each other, and most importantly they are balanced by Pauli repulsion at a short distance. London dispersion is particularly able to control the formation of a certain molecular arrangement in anisotropic systems due to its cumulative, non-local nature in contrast to the very local Pauli repulsion.^{5,6}

The structures of neutral, non-covalently bound molecular complexes involving aromatic moieties and water or alcohol molecules have been extensively studied in the gas phase (see *e.g.* ref. 7–9 and references therein). Among these studies, several complexes involving heteroaromatic moieties are found including works on indole–water,¹⁰ 7-azaindole–water,¹¹ pyrrole–¹² and carbazole–solvent complexes.^{13,14} Moreover, several studies on furan derivatives were carried out, including a comparative FTIR jet and theoretical study on 2,5-dimethylfuran– as well as the 2,3-benzofuran–methanol complexes.¹⁵ The latter have additionally been studied by laser induced fluorescence and IR fluorescence dip spectroscopy, including the respective water complexes.¹⁶ For the 2,5-dimethylfuran–methanol complex, the OH...O binding motif was identified as the preferred structure, which exhibits additional CH... π stabilization by the interaction of the methyl group with the π -cloud. The OH... π -bound isomer was also observed as a slightly less stable structure, although it turned out to cause a stronger OH stretching red-shift than the OH...O-bound structure, *i.e.* the π -cloud causes a stronger distortion of the OH bond than the lone pairs of the ether oxygen. In the case of 2,3-benzofuran–water,¹⁶ a balanced situation was found with the coexisting, nearly isoenergetic OH...O and OH... π isomers. Within that study, no preferred site could be identified, which agrees with the theoretical predictions of less than 0.5 kJ mol^{–1} energy difference for the applied methods.¹⁶

^a TU Kaiserslautern, Fachbereich Chemie & Research Center Optimas,
Erwin-Schrodinger-Str. 52, D-67663 Kaiserslautern, Germany.
E-mail: gerhards@chemie.uni-kl.de

^b Deutsches Elektronen-Synchrotron (DESY), Notkestr. 85, D-22607 Hamburg,
Germany & Institute of Physical Chemistry, Christian-Albrechts-Universität zu Kiel,
Max-Eyth-Str. 1, D-24118 Kiel, Germany. E-mail: melanie.schnell@desy.de

^c Institut für Physikalische Chemie, Universität Göttingen, Tammannstr. 6,
D-37077 Göttingen, Germany. E-mail: msuhm@gwdg.de

† Electronic supplementary information (ESI) available. See DOI: 10.1039/c9cp02635e



However, the methanol complex of 2,3-benzofuran was found to prefer the π -docking site over the oxygen, which was clearly identified by linear FTIR jet spectroscopy.¹⁵ In this case, the π -bound structure exhibits a larger OH stretching red-shift than the OH \cdots O structure, whereas theoretical predictions were ambiguous. The competing binding motifs in 2-methylfuran- and furan-methanol complexes are currently being examined in an experimental benchmarking study, with initial FTIR results already published,¹⁷ and a refined analysis with microwave support in preparation.

Several spectroscopic studies on dibenzofuran (DBF) have been performed in the condensed phase^{18–23} and in the gas phase,^{23–30} including works on the DBF dimer^{27,28,31} and mixed dimers of DBF with fluorene and benzofuran.^{28,32,33} Auty *et al.*²⁴ recorded fluorescence excitation spectra of DBF and the DBF-water complex. They assumed that the complex is hydrogen-bonded to the oxygen atom of DBF based on the spectral shift of the fluorescence excitation bands. However, there is a lack of *ab initio* calculations supporting this assumption as well as further, structurally more sensitive spectroscopic experiments.

In previous studies, we established a multi-spectroscopic approach in order to elucidate the preferred binding sites in different aromatic ether-alcohol and -water complexes.^{34–38} Within the series of diphenyl ether (DPE) complexes, we have shown that water and small alcohol molecules prefer the π -docking site, whereas larger alcohols preferably bind to the ether oxygen atom. This observation contradicts the intuitive expectation of a preferred π docking, when the size of the alcohol increases. In that study, the respective contribution of London dispersion to the interaction energy for the different complexes was analyzed in order to explain the observed trend. In addition to that, the distortion of the DPE structure, caused by a twist of the phenyl rings upon aggregation of alcohol or water molecules, was identified as another major aspect influencing the trend.

In order to gain a deeper understanding of the influence of structural deformation upon complex formation, a systematic change in the structure of the ether is valuable. One possible change is the direct connection of the two phenyl rings of DPE, which leads to dibenzofuran (DBF). By doing so, the initial flexibility of DPE is entirely disabled since DBF is planar and rigid. Considering the fact that the π system is delocalized over both phenyl rings *via* the furan ring, the molecule is expected to remain planar upon solvent aggregation in order to maximize aromaticity. Therefore, there is no deformation of the ether geometry within the solvent complexes that might influence the binding preference, contrary to the case of DPE complexes in which deformation plays a substantial role.³⁷ Moreover, the twisted structure of DPE was shown to enable CH \cdots O contacts between *ortho* CH moieties and the oxygen atom of the alcohol or water molecule. This had a significant influence on the structural preference as well. Since for DBF only in-plane CH groups are available for CH \cdots O contacts, structures mainly interacting *via* the π -cloud should not be affected by CH \cdots O contacts. Whatever the relative importance of such qualitative concepts may be, they add up to a computable and

experimentally verifiable energy difference between competing solvent docking sites.

Experimental verification of predicted structural preferences of such molecular complexes requires studies on a molecular level, where the isolated molecular aggregates can be investigated without the influence of any environment. These conditions can be fulfilled by molecular beam investigations, allowing the formation of molecular complexes and clusters in a supersonic expansion. A variety of spectroscopic methods can be combined with molecular beam experiments, including FTIR spectroscopy,^{15,34,35,38} mass- and isomer-selective IR/UV laser spectroscopy (IR/R2PI^{8,39–42}) and chirped-pulse Fourier transform microwave (CP-FTMW^{43–45}) spectroscopy. The combination of these different spectroscopic techniques yields complementary results, providing valuable experimental data ideally suited for benchmarking theoretical approaches.

In the present paper, we investigate a series of DBF complexes with water, methanol and *tert*-butyl alcohol (ROH with R = H, Me, *t*-Bu) by a multi-spectroscopic strategy, including FTIR, IR/UV and CP-FTMW spectroscopy. The experimental study is accompanied by a detailed theoretical analysis including dispersion-corrected density functional theory as well as wave function-based methods.

2 Experimental methods

2.1 FTIR spectroscopy

Linear FTIR spectra were recorded using the 'popcorn' jet set-up. DBF (alfa aesar, $\geq 99\%$) was deposited on molecular sieve and exposed to carrier gas pulses in a heatable sample compartment enclosed by two poppet valves (opening at 70 mbar differential pressure upstream and either 690 or 350 mbar downstream). Helium was used as the carrier gas at 1.5 bar. A gas pulse from a 0.069 m³ reservoir picked up the sample and was supersonically expanded into a 3.6 m³ buffer volume. A sufficiently low background pressure is ensured by a pumping system operating at 500 m³ h⁻¹. Two nozzle variants were applied: a $2 \times 10 \times 0.5$ mm double-slit nozzle and a newly designed 60×0.2 mm heatable 'V-nozzle', which is angled (162°) to approximately fit the focused IR beam shape. The alcohols (MeOH (Sigma Aldrich, $\geq 99.8\%$), MeOD (eurisotop, 99% D), *t*-BuOH (Roth, $\geq 99\%$)) were introduced upstream of the gas reservoir by a coolable saturator or by using premixed gas bottles. Each gas pulse was probed by a single synchronized scan of a Bruker IFS 66v/S FTIR spectrometer. 100–400 scans were averaged to obtain the final spectrum. More details can be found in ref. 34 and 46.

2.2 IR/UV spectroscopy

The experimental set-up for the combined IR/UV experiments is described in detail elsewhere,^{42,47} thus only a brief description is given here. The experiments were carried out in a molecular beam apparatus consisting of a differentially pumped linear time-of-flight (TOF) mass spectrometer with a pulsed valve (Series 9 with pulse driver Iota One, General Valve, 500 μ m orifice) for skimmed jet expansion. DBF was purchased from



Merck ($\geq 97.0\%$). MeOH (Sigma-Aldrich, $\geq 99.7\%$) and *t*-BuOH (Sigma-Aldrich, $\geq 99.7\%$) were each supplied *via* cooled reservoirs and co-expanded with DBF (held at room temperature) using the carrier gas neon (2.5–3.0 bar).

For the R2PI and IR/R2PI experiments, two tunable nano-second laser systems were necessary, including one independent UV laser system and one IR laser system. The UV laser radiation is obtained *via* second harmonic generation in a BBO crystal using the output of a dye laser (Cobra-Stretch, Sirah). The latter is pumped by the second harmonic (532 nm) of a Nd:YAG laser (SpitLight 600, Innolas). The IR laser radiation in the range of 3520–3750 cm^{-1} is generated by difference frequency mixing (DFM) in a LiNbO₃ crystal using the fundamental (1064 nm) of a Nd:YAG laser (Quanta-Ray Pro-230, Spectra-Physics) and the output of a second dye laser (PrecisionScan, Sirah), which is pumped by the second harmonic (532 nm) of the same Nd:YAG laser. The resulting IR radiation is amplified in an optical parametric amplification (OPA) process in another LiNbO₃ crystal using the output of the DFM process and the fundamental (1064 nm) of the Nd:YAG laser. For the IR/R2PI spectra, the IR laser was irradiated 50 ns prior to the UV laser.

2.3 CP-FTMW spectroscopy

The rotational spectra of the DBF–ROH complexes were recorded with the Hamburg CP-FTMW spectrometer COMPACT, which is operated between 2–8 GHz.^{48,49} DBF (stated purity $\geq 98\%$) was purchased from Sigma-Aldrich and used without further purification. The molecules were seeded into a supersonic expansion using a modified pulse nozzle (Parker General Valve, Series 9, 1.1 mm orifice diameter) equipped with a heatable reservoir. DBF was placed into the reservoir close to the valve orifice and heated to 100 °C. The solvent (ROH) was placed in an external reservoir upstream of the valve at a second set of tubing to regulate the amount of carrier gas that was flowed over it and thus to regulate the amount of solvent. For all of the experiments, neon (3 bar backing pressure) was used as a carrier gas to form a supersonic expansion into the vacuum chamber. Additional experiments with helium as a carrier gas (3 bar backing pressure) were performed for DBF–MeOH.

For each gas pulse, the ensemble of molecules was polarized with a series of eight microwave chirps with a 4 μs duration and spanning 2–8 GHz, following the fast-frame approach.⁵⁰ The chirps were generated with an arbitrary waveform generator, amplified by a 300 W travelling wave tube amplifier, and transmitted into the vacuum chamber with a horn antenna. Following each excitation chirp, 40 μs of the free induction decay (FID) of the macroscopic ensemble of polarized molecules was recorded, yielding a frequency resolution of 25 kHz. For the experiments, a total of 5 million averages (for DBF–H₂O) and 2 million averages (for DBF–MeOH and DBF–*t*-BuOH, respectively) were co-added and Fourier transformed with a Kaiser–Bessel window function to give the broadband rotational spectrum in the frequency domain.

All spectra were first fit to an asymmetric rotor Hamiltonian using the JB95 program.⁵¹ The transition frequencies were then refined using the AABS program suite, and the final asymmetric

rotor Hamiltonian fits were completed with SPFIT.⁵² Line lists for all three dimers are provided in the ESI.† An analysis of the observed tunneling splitting arising from internal rotation of the methanol methyl group in the dibenzofuran–methanol complex was performed using the XIAM program.⁵³ XIAM is a least squares fitting program specifically designed for analyzing spectra of molecules exhibiting internal rotors by employing the combined axis method of Woods to account for internal rotation through a potential barrier.

3 Computational methods

Input structures were manually constructed with Avogadro⁵⁴ using the MMFF94s force field⁵⁵ for pre-optimization, whereas additional geometries were generated by the simulated annealing conformational search implemented in the GFN-xTB⁵⁶ program (option -siman). Geometry optimizations and harmonic vibrational frequency calculations were performed at the DFT as well as the SCS-CC2⁵⁷ level.

For the DFT calculations, the B3LYP functional^{58–60} including the D3 dispersion correction⁶¹ with Becke–Johnson (BJ) damping⁶² was used with the basis sets def2-TZVP,⁶³ def2-QZVP⁶³ and aug-cc-pVTZ⁶⁴ (identical auxiliary basis sets for the RI approximation), while using the Berny optimization algorithm from Gaussian 09⁶⁵ combined with energies and gradients calculated with Turbomole 7.3.^{66,67} Similarly, calculations were performed with the M06-2X functional⁶⁸ including the D3 correction and the def2-TZVP basis set.

The SCS-CC2 calculations were carried out with the aug-cc-pVDZ⁶⁴ and def2-TZVP basis sets using Turbomole 7.3, while correspondingly aug-cc-pVDZ-cbas⁶⁹ and def2-TZVP-cbas⁶⁹ were chosen as the auxiliary Coulomb fitting basis sets (cbas) required by the *ricc2* module for the RI approximation. Harmonic vibrational frequencies at the SCS-CC2 level were calculated with the NumForce script of Turbomole 7.3.

All geometries were confirmed to be minima with only real harmonic vibrational frequencies. All DFT and SCS-CC2 energies were corrected for the basis set superposition error (BSSE) by applying the counterpoise correction method.⁷⁰

DLPNO-CCSD(T) single-point calculations for the B3LYP-D3(BJ)/aug-cc-pVTZ geometries were carried out with ORCA 4.0.1⁷¹ using the cc-pVTZ and cc-pVQZ basis sets⁶⁴ with corresponding cc-pVTZ/C and cc-pVQZ auxiliary basis sets⁶⁹ for the RI approximation. Additionally, the “TightPNO”⁷² and “TightSCF” options were applied. For comparison of zero-point-vibrational energy (ZPE)-corrected energies, harmonic ZPE corrections obtained at the B3LYP-D3(BJ)/aug-cc-pVTZ level were added to the DLPNO-CCSD(T)/cc-pVTZ and DLPNO-CCSD(T)/cc-pVQZ energies. Furthermore, a local energy decomposition (LED) scheme^{73,74} was applied within the DLPNO-CCSD(T)/cc-pVQZ calculations. This was mainly used for extracting physically meaningful dispersion contributions to the total interaction energies. For comparison, second order SAPT(0) calculations⁷⁵ were carried out with the truncated jun-cc-pVDZ basis set,^{64,76,77} using the PSI4 program.⁷⁸



Transition state calculations were performed with the QST3⁷⁹ module of Gaussian 09 (B3LYP-D3(BJ)/def2-TZVP) with initial transition state and barrier guesses from the woelfling⁸⁰ module of Turbomole 7.3 as well as the reaction path finder of the GFN-xTB program (option -path).

4 Results and discussion

4.1 Theoretical results

Fig. 1 shows the optimized minimum structures for DBF complexes with H₂O, MeOH and *t*-BuOH at the B3LYP-D3(BJ)/def2-TZVP level. The oxygen-bound structure, denoted as OH \cdots Op (in the DBF plane), of the DBF–H₂O complex is further stabilized by a CH \cdots O interaction, which is reflected in a slight tilt of the water with its oxygen atom towards the C–H group that is in close proximity. Within the structure of the OH \cdots π 5 isomer, the water molecule is positioned above the furan C–C bond connecting the two phenyl rings, whereas in the OH \cdots π 6 isomer the water molecule is positioned above the center of one of the six-membered phenyl rings. Upon comparing all three isomers it can be seen that there are two intermolecular contacts within each arrangement: one OH \cdots O hydrogen bond along with a CH \cdots O contact in OH \cdots Op, and two OH \cdots π contacts respectively in both OH \cdots π isomers. Considering the calculated relative energies obtained at different levels of theory (see Table 1), the OH \cdots Op isomer is mostly preferred. This suggests that the OH \cdots O hydrogen bond combined with the CH \cdots O contact outweighs the sum of two OH \cdots π contacts in terms of the strength of the intermolecular interaction.

In order to analyze the respective contributions to the interaction energy of the investigated complexes, SAPT(0)/jun-cc-pVDZ calculations were performed (see Table S1, ESI[†]) as well as more sophisticated DLPNO-CCSD(T)/cc-pVQZ calculations for which a local energy decomposition (LED) scheme was applied (see Table S2, ESI[†]). As expected, both approaches yield a larger dispersion contribution in the OH \cdots π motifs and significantly more electrostatic contribution for the OH \cdots Op structure. This supports the finding that the OH \cdots O hydrogen bond, dominated by electrostatics (see Table S1, ESI[†]), combined with the CH \cdots O contact leads to a stronger stabilization than the two OH \cdots π contacts within the other isomers.

For the DBF–MeOH complex, the calculated minimum structures at the B3LYP-D3(BJ)/def2-TZVP level are depicted in the second row of Fig. 1. In this case, two oxygen-bound isomers are found: within the *C*_s-symmetric OH \cdots O*t* isomer (on top), the methyl group of the methanol molecule is positioned above the furan ring, enabling CH \cdots π interactions. The second oxygen-bound structure is denoted as OH \cdots Op and exhibits an OH \cdots O hydrogen bond in the DBF plane with the methyl group pointing away from the DBF plane. Therefore, the OH \cdots Op isomer lacks CH \cdots π interactions in contrast to the OH \cdots O*t* arrangement. However, the in-plane hydrogen bond allows for a stabilizing CH \cdots O contact between the MeOH oxygen atom and a CH group of DBF (see Fig. 1), similar to the OH \cdots Op isomer of DBF–H₂O. The OH \cdots π 6 isomer is bound *via* an OH \cdots π contact, and it is stabilized by CH \cdots π interactions of the methyl group with the π -cloud. In contrast to the related systems 2,5-dimethylfuran–MeOH and 2,3-benzofuran–MeOH,^{15,16} no minimum structure is found with an OH \cdots π interaction

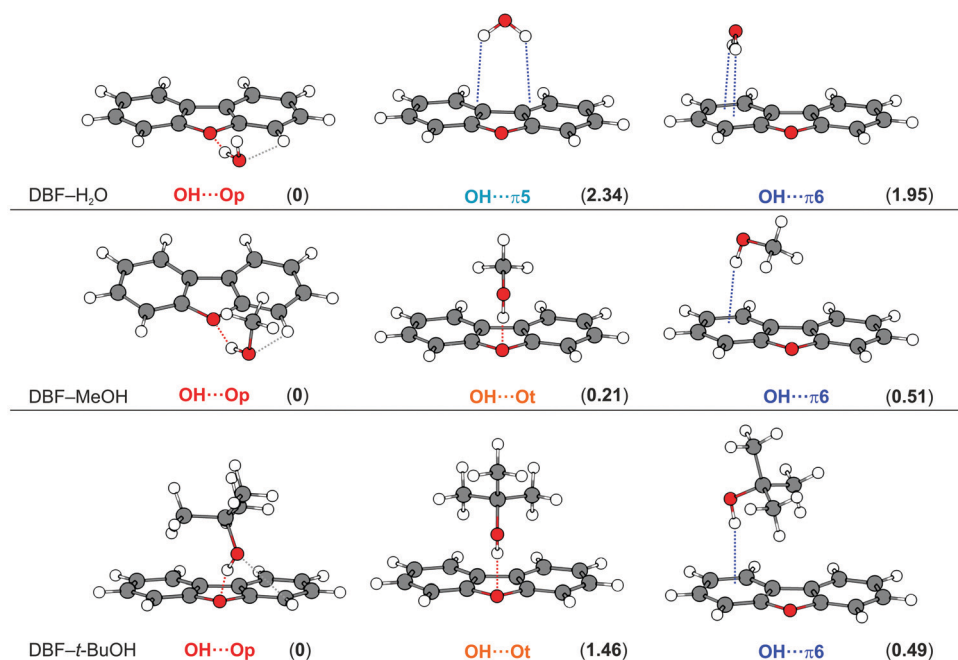


Fig. 1 Optimized minimum structures at the B3LYP-D3(BJ)/def2-TZVP level for DBF–ROH complexes (R = H, Me, *t*-Bu). Values in parentheses represent relative, ZPE-corrected energies in kJ mol^{−1} obtained at the DLPNO-CCSD(T)/cc-pVQZ level with ZPE from B3LYP-D3(BJ)/aug-cc-pVTZ calculations (see Table 1). Dashed lines qualitatively indicate different intermolecular contacts.



Table 1 Relative energies for DBF–ROH complexes with (ΔE_0) and without ZPE correction (ΔE) obtained at different levels of theory. All values are given in kJ mol^{-1} and include BSSE correction

Isomer	B3LYP-D3(BJ)/def2-TZVP		B3LYP-D3(BJ)/aug-cc-pVTZ		SCS-CC2/def2-TZVP		DLPNO-CCSD(T)/cc-pVQZ ^a	
	ΔE	ΔE_0	ΔE	ΔE_0	ΔE	ΔE_0	ΔE	ΔE_0^b
H ₂ O	OH···Op	0	0	0	0	1.58	0	0
	OH···π ₅	2.42	1.18	2.92	1.88	0.58	0	3.38
	OH···π ₆	3.79	1.47	3.87	2.02	—	—	3.80
MeOH	OH···Op	0	0.57	0.39	1.06	1.62	3.63	0
	OH···Ot	1.33	0.96	0	0.05	0.88	1.88	0.85
	OH···π ₆	1.22	0	0.03	0	0	0	1.21
<i>t</i> -BuOH	OH···Op	1.66	1.57	0	0.21	0.60	1.38	0
	OH···Ot	0	0	0.16	0.84	0.64	0.85	0.98
	OH···π ₆	2.35	1.29	0.78	0	0	0	1.48

^a Geometries were used from B3LYP-D3(BJ)/aug-cc-pVTZ calculations. ^b Harmonic ZPE correction obtained from B3LYP-D3(BJ)/aug-cc-pVTZ calculations.

involving the five-membered furan ring. This might allow for the conclusion that within the extended π system of DBF, the six-membered benzene rings are better hydrogen bond acceptors than the furan moiety. As discussed in previous works on 2-methylfuran, 2,5-dimethylfuran, and 2,3-benzofuran,^{15–17} the furan oxygen acceptor site loses attractiveness upon the introduction of methyl groups or one phenyl moiety.

Analyzing the different energy contributions shows that the largest dispersion contribution is in the OH···π₆ isomer, followed by the symmetric OH···Ot structure (see Tables S1 and S2, ESI[†]). Both arrangements contain CH···π stabilization. Accordingly, the dispersion contribution is significantly lower in OH···Op, and the structure is clearly dominated by the electrostatic contribution. The large difference in E_{elst} between the two OH···O structures might be explained by the almost coplanar arrangement of the hydrogen bond and the DBF plane in OH···Op in contrast to the clearly bent arrangement in OH···Ot.

In the latter case, this arrangement obviously reduces the electrostatic stabilization, while it simultaneously increases dispersion stabilization from CH···π interactions. Note that the OH···O hydrogen bonding angle itself is nearly identical in both structures (155°, Table S3, ESI[†]), indicating a clearly weakened hydrogen bond as it largely deviates from an ideal linear hydrogen bond. This significantly affects the OH stretching frequencies, which will be discussed in the Experimental results section.

The optimized minimum structures for the *t*-BuOH complex are shown in the last row of Fig. 1. Similar to the methanol complex, two OH···O structures and one OH···π arrangement are found as minimum geometries. The OH···Ot isomer is C_s -symmetric, identical to the OH···Ot isomer of the corresponding MeOH complex. The *t*-Bu moiety is positioned on top of the furan ring leading to CH···π interactions with the π -cloud. In contrast to the analogous MeOH complex, the hydrogen bond is less bent (177° for *t*-BuOH vs. 155° for MeOH, B3LYP-D3(BJ)/def2-TZVP level, see Table S3, ESI[†]).

In the OH···Op isomer, the *t*-BuOH moiety is tilted to one side, which indicates a slight CH···O interaction between the

alcohol oxygen atom and a neighboring CH group, resembling a somehow distorted version of the OH···Op isomer of DBF–MeOH with the alcohol being located rather above the π plane due to stronger CH···π interactions. Comparing all non- C_s -symmetric OH···Op structures, the solvent molecule increasingly approaches the π -cloud above the DBF plane going from water to *t*-BuOH. In the respective OH···π₆-bound isomer, the *t*-Bu moiety is in closer proximity to the DBF π -cloud, resulting in a larger interaction surface for CH···π interactions compared to the OH···Op isomer. However, CH···π interactions should be of similar magnitude in the OH···π and the C_s -symmetric OH···Ot isomer. This is in line with dispersion contributions obtained at the SAPT(0)/jun-cc-pVDZ and the DLPNO-CCSD(T)/cc-pVQZ levels, which are similar for the two isomers, but clearly smaller for the OH···Op isomer. As a hydrogen bond interaction is indicated by the OH stretching red-shift, calculated OH stretching frequencies can be compared for the competing structures. Calculations at the B3LYP-D3 level suggest a stronger OH···O hydrogen bond compared to OH···π. However, the contrary is predicted at the M06-2X/def2-TZVP and SCS-CC2 levels, indicating a stronger OH···π acceptor compared to OH···Ot. This aspect will be discussed later in the Experimental results section.

The calculated relative energies for all DBF–ROH complexes at different levels of theory are found in Table 1. The values for the B3LYP-D3(BJ) and SCS-CC2 levels result from geometry optimizations and harmonic frequency calculations, whereas single point calculations were performed at the DLPNO-CCSD(T)/cc-pVQZ level using the geometries obtained at the B3LYP-D3(BJ)/aug-cc-pVTZ level. No anharmonic treatments of the ZPE were used, as anharmonic corrections are expected to be small (assumed to be on the order of $<0.5 \text{ kJ mol}^{-1}$), and they have furthermore proven to perform non-systematically in relative energy predictions for similar systems.¹⁷ As shown in previous studies¹⁵ the structures with a rather localized OH···O hydrogen bond contain more ZPE than OH···π-bound structures. This is reflected in a consistent OH···Op destabilization on the order of 0.7–2.3 kJ mol^{-1} with respect to OH···π isomers when electronic (ΔE) and ZPE-corrected energies (ΔE_0) are compared.



For the water complex, the prediction of the energetic order is almost uniform: the OH \cdots Op structure is preferred by 0.6 up to 3.4 kJ mol $^{-1}$, depending on the theoretical level and basis set. The highest applied level suggests the oxygen site to be preferred by about 2 kJ mol $^{-1}$, which might raise questions about the population of a π -bound structure in molecular beam experiments unless major isomerization barriers prevent relaxation. The SCS-CC2 and M06-2X/def2-TZVP calculations (see Table S4, ESI †) prefer the OH \cdots π 5 structure. Regarding the DBF–MeOH complex, a rather undecided situation is found with an oscillation of the energetic order between an OH \cdots π 6, OH \cdots Op and even OH \cdots Ot preference. The ZPE destabilization of the oxygen-bound structures compared to the OH \cdots π 6 structure is even more relevant than in the case of water, since it switches the energetic order from a preferred OH \cdots O isomer for pure electronic energies towards OH \cdots π 6 upon ZPE correction for B3LYP-D3(BJ)/def2-TZVP calculations. The most sophisticated theoretical approach at the DLPNO-CCSD(T)/cc-pVQZ level suggests an advantage for OH \cdots Op of about 0.5 kJ mol $^{-1}$ over OH \cdots π 6 and 0.2 kJ mol $^{-1}$ over OH \cdots Ot, whereas the B3LYP-D3(BJ)/aug-cc-pVTZ calculations even predict the OH \cdots Ot and OH \cdots π 6 isomer to be isoenergetic (within 0.05 kJ mol $^{-1}$) upon ZPE correction (see Table 1). Considering the energetic range of 0.5 kJ mol $^{-1}$ for all three binding motifs obtained at the DLPNO-CCSD(T)/cc-pVQZ level – being certainly within the error bar of the method – would not exclude the presence of more than one isomer in molecular beam experiments. In the case of DBF-*t*-BuOH, the predicted binding preference is undecided as well among the different applied computational approaches: the symmetric OH \cdots Ot isomer is preferred at the B3LYP-D3(BJ)/def2-TZVP level, whereas the larger aug-cc-pVTZ basis leads to an OH \cdots π 6 preference, together with the SCS-CC2 approach. Finally, the DLPNO-CCSD(T) approach favors the OH \cdots Op structure by 0.5 kJ mol $^{-1}$ over OH \cdots π 6. Overall, the relative ZPE-corrected energies of all three binding motifs are predicted to be within a range of 1.6 kJ mol $^{-1}$. Thus, the simultaneous presence of more than one isomer cannot be excluded within supersonic jet experiments.

In order to elucidate the aspect of possibly co-existing isomers, being relevant for all investigated DBF–ROH complexes, the analysis of interconversion barriers can be helpful, aside from considering only the relative energies of the isomers. Therefore, transition state calculations were performed with the QST3 method as well as the woelfling module based on transition state guesses from the GFN-xTB method. The obtained interconversion barriers and transition state structures are shown in Fig. S1 (ESI †). In the case of the water complex, the calculated barrier of less than 1 kJ mol $^{-1}$ between the two π -bound isomers OH \cdots π 5 and OH \cdots π 6 suggests that interconversion occurs under the supersonic expansion conditions. However, barriers of about 5 kJ mol $^{-1}$ between the π -bound structures and the OH \cdots Op isomer might allow a kinetic trapping of oxygen- and π -bound isomers, respectively, in the case where they are both initially populated.

For the MeOH complex, a low barrier of about 1 kJ mol $^{-1}$ is predicted between the two oxygen-bound isomers OH \cdots Ot and

OH \cdots Op, suggesting that interconversion occurs under the experimental conditions. Similar to the water complex, the isomerization barriers between OH \cdots O and OH \cdots π binding motifs are larger than the ones between the same binding motifs, yet they are slightly lower than that for DBF–H $_2$ O at about 3 kJ mol $^{-1}$. Nevertheless, kinetic trapping of the respective lower energy isomer can be expected, in the case where more than one isomer is initially populated. Furthermore, the TS calculations suggest that the interconversion of the OH \cdots Op structure into the OH \cdots π 6 isomer involves the C $_s$ -symmetric OH \cdots Ot structure as an intermediate state.

Regarding the *tert*-butyl alcohol complex, the barrier between the oxygen-bound isomers OH \cdots Ot and OH \cdots Op is calculated to be <1 kJ mol $^{-1}$, suggesting interconversion. Similar to the case of DBF–MeOH, the TS calculations suggest that conversion of the OH \cdots Op structure into the OH \cdots π 6 isomer occurs *via* the intermediate OH \cdots Ot arrangement. The predicted isomerization barrier from the OH \cdots Ot to the OH \cdots π 6 isomer is approximately 2 kJ mol $^{-1}$. Hence, interconversion between the binding motifs should not be excluded as well. A discussion of these aspects with respect to the experimental findings will be continued in the Experimental results section.

For a comparison of theory and experiment, the structurally sensitive OH stretching vibration can serve as a spectroscopic probe to be compared to calculated harmonic OH stretching wavenumbers. In some cases, particularly if two competing structures with the same binding motif are present, the OH stretching vibrations might be indistinguishable. Therefore, the experimental rotational constants obtained from rotational spectroscopy combined with calculated dipole moment components can lead to an unambiguous structural assignment. All calculated values relevant for comparison to the experiments are found in Tables S5, S6 and S9–S11 (ESI †) and are discussed in the Experimental results section. In the end, comparison to the experiments will reveal the individual performance of each theoretical approach.

4.2 Experimental results

4.2.1 DBF–H $_2$ O

IR/UV results. For all investigated systems, R2PI spectra were recorded, revealing isomer-specific electronic excitation energies of the respective complexes (see Fig. S2, ESI †). Based on these findings, IR/R2PI spectra were measured in the OH-stretching region (3520–3750 cm $^{-1}$) for different excitation energies of the respective complexes.

The R2PI spectrum of the DBF–H $_2$ O complex reveals a S $_1$ \leftarrow S $_0$ transition that is blue-shifted by +171 cm $^{-1}$ compared to the DBF monomer transition (see Fig. S2, ESI †). This is in agreement with the findings of fluorescence excitation spectra.²⁴ No additional, red-shifted transitions with respect to the monomer were detected. The experimentally observed shift of +171 cm $^{-1}$ is in qualitative agreement with the predicted blue-shift of +174 cm $^{-1}$ for the OH \cdots Op isomer at the SCS-CC2/def2-TZVP level with respect to the DBF monomer transition (see Table S5, ESI †). In contrast, the OH \cdots π 6 isomer



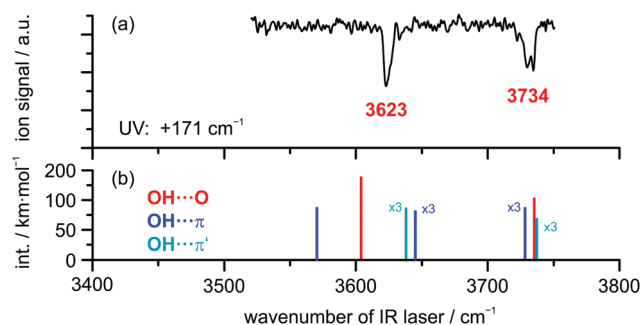


Fig. 2 (a) IR/R2PI spectrum of DBF-H₂O obtained via UV excitation at +171 cm⁻¹ compared to calculated OH stretching frequencies (b) at the B3LYP-D3(BJ)/def2-TZVP level; scaling factor: 0.9677.

is expected to have a red-shifted S₁ ← S₀ transition compared to the DBF monomer (−138 cm⁻¹; see Table S5, ESI†). Based on these findings, the assumption of an OH...O binding motif for the DBF-H₂O complex based on the early non-mass-selective study by Auty *et al.*²⁴ is confirmed by our mass-selective R2PI experiments combined with predicted S₁ ← S₀ excitation energies at the SCS-CC2/def2-TZVP level. These calculations have proven to yield robust predictions.⁵⁷

In order to obtain additional structural information, the OH stretching vibration is used as a spectroscopic probe for identifying the docking motif of the complex. Therefore, an IR/R2PI spectrum was recorded via the electronic resonance at +171 cm⁻¹, which is shown in Fig. 2 for the mass trace of the DBF-H₂O complex compared to calculated harmonic OH stretching frequencies at the B3LYP-D3(BJ)/def2-TZVP level (additional computational results are found in Table S6, ESI†). The IR/R2PI spectrum obtained for the DBF-H₂O complex (Fig. 2(a)) exhibits two OH stretching vibrations at 3623 and 3734 cm⁻¹ (confirming preliminary observations in ref. 81). Calculations uniformly predict a red-shifted symmetric $\tilde{\nu}_{\text{OH}}$ of the oxygen-bound structure compared to the π -bound structures. Mainly the symmetric $\tilde{\nu}_{\text{OH}}$ is sensitive to the docking site, whereas the asymmetric $\tilde{\nu}_{\text{OH}}$ is less affected. It is noticeable that the relative shifts of the symmetric $\tilde{\nu}_{\text{OH}}$ between OH...O and OH... π structures are quite large for the B3LYP-D3(BJ) calculations in contrast to the ones for the M06-2X functional as well as the SCS-CC2 predictions. Upon comparison of symmetric $\tilde{\nu}_{\text{OH}}$ frequencies to the experiment, the OH...O isomer matches better than the OH... π isomers for all applied theoretical approaches. In order to find a robust assignment, an additional aspect to be considered is the splitting between symmetric and asymmetric $\tilde{\nu}_{\text{OH}}$, which is significantly different for the OH...O and OH... π motifs (see Table S6, ESI†). The experimental splitting is found to be 111 cm⁻¹, while the calculated splittings range from 105–131 cm⁻¹ for the OH...Op isomer and only from 83 to 87 cm⁻¹ for OH... π structures. Moreover, the changes of the splitting with respect to the splitting of free water clearly suggest the OH...Op isomer to be the observed structure. Note that the splittings obtained from the SCS-CC2 calculations are not considered here, as they are found to be unable to reproduce the frequency splitting of the free water molecule correctly.

Table 2 Molecular rotational parameters of DBF-H₂O: the experimental parameters are based on a fit to an asymmetric rotor Hamiltonian using the JB95 program in comparison to calculated results

Parameters ^a	Experiment	B3LYP-D3(BJ)/ def2-TZVP	B3LYP-D3(BJ)/ def2-TZVP
	OH...Op	OH...Op	OH... π 5
A (MHz)	974.08	973	1339
B (MHz)	575.23	581	479
C (MHz)	362.00	365	447
Δ_J (kHz)	0.0334		
σ (kHz)	40		
N_{lines}^b (a/b/c)	65(44/21/0)		
$\mu_a/\mu_b/\mu_c$ (D)		1.3/2.2/1.3	1.1/0.2/2.3

^a A, B, and C are the experimental rotational constants, Δ_J is the centrifugal distortion constant, and σ is the standard deviation of the fit. ^b Total number of fitted lines and as distributed over a-, b-, and c-type transitions.

CP-FTMW results. Rotationally resolved spectroscopy can provide unambiguous proof of the observed clusters (a) via comparison of the experimental rotational constants with the results of quantum chemical calculations and (b) via structure determination using isotopic substitution, either in natural abundance or using enriched samples. The experimental rotational constants for DBF-H₂O obtained from broadband CP-FTMW spectroscopy are summarized in Table 2 together with the results from quantum-chemical calculations. The comparison clearly identifies the observed complex as the OH...Op structure, in agreement with the (IR)/R2PI studies, with the rotational constants of the OH... π 5 isomer being clearly different. Other complexes were not observed under the experimental conditions using neon as a carrier gas. Note that we report an average fit, *i.e.*, fitting the center frequencies of a doublet splitting arising from the internal motion of the water molecule with respect to the DBF moiety. A more detailed analysis of this internal motion is beyond the scope of the present study and will be reported elsewhere. The spectrum is dominated by a- and b-type transitions, while no c-type transitions were observed, which points to averaging due to the internal motion.

4.2.2 DBF-MeOH. In contrast to the clear-cut case of DBF-H₂O, where the different experimental and most theoretical methods match nicely in finding a single dominant isomer, a more difficult case is found for DBF-MeOH where the theoretical methods are rather undecided between up to three different structures. Therefore, we include an FTIR study, to provide an overview of the cluster distribution under warmer expansion conditions.

FTIR results. FTIR spectra of the co-expanded DBF-MeOH mixture using the double-slit nozzle are shown in Fig. 3(b). The methanol concentration of 0.15% is chosen such that almost no monomer (3686 cm⁻¹) or homodimer (3575 cm⁻¹) are visible. A distinct band at 3594 cm⁻¹ is observed, but the red-shift upon complexation seems too large to be associated with a heterodimer. Indeed, when comparing to the previously measured spectrum of 2,3-benzofuran-MeOH¹⁵ (Fig. 3(a)) this



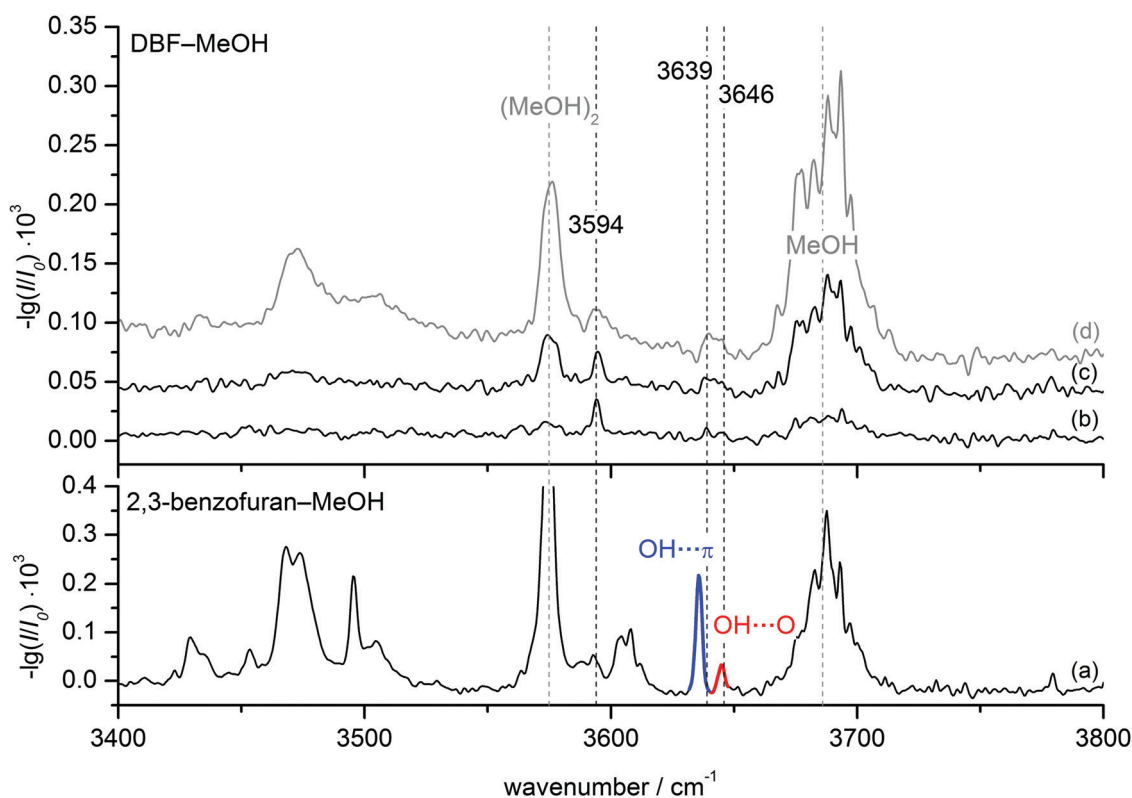


Fig. 3 FTIR spectra of DBF-MeOH (b–d) in comparison to 2,3-benzofuran-MeOH (a) taken from ref. 15. Spectrum (b) was measured using the double-slit nozzle (0.15% MeOH, $T(\text{DBF}) = 120\text{ }^\circ\text{C}$), spectra (c) and (d) using the V-nozzle introducing MeOH via the saturator at temperatures of $T(\text{MeOH}) = -25\text{ }^\circ\text{C}$ ($\approx 0.3\%$) and $T(\text{MeOH}) = -10\text{ }^\circ\text{C}$ ($\approx 1\%$), respectively. The DBF concentration is slightly decreased in these spectra ($T(\text{DBF}) = 110\text{ }^\circ\text{C}$).

band lies within the region of larger clusters. Taking the strong cohesion and excess of DBF into account, a trimer including one methanol and two DBF molecules is the most probable assignment. Further discussion on this trimer can be found in the ESI.† Searching for spectral features in proximity to the dimer bands of 2,3-benzofuran-MeOH, two peaks might be located at 3639 and 3646 cm^{-1} , hardly distinguishable from the noise level. In an attempt to alter the expansion conditions to form more mixed dimers, spectrum (c) was recorded. The methanol concentration was increased about two-fold, while the DBF concentration was slightly decreased. However, the major changes were the use of a newly developed V-nozzle, which nominally enhances the absorption path by a factor of about 6, and a simultaneous lowering of the differential opening pressure of the second check valve to 350 mbar. A small and broad spectral feature was observed between 3636 and 3650 cm^{-1} , which supports a dimer origin of the weak bands at 3639 and 3646 cm^{-1} . A further increase of the methanol concentration (spectrum (d) in Fig. 3) did not seem to enhance the dimer abundance any further. Given the weakness and broadness of these bands, only a vague assignment to a specific isomer could be made, but on comparing the dimer band positions of 2,3-benzofuran-MeOH, it is plausible that two dimers are observed due to an $\text{OH}\cdots\pi$ isomer further red-shifted than an $\text{OH}\cdots\text{O}$ isomer. The peak intensity of the further red-shifted isomer is at best two-fold higher, but given the lower

predicted IR intensity of $\text{OH}\cdots\pi$ isomers, the actual excess in abundance may be larger, even in the weakly relaxing helium expansion employed. This tentative assignment called for confirmation by complementary spectroscopic methods.

IR/UV results. IR/UV spectroscopy provides additional mass- and isomer-selective insight in addition to the results obtained from the FTIR investigations. The IR/UV experiments on the DBF-MeOH complex revealed the presence of two different isomers with distinct electronic resonances at $+135\text{ cm}^{-1}$ and -24 cm^{-1} with respect to the DBF monomer transition observed in the R2PI spectrum (see Fig. S2, ESI†; further transitions yield the same IR/R2PI spectra, thus no third isomer is found). The electronic excitation spectrum itself contains valuable information: a comparison to calculated $S_1 \leftarrow S_0$ excitation energies at the SCS-CC2/def2-TZVP level suggests that the blue-shifted transition arises from the $\text{OH}\cdots\text{O}$ isomer with a qualitatively matching predicted shift of $+126\text{ cm}^{-1}$. The slightly red-shifted transition observed at -24 cm^{-1} is in qualitative agreement with the predicted shift for the $\text{OH}\cdots\pi$ isomer (-245 cm^{-1}). The recorded IR/R2PI spectra via the electronic resonances at $+135\text{ cm}^{-1}$ and -24 cm^{-1} are depicted in Fig. 4. The spectrum shown in the upper trace (a) exhibits one OH stretching vibration at 3642 cm^{-1} . The spectrum for the second isomer in trace (b) reveals a slightly red-shifted transition at 3637 cm^{-1} .



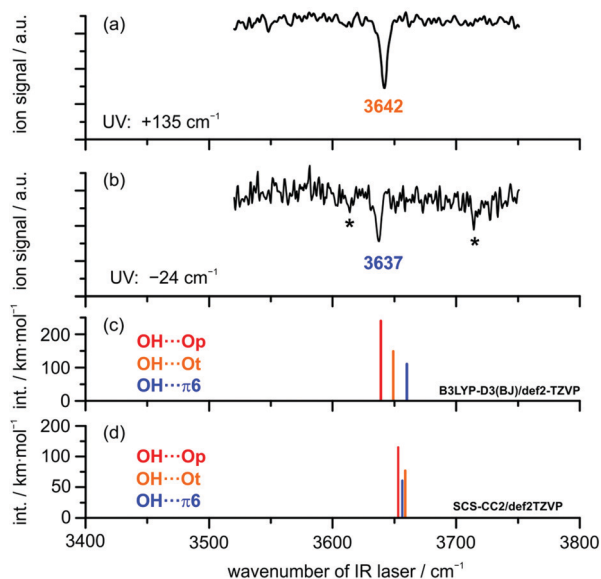


Fig. 4 IR/R2PI spectra of DBF–MeOH via UV excitations (a) of $+135\text{ cm}^{-1}$ and (b) -24 cm^{-1} compared to calculated OH stretching frequencies for OH...O and OH... π isomers (c) at the B3LYP-D3(BJ)/def2-TZVP level and (d) at the SCS-CC2/def2-TZVP level; scaling factors: (c) 0.9674 and (d) 0.9684 derived from reference calculations for MeOH, respectively. Transitions marked with an asterisk result from fragmentation of larger clusters.

The two additional features marked with an asterisk (*) originate from ionization-induced fragmentation of a mixed DBF–MeOH–H₂O cluster (see Fig. S3, ESI†). Given the overlap situation in the FTIR experiment and its relatively high nozzle temperature, as well as the different carrier gas, the wavenumber agreement between the two IR experiments is satisfactory. The observed isomer splitting of 5 cm^{-1} is probably more reliable than the 7 cm^{-1} deduced from the FTIR spectrum.

The relative order of calculated OH stretching wavenumbers for the different OH...O and OH... π structures turns out to be ambiguous: DFT calculations using the B3LYP-D3(BJ) functional predict a red-shifted OH stretch for both OH...O-bound structures compared to the OH... π 6 isomer. Interestingly, calculations at the SCS-CC2 level suggest a switch of the order: the OH... π 6 structure is predicted to have a lower OH stretching frequency than the OH...O equivalent, which suggests the π -cloud to be the stronger acceptor site. The same is observed for calculations with the functional M06-2X (see Table S6, ESI†). Note, however, that these two methods failed in predicting the correct complex with water.

Given the very small OH stretching frequency differences between the observed species, the prediction of the frequency order for a distinct theoretical method is ambiguous. Finally, based on the clear isomer assignment *via* the electronic resonances, the OH...Ot isomer is found to exhibit the less red-shifted OH stretching vibration compared to the OH... π 6 isomer. This has been observed for similar systems as well (*cf.* discussion in the ESI† and ref. 15 and 16).

Drawing conclusions on relative populations from the electronic resonances in the R2PI spectrum is difficult in this specific case, as the R2PI spectrum of the DBF–MeOH mass

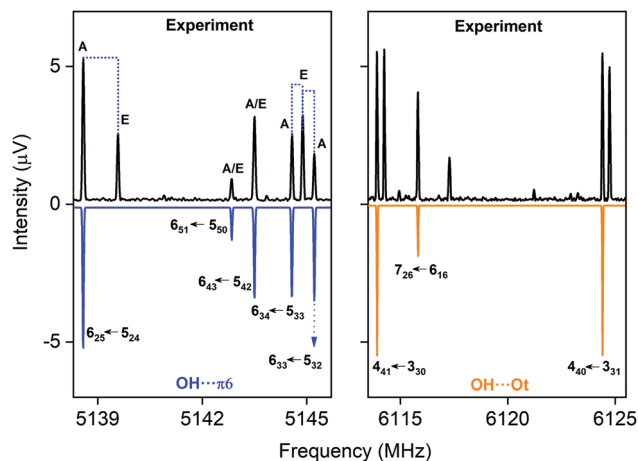


Fig. 5 Parts of the CP-FTMW broadband rotational spectrum, indicating the coexistence of the OH... π 6 and the OH...Ot isomer.

trace is influenced by very strong resonances of the DBF monomer (for further explanation see Fig. S2, ESI†). Additional structural and abundance insight will be gained by rotational spectroscopy.

CP-FTMW results. In the rotational spectrum of the DBF–MeOH mixture, we observed two DBF–MeOH complexes (see Fig. 5). The experimentally obtained rotational parameters are summarized in Table 3. The rotational constants for the two complexes are clearly different, and the spectra also differ in

Table 3 Molecular parameters of DBF–MeOH: experimental values are based on a fit to an asymmetric rotor Hamiltonian using the AABS software and the XIAM program, respectively. For OH... π 6, two sets of rotational constants are presented, with and without including the internal rotation of the methyl group (see text)

Parameters ^a	OH... π 6		OH...Ot
	Fit 1 A-states	Fit 2 XIAM	Fit 1 A-states
A (MHz)	987.3953(36)	987.3736(27)	808.91099(33)
B (MHz)	439.33213(28)	439.32995(25)	524.58247(15)
C (MHz)	417.58829(26)	417.58775(21)	375.30332(18)
A_J (kHz)	0.0529(17)	0.0554(13)	0.1434(15)
A_{JK} (kHz)	0.738(10)	0.7388(82)	1.934(71)
A_K (kHz)	56.91(80)	56.85(75)	−0.848(60)
δ_J (kHz)	—	—	1.2416(45)
F_0 (cm ^{−1})	—	159.0	—
V_3^b (cm ^{−1})	—	338.99(89)	—
V_3^b (kJ mol ^{−1})	—	4.055(11)	—
D_{pi2J} (kHz)	—	34.7(2.9)	—
Δ (rad)	—	3.883(13)	—
ϵ (rad)	—	0.579(23)	—
# A state transitions ^c	65 (49/16/0)	65 (49/16/0)	122 (0/94/28)
# E state transitions	—	41 (29/12/0)	—
σ (kHz)	6.9	7.1	7.0

^a A, B, and C are the rotational constants, A_J , A_{JK} , A_K , δ_J and δ_K are the centrifugal distortion constants, and σ is the standard deviation of the fit. ^b V_3 is the barrier to internal rotation of the methanol methyl top, F_0 is the corresponding rotational constant of the methyl top, and D_{pi2J} accounts for the internal motion-overall rotation centrifugal distortion, obtained from a global fit of both internal rotational components A and E with the program XIAM. ^c Total number of fitted lines and as distributed over a-, b-, and c-type transitions.



Table 4 Theoretical rotational constants for DBF–MeOH obtained at the B3LYP-D3(BJ)/def2-TZVP level of theory

	OH··Op	OH··Ot	OH··π6
A (MHz)	737.4	831.9	1000.3
B (MHz)	515.2	523.1	437.5
C (MHz)	316.9	381.5	418.6
V_3 (kJ mol ⁻¹)	3.8	3.1	5.1
$\mu_a/\mu_b/\mu_c$ (D)	1.9/1.6/1.3	0.01/3.1/0.5	1.1/1.2/0.2

the type of rotational transitions observed (*i.e.*, only a- and b-type transitions but no c-type transitions for one complex and only b- and c-type transitions but no a-type transitions for the other complex). Such observations provide additional input for assigning the structures. Based on a comparison of the rotational constants and the observed type of transition *vs.* calculated dipole-moment components (see Table 4), the two structures can be unambiguously assigned to the OH··π6 and the OH··Ot complexes. Thus, the results also allow us to differentiate between the two OH··O bound isomers, OH··Ot and OH··Op.

Both complexes show internal rotation splitting due to the internal rotation of the methyl group of the methanol moiety, which results in characteristic doublets for each rotational line. The fact that this internal rotation leads to sizeable splittings and is not locked points to only a loose interaction of the methyl group with DBF. For OH··π6, two sets of rotational constants are presented. Fit 1 corresponds to a fit to an asymmetric rotor Hamiltonian including only the A states due to methyl group internal rotation, thus presenting effective rotational constants. Using the program XIAM, these line splittings can be analyzed, resulting in Fit 2. It includes the analysis of the methyl group internal rotation and thus also provides information about the torsional barrier V_3 . The V_3 barrier determined from the experimental line splitting into A and E states is $V_3(\text{exp}) = 4.055(11)$ kJ mol⁻¹ (Table 3), which is in decent agreement with the calculated barrier of about 5 kJ mol⁻¹ (B3LYP-D3(BJ)/def2-TZVP). For OH··Ot, only an A-state fit is presented. An initial global fit including internal rotation *via* about 20 E-state lines resulted in standard deviations on the order of 100 kHz, potentially pointing to a second internal motion. The obtained rotational parameters of the A-state fit, however, allow a clear identification of the respective isomers.

The wealth of experimental information is thus well suited to identify and further characterize the respective molecules under study and can also be used to benchmark the theoretical models employed. Based on our experimental line intensities, the OH··π6 complex is found to be about 10 times stronger than the one for the OH··Ot complex. Considering the stronger dipole moment for the OH··Ot complex, this points to a clear energetic preference for the OH··π6 complex, which is also the global minimum at the B3LYP-D3(BJ)/def2-TZVP, B3LYP-D3(BJ)/aug-cc-pVTZ and the SCS-CC2/def2-TZVP levels. In the case of the B3LYP-D3(BJ)/aug-cc-pVTZ level, OH··π6 is nearly isoenergetic with the OH··Ot isomer. This finding agrees qualitatively with the FTIR evidence of a higher abundance of the more red-shifted

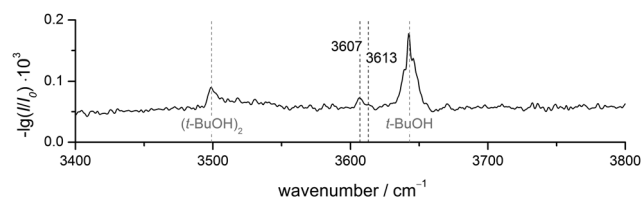


Fig. 6 FTIR spectrum of DBF–*t*-BuOH. The V-nozzle was used and the temperatures set to $T(\text{DBF}) = 110$ °C and $T(t\text{-BuOH}) = 10$ °C.

species and the corresponding results for 2,3-benzofuran.¹⁵ It also agrees with the IR/UV experiment, considering the mentioned intensity uncertainty within the R2PI spectra. Interestingly, the third complex, OH··Op, was not observed in our microwave study despite intense analysis, even though it is predicted to be the global minimum by the DLPNO-CCSD(T) approach (*cf.* Table 1). Thus, a low interconversion barrier from the OH··Op complex to one or both of the other complexes, OH··Ot and OH··π6, can be assumed.

4.2.3 DBF–*t*-BuOH

FTIR results. The FTIR spectrum of DBF–*t*-BuOH (see Fig. 6), measured in helium carrier gas with the V-nozzle, shows similar features as DBF–MeOH. The monomer and homodimer bands of *tert*-butyl alcohol are observed at 3643 cm⁻¹ and 3499 cm⁻¹, respectively. These values are slightly blue-shifted to those reported previously,⁸² which hints at warmer expansion conditions, probably due to the heated nozzle. Fortunately, the proposedly mixed dimer signals are more pronounced than for methanol, revealing one band at 3607 cm⁻¹ with a weak shoulder at 3613 cm⁻¹. Given the similarity of the experimental data, an analogous assignment to the DBF–MeOH clusters is suggestive. Therefore, the band at 3607 cm⁻¹ and the shoulder are tentatively assigned to an OH··π and an OH··O isomer, respectively. However, without complementary experimental evidence, only a single dominant complex absorbing at 3607 cm⁻¹ can be safely concluded.

IR/UV results. The IR/UV analysis of the DBF–*t*-BuOH complex yielded the presence of one single isomer in a conformationally colder neon expansion. Regarding the recorded R2PI spectrum (see Fig. S2, ESI[†]), containing pronounced vibrational progressions, the observed 0 ← 0 transition for DBF–*t*-BuOH is red-shifted by –39 cm⁻¹ compared to the DBF monomer. Considering the predicted $S_1 \leftarrow S_0$ transitions, only the OH··π6 isomer is found to exhibit a lower $S_1 \leftarrow S_0$ transition than the DBF monomer (–263 cm⁻¹), whereas for the OH··O-bound structures blue-shifted excitation energies are predicted (see Table S5, ESI[†]). Therefore, an assignment of the OH··π6 isomer can already be made based on the shift of the electronic origin. Fig. 7 shows the IR/R2PI spectrum obtained *via* the electronic transition at –39 cm⁻¹ with respect to the DBF monomer transition. It exhibits a single OH stretching vibration at 3605 cm⁻¹. The spectra obtained *via* all further transitions observed in the R2PI spectrum (see Fig. S2, ESI[†]) exhibit the same vibrational transition. Therefore, the presence of a second isomer is unlikely (see also the IR_{fixed}/R2PI spectrum in Fig. S5, ESI[†]).



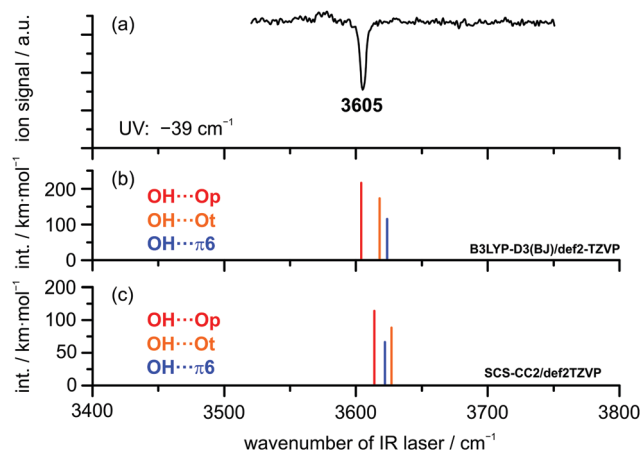


Fig. 7 (a) IR/R2PI spectrum of (a) DBF-*t*-BuOH via UV excitation at -39 cm^{-1} compared to calculated OH stretching vibrations (b) at the B3LYP-D3(BJ)/def2-TZVP level (scaling factor 0.9618) and (c) at the SCS-CC2/def2-TZVP level (scaling factor: 0.9686).

Based on the aforementioned comparison to calculated electronic excitation energies, the presence of OH \cdots O-bound structures would therefore be ruled out. Comparing the recorded IR/R2PI spectrum to the calculated OH stretching frequencies for the different optimized structures does not allow for an unambiguous assignment to one of the isomers. Calculations with the B3LYP-D3(BJ) functional yield a larger OH stretching red-shift for the oxygen-bound structures compared to the OH \cdots π isomer (see Fig. 7b and Table S6, ESI †). In contrast, M06-2X/def2-TZVP and SCS-CC2 calculations suggest a stronger red-shift for the OH \cdots π 6 structure compared to OH \cdots Ot and therefore an inverse frequency order compared to B3LYP-D3(BJ) predictions – analogous to the case of DBF-MeOH. According to the B3LYP-D3(BJ) calculations, the OH \cdots Op isomer yields the best agreement with the experimentally observed transition. On the other hand, M06-2X/def2-TZVP and SCS-CC2 predictions yield the best match for the OH \cdots π 6 isomer. Based on the similar findings for DBF-MeOH, an assignment of the OH \cdots π 6 isomer seems more reasonable, which is however very tentative, since no second isomer is present for comparison of OH stretching vibrations. Additional insight regarding the structural assignment is provided by rotational spectroscopy.

As pointed out in the theoretical results section, the isomerization barrier between the OH \cdots Op and the OH \cdots π structure of the DBF-*t*-BuOH complex is calculated to be about 2 kJ mol^{-1} , whereas the barrier between OH \cdots Ot and OH \cdots Op is smaller than 1 kJ mol^{-1} . Since only one isomer is found in the experiment with neon as the carrier gas, it might be concluded that the isomerization barriers are too low for both binding motifs to be stabilized during the supersonic expansion. This would lead to the exclusive population of the global minimum structure in the molecular beam. Comparing the IR/UV and FTIR investigations (see Fig. 6 and 7), the shoulder at 3613 cm^{-1} exclusively observed in the FTIR spectrum seems to originate either from a less stable DBF-*t*-BuOH isomer, populated due to different expansion conditions, or from a larger cluster.

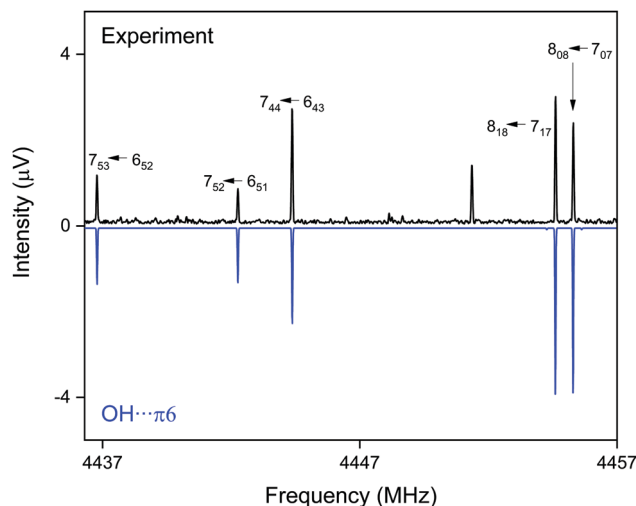


Fig. 8 Part of the CP-FTMW broadband rotational spectrum for DBF-*t*-BuOH, illustrating the presence of the OH \cdots π 6 isomer.

CP-FTMW results. The analysis of the broadband rotational spectra for the DBF-*t*-BuOH mixture also reveals the presence of only one strong spectrum, for which 162 rotational lines, distributed over a-, b-, and c-type transitions, could be identified and fitted to an asymmetric rotor Hamiltonian, with a-type transitions dominating the spectrum (see Fig. 8). The resulting molecular parameters are summarized in Table 5, together with the results from quantum chemical calculations. The widely different rotational constants for the three DBF-*t*-BuOH complexes allow their identification as the OH \cdots π 6 isomer, which is stabilized by secondary CH \cdots π interactions, in agreement with the IR/UV spectroscopic results. As in the *t*-BuOH monomer and in other complexes involving *t*-BuOH, no internal rotation splitting due to internal rotation of the three methyl groups is observed because of the high barrier hindering this motion. The OH \cdots π 6 structure is predicted to be the global

Table 5 Molecular parameters of DBF-*t*-BuOH: results of the fit of experimental rotational transitions to an asymmetric rotor Hamiltonian using the AABS software in comparison to the results from density-functional theory calculations (B3LYP-D3(BJ)/def2-TZVP)

Parameters ^a	Experiment	B3LYP-D3/ def2-TZVP	B3LYP-D3/ def2-TZVP	B3LYP-D3/ def2-TZVP
	OH \cdots π 6	OH \cdots π 6	OH \cdots Ot	OH \cdots Op
<i>A</i> (MHz)	513.73023(20)	515	453	473
<i>B</i> (MHz)	351.76117(15)	353	404	376
<i>C</i> (MHz)	269.56523(14)	269	263	246
Δ_J (kHz)	0.10324(73)			
Δ_{JK} (kHz)	-0.3604(29)			
Δ_K (kHz)	0.2601(43)			
δ_J (kHz)	0.03650(54)			
σ (kHz)	7.1			
N_{lines}^b (a/b/c)	162 (83/36/43)			
$\mu_a/\mu_b/\mu_c$ (D)		1.3/0.1/0.4	2.2/0/2.0	2.1/0.6/1.7

^a *A*, *B*, and *C* are the rotational constants, Δ_J , Δ_{JK} , Δ_K and δ_J are the centrifugal distortion constants, and σ is the standard deviation of the fit. ^b Total number of fitted lines and as distributed over a-, b-, and c-type transitions.



minimum by several quantum chemical methods (including ZPE correction, Table 1). Note the interesting basis set dependence for the dispersion corrected B3LYP-D3(BJ) approach: using the aug-cc-pVTZ basis set, the correct global minimum (after ZPE correction) is predicted, while usage of the def2-TZVP basis set leads to the OH \cdots Ot isomer as the energetic minimum structure. The fact that only one species is observed with CP-FTMW and IR/UV spectroscopy employing neon as a carrier gas, while FTIR spectroscopy using helium observes weak evidence for a second isomer gives an indication that the barrier between the OH \cdots Ot and OH \cdots π 6 structures, calculated to be 1.8 kJ mol $^{-1}$ (Fig. S1, ESI †), is indeed sufficiently low to be overcome in a neon expansion (Fig. 7 and 8).

5 Conclusions

A detailed multi-spectroscopic and theoretical analysis on a series of isolated dibenzofuran–alcohol and –water complexes is presented. By combining FTIR, IR/UV and CP-FTMW spectroscopy, the unambiguous assignment of the preferred structures for the respective complexes could be achieved. The most valuable contribution of the FTIR approach, for which DBF complexes are currently at the technological limit, is a survey over the minimum number of relevant complexes under warmer expansion conditions. The IR/UV approach is less limited in molecular size. It provides conformationally resolved IR spectra, and the UV shift from the monomer gives valuable information on the docking position, O vs. π , of the OH group. This is crucial because the spectral shifts between these two docking positions are extremely subtle such that theoretical harmonic predictions remain ambiguous. The CP-FTMW approach provides a firm structural assignment of dominant and also secondary complexes, which goes beyond the O vs. π

contact information. It discriminates between O docking geometries, which exploit secondary interactions with either peripheric C–H groups (p) or aromatic π clouds (t) in the planar acceptor molecule. The comparison to theory revealed deficiencies and strengths of different theoretical approaches.

For the DBF–H $_2$ O complex an oxygen bound structure was identified by electronic, vibrational and rotational spectroscopy, building on the early work of Auty *et al.*²⁴ Despite the prediction of nearly isoenergetic π -bound structures, no second isomer is found. The DLPNO-CCSD(T)/cc-pVQZ method as well as B3LYP-D3(BJ)/aug-cc-pVTZ calculations yield reasonable relative energies that explain the experimental observations. Regarding the methanol complex, two isomers were identified in the molecular beam experiments. The species were identified as the OH \cdots π 6 isomer and the OH \cdots Ot isomer. For the oxygen-bound structure, an interconversion of OH \cdots Op to OH \cdots Ot is expected due to a low isomerization barrier. Based on the broadband rotational spectroscopic results, the OH \cdots π 6 isomer is found to be more strongly populated than the OH \cdots Ot structure, which is confirmed by the FTIR results and is also reasonable within the uncertainty of the R2PI signal intensities. Nevertheless, within the error of the methods, the predicted relative energies at the DLPNO-CCSD(T)/cc-pVQZ and B3LYP-D3(BJ)/aug-cc-pVTZ level are in agreement with the experimental findings since both theoretical methods indicate two nearly isoenergetic structures. Furthermore, the chosen theoretical approaches largely deviate in predicting OH stretching wavenumbers, which even leads to a switch in the order between the OH stretches of the two docking motifs. This has also been observed for the related 2,5-dimethylfuran–methanol¹⁵ and 2,3-benzofuran–methanol complexes.^{15,16} The only approaches that correctly predict a red-shifted OH stretching vibration for the OH \cdots π 6 isomer compared to OH \cdots Ot are the M06-2X functional and calculations at the SCS-CC2 level. This probably indicates a

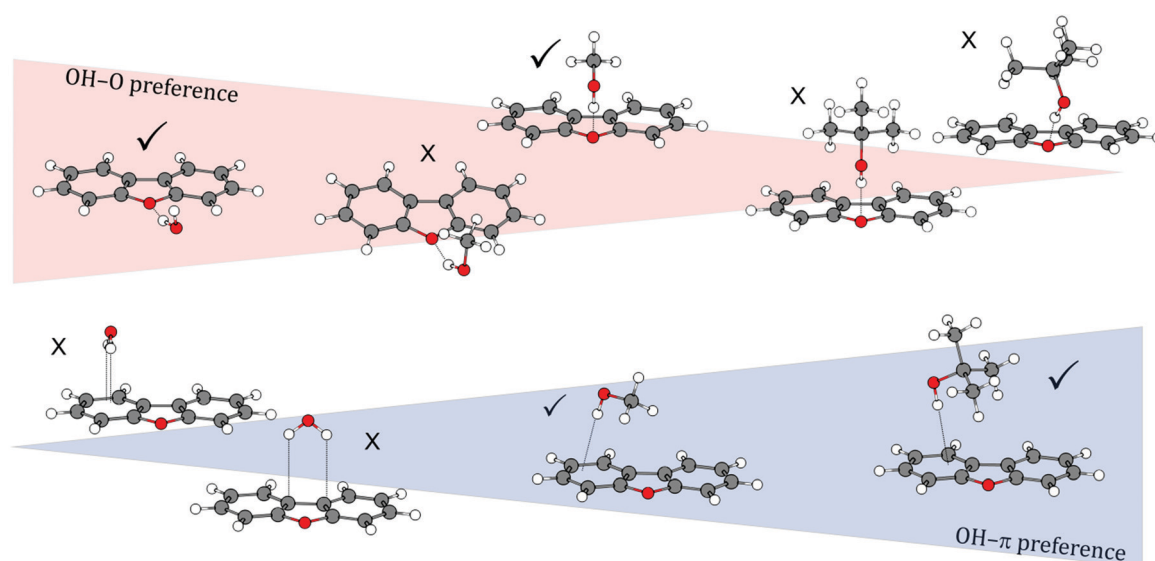


Fig. 9 Schematic overview of the transition of binding motif preferences from oxygen-bound to π -bound structures with increasingly larger solvent molecules in DBF–ROH complexes.



deficiency of the established theoretical approaches including the harmonic approximation, which should be considered in future developments.

The *tert*-butyl alcohol complex, representing the largest ether–solvent complex in this study, was shown to form only one stable isomer in the molecular beam experiments. Based on a red-shifted $S_1 \leftarrow S_0$ transition, a π -bound structure was identified. Rotational spectroscopy clearly confirmed the observed structure to be the $\text{OH} \cdots \pi_6$ isomer.

By comparing all investigated DBF–solvent complexes, we observe a binding preference that switches from oxygen *via* a balanced situation to the π site when going from small solvent molecules to larger ones (see Fig. 9). This is inverse to the trend that has been observed for the previously studied series of diphenyl ether–solvent complexes. The stabilization due to London dispersion is found to be more pronounced in π -bound structures than in oxygen motifs, indicated by dispersion contributions extracted from both SAPT(0) and DLPNO-CCSD(T) calculations. An exception is found for the *t*-BuOH complex, where the C_s -symmetric $\text{OH} \cdots \text{O}_t$ and the $\text{OH} \cdots \pi_6$ isomers are found to have similar dispersion contributions. We moreover found the influence of $\text{CH} \cdots \text{O}$ contacts on $\text{OH} \cdots \text{O}_p$ structures to decrease from the small solvent molecules to the larger ones, while simultaneously enabling stronger $\text{CH} \cdots \pi$ interactions in this series. However, their magnitude in the $\text{OH} \cdots \text{O}$ arrangements is always outweighed by the one in the respective $\text{OH} \cdots \pi$ structures. Thus, the additional $\text{CH} \cdots \text{O}$ contact leads to preferred oxygen-binding for the smaller solvent molecules, whereas for the larger *t*-BuOH, London dispersion finally outbalances the $\text{CH} \cdots \text{O}$ -stabilization, leading to preferred π -binding. Regarding relative energies, the overall performance of the B3LYP-D3(BJ)/aug-cc-pVTZ approach is satisfactory and it is, at a first glance surprisingly, even superior to the DLPNO-CCSD(T) approach that seems to slightly underestimate the stability of $\text{OH} \cdots \pi_6$ complexes compared to $\text{OH} \cdots \text{O}_p$. Given the fact that the relative energies are mostly below 1 kJ mol^{-1} and therefore in the order of ZPE corrections, this slight inconsistency might be attributed to the usually less relevant fact that the geometries are not optimized at the DLPNO-CCSD(T) level. Furthermore, neglected anharmonic contributions to the ZPE do not allow for a safe relative ranking of the two electronic structure methods at this subtle level.

Upon comparison to the series of diphenyl ether–solvent complexes³⁷ and also the phenyl vinyl ether–methanol complex,³⁸ the absence of backbone deformation in the DBF complexes proves to be true, as no structures were found involving a non-planar DBF structure, which is not surprising since aromaticity is preserved. The influence of $\text{CH} \cdots \text{O}$ contacts – playing a decisive role in DPE and PVE complexes – partly remains in the DBF–solvent structures as well. However, it is constrained to the oxygen-bound motifs, as the CH moieties of DBF available for $\text{CH} \cdots \text{O}$ contacts are within the DBF plane and therefore not in vicinity to the alcohol oxygen atoms within $\text{OH} \cdots \pi$ arrangements. This finally leads to a trend regarding the binding preference that is contrary to the series of DPE–solvent complexes. A further interesting aspect is that the central,

five-membered furan moiety in DBF is only a competitive π docking site for the water complex. In the MeOH and *t*-BuOH complexes, only structures involving the six-membered benzene moieties as π acceptors were observed.

One parameter, namely the rigidity of the aromatic chromophore (DBF *vs.* DPE), completely changes the preferred binding site within a series of solvent complexes. The big challenge is to quantify the low-temperature abundance by small energy differences between different structures. We succeeded by a comprehensive combination of different experimental and theoretical methods, which finally offers a clear structural assignment. Within the investigated series of DBF–solvent complexes, we found a variable interplay between non-covalent interactions among which London dispersion forces make an important difference in determining the final docking preference.

Conflicts of interest

There are no conflicts to declare.

Acknowledgements

The authors thank the Deutsche Forschungsgemeinschaft (DFG, Ge 961/9-2, project number 271505332; Schn 1280/4-2, project number 271359857; Su 121/5-2, project number 271107160) for financial support in the context of the priority program SPP 1807 (Control of London dispersion interactions in molecular chemistry). M. F. acknowledges support from the Hamburg International Max Planck Research School UFAST. This work is part of the PhD theses of D. B., M. F. and A. P.

References

- 1 J.-M. Lehn, *Angew. Chem., Int. Ed. Engl.*, 1988, **27**, 89–112.
- 2 K. Müller-Dethlefs and P. Hobza, *Chem. Rev.*, 2000, **100**, 143–168.
- 3 E. A. Meyer, R. K. Castellano and F. Diederich, *Angew. Chem., Int. Ed.*, 2003, **42**, 1210–1250.
- 4 J. Cerný and P. Hobza, *Phys. Chem. Chem. Phys.*, 2007, **9**, 5291–5303.
- 5 S. Rösel, C. Balestrieri and P. R. Schreiner, *Chem. Sci.*, 2017, **8**, 405–410.
- 6 S. Grimme and P. R. Schreiner, *Angew. Chem., Int. Ed.*, 2011, **50**, 12639–12642.
- 7 T. Ebata, A. Fujii and N. Mikami, *Int. Rev. Phys. Chem.*, 1998, **17**, 331–361.
- 8 T. S. Zwier, *Annu. Rev. Phys. Chem.*, 1996, **47**, 205–241.
- 9 B. Brutschy, *Chem. Rev.*, 2000, **100**, 3891–3920.
- 10 J. R. Carney, F. C. Hagemester and T. S. Zwier, *J. Chem. Phys.*, 1998, **108**, 3379–3382.
- 11 H. Yokoyama, H. Watanabe, T. Omi, S.-I. Ishiuchi and M. Fujii, *J. Phys. Chem. A*, 2001, **105**, 9366–9374.
- 12 Y. Matsumoto and K. Honma, *J. Chem. Phys.*, 2009, **130**, 54311.
- 13 M. Sakai, K. Daigoku, S.-I. Ishiuchi, M. Saeki, K. Hashimoto and M. Fujii, *J. Phys. Chem. A*, 2001, **105**, 8651–8657.



- 14 N. A. Borisevich, V. A. Povedailo, E. E. Tselesh and D. L. Yakovlev, *J. Appl. Spectrosc.*, 2007, **74**, 838–843.
- 15 A. Poblitzki, J. Altnöder and M. A. Suhm, *Phys. Chem. Chem. Phys.*, 2016, **18**, 27265–27271.
- 16 H. Sasaki, S. Daicho, Y. Yamada and Y. Nibu, *J. Phys. Chem. A*, 2013, **117**, 3183–3189.
- 17 H. C. Gottschalk, A. Poblitzki, M. A. Suhm, M. M. Al-Mogren, J. Antony, A. A. Auer, L. Baptista, D. M. Benoit, G. Bistoni, F. Bohle, R. Dahmani, D. Firaha, S. Grimme, A. Hansen, M. E. Harding, M. Hochlaf, C. Holzer, G. Jansen, W. Klopper, W. A. Kopp, L. C. Kröger, K. Leonhard, H. Mouhib, F. Neese, M. N. Pereira, I. S. Ulusoy, A. Wuttke and R. A. Mata, *J. Chem. Phys.*, 2018, **148**, 14301.
- 18 A. Bree, V. V. B. Vilkos and R. Zwarich, *J. Mol. Spectrosc.*, 1973, **48**, 124–134.
- 19 A. Bree, V. V. B. Vilkos and R. Zwarich, *J. Mol. Spectrosc.*, 1973, **48**, 135–147.
- 20 A. Bree, A. R. Lacey, I. G. Ross and R. Zwarich, *Chem. Phys. Lett.*, 1974, **26**, 329–333.
- 21 C. Taliani, A. Bree and R. Zwarich, *J. Phys. Chem.*, 1984, **88**, 2357–2360.
- 22 I. Khasawneh, *Talanta*, 1988, **35**, 267–270.
- 23 T. D. Klots and W. B. Collier, *J. Mol. Spectrosc.*, 1996, **380**, 1–14.
- 24 A. R. Auty, A. C. Jones and D. Phillips, *Chem. Phys. Lett.*, 1984, **112**, 529–533.
- 25 A. R. Auty, A. C. Jones and D. Phillips, *J. Chem. Soc., Faraday Trans. 2*, 1986, **82**, 1219.
- 26 C. Weickhardt, R. Zimmermann, U. Boesl and E. W. Schlag, *Rapid Commun. Mass Spectrom.*, 1993, **7**, 183–185.
- 27 T. Chakraborty and E. C. Lim, *Chem. Phys. Lett.*, 1993, **207**, 99–104.
- 28 W. T. Yip and D. H. Levy, *J. Phys. Chem.*, 1996, **100**, 11539–11545.
- 29 M. Baba, K. Mori, M. Yamawaki, K. Akita, M. Ito, S. Kasahara and T. Yamanaka, *J. Phys. Chem. A*, 2006, **110**, 10000–10005.
- 30 D. Quang Hoa, T. Uchimura, T. Imasaka and N. Dai Hung, *Sci. Technol. Adv. Mater.*, 2016, **7**, 714–717.
- 31 M. Fatima, A. L. Steber, A. Poblitzki, C. Pérez, S. Zinn and M. Schnell, *Angew. Chem.*, 2019, **131**, 3140–3145.
- 32 M. Yamawaki, Y. Tatamitani, A. Doi, S. Kasahara and M. Baba, *J. Mol. Spectrosc.*, 2006, **238**, 49–55.
- 33 J. T. Yi, L. Alvarez-Valtierra and D. W. Pratt, *J. Chem. Phys.*, 2006, **124**, 244302.
- 34 C. Medcraft, S. Zinn, M. Schnell, A. Poblitzki, J. Altnöder, M. Heger, M. A. Suhm, D. Bernhard, A. Stamm, F. Dietrich and M. Gerhards, *Phys. Chem. Chem. Phys.*, 2016, **18**, 25975–25983.
- 35 D. Bernhard, F. Dietrich, M. Fatima, C. Perez, A. Poblitzki, G. Jansen, M. A. Suhm, M. Schnell and M. Gerhards, *Phys. Chem. Chem. Phys.*, 2017, **19**, 18076–18088.
- 36 D. Bernhard, C. Holzer, F. Dietrich, A. Stamm, W. Klopper and M. Gerhards, *ChemPhysChem*, 2017, 3634–3641.
- 37 F. Dietrich, D. Bernhard, M. Fatima, C. Pérez, M. Schnell and M. Gerhards, *Angew. Chem., Int. Ed.*, 2018, **57**, 9534–9537.
- 38 D. Bernhard, F. Dietrich, M. Fatima, C. Pérez, H. C. Gottschalk, A. Wuttke, R. A. Mata, M. A. Suhm, M. Schnell and M. Gerhards, *Beilstein J. Org. Chem.*, 2018, **14**, 1642–1654.
- 39 R. H. Page, Y. R. Shen and Y. T. Lee, *J. Chem. Phys.*, 1988, **88**, 4621.
- 40 C. Riehn, C. Lahmann, B. Wassermann and B. Brutschy, *Chem. Phys. Lett.*, 1992, **197**, 443–450.
- 41 M. Mons, E. G. Robertson and J. P. Simons, *J. Phys. Chem. A*, 2000, **104**, 1430–1437.
- 42 M. Gerhards and C. Unterberg, *Phys. Chem. Chem. Phys.*, 2002, **4**, 1760–1765.
- 43 G. G. Brown, B. C. Dian, K. O. Douglass, S. M. Geyer, S. T. Shipman and B. H. Pate, *Rev. Sci. Instrum.*, 2008, **79**, 53103.
- 44 M. Schnell, *Z. Phys. Chem.*, 2013, **227**, 1–22.
- 45 G. B. Park and R. W. Field, *J. Chem. Phys.*, 2016, **144**, 200901.
- 46 J. Altnöder, S. Oswald and M. A. Suhm, *J. Phys. Chem. A*, 2014, **118**, 3266–3279.
- 47 C. Unterberg, A. Jansen and M. Gerhards, *J. Chem. Phys.*, 2000, **113**, 7945.
- 48 D. Schmitz, V. Alvin Shubert, T. Betz and M. Schnell, *J. Mol. Spectrosc.*, 2012, **280**, 77–84.
- 49 C. Pérez, A. Krin, A. L. Steber, J. C. López, Z. Kisiel and M. Schnell, *J. Phys. Chem. Lett.*, 2016, **7**, 154–160.
- 50 C. Pérez, S. Lobsiger, N. A. Seifert, D. P. Zaleski, B. Temelso, G. C. Shields, Z. Kisiel and B. H. Pate, *Chem. Phys. Lett.*, 2013, **571**, 1–15.
- 51 D. F. Plusquellic, R. D. Suenram, B. Maté, J. O. Jensen and A. C. Samuels, *J. Chem. Phys.*, 2001, **115**, 3057–3067.
- 52 Z. Kisiel, L. Pszczółkowski, I. R. Medvedev, M. Winnewisser, F. C. de Lucia and E. Herbst, *J. Mol. Spectrosc.*, 2005, **233**, 231–243.
- 53 H. Hartwig and H. Dreizler, *Z. Naturforsch., A: Phys. Sci.*, 1996, **51**, 923–932.
- 54 M. D. Hanwell, D. E. Curtis, D. C. Lonie, T. Vandermeersch, E. Zurek and G. R. Hutchison, *J. Cheminf.*, 2012, **4**, 17.
- 55 T. A. Halgren, *J. Comput. Chem.*, 1996, **17**, 490–519.
- 56 S. Grimme, C. Bannwarth and P. Shushkov, *J. Chem. Theory Comput.*, 2017, **13**, 1989–2009.
- 57 A. Hellweg, S. A. Grün and C. Hättig, *Phys. Chem. Chem. Phys.*, 2008, **10**, 4119–4127.
- 58 A. D. Becke, *Phys. Rev. A: At., Mol., Opt. Phys.*, 1988, **38**, 3098–3100.
- 59 C. Lee, W. Yang and R. G. Parr, *Phys. Rev. B: Condens. Matter Mater. Phys.*, 1988, **37**, 785–789.
- 60 A. D. Becke, *J. Chem. Phys.*, 1993, **98**, 5648–5652.
- 61 S. Grimme, J. Antony, S. Ehrlich and H. Krieg, *J. Chem. Phys.*, 2010, **132**, 154104.
- 62 S. Grimme, S. Ehrlich and L. Goerigk, *J. Comput. Chem.*, 2011, **32**, 1456–1465.
- 63 F. Weigend and R. Ahlrichs, *Phys. Chem. Chem. Phys.*, 2005, **7**, 3297–3305.
- 64 R. A. Kendall, T. H. Dunning and R. J. Harrison, *J. Chem. Phys.*, 1992, **96**, 6796–6806.
- 65 M. J. Frisch, G. W. Trucks, H. B. Schlegel, G. E. Scuseria, M. A. Robb, J. R. Cheeseman, G. Scalmani, V. Barone, B. Mennucci, G. A. Petersson, H. Nakatsuji, M. Caricato,



- X. Li, H. P. Hratchian, A. F. Izmaylov, J. Bloino, G. Zheng, J. L. Sonnenberg, M. Hada, M. Ehara, K. Toyota, R. Fukuda, J. Hasegawa, M. Ishida, T. Nakajima, Y. Honda, O. Kitao, H. Nakai, T. Vreven, J. A. Montgomery Jr., J. E. Peralta, F. Ogliaro, M. J. Bearpark, J. Heyd, E. N. Brothers, K. N. Kudin, V. N. Staroverov, R. Kobayashi, J. Normand, K. Raghavachari, A. P. Rendell, J. C. Burant, S. S. Iyengar, J. Tomasi, M. Cossi, N. Rega, N. J. Millam, M. Klene, J. E. Knox, J. B. Cross, V. Bakken, C. Adamo, J. Jaramillo, R. Gomperts, R. E. Stratmann, O. Yazyev, A. J. Austin, R. Cammi, C. Pomelli, J. W. Ochterski, R. L. Martin, K. Morokuma, V. G. Zakrzewski, G. A. Voth, P. Salvador, J. J. Dannenberg, S. Dapprich, A. D. Daniels, Ö. Farkas, J. B. Foresman, J. V. Ortiz, J. Cioslowski and D. J. Fox, *Gaussian 09, Revision D.01*, Gaussian, Inc, Wallingford, CT, USA, 2009.
- 66 TURBOMOLE V7.3 2018, a development of University of Karlsruhe and Forschungszentrum Karlsruhe GmbH, 1989-2007. TURBOMOLE GmbH, since 2007; available from <http://www.turbomole.com>.
- 67 R. Ahlrichs, M. Bär, M. Häser, H. Horn and C. Kölmel, *Chem. Phys. Lett.*, 1989, **162**, 165–169.
- 68 Y. Zhao and D. G. Truhlar, *Theor. Chem. Acc.*, 2008, **120**, 215–241.
- 69 F. Weigend, A. Köhn and C. Hättig, *J. Chem. Phys.*, 2002, **116**, 3175.
- 70 S. F. Boys and F. Bernardi, *Mol. Phys.*, 2006, **19**, 553–566.
- 71 F. Neese, *WIREs Comput. Mol. Sci.*, 2012, **2**, 73–78.
- 72 D. G. Liakos, M. Sparta, M. K. Kesharwani, J. M. L. Martin and F. Neese, *J. Chem. Theory Comput.*, 2015, **11**, 1525–1539.
- 73 W. B. Schneider, G. Bistoni, M. Sparta, M. Saitow, C. Riplinger, A. A. Auer and F. Neese, *J. Chem. Theory Comput.*, 2016, **12**, 4778–4792.
- 74 A. Altun, F. Neese and G. Bistoni, *Beilstein J. Org. Chem.*, 2018, **14**, 919–929.
- 75 B. Jeziorski, R. Moszynski and K. Szalewicz, *Chem. Rev.*, 1994, **94**, 1887–1930.
- 76 E. G. Hohenstein, R. M. Parrish, C. D. Sherrill, J. M. Turney and H. F. Schaefer, *J. Chem. Phys.*, 2011, **135**, 174107.
- 77 T. M. Parker, L. A. Burns, R. M. Parrish, A. G. Ryno and C. D. Sherrill, *J. Chem. Phys.*, 2014, **140**, 94106.
- 78 J. M. Turney, A. C. Simmonett, R. M. Parrish, E. G. Hohenstein, F. A. Evangelista, J. T. Fermann, B. J. Mintz, L. A. Burns, J. J. Wilke, M. L. Abrams, N. J. Russ, M. L. Leininger, C. L. Janssen, E. T. Seidl, W. D. Allen, H. F. Schaefer, R. A. King, E. F. Valeev, C. D. Sherrill and T. D. Crawford, *WIREs Comput. Mol. Sci.*, 2012, **2**, 556–565.
- 79 C. Peng and H. Bernhard Schlegel, *Isr. J. Chem.*, 1993, **33**, 449–454.
- 80 P. Plessow, *J. Chem. Theory Comput.*, 2013, **9**, 1305–1310.
- 81 S. Daicho, Y. Yamada and Y. Nibu, in Pacificchem2010, International Chemical Congress of Pacific Basin Societies, Honolulu, HI, United States, December 15–20, 2010 (Conference Abstract).
- 82 R. Medel, M. Heger and M. A. Suhm, *J. Phys. Chem. A*, 2015, **119**, 1723–1730.



4.2 Dispersive stacking in the aggregates of diphenyl ether, dibenzofuran and fluorene dimers

This study investigates structural changes in dimer formation by introducing structural deformation in diphenyl ether (DPE). DPE, dibenzofuran (DBF), and fluorene (FLU) are three similar molecules consisting of two phenyl rings connected by either an ether oxygen (DPE and DBF) or a CH₂ group (FLU). In the complexes of DPE and DBF with different alcohols (Sections 4.1.2 and 4.1.3), where the only difference between DPE and DBF molecules is an “extra” bond in DBF connecting the two phenyl rings in DPE, contrasting and counterintuitive results are observed. Therefore, interesting insights can be expected in the study of the homodimers of DPE and DBF, where the dimers could be similar due to the similarities of the two monomers, or it can be different due to the interplay of dispersion interactions. A further comparison of the similarity and interactions in these homodimers can be made by replacing the influence of a heteroatom, oxygen, in DBF with a CH₂ group in FLU.

To form homodimers, all three molecules lack the possibility of a classical OH-O hydrogen bond formation due to the absence of an OH group, but the aromatic rings of these molecules provide strong dispersion centers for CH- π or π - π interactions. The homodimers can, in principle, start to aggregate in two different arrangements: π - π stacking or CH- π T-shaped structures, similar to the well-studied benzene dimer [40, 130–134] and further resembling the interaction patterns present in biological systems, such as deoxyribonucleic acid (DNA) and proteins.

The homodimers were studied with broadband chirped-pulse microwave spectroscopy. Quantum-chemical calculations were performed at the B3LYP-D3(BJ)/def2-TZVP level of theory. Experimentally, only one homodimer of each molecule was observed, which is also the global minimum from the calculations of each system. In the DPE, the observed dimer is stabilized by four CH- π interactions, much like the T-shaped structure of the benzene dimer and an additional CH-O interaction. As observed in the DPE-alcohol complexes (Section 4.1.2), the dihedral angles of DPE monomers also twist in the DPE dimer to increase interaction. The observed DBF and FLU dimers are stabilized by π - π interaction between the two molecules and resembles the π - π stacked structure of the benzene dimer. In the DBF dimer, there is also oxygen- π repulsion, which is replaced in the FLU dimer by attractive CH- π interactions.

The interplay between different forces of the intermolecular interactions in the homodimers is quantitatively analyzed by SAPT calculations, which results in a similar contribution from dispersion interactions. Even though the intermolecular interactions in the DPE, DBF, and FLU homodimers are different, the similarity of the overall structure of these dimers is noteworthy. The relative positions of oxygen atoms in DPE dimer and DBF dimer or CH₂ part in FLU dimer is very similar. The results obtained from this study can be useful to better understand the factors at play in the first stages of molecular aggregation and can be applicable in understanding biological systems. This study was published in *Angewandte Chemie* in 2019, and is given below.

Title	Rotational Signatures of Dispersive Stacking in the Formation of Aromatic Dimers
Authors	Mariyam Fatima, Amanda L. Steber, Anja Poblitzki, Cristóbal Pérez, Sabrina Zinn, and Melanie Schnell
Journal	Angewandte Chemie
Volume	58
Year	2019
Pages	3108–3113
DOI	International Edition: 10.1002/anie.201812556 German Edition: 10.1002/ange.201812556
Pages	6 pages of main article and 30 pages of supplementary material

Proportion of the authors

Experiment	Mariyam Fatima, Amanda Steber
Analysis	Mariyam Fatima, Amanda Steber, Cristóbal Pérez
Manuscript Preparation	Mariyam Fatima, Cristóbal Pérez, Melanie Schnell

Aromatic Dimers

International Edition: DOI: 10.1002/anie.201812556
German Edition: DOI: 10.1002/ange.201812556

Rotational Signatures of Dispersive Stacking in the Formation of Aromatic Dimers

Mariyam Fatima, Amanda L. Steber, Anja Poblitzki, Cristóbal Pérez, Sabrina Zinn, and Melanie Schnell*

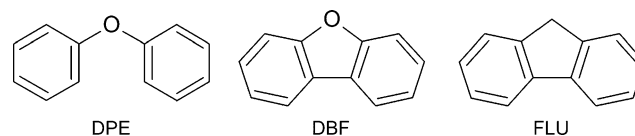
Abstract: The aggregation of aromatic species is dictated by inter- and intramolecular forces. Not only is characterizing these forces in aromatic growth important for understanding grain formation in the interstellar medium, but it is also imperative to comprehend biological functions. We report a combined rotational spectroscopic and quantum-chemical study on three homo-dimers, comprising of diphenyl ether, dibenzofuran, and fluorene, to analyze the influence of structural flexibility and the presence of heteroatoms on dimer formation. The structural information obtained shows clear similarities between the dimers, despite their qualitatively different molecular interactions. All dimers are dominated by dispersion interactions, but the dibenzofuran dimer is also influenced by repulsion between the free electron pairs of the oxygen atoms and the π -clouds. This study lays the groundwork for understanding the first steps of molecular aggregation in systems with aromatic residues.

The interplay between different intermolecular forces drives (bio)molecular aggregation and recognition.^[1] Although significant theoretical and experimental progress has been made, molecular recognition based on non-covalent interactions is still not fully understood at a quantitative molecular level.^[2] Decoupling the complex balance of forces that define non-covalent interactions and understanding exactly how the various non-covalent interactions reinforce or compete with each other in complex systems is of fundamental and practical importance. The generation of a toolbox of molecular groups that can introduce specific types of intermolecular interactions into a system would help synthetic chemists shape molecules in ways that customize the interaction forces. This can be by the inclusion of specific heteroatoms, such as oxygen and fluorine, or bulky groups that support dispersion interactions. Another aspect that has yet to receive more

attention is the role of structural flexibility.^[3] Further knowledge will help predict and design the outcome of molecular recognition events. A better quantitative description of dispersion interactions is one of the key steps towards this goal.

In molecular chemistry, dispersion interactions are omnipresent.^[4] They play an important role in stabilizing both protein and DNA through the interplay between aromatic components. These aromatic interactions also help govern the binding mechanism between DNA and protein. Mainly two arrangements of the aromatic elements can arise in these structures:^[5] edge-to-face (dominated by CH- π interactions) and stacked orientations (dominated by π - π dispersion interactions). A prototypical system for studying the subtle balance between these two assemblies is the benzene dimer. It has received much experimental attention and also acts as a benchmark for quantum-chemical calculations on systems involving these intricate dispersive interactions.^[6] By using rotational spectroscopy, the rich internal dynamics of the T-shaped global-minimum structure, and therefore the edge-to-face cooperation between the benzene molecules of the benzene dimer, were revealed.^[7]

Here, we concentrate on a comparative rotational spectroscopy study of dimers of the structurally related aromatic molecules diphenyl ether (DPE), dibenzofuran (DBF), and the polycyclic aromatic hydrocarbon (PAH) fluorene (FLU) (Scheme 1). Such complexes can be important nucleation



Scheme 1. Lewis structures of the monomers diphenyl ether (DPE), dibenzofuran (DBF), and the polycyclic aromatic hydrocarbon (PAH) fluorene (FLU).

seeds for molecular clustering and growth. This broadband rotational-spectroscopy study will provide us with important insight into the first steps of molecular aggregation, which can also be relevant for understanding the first steps of ice-grain formation.^[8] This technique can provide unprecedented structural information for isolated molecules and complexes.^[9]

Aromatic rings provide powerful dispersion centers due to their polarizable, delocalized π -electron systems and their planarity, which allows for short intermolecular contacts. All three molecules consist of these extended π -electron clouds

[*] M. Fatima, Dr. A. L. Steber, Dr. C. Pérez, Dr. S. Zinn, Prof. Dr. M. Schnell
FS-SMP, Deutsches Elektronen-Synchrotron (DESY)
Notkestrasse 85, 22607 Hamburg (Germany)
and
Institut für Physikalische Chemie, Christian-Albrechts-Universität zu Kiel
Max-Eyth-Str. 1, 24118 Kiel (Germany)
E-mail: melanie.schnell@desy.de
A. Poblitzki
Institut für Physikalische Chemie, Universität Göttingen
Tammannstrasse 6, 37077 Göttingen (Germany)

Supporting information and the ORCID identification number(s) for the author(s) of this article can be found under:
<https://doi.org/10.1002/anie.201812556>.

that are amenable to strong π - π and CH- π intermolecular interactions. As in the case of the benzene dimer, at least two qualitatively different structures are possible: a stacking configuration, mainly resulting from π - π interactions, and a T-shaped structure, due to CH- π interactions as well as combinations of CH- π and π - π interactions.

Despite their clear similarities, DPE, DBF, and FLU differ in structural flexibility, symmetry, dipole-moment magnitudes, as well as the presence or absence of an oxygen atom. Their comparative study will thus allow us to pin down the influences of these properties on the preferred dimer structure. The DBF and the FLU dimers have been previously studied using laser-spectroscopy techniques to investigate low-lying excimer states, but their structures were not unambiguously identified.^[10]

DBF is structurally related to FLU, which is a three-ring PAH with an extended π -electron system. Due to its symmetry (point group C_{2v}), FLU has a permanent dipole moment calculated to be 0.56 D along the C_2 symmetry axis. In DBF, the CH_2 group of FLU is exchanged for an oxygen atom, with the C_{2v} symmetry being preserved. The overall calculated dipole moment of DBF is 0.7 D along the C_2 symmetry axis. The calculated dipole moment of DPE is 1.17 D. While FLU and DBF are planar, rigid molecules, DPE is flexible and exhibits low-barrier tunneling between equivalent minima. We thus expect that DPE can adjust its arrangement of the phenyl rings to maximize molecular interactions upon dimer formation, as we observed in a previous study on DPE-alcohol and DPE- H_2O complexes.^[3a] For those complexes, the flexibility of DPE led to an, at first glance, counter-intuitive binding site preference for larger, bulky alcohols to DPE.

The rotational spectra of the three dimers were recorded with the Hamburg CP-FTMW spectrometer COMPACT in the 2–8 GHz range, and the cold and isolated conditions of a molecular jet were exploited.^[11] Experimental details are provided in the Experimental and Computational Section in the Supporting Information. In the following, the rotational spectroscopy results are summarized for all three dimers, and a comparative discussion of their structures and respective intermolecular interactions is provided.

Sections of the experimental spectra with simulations employing the experimentally determined rotational parameters for the complexes are shown in Figure 1. For the DPE dimer ($C_{24}O_2H_{20}$, molecular mass 340 amu), the experimental rotational constants are summarized in Table 1, together with calculated values for two dimer structures from quantum chemistry. Only one dimer species is observed in the experiment (Figure 2 a), and there is no indication of further dimer spectra. Quantum-chemical calculations predict two low-lying forms, with an energy difference of only 0.9 kJ mol⁻¹. Three further dimers are predicted to be 5.7, 9.0, and 15.9 kJ mol⁻¹ higher in energy, which are too high in energy to be sufficiently populated under the cold conditions of our molecular jet (Supporting Information, Figure S1). The two

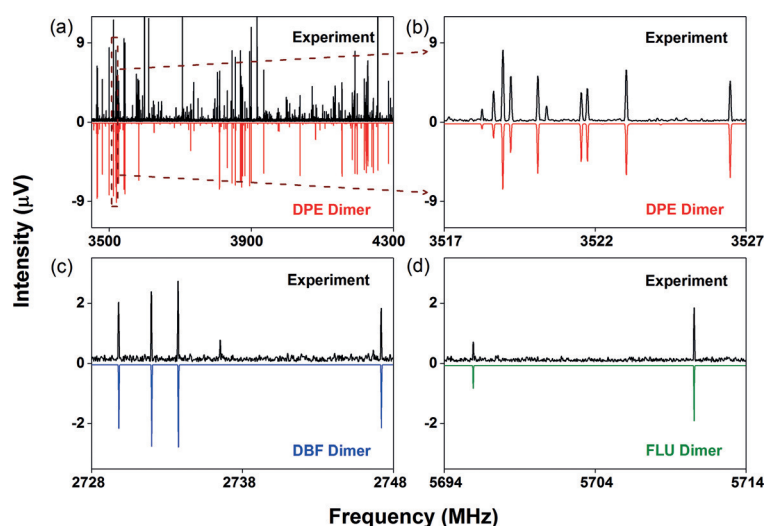


Figure 1. Portions of the broadband rotational spectra showing rotational signatures of the three dimers, a) and b) DPE, c) DBF and d) FLU. In each case, the black trace is the experimental spectrum, while the lower trace represents a simulation of the observed dimer (at 1 K) based on fitted experimental parameters.

Table 1: Comparison of experimental and calculated molecular parameters of the DPE dimer. The experimental values are determined from a fit to an asymmetric rotor Hamiltonian using the SPFIT software. The calculations were performed at the B3LYP-D3(BJ)/def2-TZVP level of theory.

Parameters ^[a]	Experimental data	Calculations for dimer 1	Calculations for dimer 2
A [MHz]	227.168244(52)	227	223
B [MHz]	179.225983(25)	205	190
C [MHz]	172.344790(25)	188	184
Δ_J [kHz]	0.019927(41)		
Δ_{JK} [kHz]	-0.01720(18)		
Δ_K [kHz]	0.01101(31)		
δ_J [kHz]	0.000713(22)		
δ_K [kHz]	-0.00900(77)		
$\mu_a \mu_b \mu_c$ [D]		0.8/0.9/0.5	0.9/0.9/0.1
ΔE [kJ mol ⁻¹]		0	0.9
σ [kHz]	4.56		
$N_{lines}^{[b]}$ (a b c)	729 (409 186 132)		

[a] A, B, and C are the rotational constants, Δ_J , Δ_{JK} , Δ_K , δ_J , and δ_K are the experimental centrifugal-distortion constants, and σ is the standard deviation of the fit. [b] Total number of rotational transitions included in the fit.

low-energy dimers, however, are structurally very similar, resulting in similar rotational constants. They differ in the relative orientation of one phenyl group: Dimer 1 has the CH- π interaction in the C2 (*ortho*) hydrogen, while for dimer 2 the C3 (*meta*) hydrogen is involved in this interaction (Supporting Information, Figure S1).

It is not possible to unambiguously assign the experimentally observed dimer to either the calculated dimer 1 or to dimer 2. Both dimers should be populated under the cold conditions of the molecular jet. The experimental rotational constants are closer to the values calculated for dimer 2, while the large number of assigned c-type transitions points to

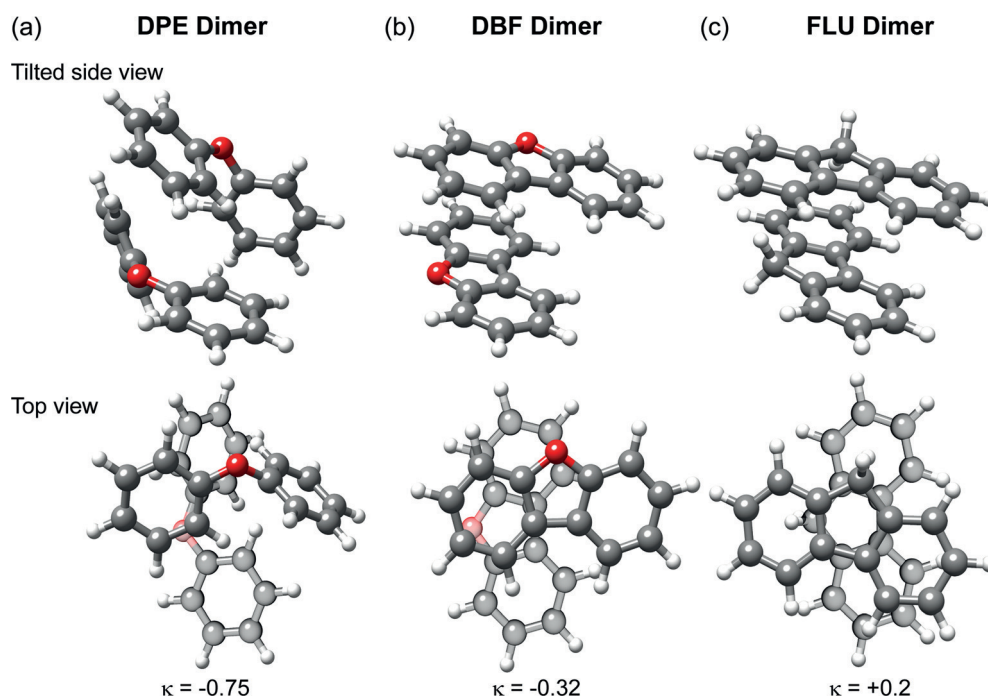


Figure 2. Optimized structures (B3LYP-D3(BJ)/def2-TZVP) of a) DPE, b) DBF, and c) FLU dimers. Top row: side view, bottom row: top view. In the top view, the bottom molecule is made transparent for better visibility and differentiation between the two moieties. Ray's asymmetry parameter κ (see text) is also included.

dimer 1 (Table 1). The observation of only one dimer could point towards a low relaxation barrier between them. Re-optimization at the MP2/aug-cc-pVTZ level led to a larger energy difference of about 4.8 kJ mol^{-1} (not ZPE corrected, with dimer 2 higher in energy).

As previously mentioned, the main intermolecular interaction in the DPE dimer is CH– π , with some additional CH–O interactions (Figure 2a), which also expresses itself in the larger electrostatic contribution to the binding energy compared to the other two dimers (DBF and FLU), based on a symmetry-adapted perturbation theory (SAPT) analysis (see below, Table 4). The shortest CH–O distances in the DPE dimer are 3.2 \AA . While rich internal dynamics were observed for the DPE monomer, these are quenched upon dimer formation. In this respect it is also interesting to compare the

dihedral angles ψ_1 and ψ_2 (defined in Figure S2 in the Supporting Information) in the two DPE molecules (DPE1 and DPE2; Supporting Information, Figure S3) to those obtained for the free monomer ($\psi_1 = \psi_2 = 37^\circ$) and other DPE complexes. The structural flexibility of DPE allows it to rearrange for optimal interactions. In dimer 1, $\psi_1 \approx 20^\circ$ and $\psi_2 \approx 85^\circ$ for DPE1, and $\psi_1 \approx 19^\circ$ and $\psi_2 \approx 53^\circ$ for DPE2, were obtained. In the recent study on DPE complexed with water, methanol, tertbutyl alcohol, and adamantol, similar values were obtained for the dihedral angles of these complexes.^[3a] A comparison of the dihedral angles for the DPE dimer with those of the other DPE complexes is given in Table S1 in the Supporting Information.

For the DBF dimer, only b-type transitions were observed (Figure 1c, Table 2). Four DBF dimer structures (Supporting

Table 2: Comparison of experimental and calculated molecular parameters of the DBF dimer. The experimental values are obtained from a fit to an asymmetric rotor Hamiltonian using the SPFIT software. The calculations were performed at the B3LYP-D3(BJ)/def2-TZVP level of theory.

Parameters ^[a]	Experimental data	Calculations for dimer 1	Calculations for dimer 2	Calculations for dimer 3	Calculations for dimer 4
DBF dimer					
A [MHz]	300.90323 (17)	303	359	334	313
B [MHz]	227.98085 (17)	232	220	230	230
C [MHz]	190.60573 (17)	192	190	201	192
B-C [MHz]	37.4	40	30	29	38
Δ_J [kHz]	0.0199(11)				
Δ_{JK} [kHz]	0.0180(18)				
ΔE [kJ mol^{-1}]		0	1.2	2.0	2.9
$\mu_a \mu_b \mu_c$ [D]		0 0.6 0	0.3 0.1 0.1	0 0 1.2	0.5 0.7 0.6
σ [kHz]	6.09				
$N_{\text{lines}}^{[b]}$ (a b c)	83 (0 83 0)				

[a] A, B, and C are the rotational constants, Δ_J and Δ_{JK} are the experimental centrifugal distortion constants, and σ is the standard deviation of the fit.
[b] Total number of rotational transitions included in the fit.

Information, Figure S4) were calculated with relative energies within 3 kJ mol^{-1} (B3LYP-D3(BJ)/def2-TZVP). All four are formed via π - π intermolecular interactions, but differ in the relative orientation of the two planar DBF molecules within the complex. These different relative orientations cause only small changes in the mass distribution because of the overall large mass of the dimer ($\text{C}_{24}\text{O}_2\text{H}_{16}$, molecular mass 336 amu). Thus, the rotational constants for the four calculated dimer structures are clearly similar (Table 2), which complicates an assignment based only on rotational constants. However, the fact that only b-type transitions were observed provides useful structural information. The monomer dipole moments along the C_2 symmetry axis have different relative arrangements in the calculated dimer structures, as indicated by arrows in Figure S4 in the Supporting Information. This gives rise to characteristic differences in the electric charge distribution and thus in the electric dipole-moment components μ_a , μ_b , and μ_c (Table 2). The observation of only b-type transitions supports the assignment of the experimental structure as dimer 1, which is also the global minimum. For dimers 2 and 3, the μ_b dipole-moment components are predicted to be identical or close to zero, so no b-type transitions are expected. For dimer 4, some additional (weak) a- and c-type transitions would be expected, which were not observed.

The assignment of the experimentally observed DBF dimer as dimer 1 is also supported by the good agreement between the experimental and calculated A rotational constant as well as the difference between the rotational constants, B-C, of 37.4 MHz. By taking all of this into account, we have sufficient evidence to assign the experimentally observed DBF dimer structure to the calculated lowest-energy isomer, dimer 1. This structure is characterized by an interesting symmetry. Based on inspection, this symmetry seems to arise from the interplay between attractive π - π interactions, on the one hand, and repulsion between the oxygen lone pairs and the π -cloud, on the other. Note that the two DBF monomers are not arranged perfectly in parallel but deviate by about 12 degrees (Supporting Information, Figure S5), which supports this interpretation.

This is different to the DPE dimer in which the ether oxygen atom is involved in an attractive (CH-O) interaction, which is supported by the flexible structure of DPE. For the DBF dimer, CH-O interactions are not possible in a stacked arrangement because of the planarity of DBF.

Despite the aforementioned differences between the DPE and the DBF dimer structures, they also show similarities (Figure 2). The positions and relative arrangements of the oxygen atoms are strikingly similar in both dimers, while a transition from CH- π to π - π bonding is observed once the binding partners become planar and rigid. The distances between the two oxygen atoms in the dimers are quite comparable with 5.2 Å for DPE and 5.4 Å for DBF, based on the quantum-chemical calculations.

The FLU dimer ($\text{C}_{26}\text{H}_{20}$, molecular mass 332 amu) completes the series. The experimentally observed dimer structure is shown in Figure 2c, with the rotational parameters reported in Table 3. It is strongly related to the structure of the DBF dimer. The FLU dimer is stacked, with the two monomers being skewed with respect to one another by

Table 3: Comparison of experimental and calculated molecular parameters of the FLU dimer. The experimental values are ascertained from a fit to an asymmetric rotor Hamiltonian using the SPFIT software. The calculations were performed at the B3LYP-D3(BJ)/def2-TZVP level of theory.

Parameters ^[a] FLU dimer	Experimental data	Calculations for dimer 1	Calculations for dimer 2
A [MHz]	260.86916(27)	266	324
B [MHz]	242.82643(10)	245	240
C [MHz]	215.586530(98)	219	176
Δ_j [kHz]	0.00702(20)		
Δ_k [kHz]	0.00639(36)		
ΔE [kJ mol ⁻¹]		0	5.5
$\mu_a \mu_b \mu_c$ [D]		0.5 0 0	0 0 0
σ [kHz]	4.47		
$N_{\text{lines}}^{\text{[b]}}$ (a b c)	116 (116 0 0)		

[a] A, B, and C are the rotational constants, Δ_j and Δ_k are the experimental centrifugal distortion constants, and σ is the standard deviation of the fit. [b] Total number of rotational transitions included in the fit.

approximately 90 degrees. Mainly two types of interaction are observed when inspecting the structures: two CH- π interactions involving the CH_2 groups and parallel-displaced π - π interaction between the aromatic rings. Different to the DBF dimer, this FLU dimer structure is almost perfectly parallel, with an angle between the two monomer planes of only 0.7 degrees (Supporting Information, Figure S5). A second, non-polar, dimer in which the two monomers are stacked, but with their long axes aligned, is about 5.5 kJ mol^{-1} higher in energy than the experimentally confirmed structure (Supporting Information, Figure S6). A T-shaped moiety, similar to the global minimum of the benzene dimer and consisting of CH- π contacts, is about 22 kJ mol^{-1} higher in energy.

It is now interesting to compare the results for the three dimers with respect to a) their structures and b) their binding energies. Ray's asymmetry parameter $\kappa = \frac{2B-A-C}{A-C}$ provides a measure of the asymmetry of the complexes. It ranges from -1 in the prolate to +1 in the oblate case. $\kappa = 0$ corresponds to the fully asymmetric structure. According to these, the DPE dimer is a near prolate asymmetric top ($\kappa = -0.75$), while the DBF dimer is significantly more asymmetric with $\kappa = -0.32$. The FLU dimer has a positive κ value ($\kappa = +0.2$) and is thus closer to an oblate top, but still quite asymmetric.

The binding energies, calculated at the B3LYP-D3(BJ)/def2-TZVP level and corrected for basis-set-superposition errors (BSSE), as well as results of symmetry-adapted perturbation theory (SAPT) calculations,^[12] which give a qualitative breakdown of the individual contributions to the binding energy, are summarized in Table 4. The binding energies of DPE and DBF are comparable (-41.2 vs. $-42.3 \text{ kJ mol}^{-1}$), while FLU is more strongly bound ($-51.1 \text{ kJ mol}^{-1}$). This might be surprising at first glance because, naively, one would expect stronger interactions for the molecules containing the heteroatom and/or the stronger dipole moment (DPE). SAPT(0)/jun-cc-pVDZ calculations, together with revisiting the structures, can help to gain better insight into these binding energies (Table 4). E_{tot} corresponds to the binding energy from the SAPT(0)/jun-cc-pVDZ

Table 4: Results of SAPT(0)/jun-cc-pVDZ calculations for the three optimized dimers. The binding energy, E_b , calculated at the B3LYP-D3(BJ)/def2-TZVP level of theory is given for comparison, as well as the respective relative contributions to the overall attractive interactions ($E_{el} + E_{ind} + E_{disp}$).^[a]

Dimer	$E_b^{[b]}$	E_{tot}	$E_{el}^{(1)}$	$E_{ind}^{(1)}$	$E_{disp}^{(1)}$	$E_{exch}^{(1)}$
DPE ₂	-41.2	-45.8	-35.3 (30.4%)	-71.8 (61.8%)	-9.0 (7.8%)	70.3
DBF ₂	-42.3	-51.5	-29.5 (26.5%)	-80.9 (72.8%)	-6.7 (6.0%)	65.6
FLU ₂	-51.1	-60.0	-33.7 (24.8%)	-93.3 (68.6%)	-9.0 (6.6%)	76.2

[a] Negative values indicate an attractive contribution to the overall energy E_{tot} , while positive values are repulsive contributions to E_{tot} .

[b] binding energy (B3LYP-D3(BJ)/def2-TZVP), BSSE corrected.

calculations (based only on the interaction energies), which shows a similar trend as E_b . The three dimers have significant dispersion contributions, accounting for 60–70% of the overall attractive interaction. For the electrostatic contribution, the DPE dimer dominates, which probably arises from its larger dipole moment and from the attractive CH–O interactions between the two molecules in the DPE dimer (see above). Furthermore, contributions from induction are small and on the same order of magnitude for all three dimers. This can be expected for such stacked structures because of the rather small polarizability of these molecules in the direction perpendicular to the aromatic plane. As expected, the contribution is somewhat larger for the DPE dimer because of the non-planarity of the DPE monomer.

Another way to visualize the different parts of intermolecular interactions is by using non-covalent interaction (NCI) plots (Supporting Information, Figure S7).^[13] NCI plots are a visualization index based on the density and its derivatives, and they enable the identification of NCIs. In contrast to the DPE dimer, the planar structures of both DBF and FLU allow for good molecular overlap. In the FLU dimer, all three rings are involved in the attractive interaction via π – π and CH– π contacts. In the DBF dimer, however, a compromise has to be found to minimize repulsion between the oxygen lone-pairs and the π -cloud of the phenyl rings. The almost perfect parallel stacking in the FLU dimer might also contribute to its larger binding energy compared to the DPE and the DBF dimers.

In summary, all three dimers show striking structural similarities, although governed by different intermolecular interactions. The DPE dimer consists of two structurally flexible DPE units, in which the internal dynamics of the DPE monomers are locked. Its structure is governed by CH– π as well as additional CH–O interactions that further stabilize the dimer. The rigid DBF dimer has mainly π – π interactions and the two monomers are skewed with respect to one another to facilitate an optimal contact and minimize electrostatic repulsion between the π -clouds and the oxygen-atom lone pairs. The two DBF molecules are not fully parallel but deviate by about 12 degrees. The dimer of FLU is dominated by π – π and CH– π interactions involving the non-aromatic hydrogen atoms, with all three rings involved in the inter-

molecular contact, forming an almost perfect parallel arrangement.

Our systematic study of these structurally related aromatic molecules shows the differences and similarities that result from dimer formation and the kind of interactions that control their aggregation. A subtle balance of forces is the main contributor to the observed geometries. The results presented here will help chemists to better understand the factors at play in the first stages of molecular aggregation, which can be relevant for soot production in combustion as well as grain formation in astrochemical environments.

Acknowledgements

This work was financially supported by the Deutsche Forschungsgemeinschaft (SCHN1280/4-2, project number 271359857; SU121/5-2, project number 271107160) in the context of the priority program SPP 1807 “Control of London dispersion interactions in molecular chemistry”. We acknowledge the use of the GWDG computer cluster and thank Sérgio R. Domingos for his help with the NCI plots. M.F. acknowledges support from the Hamburg International Max Planck Research School UFAST, and A.L.S. is supported via the Louise Johnson Fellowship.

Conflict of interest

The authors declare no conflict of interest.

Keywords: aromatic dimers · dispersion · molecular complexes · non-covalent interactions · rotational spectroscopy

How to cite: *Angew. Chem. Int. Ed.* **2019**, *58*, 3108–3113
Angew. Chem. **2019**, *131*, 3140–3145

- [1] A. J. Stone, *The Theory of Intermolecular Forces*, Clarendon, Oxford, **1997**.
- [2] a) J. N. Israelachvili, *Intermolecular and Surface Forces*, Elsevier Science, Amsterdam, **2011**; b) M. A. Strauss, H. A. Wegner, *Eur. J. Org. Chem.* **2019**, 295–302; c) A. Zehnacker, M. A. Suhm, *Angew. Chem. Int. Ed.* **2008**, *47*, 6970–6992; *Angew. Chem.* **2008**, *120*, 7076–7100; d) A. S. Mahadevi, G. N. Sastry, *Chem. Rev.* **2016**, *116*, 2775–2825; e) E. A. Meyer, R. K. Castellano, F. Diederich, *Angew. Chem. Int. Ed.* **2003**, *42*, 1210–1250; *Angew. Chem.* **2003**, *115*, 1244–1287; f) L. M. Salonen, M. Ellermann, F. Diederich, *Angew. Chem. Int. Ed.* **2011**, *50*, 4808–4842; *Angew. Chem.* **2011**, *123*, 4908–4944; g) S. Tsuzuki, A. Fujii, *Phys. Chem. Chem. Phys.* **2008**, *10*, 2584–2594; h) A. Fujii, H. Hayashi, J. W. Park, T. Kazama, N. Mikami, S. Tsuzuki, *Phys. Chem. Chem. Phys.* **2011**, *13*, 14131–14141; i) O. Takahashi, Y. Kohno, M. Nishio, *Chem. Rev.* **2010**, *110*, 6049–6076; j) J. W. G. Bloom, R. K. Raju, S. E. Wheeler, *J. Chem. Theory Comput.* **2012**, *8*, 3167–3174; k) Editorial, *Phys. Chem. Chem. Phys.* **2008**, *10*, 2581–2583.
- [3] a) F. Dietrich, D. Bernhard, M. Fatima, C. Pérez, M. Schnell, M. Gerhards, *Angew. Chem. Int. Ed.* **2018**, *57*, 9534–9537; *Angew. Chem.* **2018**, *130*, 9678–9682; b) S. R. Domingos, C. Pérez, C. Medcraft, P. Pinacho, M. Schnell, *Phys. Chem. Chem. Phys.* **2016**, *18*, 16682–16689; c) N. A. Seifert, I. A. Finneran, C. Perez, D. P.

- Zaleski, J. L. Neill, A. L. Steber, R. D. Suenram, A. Lesarri, S. T. Shipman, B. H. Pate, *J. Mol. Spectrosc.* **2015**, *312*, 13–21.
- [4] J. P. Wagner, P. R. Schreiner, *Angew. Chem. Int. Ed.* **2015**, *54*, 12274–12296; *Angew. Chem.* **2015**, *127*, 12446–12471.
- [5] a) J. A. Frey, C. Holzer, W. Klopper, S. Leutwyler, *Chem. Rev.* **2016**, *116*, 5614–5641; b) C. F. R. A. C. Lima, M. A. A. Rocha, L. R. Gomes, J. N. Low, A. M. S. Silva, L. M. N. B. F. Santos, *Chem. Eur. J.* **2012**, *18*, 8934–8943.
- [6] a) P. Hobza, H. L. Selzle, E. W. Schlag, *J. Am. Chem. Soc.* **1994**, *116*, 3500–3506; b) A. van der Avoird, R. Podeszwa, K. Szalewicz, C. Leforestier, R. van Harrevelt, P. R. Bunker, M. Schnell, G. von Helden, G. Meijer, *Phys. Chem. Chem. Phys.* **2010**, *12*, 8219–8240; c) K. C. Janda, J. C. Hemminger, J. S. Winn, S. E. Novick, S. J. Harris, W. Klemperer, *J. Chem. Phys.* **1975**, *63*, 1419–1421; d) B. F. Henson, G. V. Hartland, V. A. Ventura, P. M. Felker, *J. Chem. Phys.* **1992**, *97*, 2189–2208; e) E. Arunan, H. S. Gutowsky, *J. Chem. Phys.* **1993**, *98*, 4294–4296; f) C. D. Pibel, *J. Am. Chem. Soc.* **1999**, *121*, 10669–10669; g) R. Podeszwa, R. Bukowski, K. Szalewicz, *J. Phys. Chem. A* **2006**, *110*, 10345–10354.
- [7] M. Schnell, U. Erlekam, P. R. Bunker, G. von Helden, J. U. Grabow, G. Meijer, A. van der Avoird, *Angew. Chem. Int. Ed.* **2013**, *52*, 5180–5183; *Angew. Chem.* **2013**, *125*, 5288–5292.
- [8] A. L. Steber, C. Pérez, B. Temelso, G. C. Shields, A. M. Rijs, B. H. Pate, Z. Kisiel, M. Schnell, *J. Phys. Chem. Lett.* **2017**, *8*, 5744–5750.
- [9] a) G. B. Park, R. W. Field, *J. Chem. Phys.* **2016**, *144*, 200901–200901; b) C. Pérez, M. T. Muckle, D. P. Zaleski, N. A. Seifert, B. Temelso, G. C. Shields, Z. Kisiel, B. H. Pate, *Science* **2012**, *336*, 897–901; c) C. Pérez, J. C. López, S. Blanco, M. Schnell, *J. Phys. Chem. Lett.* **2016**, *7*, 4053–4058; d) S. T. Shipman, J. L. Neill, R. D. Suenram, M. T. Muckle, B. H. Pate, *J. Phys. Chem. Lett.* **2011**, *2*, 443–448; e) E. J. Cocinero, A. Lesarri, P. Écija, Á. Cimas, B. G. Davis, F. J. Basterretxea, J. A. Fernández, F. Castaño, *J. Am. Chem. Soc.* **2013**, *135*, 2845–2852.
- [10] a) H. Saigusa, M. Itoh, *J. Phys. Chem.* **1985**, *89*, 5486–5488; b) T. Chakraborty, E. C. Lim, *Chem. Phys. Lett.* **1993**, *207*, 99–104; c) J. Wessel, S. Beck, C. Highstrete, *J. Chem. Phys.* **1994**, *101*, 10292–10302; d) W. T. Yip, D. H. Levy, *J. Phys. Chem.* **1996**, *100*, 11539–11545.
- [11] D. Schmitz, V. Alvin Shubert, T. Betz, M. Schnell, *J. Mol. Spectrosc.* **2012**, *280*, 77–84.
- [12] a) T. M. Parker, L. A. Burns, R. M. Parrish, A. G. Ryno, C. D. Sherrill, *J. Chem. Phys.* **2014**, *140*, 094106; b) B. Jeziorski, R. Moszynski, K. Szalewicz, *Chem. Rev.* **1994**, *94*, 1887–1930.
- [13] J. Contreras-García, E. R. Johnson, S. Keinan, R. Chaudret, J. P. Piquemal, D. N. Beratan, W. Yang, *J. Chem. Theory Comput.* **2011**, *7*, 625–632.

Manuscript received: November 1, 2018

Revised manuscript received: January 17, 2019

Accepted manuscript online: January 23, 2019

Version of record online: February 7, 2019

Monographic part

Chapter 5

Monographic part

5.1 Side-chain length influencing dispersion interaction in camphor-alcohol complexes

Camphor is a rigid bicyclic terpene molecule that offers only one polar group to form OH-O hydrogen-bonded complexes with an alcohol. Unlike in the ether/benzofuran molecules, there is no dispersive π -cloud density in camphor to form OH- π bound complex with an alcohol. Further, the rigidity of the camphor molecule cannot allow it to adjust to the binding partner to increase dispersion interactions, as in the diphenyl ether-alcohol clusters. This makes camphor an interesting system to investigate on how oxygen bonded complex formation can be affected by dispersion interactions when the chain length of the respective aliphatic alcohol is increased.

Camphor and its complexes with water have been studied using microwave spec-

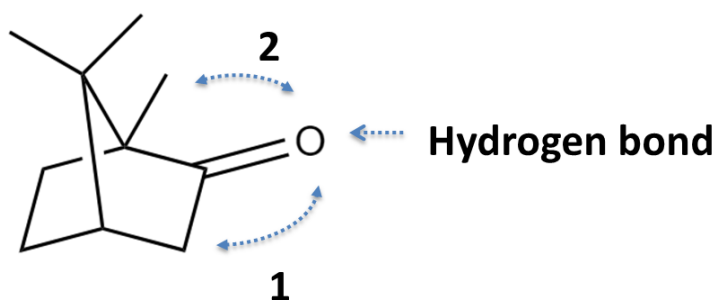


Figure 5.1: *The structure of camphor, where the keto group for hydrogen bonding interaction is highlighted, with dispersion interaction sites at either a CH₂ (denoted as 1) or a CH₃ (denoted as 2) group of camphor.*

troscopy before [81, 86], where the effect of dispersion already became apparent. Camphor is a chiral molecule and has only one conformation. It has three methyl tops, but the barrier to the internal rotation is high enough that no splitting is observed in the spectrum. A water molecule establishes a strong hydrogen bond with the keto group of camphor, and the two observed one water complexes differ in the secondary interaction of water with either a CH₂ or a CH₃ group of camphor, as shown in Figure 5.1. For these complexes, symmetry adapted perturbation theory (SAPT) predicts that electrostatic contributions to the interaction energy (mainly corresponding to hydrogen bonding) dominate with about 50 kJ mol⁻¹, while dispersion already amounts to about 12 kJ mol⁻¹. Complexes of camphor with methanol have been studied using matrix isolation infrared spectroscopy [135], where the two identified structures are similar to the two camphor-water complexes.

In this work, we present the rotational spectra and quantum-chemical calculations of complexes of camphor with methanol and ethanol, respectively, and compare it with the complexes of camphor-water in order to learn about the binding preference of alcohol with terpenes. In the experimental camphor-methanol spectrum, we observed splitting due to the internal rotation of the methyl group of methanol in the camphor-methanol complexes. From the analysis of these splittings we determined the V_3 barrier height and the orientation of the methyl group with respect to the principal axis system. In the camphor-ethanol spectrum, we were also able to obtain the rotational constants for all the mono-substituted ¹³C-isotopologues of the lowest energy isomer of camphor-ethanol in natural abundance and hence determine its carbon backbone structure using the Kraitchman's equations (r_s -structure) and an effective method (r_0 -structure). A comparison with camphor-water complexes provides further insight into the interplay between different types of intermolecular interactions.

5.1.1 Experimental details

Camphor (stated purity $\geq 99\%$), methanol (stated purity $\geq 99.8\%$), and ethanol (stated purity $\geq 99\%$) were purchased from Sigma-Aldrich and used without further purification. Camphor was placed in a small sample reservoir in front of the solenoid, close to the valve orifice, and heated to 85 °C. The alcohol (methanol or ethanol) was placed in a reservoir on a separate section of tubing outside of the vacuum chamber. The carrier gas (neon, 3 bar backing pressure) was allowed to flow over the alcohol and then mix with the camphor vapor, and a supersonic expansion into the chamber of the COMPACT spectrometer was created.

As given in Section 3.3 (the Hamburg COMPACT Spectrometer), for each gas pulse,

the ensemble of molecules was polarized with a series of eight microwave chirps of 4 μs duration spanning 2 \rightarrow 8 GHz using the fast-frame option of the oscilloscope. Following each excitation, 40 μs of the free induction decay (FID) of the macroscopic ensemble of polarized molecules was recorded. This yielded a frequency resolution of 25 kHz. A total of 2 million FIDs were co-added and Fourier transformed with a Kaiser-Bessel window function to obtain the broadband rotational spectrum in the frequency domain.

Prediction for minimum energy structures for the camphor-alcohol complexes was conducted using the Artificial Bee Colony (ABCcluster) method [109]. Twenty semi-empirical structures were calculated for camphor-methanol and camphor-ethanol (*t*, *g+* and *g-*). Here *t*, *g-* and *g+* represent *trans* and *gauche* forms of ethanol. These structures were optimized using the Gaussian 09 software at the B3LYP-D3/aug-cc-pVTZ level. For selected stationary points, the structures obtained were then re-optimized using MP2/6-311++G(d,p). All the reported structures at both levels of theory were confirmed as minima by harmonic frequency calculations. In addition, for qualitative analysis of the intermolecular interactions in the observed clusters, symmetry adapted perturbation theory (SAPT) calculations at zeroth order were performed using the jun-ccpVDZ basis set [115–117]. The jun-ccpVDZ corresponds to a reduced aug-cc-pVDZ basis set (without diffuse functions on hydrogen atoms and without diffuse d functions on heavy atoms).

The spectra were first fit using the JB95 program [97], then further refined with the AABS program suite [99, 100]. A detailed analysis of the observed tunneling splitting arising from the internal rotation of the methyl group of methanol in the camphor-methanol complex was performed using the XIAM program [101].

5.1.2 Results and discussion

5.1.2.1 Camphor-methanol clusters

Quantum-chemical calculations at the B3LYP-D3 level of theory predicted seven low-energy 1:1 camphor-methanol isomers with relative energies between 0-1 kJ mol⁻¹, starting from twenty isomers obtained from ABCcluster method. As camphor is a rigid molecule with only one conformer, the structural variety arises from different orientations of methanol relative to camphor. These seven structures were re-optimized at the MP2 level. The three lowest energy isomers with relative energies around 1 kJ mol⁻¹ with the global minimum from both levels of theory are shown in Figure 5.2, and the rotational parameters are summarized in Table 5.1. The next available isomer is \sim 2.6 kJ mol⁻¹ higher in energy than the global minimum at both the levels of theory and is not shown here, but it was searched for

in the experiment. In all three 1:1 isomers, that we denote as 1Me(I), 1Me(II), and 1Me(III), respectively, a well defined OH-O hydrogen bond is formed between the methanol hydrogen and the camphor keto group as in the camphor-water complexes [86], while the methanol methyl group points away from camphor. In the three isomers, the O-O distance is ~ 2.8 Å and the OH-O bond angle is greater than 160° , from these two features the hydrogen bond can be determined as close to a strong bond [12]. The main difference between the isomers stems from the relative orientation of the methanol moiety with respect to camphor via different secondary interactions, i.e., either to a CH_2 group in Me(I) or a CH_3 group in Me(II) and Me(III) of camphor. This difference also manifests itself as a small change in the dihedral angle $\angle\text{CCOO}$, as indicated in Figure 1 for 1Me(I).

The CH_2 group of camphor is in the α position to the keto group. The resonance-assisted activation of the $\text{C}(\alpha)\text{-H}$ due to the hydrogen bond can explain the preference of secondary interactions towards the CH_2 over the CH_3 group. In 1Me(II) and 1Me(III), the structures differ in the orientation of the methanol methyl group, while exhibiting similar secondary interactions, resulting in similar relative energies with respect to 1Me(I). As the energy difference between the complexes is around 1 kJ mol^{-1} and the a-type dipole moment component is approximately the same, it can be expected that all the three isomers are observed in the spectrum.

In the broadband rotational spectrum, most of the stronger lines belonged to the

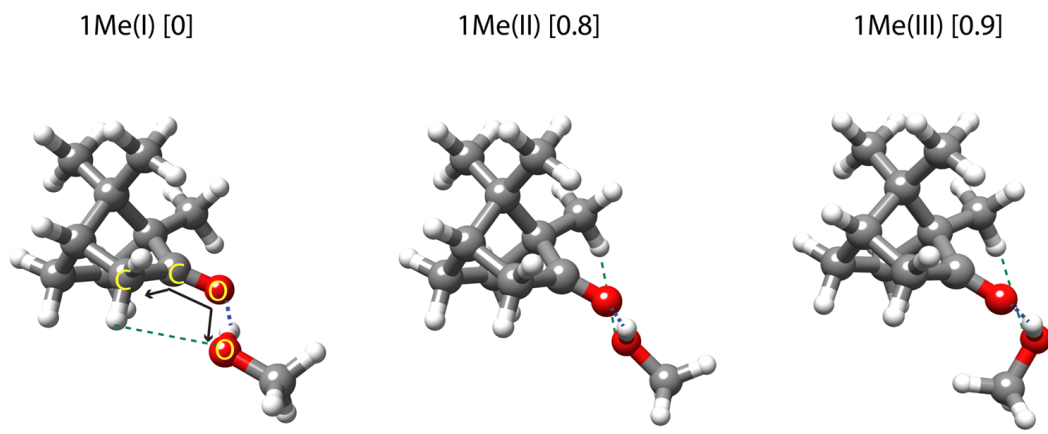


Figure 5.2: Structures of the most stable camphor–methanol 1:1 complexes optimized at the $B3LYP\text{-}D3/\text{aug-cc-pVTZ}$ level of theory with relative zero-point-energy-corrected energies in kJ mol^{-1} in square brackets. Hydrogen bonding and secondary interactions, either to a CH_2 or CH_3 part of camphor, are indicated by dashed lines.

Table 5.1: Calculated rotational parameters for the lowest energy conformers of camphor–methanol, performed at the B3LYP-D3/aug-cc-pVTZ and MP2/6-311++G(d,p) levels.

Parameters	1Me(I)		1Me(II)		1Me(III)	
	B3LYP	MP2	B3LYP	MP2	B3LYP	MP2
A (MHz)	1337.1	1205.1	1327.3	1321.1	1280.8	1278.3
B (MHz)	441.5	540.5	470.6	476.5	503.8	518.1
C (MHz)	429.6	524.9	462.3	469.4	493.8	509.1
μ_a (D)	3.0	2.9	3.0	2.8	4.0	3.5
μ_b (D)	0.4	1.0	0.5	0.9	1.2	1.9
μ_c (D)	0.1	0.4	0.3	0.3	1.0	0.4
V_3 (cm ⁻¹)	268.6	367.8	253.5	326.0	256.8	330.0
V_3 (kJ mol ⁻¹)	3.2	4.4	3.0	3.9	3.1	4.0
δ^a (°)	24.0	65.6	19.6	28.1	67.9	65.3
ϵ^a (°)	6.7	52.0	38.6	14.3	19.3	3.2
ΔE_{ZP} (kJ mol ⁻¹)	0.0	0.0	0.8	1.2	0.9	1.0

^a δ , ϵ are angles between the methyl rotor of the methanol unit and the inertial axes.

camphor monomer and the methanol dimer. After removing these lines, a rich spectrum remained, and we were able to assign and fit the spectra of two 1:1 camphor–methanol isomers. A zoom-in to the broadband experimental spectrum is shown in Figure 5.3, highlighting the $J_{K_a K_c}$: $4_{04} \leftarrow 3_{03}$, $4_{23} \leftarrow 3_{22}$ and $4_{22} \leftarrow 3_{21}$ rotational transitions of 1Me(I). Most of the assigned transitions of the camphor–methanol spectrum show an obvious splitting into doublets that can be attributed to internal rotation of the methyl group of methanol, which are denoted as A and E states according to their symmetry, as shown in Figure 5.3 for Me(I) complex. This internal rotation splitting can be understood from the optimized structures, where the methyl group is not interacting with camphor, so a low barrier to internal rotation, similar to that observed for free methanol, can be expected. We first performed a semi-rigid rotor fit to assign the A-state lines. The E-state lines were subsequently assigned using the calculated molecular parameters and fitted with the program XIAM [101], similar to the cases of phenyl vinyl ether–methanol (PVE–MeOH), dibenzofuran–methanol (DBF–MeOH) [Chapter 4, Sections 1 and 3] and diphenyl ether–methanol (DPE–

MeOH) complexes [87]. A global fit of both the A and E states using the XIAM fitting program was then used to determine the experimental barrier height (V_3) for the internal rotation of the methyl top. The results are summarized in Table 5.2. The experimental rotational constants are in agreement with the calculated values (B3LYP-D3) for 1Me(I). Note that the MP2 level calculation changes the orientation of the methanol with respect to camphor after re-optimizing the B3LYP structure, resulting in a slightly different global minimum.

The rotational transitions corresponding to a second camphor-methanol 1:1 isomer could also be identified and fit to an asymmetric rotor Hamiltonian. The most intense line for this isomer is about fifteen times weaker than for 1Me(I). Only 25 a-type A state transitions were assigned. Therefore, the A rotational constant is not well determined (Table 2). However, comparison of the molecular parameters for this complex with quantum-chemical calculations suggests it to be 1Me(II) (Figure 1). The energy difference between 1Me(II) and 1Me(III) is negligible at both levels of theory. We do not observe any b-type transitions for this complex, which should be rather pronounced for 1Me(III). Their absence further supports our assignment to 1Me(II) and points to a low interconversion barrier from 1Me(III) to 1Me(II) and/or 1Me(I), resulting in an efficient depopulation of 1Me(III). The next available isomer, which is 2.6 kJ mol^{-1} higher in energy and could be present in the expansion but remained untraceable in the spectrum.

Barrier height (V_3) for the internal rotation of the methyl group of methanol

From using the XIAM program, the V_3 barrier was determined to be $208.184(84) \text{ cm}^{-1}$ (2.5 kJ mol^{-1}) for 1Me(I) and $210.63(25) \text{ cm}^{-1}$ for 1Me(II), as summarized in Table 2. These values are lower than the predicted barrier heights of 267 cm^{-1} and 254 cm^{-1} calculated at the B3LYP level, as well as the barrier heights observed for free methanol (373 cm^{-1}), DPE-MeOH (480 cm^{-1} , Fit 2 [87]), and PVE-MeOH (261 cm^{-1}). Comparison of the barrier height with free methanol gives an indication of the environment around methanol. For DPE-MeOH, the higher barrier height indicates that the CH_3 group is involved in a CH- π interaction, whereas in PVE-MeOH the lower barrier height points towards no interaction of the methyl group with PVE and could indicate a weakening of the C-O bond of methanol due to the hydrogen bonding. In 1Me(I) and 1Me(II) (Figure 1), the methyl group is not interacting with camphor, but V_3 is even lower than for PVE-MeOH.

This decrease could point towards the molecular parameters used for the fit. For DPE-MeOH, for example, V_3 is dependent on the F value, which is the rotational

Table 5.2: Experimentally determined molecular parameters of the camphor-methanol 1:1 isomers: results of the global fit based on the experimentally observed transitions, including internal rotation of the methanol methyl group using the XIAM program for 1Me(I) and 1Me(II).

Parameters	1Me(I)	1Me(II)
A (MHz)	1325.0644(19)	1334.2(12)
B (MHz)	442.01559(31)	470.4897(13)
C (MHz)	431.48600(30)	463.2808(13)
Δ_J (kHz)	0.0812(15)	0.3083(38)
Δ_{JK} (kHz)	3.0844(68)	—
δ_J (kHz)	—	0.0371(65)
D_{pi2J} ^a	—	65.7(14)
F (cm ⁻¹) ^b	[5.3] ^e	[5.3] ^e
V ₃ (cm ⁻¹)	208.184(84)	210.63(25)
V ₃ (kJ mol ⁻¹)	2.4904(10)	2.5197(30)
δ (°) ^c	22.10(17)	24.07(34)
ϵ (°) ^c	[0.0] ^f	21.1(28)
σ (kHz) ^d	6.9	10.4
A state transition(a/b/c)	38/0/0	25/0/0
E state transition(a/b/c)	30/0/0	21/0/0

^a D_{pi2J} accounts for the internal motion-overall rotation centrifugal distortion, obtained from a global fit of both internal rotational components A and E with the program XIAM.

^b F is the rotational constant of the internally rotating methyl top and it is fixed to 5.3 cm⁻¹.

^c δ , ϵ are angles between the methyl rotor of the methanol unit and the inertial axes.

^d σ is the standard deviation of the fit.

^e fixed to the the barrier height of internally rotation methyl top in methanol complexes.

^f fixed to the calculated value at the B3LYP-D3/aug-cc-pvtz level of theory.

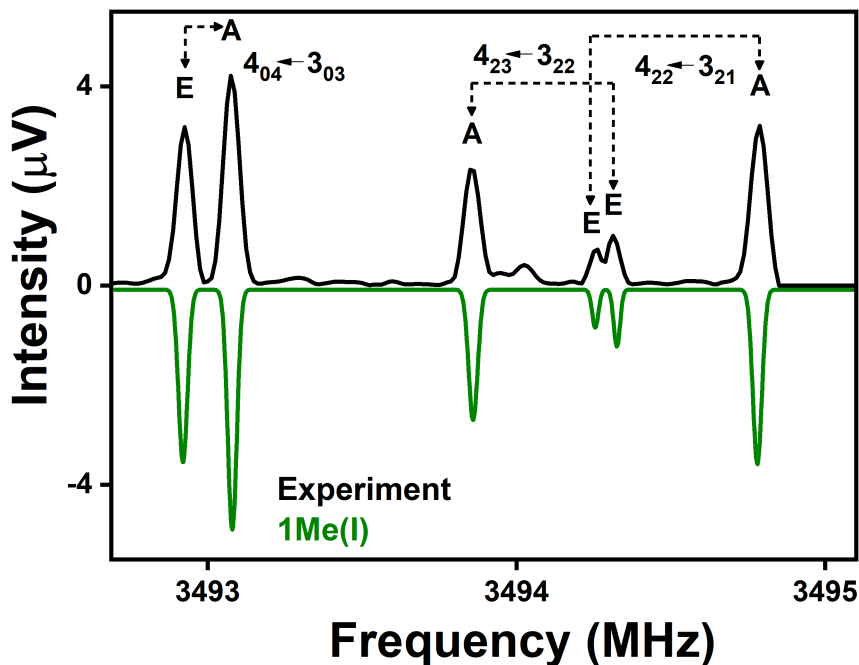


Figure 5.3: Portion of the experimental rotational spectrum using a mixture of camphor-methanol (2 million acquisitions), illustrating the $J_{K_a K_c}$: $4_{04} \leftarrow 3_{03}$, $4_{23} \leftarrow 3_{22}$ and $4_{22} \leftarrow 3_{21}$ rotational transitions of 1Me(I). The upper experimental trace in black is compared with a simulation based on fitted parameters that can be assigned to 1Me(I) (green) at a temperature of 1.5 K. The observed complex has a clear splitting pattern due to the internal rotation of the methyl group of methanol, labeled with A and E.

constant of the internally rotating methyl top. For most studies with methanol complexes, F is fixed to 5.3 cm^{-1} . For DPE-MeOH, to get a more realistic value of the barrier height, F was allowed to be optimized during the fit, as given in Table 2 by Medcraft et al. [87]. Interestingly, for 1Me(I) and 1Me(II), there are no significant changes observed for V_3 and F when F is allowed to float.

5.1.2.2 Camphor-ethanol clusters

The ABCluster method gave 19 structures for the camphor-ethanol complex with relative energies within 4 kJ mol^{-1} after optimization at the B3LYP-D3 level of theory. From this set, six low energy structures between $0\text{-}1.5 \text{ kJ mol}^{-1}$ were then re-optimized at the MP2 level of theory, as shown in Figure 3, which are denoted

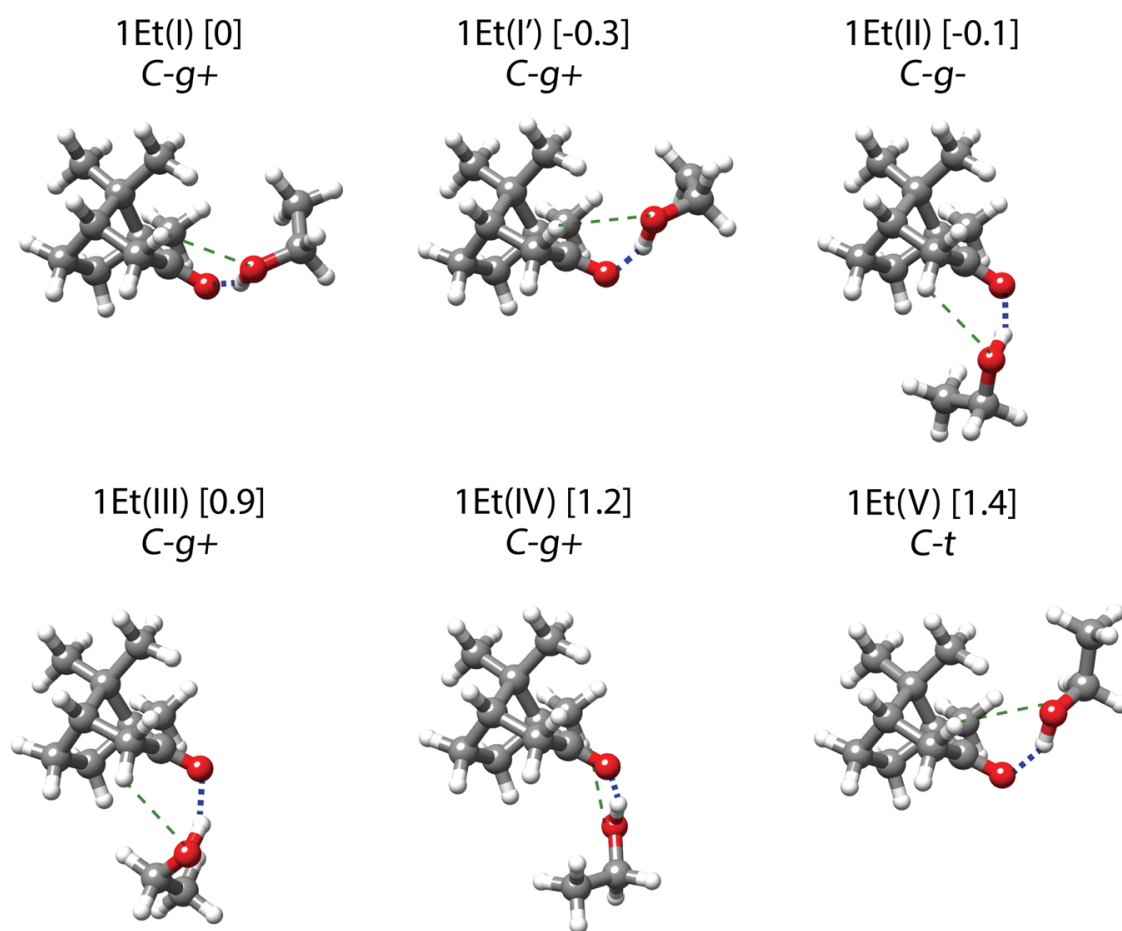


Figure 5.4: Structures of the most stable camphor–ethanol 1:1 complexes obtained at the *B3LYP-D3/aug-cc-pVTZ* level with relative zero-point-corrected energies in kJ mol^{-1} in square brackets. Hydrogen bonding and secondary interactions, either to a CH_2 or a CH_3 part of camphor, are indicated by dashed lines.

as C for camphor and ethanol configurations as *trans* (*t*), *gauche*(+) (*g+*), and *gauche*(-) (*g-*). All the six structures from both the level of calculations are real minima. Table 5.3 summarizes the calculated rotational constants and dipole-moment components for the six isomers. In all the six isomers, as in the camphor-water and camphor-methanol complexes, the ethanol molecule is bound by a well-defined O–H–O hydrogen bond to the keto group of camphor. In the six isomers, the O–O distance is ~ 2.9 Å and the OH–O bond angle is around 150° , from these two features the hydrogen bond can be determined as close to a strong bond [12]. In these complexes, 1Et(I), 1Et(I'), 1Et(II), 1Et(III), and 1Et(V), have a secondary interaction with a CH₂ part of camphor, and 1Et(IV) has a secondary interaction with a CH₃ group of camphor. As in the camphor-methanol case, complexes with secondary interactions to the CH₂ group in the α position are lower in energy than those with secondary interactions to a CH₃ group. In addition, the arrangement of the ethanol either in *trans* or *gauche* form also leads to some tertiary interactions with camphor, which are mainly dispersive. These tertiary interactions are between the methyl part of ethanol with different CH₂ or CH₃ moieties of camphor. The C–C distance of the methyl or methylene groups in these complexes are around 4 Å and the Van der Waal radii for methyl and methylene groups are 4 Å, this could potentially imply weak methyl-methyl interactions [Page 261, Reference [136]]. Structures of 1Et(I) and 1Et(I') obtained at the B3LYP-D3 level optimize to the same complex (namely 1Et(I)) at the MP2 level. Note here that at the B3LYP-D3 level 1Et(I') is the global minimum structure. The overall structures of 1Et(I) and 1Et(I') at the B3LYP-D3 level are very similar, and they only differ in a slight shift of the ethyl group. As in the study of camphor-methanol complexes, with the small energy difference and almost the same a-type dipole moment components between the camphor-ethanol complexes, it can be expected that all the six isomers of camphor-ethanol are present in the spectrum.

A section from the broadband spectrum of the camphor-ethanol mixture is shown in Figure 5.5. Four 1Et complexes were observed. The observed rotational constants are given in Table 4. To identify the complexes, quantum-chemical rotational constants obtained at the B3LYP-D3 and the MP2 level were compared with the experimental rotational constants. The most intense complex belongs to 1Et(I). The energy ordering is different at the two levels of calculation, but the differences in their rotational constants allow for their unequivocal assignment. By comparing the experimental rotational constants and the type of transitions (a-, b-, or c-type) with the calculated dipole moment components, the other observed 1Et complexes have been assigned to 1Et(II), 1Et(V) and 1Et(IV), based on their relative intensity with respect to Et(I). Theoretical predictions for 1Et(III) suggest that the spectrum consists of weak b-type and strong c-type transitions, but in all of the four observed

Table 5.3: Calculated rotational parameters for the lowest energy conformers of camphor-ethanol, performed at the B3LYP-D3/aug-cc-pVTZ and MP2/6-311++G(d,p) levels.

Parameters	1Et(I) [C- <i>g</i> +]		1Et(I') [C- <i>g</i> +]		1Et(II) [C- <i>g</i> -]	
	B3LYP	MP2	B3LYP	MP2	B3LYP	MP2
A (MHz)	1115.2	1115.2	1106.3	-	1198.6	1199.3
B (MHz)	412.2	425.4	432.5	-	401.9	398.0
C (MHz)	396.1	413.3	417.5	-	396.0	393.8
μ_a (D)	3.3	2.4	2.9	-	3.3	3.0
μ_b (D)	1.4	1.2	1.2	-	1.8	1.8
μ_c (D)	0.4	0.1	0.2	-	0.5	0.8
ΔE_{ZP} (kJ mol ⁻¹)	0.0	0.0	-0.3	-	-0.1	1.4
	1Et(III) [C- <i>g</i> +]		1Et(IV) [C- <i>g</i> +]		1Et(V) [C- <i>t</i>]	
	B3LYP	MP2	B3LYP	MP2	B3LYP	MP2
A (MHz)	1182.1	1183.0	1176.3	1175.5	1079.6	1088.4
B (MHz)	420.6	418.2	413.7	420.8	432.9	428.6
C (MHz)	414.0	411.3	397.0	405.2	406.7	404.6
μ_a (D)	4.0	3.8	3.3	2.6	2.8	2.6
μ_b (D)	0.7	0.4	2.1	2.0	1.7	1.5
μ_c (D)	2.0	2.0	0.3	0.2	0.2	0.4
ΔE_{ZP} (kJ mol ⁻¹)	0.9	1.1	1.2	1.0	1.4	0.2

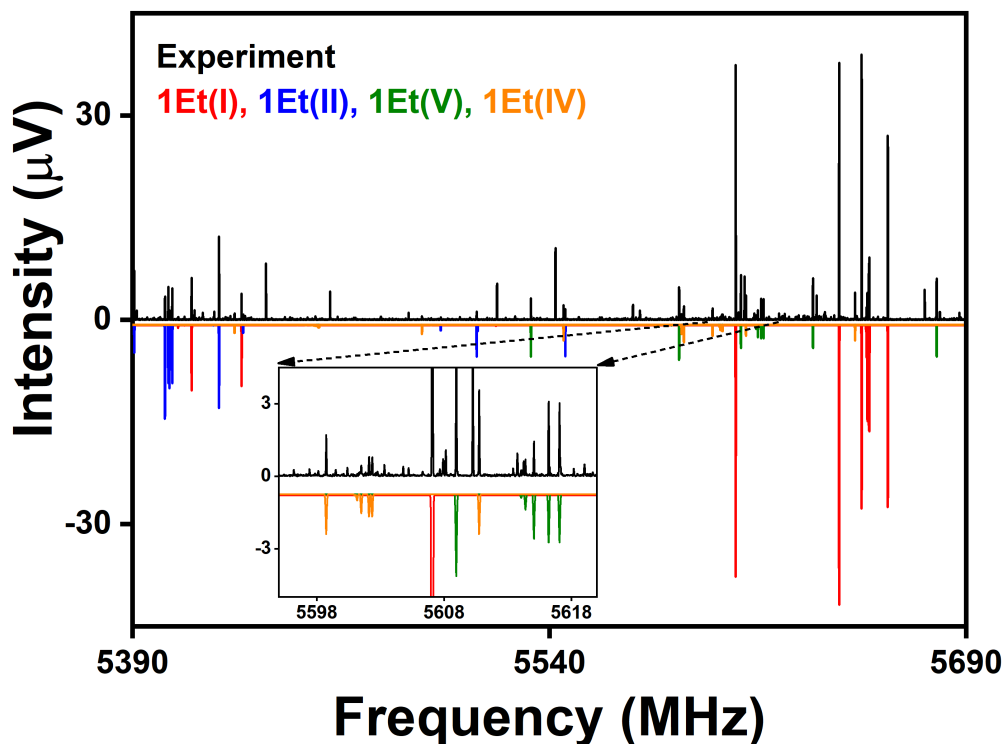


Figure 5.5: Portion of the 2-8 GHz spectrum (2 million acquisitions) of camphor-ethanol. The black trace shows the experimental spectrum, while the lower traces represent simulations based on fitted parameters for four camphor-ethanol 1:1 complexes (1Et(I) [red], 1Et(II) [blue], 1Et(V) [green], and 1Et(IV) [orange]) at a temperature of 1.5 K.

isomers, b-type transitions are stronger than c-type transitions, and so it can be concluded that 1Et(III) was not present in sufficient amount to be detected. In all the four observed isomers, no internal rotation splitting was observed due to the methyl end of ethanol, which is in agreement with other weakly bound complexes with ethanol [44].

The interplay between hydrogen bonding and dispersion interaction plays an important role in stabilizing the different 1:1 camphor-ethanol clusters. In 1Et(I), 1Et(II), and 1Et(IV), ethanol is in the *gauche* form, whereas in 1Et(V), it is in the *trans* form. In the case of the ethanol monomer, *trans* ethanol has been found to be slightly more stable than *gauche* ethanol [137], but when forming a complex, the

gauche form has been observed to be the most stable conformation of ethanol [44, 138]. These findings thus confirm that dispersion interactions, although weak, are able to overcome the conformational differences in complex formation.

CP-FTMW spectroscopy provides useful intensity information to estimate relative populations. The estimated population ratios of 25:7:4:1 based on the observed intensity ratios for 1Et(I), 1Et(II), 1Et(V), and 1Et(IV) do not correspond to those expected from theory for a sample at 298.5 K. Assuming that entropic differences between the four dimers are negligible and that the barriers between the isomers are sufficiently high so that no or only little interconversion occurs between them during the supersonic expansion, theory predicts a mixture composition of 1.8:1.8:1.1:1 from the energy difference of 0, -0.1, 1.2, 1.4 kJ mol⁻¹ at the B3LYP-D3 level and of 1.8:1:1.2:1.6 from the energy difference of 0, 1.4, 1 and 0.2 kJ mol⁻¹ at the MP2 level. This difference can be partially rationalized considering that the experimentally observed population ratios are related to the complex formation kinetics in the supersonic expansion, which can be frozen far from equilibrium if the barriers between the different isomers are sufficiently high. In the present case both energy factors (balance of attractive/repulsive forces) and kinetic factors seem to favor the formation of 1Et(I). This strong preference of 1Et(I) over the other isomers can also indicate rather low interconversion barriers so that the global minimum structure is strengthened during the supersonic expansion using neon as a carrier gas.

The experimental rotational constants have a good agreement with the calculations within 3% accuracy at both the levels, but clearly the energy ordering does not agree well with the observed abundance ratio of the complexes. An improvement in the available quantum-chemical methods is required for systems like camphor-alcohol, which have a flat potential energy surface to accurately predict the energy of these complexes.

Experimental structure of 1Et(I)

For 1Et(I), the signal-to-noise ratio was sufficient to observe all singly substituted ¹³C isotopologues in natural abundance (1.1 %). In the respective fits to asymmetric rotor Hamiltonians, the centrifugal distortion constants for the 12 isotopologues were fixed to the values obtained for the parent species (a summary of the rotational constants of the ¹³C isotopologues is given in Table 5.5). The Kraitchman equations (r_s structure [106]) were used to determine the experimental carbon backbone substitution structure for 1Et(I). To confirm that the structure is Et(I) and not Et(I'), another procedure was employed to determine the experimental positions of the atoms by using the r_0 -effective structure method [105]. The primary parameters

Table 5.4: Molecular parameters of the camphor-ethanol 1:1 isomers: results of the fit based on the experimentally observed transitions using the AABS software.

Parameters	1Et(I)	1Et(II)	1Et(V)	1Et(IV)
A (MHz)	1117.11284(34)	1199.97903(48)	1093.32171(47)	1179.69392(55)
B (MHz)	410.21456(15)	388.56843(16)	411.41706(26)	407.55863(20)
C (MHz)	397.49279(14)	383.31605(15)	390.42560(21)	392.53267(20)
Δ_J (kHz)	0.1580(12)	0.0971(10)	0.1880(14)	0.1580(14)
Δ_{JK} (kHz)	0.4260(35)	0.3787(39)	-0.1358(53)	0.1112(76)
δ_J (kHz)	—	—	0.0254(12)	—
σ^a (kHz)	7.4	7.2	6.3	7.6
N_{lines} (a/b/c)	127(56/55/16)	109(53/42/14)	84(57/27/0)	81(50/31/0)

^a σ is the standard deviation of the fit.

Table 5.5: Spectroscopic parameters for camphor-ethanol 1Et(I), and its 12 singly substituted ^{13}C isotopologues. Centrifugal distortion constants for all isotopologues are held fixed to the reported parent species values (denoted as 'a' in the table). The atom labeling is shown in Figure 5.6.

	A (MHz)	B (MHz)	C (MHz)	Δ_J (kHz)	Δ_{JK} (kHz)	N_{lines}	σ^a (kHz)
1Et(I)	1117.11284(34)	410.21456(15)	397.49279(14)	0.1580(12)	0.4260(35)	127	7.4
$^{13}\text{C}1$	1115.46(18)	410.11830(32)	397.34917(32)	a	a	25	6.1
$^{13}\text{C}2$	1110.96(17)	410.02209(31)	396.85072(30)	a	a	26	6.2
$^{13}\text{C}3$	1112.06(18)	408.93314(29)	396.54264(30)	a	a	24	4.5
$^{13}\text{C}4$	1112.86(17)	407.82619(42)	394.72929(38)	a	a	24	6.3
$^{13}\text{C}5$	1112.90(15)	407.99760(38)	395.63553(36)	a	a	25	5.1
$^{13}\text{C}6$	1114.63(31)	409.57081(48)	397.06552(50)	a	a	22	8.7
$^{13}\text{C}7$	1115.03(23)	409.41489(34)	396.72249(34)	a	a	26	6.4
$^{13}\text{C}8$	1107.86(22)	409.70612(36)	396.81754(34)	a	a	22	6.5
$^{13}\text{C}9$	1109.55(18)	407.63145(44)	394.52156(43)	a	a	24	6.8
$^{13}\text{C}10$	1104.18(21)	408.87246(41)	396.66438(39)	a	a	23	5.4
$^{13}\text{C}11$	1117.50(16)	404.48221(34)	392.13470(32)	a	a	25	5.6
$^{13}\text{C}12$	1112.84(14)	405.68836(30)	392.78646(31)	a	a	29	5.7

^a σ is the standard deviation of the fit.

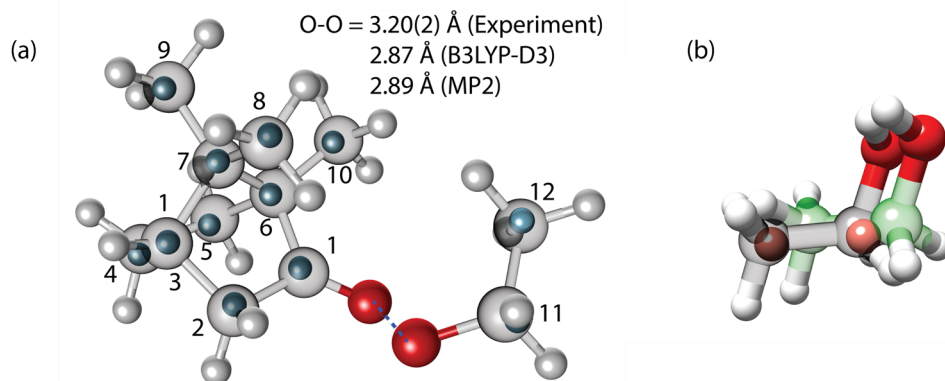


Figure 5.6: (a) Experimental structure of the most stable camphor-ethanol 1:1 cluster ($1Et(I)$). The r_0 experimental parameters (upper value) are obtained in each case from a fit to 39 moments of inertia: the parent and the twelve singly-substituted ^{13}C isotopologues. The O-O distance obtained from the fit is compared with results from B3LYP-D3/aug-cc-pVTZ and MP2/6-311++g(d,p) calculations. (b) Comparison of the position of ethanol in isomer $1Et(I')$ calculated at the B3LYP-D3 level (in green) with the experimental position (in orange) and the MP2 level calculated structure (in grey) of ethanol, illustrating the slight rotation between the two theoretical methods.

of the fit were the O-O distance and dihedral angles. The other parameters were taken from the MP2/6-311++G(d,p) calculation and allowed to float. Figure 5.6(a) shows the overlap of the experimental atom positions obtained from the r_0 method (blue atoms) with the calculated structure at the MP2 level of theory. In 5.6(b) the difference in the position of ethanol in $1Et(I')$, which is the global minimum at the B3LYP-D3 level, with the experimental position and MP2 level calculated structure of ethanol is shown. This analysis provides us with precise structural information, further confirming our assignment to Et(I).

5.1.3 SAPT calculations

The SAPT calculation results (Table 5.6) for the observed 1Me and 1Et complexes provide a useful insight into the individual contributions to their intermolecular energy for the observed dimers. Here, a comparison with the two previously observed camphor-H₂O 1:1 complexes is particularly interesting with respect to the role of dispersion interactions. The six dimers have significant electrostatic contribution, accounting for 55-65% of the overall attractive interaction. For the dispersion contributions, an increase in the contribution can be seen from camphor-water to camphor-ethanol complexes.

Table 5.6: Energy decompositions from a SAPT(0)/jun-cc-pVDZ analysis of the observed isomers of camphor-methanol (C-MeOH, 1Me) and camphor-ethanol (C-EtOH, 1Et) compared with camphor-water (C-H₂O, 1w) [86]

	C-H ₂ O		C-MeOH		EtOH			
	1w		1Me		1Et			
	(I)	(II)	(I)	(II)	(I)	(II)	(IV)	(V)
ΔE_{elst} (kJ mol ⁻¹)	-49.2	-46.0	-41.4	-47.8	-44.0	-43.7	-43.0	-41.5
	(65%)	(64%)	(61%)	(63%)	(58%)	(60%)	(57%)	(57%)
ΔE_{ind} (kJ mol ⁻¹)	-14.6	-13.6	-10.3	-14.9	-11.9	-12.3	-12.4	-10.5
	(19%)	(19%)	(15%)	(20%)	(16%)	(17%)	(16%)	(15%)
ΔE_{disp} (kJ mol ⁻¹)	-11.6	-12.6	-16.1	-13.8	-20.2	-17.7	-20.7	-20.4
	(15%)	(18%)	(24%)	(18%)	(27%)	(24%)	(27%)	(28%)
ΔE_{exch} (kJ mol ⁻¹)	43.6	42.1	37.3	44.9	42.7	43.1	43.9	42.1
ΔE_{tot} (kJ mol ⁻¹)	-31.8	-30.2	-30.5	-31.5	-33.4	-30.5	-32.2	-30.3

For the camphor-methanol complex 1Me(I), an increase in the dispersion energy contribution compared to 1w(I) is observed. The secondary interaction with the CH₂ moiety of camphor is stronger with methanol than water, resulting in an overall increase in dispersion interaction. For 1Me(II), all energy contributions are comparable to 1w(II), which points to only weak secondary interactions in this complex. Whereas, in all four observed camphor-ethanol complexes, apart from the secondary interactions, the flexibility of ethanol to be in either the *trans* or *gauche* form influences weak methyl-methyl dispersive interactions, and so an increase in the dispersion energy is observed. Furthermore, contributions from induction are around 15-20% and on the same order of magnitude for all six dimers. As induction interactions represent dipole-induce dipole interactions, a fair contribution of this interaction can be expected in these complexes due to the high polarizability of camphor and alcohol molecules.

5.1.4 Summary and conclusions

In this systematic study, we present the effect of the chain length of the aliphatic alcohols methanol and ethanol as binding partners to the ketone camphor by employing a combination of high-resolution broadband rotational spectroscopy in the gas phase and quantum-chemical calculations. A previous study on camphor-water complexes already showed the influence of dispersion interactions in cluster forma-

tion, where the secondary interaction of the oxygen atom of water is either with a CH_2 moiety or a CH_3 group of camphor. By replacing the non-interacting hydrogen of water with the CH_3 group, for camphor-methanol complexes, or the CH_2CH_3 group, for camphor-ethanol complexes, the increasing contribution from dispersion interactions led to many possible complex formations.

For camphor-methanol 1:1 complexes, two structures similar to 1:1 camphor-water complexes were identified, while in the case of camphor complexed with ethanol, four 1:1 complexes were observed, indicating the structural flexibility of the larger system. The experimental rotational constants for these complexes are in good agreement with those obtained at the B3LYP-D3 and the MP2 levels of theory. However, the energy ordering of the individual isomers is not well determined by theory. The subtle interplay between hydrogen bonding and dispersion interaction leads to complex potential energy surfaces for these systems, resulting in similar and almost iso-energetic structures such that the correct energy ordering cannot be predicted by these quantum-chemical methods.

An SAPT analysis revealed that for the 1Me(I) cluster the methyl group of methanol increases the contribution of dispersion interaction compared to 1w(I). This is further increased for the 1:1 camphor-ethanol complexes. The flexibility of ethanol allows the complex to maximize the dispersion interactions with camphor through secondary (CH-O) and tertiary (methyl-methyl) interactions. This increase in dispersion interactions further leads to an increase in the experimental O-O distance for 1Et(I) compared to 1w(I) from 2.854(4) Å to 3.20(4) Å. Though there is no experimental data for 1Me(I), the calculated O-O distance at the B3LYP-D3 level of theory is comparable to experimental value for 1w(I) and is 2.8 Å.

Chapter 6

Summary and outlook

The primary focus of this thesis is to systematically investigate the interplay of dispersion interactions and hydrogen bonding in weakly bound clusters. Until recently, the contributions from dispersion interactions on the total intra- and intermolecular energy in molecular systems were neglected because it was assumed that they were very small. However, recently, it has been realized that they can amount to tens of kcal mol⁻¹ with increasing size of molecular systems, and therefore have a significant contribution to the structure, stability, and reactivity of a chemical system. For this reason, model systems, where the interplay of hydrogen bonding and dispersion interactions are present, have been studied. The spectroscopy of these model systems in a cold environment in the gas phase gives spectroscopic data of these systems at low temperatures and in isolated conditions, and this data can be directly compared with various theoretical methods. Therefore, these model systems can also be used to benchmark quantum-chemical calculations because of their small energy difference between potentially different structural isomers arising from different docking positions.

For the studies reported in this thesis, chirped-pulse Fourier transform microwave (CP-FTMW) spectroscopy between 2-8 GHz was employed. The high resolution and high sensitivity of the technique allows us to detect and identify the precise molecular clusters with different docking sites in the gas phase. A microwave spectrum is like the fingerprint of the studied molecule or the molecular complex. Small changes in a molecular cluster, like a slight change in the orientation of the docking partner or mono-substitution by an isotope, results in changes in the moments of inertia, which further gives rise to different rotational spectrum for each species. The structure of a complex can in principle be calculated by systematic isotope substitution, but increasing system size can limit this. In such cases, it is often sufficient to compare theoretically predicted rotational constants and dipole moment components with experimental rotational constants and relative intensities to distinguish isomers and

achieve a clear assignment. In the present experimental setup, it is not possible to determine experimental values for the dipole moments. With the observed intensities of the type of transitions, i.e., *a*-, *b*- or *c*-type, and the number of transitions in the rotational spectrum, complexes with almost similar rotational constants can be differentiated between (which lie within the error limits of a calculation). Further, the energy ordering of different complexes in a model system can be obtained from the relative intensities of different species in the spectra. Additionally, information about the internal dynamics in a system can also be obtained via the CP-FTMW technique. Features such as the splitting of rotational transitions in a spectrum due to internal rotation of a methyl top can be utilized to determine the barrier to the methyl group rotation, which can be used to understand the orientation and chemical environment of the methyl group.

Three different experimental setups have been used in this thesis, two of which employ different frequency regions of the Hamburg COMPACT spectrometer. The experimental setup of this CP-FTMW spectrometer in the 2-8 GHz frequency range is presented in Chapter 3. During the course of this thesis, the Hamburg COMPACT spectrometer was extended to operate up to 18 GHz. A description of this extension is also presented in Chapter 3.

One focus of this thesis was the construction and development of a newly-designed segmented 18-26 GHz CP-FTMW spectrometer for astrochemical and analytical applications as presented in Chapter 3, Section 3.5. The principle design of the spectrometer is based on the segmented chirped-pulse approach and multi-train method and is different from the conventional approach of building CP-FTMW spectrometers, which is based on a single chirp spanning the full operating bandwidth. The advantage of this new design is that it can decrease the cost of microwave instruments, without compromising on performance, when compared to the first 18-26 GHz CP-FTMW spectrometer developed at the University of Virginia, USA [122] which was built using the conventional approach. Table 6.1 shows a cost comparison of this new design in the microwave region to the previously reported broadband CP-FTMW instruments [122]. By replacing the expensive traveling wave tube amplifier (TWTA) with a solid-state amplifier (SSA), the standard 10 MHz rubidium (Rb) oscillator with an internal temperature compensated crystal oscillator (TCXO) clock of the Valon synthesizer, and the oscilloscope with a digitizer card, it is possible to decrease the cost of the instrument by two-thirds, without compromising on the instrument's performance.

The performance of the segmented 18-26 GHz CP-FTMW spectrometer was characterized primarily with carbonyl sulfide (OCS). With the single chirp 18-26 GHz

CP-FTMW instrument, for the parent species of OCS after 200 000 averages using three nozzles, a signal-to-noise ratio (SNR) of 180 000:1 is obtained, which, on scaling for one nozzle, is 90 000:1. With the segmented chirp 18-26 GHz CP-FTMW spectrometer with one nozzle, we obtain a similar SNR of 100 000:1. With this example, and hexanal (as presented in Section 3.5.2, Dynamic range), it is confirmed that the performance of the segmented 18-26 GHz CP-FTMW spectrometer is similar to the single chirp 18-26 GHz CP-FTMW instrument, despite requiring less funds to construct. The state-of-the-art approach towards building microwave instruments shown in this work is also aimed at widening the use of rotational spectroscopy in research groups or in teaching laboratories without the need to invest in expensive components.

The frequency range of the segmented 18-26 GHz spectrometer overlaps with some modern radio observatories, for example, with the Jansky Very Large Array (JVLA) in Mexico, the Radio Telescope Effelsberg in Germany, the Australian Square Kilometer Array Pathfinder (ASKAP) in Australia, among others, enabling the studies of astrochemically relevant molecules from our laboratory to be more directly compared to observational datasets. This instrument has the capability to incorporate electrical discharge and laser ablation techniques to study unstable species or molecules with low vapor pressure, which will widen even further the scope of applicability of the low cost 18-26 GHz spectrometer. Electrical discharge experiments in

Table 6.1: An approximate cost comparison of the single chirp 18-26 GHz CP-FTMW spectrometer at UVa [122] with the segmented 18-26 GHz CP-FTMW spectrometer built and characterized in this thesis.

	CP-FTMW	Segmented CP-FTMW
Effective Rep. Rate	30 Hz	30 Hz
Power/GHz	5 W/GHz	6 W/GHz
Bandwidth	8 GHz/segment	800 MHz/segment
Number of nozzles	3	1
FID Duration	10 μ s	10 μ s
LNA	48 dB	45 dB
Cost	\sim €350,000	\sim €150,000
SNR of $^{18}\text{O}^{12}\text{C}^{32}\text{S}$ (200 000 averages)	90 000:1 ^a	100 000:1

^a scaled for one nozzle.

particular can help in determining reaction pathways for molecular formation in the harsh conditions of the interstellar medium. The frequency range of this instrument is also suited for studying medium-sized molecules or clusters, as their intensity at low temperature will be at their maximum in this region. Clusters of molecules with small binding partners such as hydrogen (H_2), which can be relevant for energy research to understand H_2 storage, or biologically relevant molecular systems can be studied, such as alanine with water, which can help in understanding intermolecular interactions in amino acid-water complexes.

The precise structural parameters and information on internal dynamics and intermolecular interactions that can be obtained with rotational spectroscopy are investigated with a number of model systems. The aim is to learn about the interplay of hydrogen bonding and dispersion interactions in a systematic approach within weakly bound complexes. The model systems investigated in this work can be further subdivided into three categories. The first category investigates the effect of dispersion interactions when complexes are dominated by a strong classical OH-O hydrogen bond (Chapter 5, Section 1). For this, complexes of camphor with methanol and ethanol have been investigated and compared with a previous study on camphor-water clusters. For the observed clusters of camphor-alcohol, the calculated energy difference between the different isomers in each system (two for camphor-methanol and four for camphor-ethanol) is within 2 kJ mol^{-1} (170 cm^{-1} or $0.48 \text{ kcal mol}^{-1}$). From calculations, the relative abundances of the different isomers in the experiment should be around half the intensity compared to their global minima. However, in their corresponding spectra, the observed population ratios for these complexes do not correspond to the calculated energy differences, and the global minima in both the systems are ten times more abundant than the next isomer. The obtained experimental rotational constants for these systems have a good agreement with the calculations within 3% accuracy at both the levels, but clearly the energy ordering does not agree well with the observed abundance ratio of the complexes. From the perspective of quantifying intermolecular energy using SAPT0 calculations, it can be seen that upon increasing the side-chain length of the alcohol, the contribution from dispersion interactions increases from 15% to 28%, whereas the hydrogen bonding contributions lie within 60-65% (Chapter 5, Table 5.6). The dispersion interactions in these complexes are mainly due to CH-O interactions. However, for camphor-ethanol, there is the presence of some weak additional interaction, which is dispersive, between the methyl end of ethanol and different CH_3 or CH_2 moieties of camphor. This additional stability results in doubling the contribution from dispersion interactions compared to the two complexes of camphor-water and increases the number of observed complexes.

The second category investigates complex formation when strong, classical OH-O hydrogen bond and weaker OH- π hydrogen bond sites are present (Chapter 4, Sections 1, 2, and 3) and how dispersion interactions play a role in such complexes. This work has been performed in collaboration with complementary FTIR and IR/UV double resonance techniques in a multi-spectroscopic approach. Phenyl vinyl ether (PVE), diphenyl ether (DPE), and dibenzofuran (DBF) have been chosen as the main molecules, as they offer equivalent (the lone pair of electrons on oxygen and the π cloud) binding sites. The binding partner is varied in size and complexity, from water, to methanol, tert-butyl alcohol (TBA), and adamantanol. Generally, small binding partners have a tendency to form an oxygen bound complex, and larger side groups are better dispersion energy donors. In the study of PVE with methanol, a strong oxygen bound complex and a weak π (phenyl) bound complex are observed. The oxygen bound complex also shows an additional CH-O interaction of methanol with the phenyl ring of PVE. In the formation of π bound complexes, other than phenyl bound, an ethylene bound complex could also form with additional CH-O interaction. However, its absence in the spectra implies that a CH- π interaction with the phenyl group is stronger than the ethylene group of PVE.

For DPE clusters with the small binding partners water and methanol, the π bound cluster is favored over the oxygen bound cluster, which is opposite to the results of the PVE-methanol study and counter-intuitive to the expected behavior. This observation is rationalized based on the increase in the dispersion energy due to the secondary CH-O interaction of water/methanol with a CH part of DPE in the two π bound clusters. This additional interaction influences the structure of the DPE monomer to twist to optimize the interaction area. On increasing the complexity and the size of the binding partner with DPE, again, counter-intuitive results are obtained. For the observed DPE-TBA (two isomers) and DPE-adamantanol (one isomer) clusters, the oxygen bound cluster is favored over the π bound cluster. In these clusters, the contribution from dispersion energy is similar/larger due to the larger interaction area of the phenyl ring and the tert-butyl or adamantyl moieties in the oxygen bound compared to π bound complexes. Again, in these clusters, this interaction causes the DPE monomer to twist to optimize the interaction area.

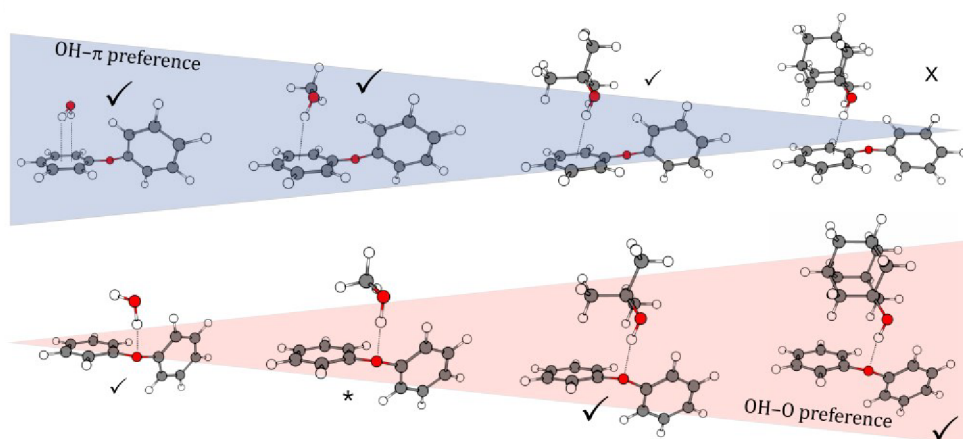
The influence of dispersion interactions with the structural change from PVE to DPE on complex formation is extended with DBF. In the observed DBF-water cluster (one isomer), for a small binding partner, an oxygen bound complex is favored, as expected. However, this is opposite to the DPE-water clusters. In the absence of the influence of secondary interactions on the π bound complex, which is present in the DPE-water π bound complex, the more favored oxygen bound complex is formed. The oxygen bound DBF-water complex also shows an additional CH-O

interaction of water with the CH part of DBF. When the binding partner is changed to methanol (two isomers are observed), the π bound complex takes precedence over the oxygen bound one, in line with the observation for DPE-methanol and opposite to PVE-methanol. The rigidity and aromaticity of DBF does not allow it to change its structure like DPE upon complex formation. In DBF, as in DPE, the observation of OH- π being more abundant is based on the increase in dispersion interaction, where the methyl group of methanol is interacting with the π cloud of DBF to increase the interaction area. In the DBF-TBA cluster (one isomer), the π bound complex is favored due to the larger interaction area of the tert-butyl group with the π cloud density of DBF. Hence, upon increasing the size and complexity of the binding partner, the preference of complex formation in DBF-alcohol clusters are reversed compared to DPE-alcohols, due to the influence of dispersion interactions in complex formation, as depicted in Figure 6.1.

In all of the ether/furan-alcohol clusters, dispersion interactions are significantly influencing the complex formation by secondary interactions. The presence of CH- π and CH-O interactions in these clusters is affecting the preference towards oxygen bound or π bound cluster formation, and the greater stability of a cluster is dependent on the strength of dispersion interaction. The observed complexes of ether/furan-alcohol have also been used to benchmark different theoretical methods, where various theoretical calculations at different levels have been performed in the collaboration. With the obtained results, it is not possible to choose a unique theoretical method which can be used to identify the observed complex abundance.

The third category of complexes investigates the formation of aggregates in the absence of strong classical hydrogen bond formation for the homodimers of DPE, DBF, and fluorene (FLU) (Chapter 4, Section 4). The three molecules are similar as they each have two phenyl rings, but differ in their flexibility, aromaticity, and planarity. FLU molecules also eliminate the influence of the oxygen heteroatom on dimer formation. In each case, one dimer structure has been observed, where the structure of these dimers are either formed by CH- π interactions or π - π interactions. Different sets of dispersion interactions are stabilizing each type of dimer, but their overall structures show similarities with respect to the relative position of oxygen atoms (DPE and DBF) or CH₂ groups (FLU). The subtle balance of CH-O, CH- π , or π - π interactions contributes to the stability of these homodimers. The dispersion contribution of the dimers is within 60-70% of the attractive part of the intermolecular energy, but interestingly, the FLU dimer is the strongest when the binding energies are compared. Due to the parallel stacked structure of the FLU dimer, the overlap between the two molecules in the dimer increases, resulting in larger binding energy.

Diphenyl ether-alcohol clusters



Dibenzofuran-alcohol clusters

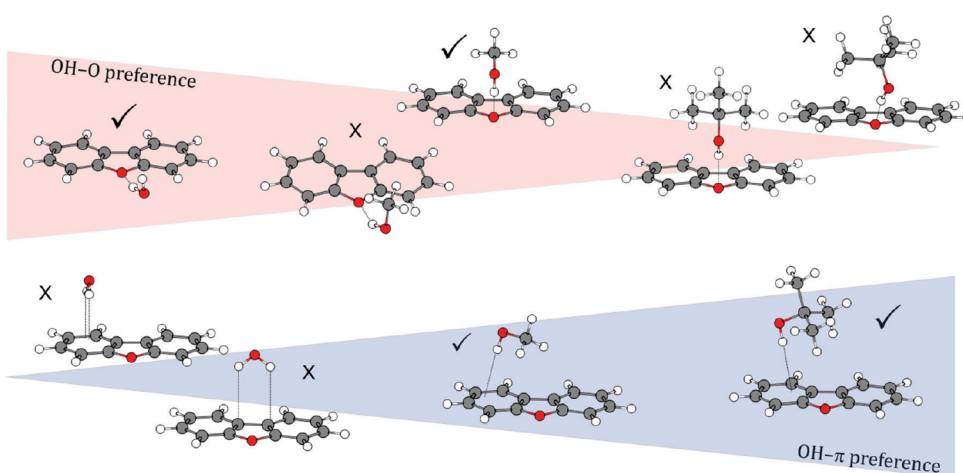


Figure 6.1: Schematic overview of the transition of binding preferences from oxygen-bound to π -bound structures with increasingly larger alcohol binding partners in diphenyl ether-alcohol and dibenzofuran-alcohol complexes. The tick marks represent that the complexes were observed in the multi-spectroscopic study, and the size of the tick indicates their abundance determined by microwave spectroscopy. The cross mark represents that these complexes were not observed experimentally. The star indicates this complex was not observed in the microwave spectrum. The figure is adapted from the publications presented in Chapter 4, Sections 4.1.2 and 4.1.3.

In conclusion, the binding preference of the different systems presented in this work significantly depends on the contribution of dispersion interactions, and when this contribution increases, the preferred complex formation can even cause a shift in preferred binding from hydrogen-bonded to dispersion bound or vice versa. For all of the above model systems, the overall performance of the B3LYP-D3 and B3LYP-D3(BJ) levels of theory have shown a good agreement between the theoretical rotational constants and the experimental rotational constants. However, the comparison between experiment and the various levels of theory performed within this work revealed some inconsistencies, especially with respect to energy ordering as predicted by the theoretical methods. The comparisons show that when dispersion is more pronounced, the energy ordering cannot be effectively captured by theory. The experimental results presented in this work can further be used to serve as cases for testing the performance of quantum-chemical methods, which aim for a better description of dispersion.

To further build on the studies presented here, it will be interesting to extend the systematic approach to other, related molecules, such as complexes of camphor with 1,2-propanediol ($C_3H_8O_2$) and fenchol ($C_{10}H_{18}O$). The increasing length and bulkiness of the side group of the respective alcohol will help in quantifying the effect of dispersion interaction on complex formation. Changing some of the molecular features and studying them with different binding partners or their homodimers will help in defining a molecular scale to the role of dispersion interaction on cluster formation. Examples of such small changes in the main molecule will be from an ether group to a ketone (as in benzophenone $C_{13}H_{10}O$), or adding a CH_2 group in DBF (as in xanthene $CH_2[C_6H_4]_2O$), or changing the heteroatom from an oxygen in DBF to an amine (as in carbazole $C_{12}H_9N$).

In this thesis, the interplay of hydrogen bonding and dispersion forces on intermolecular interactions has been studied, where the classical OH-O hydrogen bond interaction, weak hydrogen bonds (OH- π , CH- π , CH-O), and π - π dispersion interactions were the main focus. Nevertheless, to better understand the relevance of intermolecular interactions in biological complexes, there are other unconventional hydrogen bonds (such as N-H \cdots S, C-H \cdots Y, where Y= nitrogen or sulphur) where the influence of dispersion interactions have to be investigated in great depth. Biological molecules with the nitrogen atom, such as purine and pyrimidine DNA bases, have been studied using microwave spectroscopy [139, 140]. The next step would be, for example, to investigate their interaction with water. However, the presence of more than one nitrogen atom in a molecule can make the microwave spectrum complicated to analyze. The nuclear spin of nitrogen is one, which creates hyperfine structures in the spectra, and thus can lead to a complex hyperfine pattern. This,

combined with potential splitting due to water tunneling motions in the spectra of complexes, can be challenging. Therefore, a molecule closely resembling the DNA bases and exhibiting only one nitrogen atom, such as isoindoline (C_8H_9N), would be a good starting point. Amino acid molecules containing sulfur, such as cysteine ($C_3H_7NO_2S$) [141] and allyl cysteine ($C_6H_{11}NO_2S$), and their interaction with water or other small binding partners can be studied to expand the understanding of C-H \cdots S bonds. These molecules are flexible and also contain nitrogen and oxygen atoms, so their interaction with water can be used to explore conformational flexibility under solute-solvent interactions and understand the preferred interaction sites.

Other than biological systems, intermolecular interactions are also relevant in other fields of chemistry such as catalytic chemistry, where the solute-solvent interactions play an important role in increasing the percentage yield of a reaction pathway; or astrochemistry, to understand ice grain formation and chemical processes on these grains. With the latest developments in rotational spectroscopy, as also presented as part of this thesis, the effect of dispersion interactions in molecular complexes will be explored in these different fields of chemistry.

Bibliography

- [1] A. G. Street and S. L. Mayo, “Intrinsic β -sheet propensities result from van der Waals interactions between side chains and the local backbone”, *Proceedings of the National Academy of Sciences* **96**, 9074–9076 (1999).
- [2] K. Autumn, M. Sitti, Y. A. Liang, A. M. Peattie, W. R. Hansen, S. Sponberg, T. W. Kenny, R. Fearing, J. N. Israelachvili, and R. J. Full, “Evidence for van der Waals adhesion in gecko setae”, *Proceedings of the National Academy of Sciences* **99**, 12252–12256 (2002).
- [3] K. S. Pitzer and E. Catalano, “Electronic Correlation in Molecules. III. The Paraffin Hydrocarbons¹”, *Journal of the American Chemical Society* **78**, 4844–4846 (1956).
- [4] P. Hyldgaard and T. S. Rahman, “Van der Waals interactions in advanced materials, in memory of David C Langreth”, *Journal of Physics: Condensed Matter* **24**, 420201 (2012).
- [5] W. Klemperer, “Intermolecular Interactions”, *Science* **257**, 887–888 (1992).
- [6] J. P. Wagner and P. R. Schreiner, “London Dispersion in Molecular Chemistry-Reconsidering Steric Effects”, *Angewandte Chemie International Edition* **54**, 12274–12296 (2015).
- [7] A. Stone, *The Theory of Intermolecular Forces* (Oxford, Jan. 2013).
- [8] S. Y. Buhmann, *Dispersion Forces I: Macroscopic Quantum Electrodynamics and Ground-State Casimir, Casimir-Polder and van der Waals Forces* (Springer, Jan. 2013).
- [9] P. R. Schreiner, “Dispersion interactions”, *Beilstein Journal of Organic Chemistry* **14**, 3076–3077 (2018).
- [10] W. M. Latimer and W. H. Rodebush, “Polarity and ionization from the standpoint of the Lewis theory of valence.”, *Journal of the American Chemical Society* **42**, 1419–1433 (1920).

- [11] E. Arunan, “Volume 100 of the Journal of the Indian Institute of Science and 100 Years of the Latimer and Rodebush Paper on Hydrogen Bonding”, *Journal of the Indian Institute of Science* **100**, 3–4 (2020).
- [12] E. Arunan, G. R. Desiraju, R. A. Klein, J. Sadlej, S. Scheiner, I. Alkorta, D. C. Clary, R. H. Crabtree, J. J. Dannenberg, P. Hobza, H. G. Kjaergaard, A. C. Legon, B. Mennucci, and D. J. Nesbitt, “Definition of the hydrogen bond (IUPAC Recommendations 2011)”, *Pure and Applied Chemistry* **83**, 1637–1641 (2011).
- [13] N. Mohan and C. H. Suresh, “A Molecular Electrostatic Potential Analysis of Hydrogen, Halogen, and Dihydrogen Bonds”, *The Journal of Physical Chemistry A* **118**, 1697–1705 (2014).
- [14] D. J. Liptrot and P. P. Power, “London dispersion forces in sterically crowded inorganic and organometallic molecules”, *Nature Reviews Chemistry* **1**, 1–12 (2017).
- [15] F. London, “Zur Theorie und Systematik der Molekularkräfte”, *Zeitschrift für Physik* **63**, 245–279 (1930).
- [16] M. A. Strauss and H. A. Wegner, “Molecular Systems for the Quantification of London Dispersion Interactions”, *European Journal of Organic Chemistry* **2019**, 295–302 (2019).
- [17] E. A. Colbourn and A. E. Douglas, “The spectrum and ground state potential curve of Ar₂”, *The Journal of Chemical Physics* **65**, 1741–1745 (1976).
- [18] T. Weber, E. Riedle, H. J. Neusser, and E. W. Schlag, “Van der Waals bond lengths and electronic spectral shifts of the benzene-Kr and benzene-Xe complexes”, *Chemical Physics Letters* **183**, 77–83 (1991).
- [19] A. Mukhopadhyay, W. T. S. Cole, and R. J. Saykally, “The water dimer I: Experimental characterization”, *Chemical Physics Letters* **633**, 13–26 (2015).
- [20] E. Bourgeat-Lami, J. Faucheu, and A. Noël, “Latex routes to graphene-based nanocomposites”, *Polymer Chemistry* **6**, 5323–5357 (2015).
- [21] *Control of London dispersion interactions in molecular chemistry*, <http://www.uni-giessen.de/fbz/fb08/dispersion/londondispersion>.
- [22] W. Sun, O. P. Sogeke, W. G. D. P. Silva, and J. van Wijngaarden, “Dispersion-driven conformational preference in the gas phase: Microwave spectroscopic and theoretical study of allyl isocyanate”, *The Journal of Chemical Physics* **151**, 194304 (2019).
- [23] C. Møller and M. S. Plesset, “Note on an Approximation Treatment for Many-Electron Systems”, *Physical Review* **46**, 618–622 (1934).

- [24] S. Grimme, J. Antony, S. Ehrlich, and H. Krieg, “A consistent and accurate ab initio parametrization of density functional dispersion correction (DFT-D) for the 94 elements H-Pu”, *The Journal of Chemical Physics* **132**, 154104 (2010).
- [25] S. Grimme, S. Ehrlich, and L. Goerigk, “Effect of the damping function in dispersion corrected density functional theory”, *Journal of Computational Chemistry* **32**, 1456–1465 (2011).
- [26] A. D. Becke, “Density-functional thermochemistry. III. The role of exact exchange”, *The Journal of Chemical Physics* **98**, 5648–5652 (1993).
- [27] C. Lee, W. Yang, and R. G. Parr, “Development of the Colle-Salvetti correlation-energy formula into a functional of the electron density”, *Physical Review B* **37**, 785–789 (1988).
- [28] C. Pérez, J. C. López, S. Blanco, and M. Schnell, “Water-Induced Structural Changes in Crown Ethers from Broadband Rotational Spectroscopy”, *The Journal of Physical Chemistry Letters* **7**, 4053–4058 (2016).
- [29] S. Rösel, H. Quanz, C. Logemann, J. Becker, E. Mossou, L. Cañadillas-Delgado, E. Caldeweyher, S. Grimme, and P. R. Schreiner, “London Dispersion Enables the Shortest Intermolecular Hydrocarbon H...H Contact”, *Journal of the American Chemical Society* **139**, 7428–7431 (2017).
- [30] M. Heger, J. Altnöder, A. Poblitzki, and M. A. Suhm, “To π or not to π - how does methanol dock onto anisole?”, *Physical Chemistry Chemical Physics* **17**, 13045–13052 (2015).
- [31] H. C. Gottschalk, J. Altnöder, M. Heger, and M. A. Suhm, “Control over the Hydrogen-Bond Docking Site in Anisole by Ring Methylation”, *Angewandte Chemie International Edition* **55**, 1921–1924 (2016).
- [32] J. Altnöder, S. Oswald, and M. A. Suhm, “Phenyl- vs Cyclohexyl-Substitution in Methanol: Implications for the OH Conformation and for Dispersion-Affected Aggregation from Vibrational Spectra in Supersonic Jets”, *The Journal of Physical Chemistry A* **118**, 3266–3279 (2014).
- [33] J. Řezáč, D. Nachtigallová, F. Mazzoni, M. Pasquini, G. Pietraperzia, M. Baccucci, K. Müller-Dethlefs, and P. Hobza, “Binding Energies of the π -Stacked Anisole Dimer: New Molecular Beam-Laser Spectroscopy Experiments and CCSD(T) Calculations”, *Chemistry – A European Journal* **21**, 6740–6746 (2015).
- [34] N. A. Seifert, A. L. Steber, J. L. Neill, C. Pérez, D. P. Zaleski, B. H. Pate, and A. Lesarri, “The interplay of hydrogen bonding and dispersion in phenol dimer and trimer: structures from broadband rotational spectroscopy”, *Physical Chemistry Chemical Physics* **15**, 11468–11477 (2013).

- [35] N. A. Seifert, A. S. Hazrah, and W. Jäger, “The 1-Naphthol Dimer and Its Surprising Preference for π – π Stacking over Hydrogen Bonding”, *The Journal of Physical Chemistry Letters* **10**, 2836–2841 (2019).
- [36] D. Schmitz, V. Alvin Shubert, T. Betz, and M. Schnell, “Multi-resonance effects within a single chirp in broadband rotational spectroscopy: The rapid adiabatic passage regime for benzonitrile”, *Journal of Molecular Spectroscopy, Broadband Rotational Spectroscopy* **280**, 77–84 (2012).
- [37] G. B. Park and R. W. Field, “Perspective: The first ten years of broadband chirped pulse Fourier transform microwave spectroscopy”, *The Journal of Chemical Physics* **144**, 200901 (2016).
- [38] D. Loru, M. A. Bermúdez, and M. E. Sanz, “Structure of fenchone by broadband rotational spectroscopy”, *The Journal of Chemical Physics* **145**, 074311 (2016).
- [39] A. Lesarri, S. Mata, J. C. López, and J. L. Alonso, “A laser-ablation molecular-beam Fourier-transform microwave spectrometer: The rotational spectrum of organic solids”, *Review of Scientific Instruments* **74**, 4799–4804 (2003).
- [40] M. Schnell, U. Erlekam, P. R. Bunker, G. von Helden, J.-U. Grabow, G. Meijer, and A. van der Avoird, “Structure of the Benzene Dimer-Governed by Dynamics”, *Angewandte Chemie International Edition* **52**, 5180–5183 (2013).
- [41] W. Caminati, “Microwave Spectroscopy of Large Molecules and Molecular Complexes”, in *Handbook of High-resolution Spectroscopy* (American Cancer Society, 2011).
- [42] I. Peña, A. M. Daly, C. Cabezas, S. Mata, C. Bermúdez, A. Niño, J. C. López, J.-U. Grabow, and J. L. Alonso, “Disentangling the Puzzle of Hydrogen Bonding in Vitamin C”, *The Journal of Physical Chemistry Letters* **4**, 65–69 (2013).
- [43] J. Thomas, O. Sukhorukov, W. Jäger, and Y. Xu, “Direct Spectroscopic Detection of the Orientation of Free OH Groups in Methyl Lactate–(Water)_{1,2} Clusters: Hydration of a Chiral Hydroxy Ester”, *Angewandte Chemie International Edition* **53**, 1156–1159 (2014).
- [44] D. Loru, I. Peña, and M. E. Sanz, “The role of secondary interactions on the preferred conformers of the fenchone–ethanol complex”, *Physical Chemistry Chemical Physics* **21**, 2938–2945 (2019).

- [45] S. Melandri, M. E. Sanz, W. Caminati, P. G. Favero, and Z. Kisiel, “The Hydrogen Bond between Water and Aromatic Bases of Biological Interest: An Experimental and Theoretical Study of the 1:1 Complex of Pyrimidine with Water”, *Journal of the American Chemical Society* **120**, 11504–11509 (1998).
- [46] V. A. Shubert, D. Schmitz, D. Patterson, J. M. Doyle, and M. Schnell, “Identifying Enantiomers in Mixtures of Chiral Molecules with Broadband Microwave Spectroscopy”, *Angewandte Chemie International Edition* **53**, 1152–1155 (2014).
- [47] D. Patterson and M. Schnell, “New studies on molecular chirality in the gas phase: enantiomer differentiation and determination of enantiomeric excess”, *Physical Chemistry Chemical Physics* **16**, 11114–11123 (2014).
- [48] S. R. Domingos, C. Pérez, and M. Schnell, “Sensing Chirality with Rotational Spectroscopy”, *Annual Review of Physical Chemistry* **69**, 499–519 (2018).
- [49] *European Southern Observatory - Atacama Large Millimeter/submillimeter Array*.
- [50] *Herschel Space Observatory*, <https://sci.esa.int/web/herschel/>.
- [51] E. Herbst and J. T. Yates, “Introduction: Astrochemistry”, *Chemical Reviews* **113**, 8707–8709 (2013).
- [52] E. F. v. Dishoeck, “Astrochemistry: overview and challenges”, *Proceedings of the International Astronomical Union* **13**, 3–22 (2017).
- [53] P. Banerjee and T. Chakraborty, “Weak hydrogen bonds: insights from vibrational spectroscopic studies”, *International Reviews in Physical Chemistry* **37**, 83–123 (2018).
- [54] M. A. Suhm, “Hydrogen Bond Dynamics in Alcohol Clusters”, in *Advances in Chemical Physics* (John Wiley & Sons, Ltd, 2008), pp. 1–57.
- [55] M. Mons, E. G. Robertson, and J. P. Simons, “Intra- and Intermolecular π -Type Hydrogen Bonding in Aryl Alcohols: UV and IR-UV Ion Dip Spectroscopy”, *The Journal of Physical Chemistry A* **104**, 1430–1437 (2000).
- [56] K. Schwing and M. Gerhards, “Investigations on isolated peptides by combined IR/UV spectroscopy in a molecular beam - structure, aggregation, solvation and molecular recognition”, *International Reviews in Physical Chemistry* **35**, 569–677 (2016).
- [57] J. Lehmann, E. Kleinpeter, and J. Krechl, “¹H NMR spectroscopy as a probe of intermolecular interactions in β -cyclodextrin inclusion compounds”, *Journal of inclusion phenomena and molecular recognition in chemistry* **10**, 233–239 (1991).

- [58] J. Fattori, F. H. S. Rodrigues, J. G. M. Pontes, A. Paula Espíndola, and L. Tasic, “Chapter 6 - Monitoring Intermolecular and Intramolecular Interactions by NMR Spectroscopy”, in *Applications of NMR Spectroscopy: Volume 3*, edited by A. ur-Rahman and M. I. Choudhary (Bentham Science Publishers, Jan. 2015), pp. 180–266.
- [59] K. Wüthrich, “The way to NMR structures of proteins”, *Nature Structural Biology* **8**, 923–925 (2001).
- [60] L. E. Kay, “NMR studies of protein structure and dynamics”, *Journal of Magnetic Resonance* **173**, 193–207 (2005).
- [61] P. Wernet, K. Kunnus, S. Schreck, W. Quevedo, R. Kurian, S. Techert, F. M. F. de Groot, M. Odellius, and A. Föhlisch, “Dissecting Local Atomic and Intermolecular Interactions of Transition-Metal Ions in Solution with Selective X-ray Spectroscopy”, *The Journal of Physical Chemistry Letters* **3**, 3448–3453 (2012).
- [62] M. Nagasaka, H. Yuzawa, and N. Kosugi, “Intermolecular Interactions of Pyridine in Liquid Phase and Aqueous Solution Studied by Soft X-ray Absorption Spectroscopy”, *Zeitschrift für Physikalische Chemie* **232**, 705–722 (2018).
- [63] J. L. Derissen, “A reinvestigation of the molecular structure of acetic acid monomer and dimer by gas electron diffraction”, *Journal of Molecular Structure* **7**, 67–80 (1971).
- [64] I. N. Kolesnikova, A. N. Rykov, M. V. Shuvalov, and I. F. Shishkov, “Internal rotation and intramolecular hydrogen bonding in thiosalicylamide: gas phase electron diffraction study supported by quantum chemical calculations”, *Structural Chemistry* **30**, 1993–2001 (2019).
- [65] A. A. Fokin, T. S. Zhuk, S. Blomeyer, C. Pérez, L. V. Chernish, A. E. Pashenko, J. Antony, Y. V. Vishnevskiy, R. J. F. Berger, S. Grimme, C. Logemann, M. Schnell, N. W. Mitzel, and P. R. Schreiner, “Intramolecular London Dispersion Interaction Effects on Gas-Phase and Solid-State Structures of Diamondoid Dimers”, *Journal of the American Chemical Society* **139**, 16696–16707 (2017).
- [66] M. Gao, C. Lu, H. Jean-Ruel, L. C. Liu, A. Marx, K. Onda, S.-y. Koshihara, Y. Nakano, X. Shao, T. Hiramatsu, G. Saito, H. Yamochi, R. R. Cooney, G. Moriena, G. Sciaini, and R. J. D. Miller, “Mapping molecular motions leading to charge delocalization with ultrabright electrons”, *Nature* **496**, 343–346 (2013).
- [67] K. B. McAfee, R. H. Hughes, and E. B. Wilson, “A Stark-Effect Microwave Spectrograph of High Sensitivity”, *Review of Scientific Instruments* **20**, 821–826 (1949).

- [68] G. Ehrenstein, C. H. Townes, and M. J. Stevenson, “Ground State Λ -Doubling Transitions of OH Radical”, *Physical Review Letters* **3**, 40–41 (1959).
- [69] R. H. Dicke and R. H. Romer, “Pulse Techniques in Microwave Spectroscopy”, *Review of Scientific Instruments* **26**, 915–928 (1955).
- [70] D. G. Scroggin, J. M. Riveros, and E. B. Wilson, “Microwave spectrum and rotational isomerism of ethyl nitrate”, *The Journal of Chemical Physics* **60**, 1376–1385 (1974).
- [71] R. G. Ford and R. A. Beaudet, “Microwave Spectrum, Barrier to Internal Rotation, and Dipole Moment of cis-3-Pentene-1-yne”, *The Journal of Chemical Physics* **55**, 3110–3113 (1971).
- [72] J. B. Anderson, R. P. Andres, and J. B. Fenn, “Supersonic Nozzle Beams”, in *Advances in Chemical Physics* (John Wiley & Sons, Ltd, 2007), pp. 275–317.
- [73] T. R. Dyke, B. J. Howard, and W. Klemperer, “Radiofrequency and Microwave Spectrum of the Hydrogen Fluoride Dimer; a Nonrigid Molecule”, *The Journal of Chemical Physics* **56**, 2442–2454 (1972).
- [74] R. E. Smalley, L. Wharton, and D. H. Levy, “Molecular optical spectroscopy with supersonic beams and jets”, *Accounts of Chemical Research* **10**, 139–145 (1977).
- [75] J. Ekkers and W. H. Flygare, “Pulsed microwave Fourier transform spectrometer”, *Review of Scientific Instruments* **47**, 448–454 (1976).
- [76] E. J. Campbell, L. W. Buxton, T. J. Balle, M. R. Keenan, and W. H. Flygare, “The gas dynamics of a pulsed supersonic nozzle molecular source as observed with a Fabry–Perot cavity microwave spectrometer”, *The Journal of Chemical Physics* **74**, 829–840 (1981).
- [77] E. J. Campbell, L. W. Buxton, T. J. Balle, and W. H. Flygare, “The theory of pulsed Fourier transform microwave spectroscopy carried out in a Fabry–Perot cavity: Static gas”, *The Journal of Chemical Physics* **74**, 813–828 (1981).
- [78] T. J. Balle and W. H. Flygare, “Fabry–Perot cavity pulsed Fourier transform microwave spectrometer with a pulsed nozzle particle source”, *Review of Scientific Instruments* **52**, 33–45 (1981).
- [79] *NMR Spectroscopy: Basic Principles, Concepts and Applications in Chemistry, 3rd Edition — Wiley.*
- [80] J. Grabow, W. Stahl, and H. Dreizler, “A multioctave coaxially oriented beam-resonator arrangement Fourier-transform microwave spectrometer”, *Review of Scientific Instruments* **67**, 4072–4084 (1996).

- [81] Z. Kisiel, O. Desyatnyk, E. Białkowska-Jaworska, and L. Pszczółkowski, “The structure and electric dipole moment of camphor determined by rotational spectroscopy”, *Physical Chemistry Chemical Physics* **5**, 820–826 (2003).
- [82] S. Blanco, A. Lesarri, J. C. López, and J. L. Alonso, “The Gas-Phase Structure of Alanine”, *Journal of the American Chemical Society* **126**, 11675–11683 (2004).
- [83] G. G. Brown, B. C. Dian, K. O. Douglass, S. M. Geyer, S. T. Shipman, and B. H. Pate, “A broadband Fourier transform microwave spectrometer based on chirped pulse excitation”, *Review of Scientific Instruments* **79**, 053103 (2008).
- [84] D. P. Zaleski, S. L. Stephens, and N. R. Walker, “A perspective on chemistry in transient plasma from broadband rotational spectroscopy”, *Physical Chemistry Chemical Physics* **16**, 25221–25228 (2014).
- [85] J. L. Neill, B. J. Harris, A. L. Steber, K. O. Douglass, D. F. Plusquellic, and B. H. Pate, “Segmented chirped-pulse Fourier transform submillimeter spectroscopy for broadband gas analysis”, *Optics Express* **21**, 19743–19749 (2013).
- [86] C. Pérez, A. Krin, A. L. Steber, J. C. López, Z. Kisiel, and M. Schnell, “Wetting Camphor: Multi-Isotopic Substitution Identifies the Complementary Roles of Hydrogen Bonding and Dispersive Forces”, *The Journal of Physical Chemistry Letters* **7**, 154–160 (2016).
- [87] C. Medcraft, S. Zinn, M. Schnell, A. Poblitzki, J. Altnöder, M. Heger, M. A. Suhm, D. Bernhard, A. Stamm, F. Dietrich, and M. Gerhards, “Aromatic embedding wins over classical hydrogen bonding – a multi-spectroscopic approach for the diphenyl ether–methanol complex”, *Physical Chemistry Chemical Physics* **18**, 25975–25983 (2016).
- [88] M. Born and R. Oppenheimer, “Zur Quantentheorie der Molekeln”, *Annalen der Physik* **389**, 457–484 (1927).
- [89] F. Merkt and M. Quack, “Molecular Quantum Mechanics and Molecular Spectra, Molecular Symmetry, and Interaction of Matter with Radiation”, in *Handbook of High-resolution Spectroscopy* (American Cancer Society, 2011).
- [90] P. R. Bunker and P. Jensen, *Molecular Symmetry and Spectroscopy, 2nd Ed.* (NRC Research Press, Jan. 2006).
- [91] W. Gordy and R. L. Cook, *Microwave Molecular Spectra* (Interscience Publishers, 1970).
- [92] C. H. Townes and J. A. Schawlow Arthur L., *Microwave spectroscopy* (New York : Dover Publications, 1975).

- [93] J. K. G. Watson, “Determination of Centrifugal Distortion Coefficients of Asymmetric-Top Molecules”, *The Journal of Chemical Physics* **46**, 1935–1949 (1967).
- [94] J. K. G. Watson, “Simplification of the molecular vibration-rotation hamiltonian”, *Molecular Physics* **15**, 479–490 (1968).
- [95] S. A. Cooke and P. Ohring, *Decoding Pure Rotational Molecular Spectra for Asymmetric Molecules*, Research article, 2013.
- [96] M. Gerhards, M. Schmitt, K. Kleinermanns, and W. Stahl, “The structure of phenol(H₂O) obtained by microwave spectroscopy”, *The Journal of Chemical Physics* **104**, 967–971 (1996).
- [97] D. F. Plusquellic, R. D. Suenram, B. Maté, J. O. Jensen, and A. C. Samuels, “The conformational structures and dipole moments of ethyl sulfide in the gas phase”, *JChPh* **115**, 3057–3067 (2001).
- [98] C. M. Western, “PGOPHER: A program for simulating rotational, vibrational and electronic spectra”, *Journal of Quantitative Spectroscopy and Radiative Transfer, Satellite Remote Sensing and Spectroscopy: Joint ACE-Odin Meeting*, October 2015 **186**, 221–242 (2017).
- [99] Z. Kisiel, L. Pszczółkowski, I. R. Medvedev, M. Winnewisser, F. C. De Lucia, and E. Herbst, “Rotational spectrum of trans–trans diethyl ether in the ground and three excited vibrational states”, *Journal of Molecular Spectroscopy* **233**, 231–243 (2005).
- [100] Z. Kisiel, L. Pszczółkowski, B. J. Drouin, C. S. Brauer, S. Yu, J. C. Pearson, I. R. Medvedev, S. Fortman, and C. Neese, “Broadband rotational spectroscopy of acrylonitrile: Vibrational energies from perturbations”, *Journal of Molecular Spectroscopy, Broadband Rotational Spectroscopy* **280**, 134–144 (2012).
- [101] H. Hartwig and H. Dreizler, “The Microwave Spectrum of trans-2,3-Dimethyloxirane in Torsional Excited States”, *Zeitschrift für Naturforschung A* **51**, 923–932 (2014).
- [102] *PROSPE Programs for ROtational SPEctroscopy, at IFPAN*, <http://www.ifpan.edu.pl/~kisiel/prospe.htm>.
- [103] J. D. Dunitz, “Accurate molecular structures, their determination and importance. (IUCr Monograph on Crystallography No. 1) edited by A. Domenicano and I. Hargittai”, *Acta Crystallographica Section B: Structural Science* **49**, 145–146 (1993).

- [104] J. Demaison, “Accurate structures of non-rigid molecules by microwave spectroscopy”, in *Structures and Conformations of Non-Rigid Molecules*, edited by J. Laane, M. Dakkouri, B. van der Veken, and H. Oberhammer, NATO ASI Series (Springer Netherlands, Dordrecht, 1993), pp. 239–256.
- [105] Z. Kisiel, “Least-squares mass-dependence molecular structures for selected weakly bound intermolecular clusters”, *Journal of Molecular Spectroscopy* **218**, 58–67 (2003).
- [106] J. Kraitchman, “Determination of Molecular Structure from Microwave Spectroscopic Data”, *American Journal of Physics* **21**, 17–24 (1953).
- [107] M. J. Frisch, G. W. Trucks, H. B. Schlegel, G. E. Scuseria, M. A. Robb, J. R. Cheeseman, G. Scalmani, V. Barone, B. Mennucci, G. A. Petersson, H. Nakatsuji, M. Caricato, X. Li, H. P. Hratchian, A. F. Izmaylov, J. Bloino, G. Zheng, J. L. Sonnenberg, M. Hada, M. Ehara, K. Toyota, R. Fukuda, J. Hasegawa, M. Ishida, T. Nakajima, Y. Honda, O. Kitao, H. Nakai, T. Vreven, J. A. Montgomery Jr., J. E. Peralta, F. Ogliaro, M. Bearpark, J. J. Heyd, E. Brothers, K. N. Kudin, V. N. Staroverov, R. Kobayashi, J. Normand, K. Raghavachari, A. Rendell, J. C. Burant, S. S. Iyengar, J. Tomasi, M. Cossi, N. Rega, J. M. Millam, M. Klene, J. E. Knox, J. B. Cross, V. Bakken, C. Adamo, J. Jaramillo, R. Gomperts, R. E. Stratmann, O. Yazyev, A. J. Austin, R. Cammi, C. Pomelli, J. W. Ochterski, R. L. Martin, K. Morokuma, V. G. Zakrzewski, G. A. Voth, P. Salvador, J. J. Dannenberg, S. Dapprich, A. D. Daniels, Ö. Farkas, J. B. Foresman, J. V. Ortiz, J. Cioslowski, and D. J. Fox, *Gaussian 09 Revision D.01*, Gaussian Inc. Wallingford CT 2009.
- [108] F. Neese, “The ORCA program system”, *WIREs Computational Molecular Science* **2**, 73–78 (2012).
- [109] J. Zhang and M. Dolg, “ABCluster: the artificial bee colony algorithm for cluster global optimization”, *Physical Chemistry Chemical Physics* **17**, 24173–24181 (2015).
- [110] D. R. Hartree, “The Wave Mechanics of an Atom with a Non-Coulomb Central Field. Part II. Some Results and Discussion”, *Mathematical Proceedings of the Cambridge Philosophical Society* **24**, 111–132 (1928).
- [111] F. Weigend and R. Ahlrichs, “Balanced basis sets of split valence, triple zeta valence and quadruple zeta valence quality for H to Rn: Design and assessment of accuracy”, *Physical Chemistry Chemical Physics* **7**, 3297–3305 (2005).
- [112] R. Ditchfield, W. J. Hehre, and J. A. Pople, “Self-Consistent Molecular-Orbital Methods. IX. An Extended Gaussian-Type Basis for Molecular-Orbital Studies of Organic Molecules”, *The Journal of Chemical Physics* **54**, 724–728 (1971).

- [113] R. Krishnan, J. S. Binkley, R. Seeger, and J. A. Pople, “Self-consistent molecular orbital methods. XX. A basis set for correlated wave functions”, *The Journal of Chemical Physics* **72**, 650–654 (1980).
- [114] T. H. Dunning, “Gaussian basis sets for use in correlated molecular calculations. I. The atoms boron through neon and hydrogen”, *The Journal of Chemical Physics* **90**, 1007–1023 (1989).
- [115] T. M. Parker, L. A. Burns, R. M. Parrish, A. G. Ryno, and C. D. Sherrill, “Levels of symmetry adapted perturbation theory (SAPT). I. Efficiency and performance for interaction energies”, *The Journal of Chemical Physics* **140**, 094106 (2014).
- [116] B. Jeziorski, R. Moszynski, and K. Szalewicz, “Perturbation Theory Approach to Intermolecular Potential Energy Surfaces of van der Waals Complexes”, *Chemical Reviews* **94**, 1887–1930 (1994).
- [117] R. M. Parrish, L. A. Burns, D. G. A. Smith, A. C. Simmonett, A. E. DePrince, E. G. Hohenstein, U. Bozkaya, A. Y. Sokolov, R. Di Remigio, R. M. Richard, J. F. Gonthier, A. M. James, H. R. McAlexander, A. Kumar, M. Saitow, X. Wang, B. P. Pritchard, P. Verma, H. F. Schaefer, K. Patkowski, R. A. King, E. F. Valeev, F. A. Evangelista, J. M. Turney, T. D. Crawford, and C. D. Sherrill, “Psi4 1.1: an open-source electronic structure program emphasizing automation, advanced libraries, and interoperability”, *Journal of Chemical Theory and Computation* **13**, 3185–3197 (2017).
- [118] D. H. Levy, “Laser Spectroscopy of Cold Gas-Phase Molecules”, *Annual Review of Physical Chemistry* **31**, 197–225 (1980).
- [119] J. C. McGurk, T. G. Schmalz, and W. H. Flygare, “Fast passage in rotational spectroscopy: Theory and experiment”, *The Journal of Chemical Physics* **60**, 4181–4188 (1974).
- [120] J.-U. Grabow, “Fourier Transform Microwave Spectroscopy Measurement and Instrumentation”, in *Handbook of High-resolution Spectroscopy* (American Cancer Society, 2011).
- [121] B. E. Arenas, S. Gruet, A. L. Steber, B. M. Giuliano, and M. Schnell, “Chirped-pulse Fourier transform millimeter-wave spectroscopy of ten vibrationally excited states of i-propyl cyanide: exploring the far-infrared region”, *Physical Chemistry Chemical Physics* **19**, 1751–1756 (2017).
- [122] N. A. Seifert, I. A. Finneran, C. Perez, D. P. Zaleski, J. L. Neill, A. L. Steber, R. D. Suenram, A. Lesarri, S. T. Shipman, and B. H. Pate, “AUTOFIT, an automated fitting tool for broadband rotational spectra, and applications to 1-hexanal”, *Journal of Molecular Spectroscopy* **312**, 13–21 (2015).

- [123] D. P. Zaleski, J. L. Neill, M. T. Muckle, N. A. Seifert, P. Brandon Carroll, S. L. Widicus Weaver, and B. H. Pate, “A Ka-band chirped-pulse Fourier transform microwave spectrometer”, *Journal of Molecular Spectroscopy, Broadband Rotational Spectroscopy* **280**, 68–76 (2012).
- [124] D. P. Zaleski, “Exploring Interstellar Chemistry with Broadband Reaction Screening”, PhD thesis (University of Virginia, May 2013).
- [125] M. A. Suhm and F. Kollipost, “Femtosecond single-mole infrared spectroscopy of molecular clusters”, *Physical Chemistry Chemical Physics* **15**, 10702–10721 (2013).
- [126] A. Poblitzki, H. C. Gottschalk, and M. A. Suhm, “Tipping the Scales: Spectroscopic Tools for Intermolecular Energy Balances”, *The Journal of Physical Chemistry Letters* **8**, 5656–5665 (2017).
- [127] H. Fricke, K. Bartl, A. Funk, A. Gerlach, and M. Gerhards, “Proton/Hydrogen-Transfer Coordinate of 2,5-Dihydroxybenzoic Acid Investigated in a Supersonic Beam: Combined IR/UV Spectroscopy in the S₀, S₁, and D₀ States”, *ChemPhysChem* **9**, 2592–2600 (2008).
- [128] Y. Inokuchi, Y. Kobayashi, T. Ito, and T. Ebata, “Conformation of l-Tyrosine Studied by Fluorescence-Detected UV-UV and IR-UV Double-Resonance Spectroscopy”, *The Journal of Physical Chemistry A* **111**, 3209–3215 (2007).
- [129] D. Bernhard, F. Dietrich, M. Fatima, C. Perez, A. Poblitzki, G. Jansen, M. A. Suhm, M. Schnell, and M. Gerhards, “Multi-spectroscopic and theoretical analyses on the diphenyl ether–tert-butyl alcohol complex in the electronic ground and electronically excited state”, *Physical Chemistry Chemical Physics* **19**, 18076–18088 (2017).
- [130] K. C. Janda, J. C. Hemminger, J. S. Winn, S. E. Novick, S. J. Harris, and W. Klemperer, “Benzene dimer: A polar molecule”, *The Journal of Chemical Physics* **63**, 1419–1421 (1975).
- [131] B. F. Henson, G. V. Hartland, V. A. Ventura, and P. M. Felker, “Raman-vibronic double-resonance spectroscopy of benzene dimer isotopomers”, *The Journal of Chemical Physics* **97**, 2189–2208 (1992).
- [132] E. Arunan and H. S. Gutowsky, “The rotational spectrum, structure and dynamics of a benzene dimer”, *The Journal of Chemical Physics* **98**, 4294–4296 (1993).
- [133] A. v. d. Avoird, R. Podeszwa, K. Szalewicz, C. Leforestier, R. v. Harrevelt, P. R. Bunker, M. Schnell, G. v. Helden, and G. Meijer, “Vibration–rotation–tunneling states of the benzene dimer: an ab initio study”, *Physical Chemistry Chemical Physics* **12**, 8219–8240 (2010).

- [134] J. R. Grover, E. A. Walters, and E. T. Hui, “Dissociation energies of the benzene dimer and dimer cation”, *The Journal of Physical Chemistry* **91**, 3233–3237 (1987).
- [135] P. Banerjee, P. Pandey, and B. Bandyopadhyay, “Stereo-preference of camphor for H-bonding with phenol, methanol and chloroform: A combined matrix isolation IR spectroscopic and quantum chemical investigation”, *Spectrochimica Acta. Part A, Molecular and Biomolecular Spectroscopy* **209**, 186–195 (2019).
- [136] L. Pauling, *The Nature of the Chemical Bond and the Structure of Molecules and Crystals: An Introduction to Modern Structural Chemistry* (Cornell University Press, 1960).
- [137] J. Pearson, K. Sastry, E. Herbst, and F. De Lucia, “Gauche Ethyl Alcohol: Laboratory Assignments and Interstellar Identification”, *Astrophys. J.* **480**, 420–431 (1997).
- [138] N. Borho and Y. Xu, “Molecular recognition in 1 : 1 hydrogen-bonded complexes of oxirane and trans-2,3-dimethyloxirane with ethanol: a rotational spectroscopic and ab initio study”, *Physical Chemistry Chemical Physics* **9**, 4514–4520 (2007).
- [139] G. L. Blackman, R. D. Brown, and F. R. Burden, “The microwave spectrum, dipole moment, and nuclear quadrupole coupling constants of pyrimidine”, *Journal of Molecular Spectroscopy* **35**, 444–454 (1970).
- [140] L. B. Favero, I. Uriarte, L. Spada, P. Écija, C. Calabrese, W. Caminati, and E. J. Cocinero, “Solving the Tautomeric Equilibrium of Purine through Analysis of the Complex Hyperfine Structure of the Four ^{14}N Nuclei”, *The Journal of Physical Chemistry Letters* **7**, 1187–1191 (2016).
- [141] M. E. Sanz, S. Blanco, J. C. López, and J. L. Alonso, “Rotational Probes of Six Conformers of Neutral Cysteine”, *Angewandte Chemie International Edition* **47**, 6216–6220 (2008).

Appendix 1

Table 1: Linelist of conformer 1 of hexanal obtained from the segmented 18-26 GHz CP-FTMW spectrometer (Hamburg). The labelling $J_{K_a K_c} \leftarrow J'_{K'_a K'_c}$ represents the quantum numbers of the assigned rotational transitions of conformer 1. The fixed values of observed-calculated (o-c) represents the difference between the calculated frequency values of UVa 18-26 GHz CP-FTMW with the measured transitions obtained from Hamburg. The float o-c values are the difference between the measured and calculated frequency value obtained Hamburg.

J	K_a	K_c		J'	K'_a	K'_c	Hamburg	fixed o-c	float o-c
11	1	11	\leftarrow	10	1	10	18272.9760	0.0130	-0.0012
11	0	11	\leftarrow	10	0	10	18514.2640	0.0132	-0.0036
6	1	6	\leftarrow	5	0	5	18525.9833	0.0130	-0.0062
11	2	10	\leftarrow	10	2	9	18553.5751	0.0113	-0.0037
11	5	7	\leftarrow	10	5	6	18563.6154	0.0086	0.0065
11	4	8	\leftarrow	10	4	7	18564.6171	0.0060	-0.0017
11	3	9	\leftarrow	10	3	8	18566.8922	0.0194	0.0072
11	3	8	\leftarrow	10	3	7	18567.5916	-0.0041	-0.0164
15	0	15	\leftarrow	14	1	14	18616.0808	0.0084	0.0054
4	2	2	\leftarrow	5	1	5	18722.6930	0.0109	0.0051
11	1	10	\leftarrow	10	1	9	18825.7949	0.0133	-0.0062
12	1	12	\leftarrow	11	1	11	19931.8250	0.0100	0.0019
7	1	7	\leftarrow	6	0	6	20041.8871	0.0142	-0.0041
12	0	12	\leftarrow	11	0	11	20187.7581	0.0107	0.0001
12	2	11	\leftarrow	11	2	10	20238.5833	0.0124	0.0035

12	5	7	←	11	5	6	20251.5656	0.0012	0.0064
12	4	9	←	11	4	8	20252.9098	0.0066	0.0056
12	3	10	←	11	3	9	20255.7929	0.0155	0.0097
12	3	9	←	11	3	8	20256.9055	0.0037	-0.0020
12	2	10	←	11	2	9	20298.8864	0.0120	0.0019
12	1	11	←	11	1	10	20534.5539	0.0109	-0.0026
16	0	16	←	15	1	15	20567.6169	-0.0126	-0.0026
8	1	8	←	7	0	7	21535.6561	0.0138	-0.0023
13	1	13	←	12	1	12	21590.0992	0.0039	0.0037
13	0	13	←	12	0	12	21858.8462	0.0111	0.0086
13	2	12	←	12	2	11	21923.1390	-0.0014	-0.0021
13	4	10	←	12	4	9	21941.3323	-0.0187	-0.0109
13	3	11	←	12	3	10	21944.9123	0.0026	0.0052
13	3	10	←	12	3	9	21946.5817	-0.0134	-0.0109
13	2	11	←	12	2	10	21999.6310	0.0026	0.0004
13	1	12	←	12	1	11	22242.5747	0.0049	-0.0006
17	0	17	←	16	1	16	22523.0901	-0.0274	-0.0014
9	1	9	←	8	0	8	23008.3685	0.0142	0.0016
14	1	14	←	13	1	13	23247.7630	-0.0077	0.0022
14	0	14	←	13	0	13	23527.3723	-0.0017	0.0060
15	2	13	←	15	1	14	24308.8210	-0.0168	-0.0015
10	1	10	←	9	0	9	24461.2573	0.0131	0.0058
13	2	11	←	13	1	12	24804.8827	-0.0233	-0.0142
15	1	15	←	14	1	14	24904.7836	-0.0275	-0.0051
12	2	10	←	12	1	11	25047.8543	0.0068	0.0125
15	0	15	←	14	0	14	25193.2218	-0.0262	-0.0058
11	2	9	←	11	1	10	25283.5124	-0.0037	-0.0014
10	2	8	←	10	1	9	25509.2206	-0.0014	-0.0026
9	2	7	←	9	1	8	25722.4758	0.0058	0.0011

11	1	11	←	10	0	10	25895.7089	0.0069	0.0065
8	2	6	←	8	1	7	25920.9812	0.0090	0.0010

Table 2: Linelist of the ^{18}O isotopologue of conformer 1 of hexanal obtained from the segmented 18-26 GHz CP-FTMW spectrometer (Hamburg). The labelling $J_{K_a K_c} \leftarrow J'_{K'_a K'_c}$ represents the quantum numbers of the assigned rotational transitions of ^{18}O isotopologue of conformer 1. The fixed values of observed-calculated (o-c) represents the difference between the calculated frequency values of UVa 18-26 GHz CP-FTMW with the measured transitions obtained from Hamburg. The float o-c values are the difference between the measured and calculated frequency value obtained Hamburg.

J	K_a	K_c		J'	K'_a	K'_c	Hamburg	fixed o-c	float o-c
7	1	7	←	6	0	6	19476.3309	0.0313	0.0046
8	1	8	←	7	0	7	20924.6072	0.0167	-0.0020
9	1	9	←	8	0	8	22352.2767	-0.0070	-0.0153
10	1	10	←	9	0	9	23760.6029	0.0073	0.0122
5	2	3	←	5	1	4	25716.3034	-0.0041	-0.0061
4	2	2	←	4	1	3	25834.8541	0.0189	0.0063

Appendix 2

Hazardous substances according to the Global Harmonised System (GHS) within the EU:

Chemical	Hazard statements(s)	Precautionary statement(s)	GHS labeling
Water (H ₂ O)	–	–	–
Methanol (CH ₃ OH)	225-301 + 311 + 331-370	210-280-302 + 352 + 312-304 + 340 + 312-370 + 378-403 + P235	GHS02, GHS06, GHS08
Ethanol (C ₂ H ₅ OH)	225-319	P210-P305 + P351 + P338-P370 + P378-P403 + P235	GHS02, GHS07
Carbonyl sulfide (OCS)	220-280-315- 319-331-335	P210-P261-P305 + P351 + P338-P311-P410 + P403	GHS02, GHS06
<i>tert</i> -Butanol (C ₄ H ₁₀ O)	225-319-332- 335-336	P210-P261-P305 + P351 + P338-P370 + P378-P403 + P235	GHS02, GHS07
Hexanal (C ₆ H ₁₂ O)	226-319	P305 + P351 + P338	GHS02, GHS07
Phenyl vinyl ether (C ₈ H ₈ O)	225-302-317	P210-P280	GHS02, GHS07
1-adamantanol (C ₁₀ H ₁₆ O)	–	–	–
Camphor (C ₁₀ H ₁₆ O)	228-302 + 332-371	P210-P260-P301 + P312 + P330-P370 + P378	GHS02, GHS07, GHS08
Dibenzofuran (C ₁₂ H ₈ O)	302-411	P273	GHS07, GHS09
Diphenyl ether (C ₁₂ H ₁₀ O)	410	P273-P391-P501	GHS09
Fluorene (C ₁₃ H ₁₀)	410	P273-P501	GHS09



GHS01 Explosive



GHS04 Compressed Gas



GHS07 Harmful



GHS02 Flammable



GHS05 Corrosive



GHS08 Health Hazard



GHS03 Oxidizing



GHS06 Toxic



GHS09 Environmental Hazard

Acknowledgments

The doctoral journey of four and a half years in Hamburg would not have been possible without the love and support of so many people. I would like to thank all of them for being there for me and encouraging me to achieve my goal finally. This journey would never have started if it weren't for my cousin, Mohammad Ali Haider. He helped me during my application and presentation time to apply for the IMPRS position in the group of Melanie Schnell. He is and has always been an academic guide for me, and I thank him for where I am today.

I am really grateful to have Melanie Schnell as my doctorate supervisor. She is an amazing and very inspiring person. One of the best things about her, that has always kept me motivated, is that she always has a smile on her face. This has always encouraged me to be positive, no matter how stressful life can sometimes be. I really thank her for accepting me in her group, honing my skills through the years, and for all her support and patience with me. Most of all, for trusting me and inculcating an independent spirit in me.

I am thankful to Cristóbal Pérez and Amanda Steber. After Melanie, both of them have unofficially been my academic mentors. From Cristóbal, I learned a lot about dispersion interactions. Whenever I had any work problem, I could always go and knock on his door, and no matter how busy he was, he was always willing to help me. With Amanda, I learned the ins and outs of how to build the 18-26 GHz spectrometer, and also for fun, how to make cake and samosas. A lot of what I have learned in the field of microwave spectroscopy I owe to both of them.

I would like to thank all the members of the FS-SMP group (old: CoCoMol) Benjamin Arenas, Pragya Chopra, Cristóbal, Amanda, Sébastien Gruet, Anna Krin, Jack Graneek, Sérgio Domingos, Sabrina Zinn, Chris Medcraft, Donatella Loru, Maria del Mar Quesada Moreno, Pablo Pinacho, Daniel Obenchain, Weixing Li, Denis Tikhonov, Jason Lee, Diksha Garg, Gayatri Batra, Himanshi Singh and Maureen Ayon Alfaro. It was really wonderful to have all of them as my colleagues. Not only have they helped me at work, but they also taught me a lot about different

cultures around the world. They have been my lunch group as well as my evening outing group.

Within the group, I would also especially like to thank my officemates Benjamin Arenas and Pragya Chopra. I have been fortunate to have Ben as my work buddy from the very beginning. From brainstorming great ideas to having silly discussions, he's always my go-to person for everything and anything at work. From the time Pragya joined the FS-SMP group and our office, she is also the person with whom I like discussing great/stupid ideas. Both of them have always been there for me, and have given me a lot of moral support. I will miss both of them a lot, and mostly the time when both of them used to start singing in the office just to annoy me (kidding ;)).

I would also especially like to thank Sébastien Gruet, who left the group two years ago. During his time here, he has helped me a lot in building the 18-26 GHz spectrometer and taught me so many cool things.

I am grateful to Prof. Robert Field for giving me the opportunity to work in his lab at the Massachusetts Institute of Technology (MIT) for three months. My discussions with him have always encouraged me. I would also like to thank all his group members, especially Timothy J. Barnum, for helping me during my time there. Because of Tim, I learned how to work with lasers and buffer gas cell.

I would like to thank all my co-doctorate students in the multi-spectroscopic study, Anja Pablotzki, Dominic Bernhard, and Fabian Dietrich, and their supervisors Prof. Martin Suhm and Prof. Markus Gerhards, for all the great discussions. I would also like to thank Prof. Suhm again for hosting me in his group for two weeks and Anja, Robert Medel, and Hannes G. Gottschalk, for helping me during my stay in their group.

I would like to thank the administrative staff of MPSD and DESY, who have helped me at every step to settle in Hamburg and for always helping me deal with any administrative problems.

A special thanks go to the people who have helped me a lot during my thesis writing. Pablo, Ben, Amanda, Cristóbal, and Maria for proofreading my thesis. Andreas Przystawik and Hermann Hombrecher for helping me translate my thesis abstract to German. And Pragya for taking care of me.

Coming alone from India and settling in Hamburg, I would like to thank my friends

in Hamburg, who are now like family for me. Swathi Sasikumar for always being there for me, for taking care of me during all the ups and downs in life and also for making amazing home-cooked food for me. Pankaj Mishra for encouraging me to learn driving and for all the long coffee sessions in CFEL, and especially for teaching me how to make good coffee. Hermann and Melanie Peuker, for inviting me so many times for amazing breakfasts and being there all the time.

I am really indebted to all my friends from India. Their love and support have kept me strong in many ways throughout my life. This list will never be complete, but I would especially like to acknowledge Atul Mantri, Ankush Checkerbarty, Kodaman-chali Rahul, Kartik Srivastav, Sapna Meena, Sonali Mohapatra, Ananya Kundu, Neetu Sharma, Nirdosh Dadwal and Ravi Yadav.

Lastly, I would like to thank my relatives and family members. I am really very grateful for all your love and support. Khursheed Anwer (dad), Masarrat Anwer (mom), Zehra Fatima (sister), and Mohammad Ali (brother), I cannot have reached this stage in my life without their encouragement. I thank them for calling me almost every day and making sure that I am fine. At times when I have given up, my mom and dad have always been by my side and stood up for me. My family is the biggest support for me, and I know I can always count on them no matter what happens in the future.

Declaration

I hereby declare that this thesis is my original work and it has been written by me in its entirety. I have duly acknowledged all the sources of information which have been used in the thesis.

September 14, 2020
Hamburg

Mariyam Fatima

I hereby declare that I have contributed the following share in the publications emerging from the work presented in this thesis:

1. D. Bernhard, F. Dietrich, M. Fatima, C. Pérez, A. Poblitzki, G. Jansen, M. A. Suhm, M. Schnell, M. Gerhards *Multi-spectroscopic and theoretical analyses on the diphenyl ether-tert-butyl alcohol complex in the electronic ground and electronically excited state*, Phys. Chem. Chem. Phys. **19**, 18076-18088 (2017).
 - Proportion of practical work in the microwave part: 70%
 - Share of manuscript formulation: 20%
2. F. Dietrich, D. Bernhard, M. Fatima, C. Pérez, M. Schnell, M. Gerhards *The Effect of Dispersion on the Structure of Diphenyl Ether Aggregates*, Angew. Chem. Int. Ed. **57**, 9534 (2018).
 - Proportion of practical work in the microwave part: 70%
 - Share of manuscript formulation: 30%

3. D. Bernhard, F. Dietrich, M. Fatima, C. Pérez, H.C. Gottschalk, A. Wuttke, R. A. Mata, M.A. Suhm, M. Schnell, M. Gerhards *The phenyl vinyl ether–methanol complex: a model system for quantum chemistry benchmarking*, Beilstein J. Org. Chem. **14**, 1642–1654 (2018).
 - Proportion of practical work in the microwave part: 90%
 - Share of manuscript formulation: 30%
4. M. Fatima, A. L. Steber, A. Poblitzki, C. Pérez, S. Zinn, M. Schnell *Rotational Signatures of Dispersive Stacking in the Formation of Aromatic Dimers*, Angew. Chem. Int. Ed. **58**, 3108 (2019).
 - Proportion of practical work in the microwave part: 70%
 - Share of manuscript formulation: 50%
5. D. Bernhard, M. Fatima, A. Poblitzki, A. L. Steber, C. Pérez, M. A. Suhm, M. Schnell and M. Gerhards *Dispersion-controlled docking preference: multi-spectroscopic study on complexes of dibenzofuran with alcohols and water*, Phys. Chem. Chem. Phys. **21**, 16032-16046 (2019).
 - Proportion of practical work in the microwave part: 80%
 - Share of manuscript formulation: 30%

Mariyam Fatima